

**ADVANCES OF MID-INFRARED PHOTOTHERMAL MICROSCOPY
FOR IMPROVED CHEMICAL IMAGING**

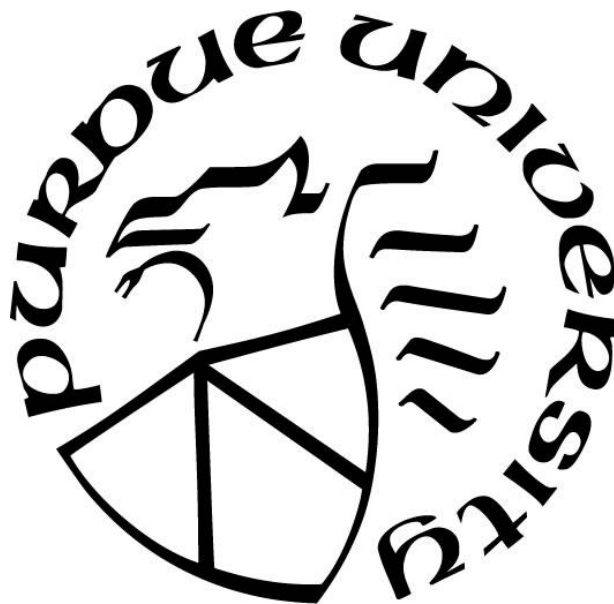
by
Chen Li

A Dissertation

Submitted to the Faculty of Purdue University

In Partial Fulfillment of the Requirements for the degree of

Doctor of Philosophy



Department of Chemistry

West Lafayette, Indiana

May 2020

**THE PURDUE UNIVERSITY GRADUATE SCHOOL
STATEMENT OF COMMITTEE APPROVAL**

Dr. Garth J. Simpson, Chair

Department of Chemistry

Dr. Ji-Xin Cheng

School of Biomedical Engineering, Boston University

Dr. Libai Huang

Department of Chemistry

Dr. Fang Huang

Weldon School of Biomedical Engineering

Approved by:

Dr. Christine Hrycyna

Dedicated to Ruoxing, my parents, and all my friends, who stay with me through all the difficulties.

ACKNOWLEDGMENTS

I am grateful to all professors, collaborators, colleagues, and friends, who helped me to accomplish so many commitments during the past five years. First of all, I want to thank my parents, Jinsong Li and Kaixia Lu, for your fully support of all my decisions. I can always receive encouragement and comfort that carried me through the mist from you whenever I feel depressed.

Then, I would like to thank my two advisors, Dr. Garth J. Simpson and Dr. Ji-Xin Cheng. Both professors are brilliant and enthusiastic. I have learned not only priceless knowledge but also approaches to reveal the solutions to one and another problems. In particular, I appreciate Dr. Cheng as a strict advisor, who motivates me to always pursue the best. I thank Dr. Simpson as a patient mentor who turns complex mathematical equations to a joyful journey.

I also want to show my thanks to my collaborators and former colleagues who are now in Boston University and Zhejiang University. Dr. Delong Zhang and Dr. Yeran Bai were my best mentor and lab mates in Cheng group. I could not make such progresses without your efforts. I thank Dr. Andy Chen, Dr. Putting Dong, Dr. Jie Hui, Dr. Weili Hong, Dr. Kai-Chih Huang, Dr. Lu Lan, Dr. Hyeon Jeong Lee, Dr. Junjie Li, Dr. Rui Li, Dr. Mikhail Slipchenko, Dr. Pu Wang, Dr. Chi Zhang, Haonan Lin, Peng Lin, Ying Jiang, and Jiayingzi Wu for all the unforgettable moments I shared with you in my first two years in Purdue.

I must also thank every colleague and friend in the Simpson group for your colorful activities, excellent bakeries, unconditional support to each other during the past three years. Even some of you have graduated, I keep in close touch with you as you are already a part of my life. My gratefulness to Dr. Changqin Ding, Dr. Fengyuan Deng, Dr. Sreya Sakar, Dr. Zhengtian Song, Dr. Shijie Zhang, Dr. James Ulcickas, Dr. Scott Griffin, Dr. Casey Smith, Hilary Florian, Andreas Geiger, Youlin Liu, Alex Sherman, Ziyi Cao, Minghe Li, Jiayue Rong, Nita Takanti.

Furthermore, I want to thank all my friends who created numerous great memories with me in Purdue. Aaron Chen, Fan Pu, Pei Su, Zhuoer Xie, Yun Yang, Yiyang Zhou, Heng Du, Jingshuang Chen, Dali Guo, Xiaodong Huang, Xiaofeng Ou, Yifu Wang, Jiahao Zhang, thank you all for all the parties, dishes, and soccer matches we enjoyed together. Some special thanks to the friends including Jeffwhy, Haksal, NBCLASS, Howoldareyou, St3fan, Domino, Cholanes, Zeroomega, QiQi, and KevinHou, who have been playing overwatch together with me during the past 3 years.

Last but not the least, I want to thank a great woman who stands with me, supports me, and will soon be marrying me. Ruoxing, you are the origin of all my strength, courage, and ambitions. I will accompany you, as how you has been doing to me, to achieve our shared goals in the rest of my life.

TABLE OF CONTENTS

LIST OF TABLES	10
LIST OF FIGURES	11
LIST OF ABBREVIATIONS.....	14
ABSTRACT.....	16
CHAPTER 1. INTRODUCTION	17
1.1 Label-free chemical imaging based on vibrational spectroscopy	17
1.2 Mid-infrared spectroscopic imaging.....	18
1.3 Wavefront shaping for enhanced optical imaging.....	19
1.4 Dissertation overview	20
1.5 References.....	21
CHAPTER 2. DEPTH-RESOLVED MID-INFRARED PHOTOTHERMAL IMAGING OF LIVING CELLS AND ORGANISMS WITH SUBMICROMETER SPATIAL RESOLUTION	25
2.1 Introduction.....	25
2.2 Methods	27
2.2.1 Origin of the MIP contrast.....	27
2.2.2 Strategies to improve the SNR	28
2.2.3 Schematic of the MIP microscope.....	29
2.2.4 Materials and sample preparation.....	31
2.2.5 Image analysis	32
2.3 Results.....	32
2.3.1 Spectral fidelity and LoD of the MIP spectromicroscopy	32
2.3.2 Characterization of the spatial resolution of the MIP microscope	33
2.3.3 Multiscale MIP imaging of lipids in live cells	35
2.3.4 Multispectral MIP imaging of intracellular molecules.....	36
2.3.5 <i>In vivo</i> MIP imaging of living <i>C. elegans</i>	37
2.4 Discussion.....	39
2.5 References.....	40
CHAPTER 3. MID-INFRARED PHOTOTHERMAL IMAGING OF ACTIVE PHARMACEUTICAL INGREDIENTS AT SUBMICROMETER SPATIAL RESOLUTION.	43

3.1	Introduction.....	43
3.2	Methods	45
3.2.1	Components of the epi-detected MIP microscope	45
3.2.2	Fourier-transform infrared spectra measurement	46
3.2.3	Samples	46
3.3	Results and discussion	47
3.3.1	Schematic of the microscope.....	47
3.3.2	Characterization.....	47
3.3.3	Tablet imaging.....	49
3.4	Conclusion	53
3.5	References.....	53
CHAPTER 4. MID-INFRARED PHOTOTHERMAL IMAGING OF NEWLY SYNTHESIZED LIPIDS IN CELLS BY FEMTOSECOND LASER.....		57
4.1	Introduction.....	57
4.2	Theoretical calculation.....	59
4.3	Methods	61
4.3.1	DFG Implementation.....	61
4.3.2	MIP microscope	62
4.3.3	Spectral focusing	63
4.3.4	A549 cell imaging	63
4.4	Results.....	63
4.4.1	DFG output.....	63
4.4.2	Improved spectral resolution based on spectral focusing.....	64
4.4.3	Spectral fidelity of DFG-pumped MIP microscope	65
4.4.4	High-wavenumber MIP imaging of live A549 cells	66
4.5	Conclusions.....	68
4.6	References.....	68
CHAPTER 5. POLARIZATION WAVEFRONT SHAPING FOR QUANTITATIVE PHASE CONTRAST IMAGING BY AXIALLY-OFFSET DIFFERENTIAL INTERFERENCE CONTRAST (ADIC).....		72
5.1	Introduction.....	72

5.2	Methods	74
5.2.1	Polarization wavefront shaping of μ RA	74
5.2.2	Instrumentation.....	76
5.2.3	Sample preparation.....	78
5.2.4	Quantitative phase recovery	78
5.3	Results and discussion	79
5.3.1	Axially-offset dual-foci produced by μ RA.....	79
5.3.2	Quantitative phase contrast imaging using ADIC	81
5.3.3	Limit of detection (LoD) of quantitative phase recovery	81
5.3.4	Refractive index calculation of microspheres	82
5.4	Conclusion	83
5.5	References.....	83
CHAPTER 6. DEPTH-OF-FIELD EXTENSION IN OPTICAL IMAGING FOR RAPID CRYSTAL SCREENING.....		86
6.1	Introduction.....	86
6.2	Experimental Methods.....	88
6.3	Results and Discussion	89
6.4	Conclusion	96
6.5	References.....	97
CHAPTER 7. MULTIFOCUS IMAGING VIA POLARIZATION WAVEFRONT SHAPING .		99
7.1	Introduction.....	99
7.2	Theory	100
7.2.1	Multifocus generation via polarization wavefront shaping.....	100
7.2.2	Demultiplexing of multifocus images in bright field microscopy	103
7.2.3	Demultiplexing of multifocus images in TPEF microscopy	104
7.3	Methods	106
7.3.1	Microscopy.....	106
7.3.2	Sample preparation.....	107
7.4	Results and discussion	107
7.4.1	Demonstration of multifocus imaging in bright field microscopy	107

7.4.2 Demonstration of multifocus imaging in TPEF microscopy.....	107
7.5 References.....	109
VITA.....	111
PUBLICATIONS.....	112

LIST OF TABLES

Table 6-1 Comparison of crystal counts in 9 different wells with the extended DoF approach and conventional SHG microscopy.	94
--	----

LIST OF FIGURES

Figure 2-1 Strategies for improved SNR of MIP microscopy..	29
Figure 2-2 Schematic of the MIP microscope..	30
Figure 2-3 (A) Raw MIP spectrum of polystyrene film. (B) Infrared power across the spectral window, recorded by the MCT detector. Negative spikes in the curve are due to water vapor absorption. (C) MIP spectrum after power normalization. The power drop at around 1629 cm^{-1} are due to the gap between two laser tuners. (D) Infrared power profile when the system is being purged by dry nitrogen. This step can eliminate the errors caused by the water vapor absorption. (E) Spectral fidelity. Comparison of MIP spectral profiles (red) and FTIR spectra (black) of polystyrene film (top) and olive oil (bottom). The FTIR spectra were acquired by an attenuated total reflection FTIR spectrometer. (F) Sensitivity. MIP signal of γ -valerolactone in carbon disulfide at various concentrations. Inset shows the molecular structure.	34
Figure 2-4 Spatial resolution. MIP imaging of a 500-nm PMMA bead.	35
Figure 2-5 3D MIP imaging of lipids in live cells...	36
Figure 2-6 (A). IR spectra of JZ-184 (top) and lipid content (bottom). A stack of MIP images acquired at 9 different frequencies were analyzed with MCR-ALS to generate the intracellular distribution of the drug molecule (B) and lipid droplets (C).	37
Figure 2-7 In vivo MIP imaging of lipid and protein in <i>C. elegans</i> ..	38
Figure 3-1 Schematic of the epi-MIP microscope..	47
Figure 3-2 Characterization of the epi-MIP microscope.	48
Figure 3-3 The structures of selected molecules in Tylenol. (A): acetaminophen, (B): starch (corn), (C): PVP and (D): starch glycolate (the acid form of sodium starch glycolate).	49
Figure 3-4 Identification of different species in Tylenol tablet.	50
Figure 3-5 Epi-MIP images of API and excipients in a Tylenol tablet.	51
Figure 3-6 Epi-MIP imaging of acetaminophen at 5 different depth covering a 40 μm range from the surface. The intensity of 5 images are uniform. MIR excitation wavenumber: 1502 cm^{-1} .	52
Figure 4-1 Focusing function $h(\xi)$ versus ξ calculated for $\lambda p = 830 \text{ nm}$, $\lambda s = 1080 \text{ nm}$, and crystal length of 5 mm. The typical values of 5 lenses with different focal length were labeled in the curve.	60
Figure 4-2 Schematic of a DFG-pumped MIP microscope..	62
Figure 4-3 DFG average output idler powers versus input pump powers with the signal power fixed at 280 mW. Maximum of 30.2 mW was achieved with the pump power of 360 mW.	64
Figure 4-4 Performance and calibration of spectral focusing..	65

Figure 4-5 Spectral fidelity of the DFG-pumped MIP microscope. FTIR (dashed) and MIP spectrum (solid) showed overall consistency. Raw MIP spectra were normalized by the mid-IR intensities recorded by the MCT detector.....	65
Figure 4-6 High-wavenumber MIP image of A549 lung cancer cells.....	67
Figure 5-1 (A) The design of μ RA as half-wave retardance with the spatially varied azimuthal orientation of the fast-axis targeted for 532 nm light. Scale bar: 500 μ m. Bottom: part of the measured different intensity distribution with horizontal (H) and vertical (V) polarization detection when horizontally polarized light passing through the μ RA. (B) The working principle of ADIC microscope. L1 and L2: lens; RP: reference plane; SP: sample plane.....	75
Figure 5-2 Instrumentation set-up for ADIC with a 10x objective to recover both bright field images and quantitative phase contrast images..	77
Figure 5-3 Measured point spread functions in the x-z plane without (A) and with (B) the μ RA placed in the beam path.....	80
Figure 5-4 Images measured from LIA detection with $1f$ (A, B) and $2f$ (C, D) as the reference, and the recovered transmittance bright field image (E) and quantitative phase contrast image (F) of a single FoV of mouse tail section. Color bar unit: (E) transmittance percentage, (F) phase shift in radian. Scale bar: 50 μ m.	82
Figure 5-5 Recovered transmittance (A) and quantitative phase contrast images (B) of the same FoV of 8 μ m silica microbeads. Color bar unit: (A) transmittance percentage; (B) phase shift in radian. (C) Phase shift line profiles of the cross line in the insert.	83
Figure 6-1 Schematic of the μ RA and the extension of the DoF.....	90
Figure 6-2 SHG images of BaTiO ₃ nanoparticles immobilized in PEG.....	91
Figure 6-3 (A) Z-projection of a series of SHG images of ritonavir crystals measured with conventional method. (B) Single SHG image of the same field-of-view with the μ RA. (C) An overlay of (A) and (B).....	92
Figure 6-4 (A-C) SHG images of intercalated lysozyme crystals at various z-axis positions. (D) Z-projection of (A-C). SHG image of the same field-of-view with the μ RA using (E) the same exposure time and (F) doubled exposure time.....	93
Table 6-1 Comparison of crystal counts in 9 different wells with the extended DoF approach and conventional SHG microscopy.	94
Figure 6-5 Measured point spread functions in the x-z plane before (A) and after (B) the installation of the μ RA in the optical beam path. (C) Point spread functions along z-axis with and without the μ RA provide quantitative analysis of the extension ratio of the DoF as 2.8.	94
Figure 6-6 (A) Depth-resolved SHG intensity of z-cut quartz measured with extended DoF and varied excitation wavelength. (B) Comparison of theoretical prediction (red line) and measurements (plots) of the extended DoF as a function of excitation wavelength.	97

Figure 7-1 Instrument schematic of the custom-built beam-scanning microscope for method validation. The μ RA is installed right before the objective lens. The system was operated in one channel mode (photodiode only) for bright-field imaging. 101

Figure 7-2 Workflow of the demultiplexing and 3D reconstruction process of multifocus imaging via PWS. The blue and red particles represent different species with various special locations. 104

Figure 7-3 Instrument schematic of the custom-built beam-scanning microscope for method validation. The μ RA is installed before the objective lens. 106

Figure 7-4 Demultiplexed bright field images of microsphere mixture at three focal planes. The raw image stack was acquired within half second... 108

Figure 7-5 Demultiplexed TPEF images of Rhodamine 6G at three focal planes. The raw image stack was acquired within half second..... 109

LIST OF ABBREVIATIONS

ADIC	Axially-offset differential interference contrast
AOM	Acousto-optic modulator
API	Active pharmaceutical ingredient
ASD	Amorphous solid dispersion
ATR-FTIR	Attenuated total reflectance-Fourier transform infrared
DIC	Differential interference contrast
DFG	Difference frequency generation
DM	Dichroic mirror
DoF	Depth-of-field
FoV	Field-of-view
FTIR	Fourier transform infrared
FWHM	Full-width at half-maximum
FZP	Fresnel zone plate
GSD	Ground state depletion
HWP	Half wave plate
IR	Infrared
LCP	Left circular polarized
LED	Light-emitting diode
LIA	Lock-in amplifier
MCT	Mercury-Cadmium-Telluride
MCR-ALS	Multivariate curve resolution- alternating least square
MIP	Mid-infrared photothermal
MIR	Mid-infrared

NA	Numerical aperture
NIR	Near-infrared
OPA	Optical parametric amplifier
OPO	Optical parametric oscillator
PEG	Polyethylene glycol
PEM	Photoelastic electro-modulator
PMMA	Polymethyl methacrylate
PMT	Photomultiplier tube
PSF	Point-spread-function
PVP	Polyvinylpyrrolidone
QCL	Quantum cascade laser
QPI	Quantitative phase imaging
QPM	Quantitative phase microscopy
QWP	Quarter wave plater
RCP	Right circular polarization
SHG	Second harmonic generation
SNR	Signal-to-noise ratio
SSG	Sodium starch glycolate
STED	Stimulated emission depletion
TPEF	Two-photon excited fluorescence
TPE-UVF	Two-photon excited-ultraviolet fluorescence
μ RA	Micro-retarder array
3D	Three dimensional

ABSTRACT

Vibrational spectroscopic imaging has become an emerging platform for chemical visualization of biomolecules and materials in complex systems. For over a century, both Raman and infrared spectroscopy have demonstrated the capability to recognize molecules of interest by harnessing the characteristic features from molecular fingerprints. With the recent development of hyperspectral vibrational spectroscopy imaging, which records the chemical information without sacrificing the spatial-temporal resolution, numerous discoveries have been achieved in the field of molecular and cellular biology. Despite the ability to provide complimentary chemical information to Raman-based approaches, infrared spectroscopy has not been extensively applied in routine studies due to several fundamental limitations: 1). the poor spatial resolution; 2). inevitable strong water absorption; 3). lack of depth resolution.

Mid-infrared photothermal (MIP) microscopy overcame all the above mentioned problems and for the first time, enabled depth-resolved *in vivo* infrared imaging of live cells, microorganisms with submicrometer spatial resolution. The development of epi-detected MIP microscopy further extends its application in pharmaceutical and materials sciences. With the deployment of difference frequency generation and other nonlinear optical techniques, the spectral coverage of the MIP microscopy was significantly enhanced to enable chemical differentiation in complex systems across the broad mid-infrared region. In addition to the efforts to directly improve the performance of MIP microscopy, a novel quantitative phase imaging approach based on polarization wavefront shaping via custom-designed micro-retarder arrays was developed to take advantage of the highly sensitive phase measurement in combination with the photothermal effect. Besides, the extended depth-of-field and multifocus imaging enabled by polarization wavefront shaping could both improve the performance of MIP microscopy for volumetric imaging.

CHAPTER 1. INTRODUCTION

1.1 Label-free chemical imaging based on vibrational spectroscopy

Ever since Robert Hooke invented one of the first compound microscopes and discovered what he later called ‘cells’ in 1665, biological science has entered the era of cell biology, which aims to reveal the secret of life by understanding the elemental unit of organisms. Over the centuries, there has been an increasing demand for advanced microscopic techniques to investigate the morphology of subcellular structures and organelles. The invention of Köhler illumination,¹ phase contrast microscopy,²⁻³ differential interference contrast microscopy⁴ and fluorescence microscopy⁵ enabled numerous discoveries based on the high quality morphological information. In the meantime, advances of *in vitro* analytical tools and methods in analytical chemistry and biochemistry have also resulted in many milestones in the field of molecular biology.⁶⁻⁸ However, cell is a complex micro-factory instead of a vial of molecules, where thousands of organelles, enzymes, and signaling molecules work collectively to transform elemental molecules to essential products that sustain the activity of cells and the whole organisms.⁹ To better understand the intracellular and intercellular biochemical reaction networks, analytical tools that are capable to extract the chemical information while retaining spatial temporal resolution with minimal invasion to cells are in need.

Chemical imaging became an emerging field to address the abovementioned problem since the discovery of green fluorescent protein which revolutionized the fluorescence microscopy and enabled targeted investigation of certain biochemical reactions in organisms.¹⁰⁻¹² From late 90th, a multitude of far-field super-resolution microscopic technique including STED,¹³⁻¹⁵ GSD,¹⁶⁻¹⁷ RESOLF,¹⁸⁻¹⁹ etc. have enabled chemical imaging at nanoscale resolution. Furthermore, efforts dedicated to the development of novel fluorescent probes have contributed to the rapidly growing discoveries in oncology,²⁰ neuroscience,²¹ and microbiology²² related to specifically labeled proteins and nucleic acids. Despite all the scientific advances enabled by the fluorescence-based super-resolution microscopy, there are several limitations remaining in the labeling approaches: 1) the relatively large fluorescent labels are unable to be used to study small molecules such as lipids, amino acids, and neurotransmitters; 2) labeling could perturb the normal functions of a

biomolecule or structure; 3).delivery of fluorescent probes to the targeted receptors could be difficult; 4). external labels can have potential toxicity which hinders applications in *in vivo* studies.

To circumvent these barriers, label-free chemical imaging based on vibrational spectroscopy emerged as a promising platform for *in vivo* studies.²³ By harnessing the characteristic features in vibrational spectra, molecules can be recognized distinctively from others without external labels. Although both mid-infrared (mid-IR) and Raman spectroscopy can record the “fingerprints” of molecules, only Raman has been extensively utilized to study live cells or tissues, because the strong water absorption hampered the application of mid-IR in aqueous mediums. The transition from vibration spectroscopy is not only integrating a spectrometer to a conventional microscope but also a continuous pursuit of higher signal-to-noise ratio and faster electronic components in order to achieve decent performance. Spontaneous Raman microscope, which detects the weak frequency-shifted scattering photons generated from excited molecules, has come a long way to achieve millisecond per pixel imaging speed.²⁴ More recently, coherent Raman microscopy such as coherent anti-Stokes Raman scattering²⁵ and stimulated Raman scattering²⁶ has both demonstrated video rate imaging by taking advantage of the nonlinear optical processes. In particular, stimulated Raman scattering has enabled further understanding of the mechanism of cholesterol ester accumulation in aggressive prostate cancers.²⁷ However, the extremely small cross section of the Raman scattering (10^{-30} cm²/sr) determines that the limit of detection of such techniques is hard to break through the physical limit. As a complementary approach to probe chemical bond vibrations, mid-IR spectroscopy, which directly measures the linear absorption of chemical bonds, has a much larger cross section (10^{-22} cm²/sr).²⁸ The resolving power for low concentration analysis could be improved significantly if mid-IR absorption is utilized as a contrast mechanism in the investigation of living systems.

1.2 Mid-infrared spectroscopic imaging

Infrared (IR) was first discovered by Frederick William Herschel when he observed that the temperature increase of a thermometer was the largest when it was illuminated by the far-red invisible portion of sunlight split by a prism.²⁹ Centuries later, IR spectroscopy has been widely used to characterize various molecules and W.W. Coblentz built the first high-quality mid-IR database using a home-built IR spectrometer.³⁰ With the development of molecular orbital theory in physical chemistry, it was realized that the mid-IR absorption directly represents the vibrations

of chemical bonds which are the elemental units of all molecules. After the development of Fourier transform IR spectrometer³¹ and focal plane array detector,³² the applications of mid-IR spectroscopic imaging has extended to numerous fields including cell biology,³³ biomedical tissue diagnostics, polymeric, forensic samples, and plants.³⁴⁻³⁶ Most recently, the rapid development of high quality mid-IR laser source, such as quantum cascade laser (QCL) and optical parametric amplifier (OPA) laser, has allowed for fast IR measurements with high signal-to-noise ratio. However, several fundamental limitations have long been hindering the broad applications of mid-IR spectroscopic imaging in biological and biomedical sciences. First, the long wavelength of mid-IR provides no better than 5 μm spatial resolution, which is already half the diameter of most cells. Second, strong water band has been a barrier for all direct measurements of mid-IR absorption. Finally, the linear absorption mechanism results in the loss of depth resolution, which preclude the mid-IR spectroscopic imaging techniques from multidimensional imaging. To address the abovementioned problems, a novel mechanism is needed to enable subcellular mid-IR spectroscopic imaging for live cells and organisms with extraordinary sensitivity.

1.3 Wavefront shaping for enhanced optical imaging

In addition to efforts dedicated to developing new contrast mechanisms for vibrational spectroscopic imaging, researchers in the field of label-free chemical imaging have also been exploring innovations to enable lower detection limit, higher sensitivity, and larger throughput. Wavefront shaping has shown its potentials to improve the performances of optical microscopic modalities. For instance, wavefront shaping using an optimized phase pupil mask has been demonstrated to extend the depth-of-field of the imaging system to achieve higher throughput for multidimensional imaging.³⁷ It is especially useful for nonlinear optical imaging, such as stimulated Raman scattering, two-photon fluorescence, second harmonic generation, etc., since the depth-of-field is much smaller compared to that of single photon process. In another example, active wavefront shaping was performed in real-time with a spatial light modulator to image through scattering media.³⁸ This opens the opportunity for deep tissue imaging which has been problematic due to strong scattering and deformation of the wavefront induced by the refractive index mismatch of tissue contents. The field of wavefront shaping has generated numerous creative approaches to tackle various problems. This dissertation, however, will introduce a wavefront shaping approach based on polarization spatial modulation to achieve quantitative phase imaging,

extended depth-of-field, and multifocus imaging by fully exploiting the encoded polarization information. All of the demonstrations enabled by polarization wavefront shaping have the potential to benefit the performance of mid-IR spectromicroscopy to provide complementary approaches to unveil the unknown mysteries in biological systems.

1.4 Dissertation overview

The following chapters of this dissertation includes a collection of works on the development of the mid-infrared photothermal microscopy (MIP) as well as its applications in biological and pharmaceutical sciences. This novel infrared spectroscopic imaging approach was demonstrated in both transmittance and back-reflectance configurations. Attempt to extend the spectral coverage by implementing new laser source was also covered. Apart from efforts that are directly relating to the photothermal microscopy, this dissertation introduces several innovations enabled by polarization wavefront shaping including quantitative phase imaging, depth-of-field extension, and rapid multifocus imaging, which all have the potential to improve the performance of the MIP microscopy.

Chapter 2 illustrates the state of art of the depth-resolved MIP microscopy, which achieved *in vivo* mid-IR spectroscopic imaging with submicrometer spatial resolution for the first time. Detailed contrast mechanism as well as the schematics The MIP approach was successfully demonstrated through selective imaging of endogenous biomolecules and drug molecules including lipid contents, proteins, and lipase inhibitor in live cells and microorganisms. It also covers an in-depth discussion of the potential future works to further improve this technique.

The work illustrated in *Chapter 3* was based on the fundamental framework in *Chapter 1* but moved a step further to achieve the epi-detected MIP microscope for chemical imaging of opaque samples. Pharmaceutical tablets were used as the testbed to demonstrate multispectral chemical mapping of active pharmaceutical ingredient as well as abundant excipients with submicrometer spatial resolution. It promises potential applications of such technique in pharmaceutical industry for quality control, process analysis, online monitoring, and etc.

Chapter 4 is another extended work on the basis of *Chapter 2*, which introduces a strategy to extend the spectral coverage in high-wavenumber region by utilizing differential frequency generation pumped by existing femtosecond lasers. Such amendment enabled mid-IR

spectroscopic imaging of deuterated molecules to facilitate the investigation of lipogenesis or proteogenesis in cells.

The works enabled by polarization wavefront shaping for the enhancement of the performances of optical microscopy were illustrated in *Chapter 5*, *6*, and *7*. Among them, *Chapter 5* introduces a novel quantitative phase imaging approach which enables per pixel based optical phase analysis in a common path scheme by generating multiple axially offset foci. More importantly, the presented method is compatible with almost any existing optical microscopes, which opens the opportunity for broad applications in numerous well-developed microscopic techniques. In particular, its capability to quantify the optical phase (refractive index) with high sensitivity could potentially be deployed in MIP microscopy to achieve much lower detection limit. To improve the throughput of multidimensional optical imaging systems, *Chapter 6* illustrates a simple approach to extend the depth-of-field of microscopes via polarization wavefront shaping. Such approach was demonstrated in a beam-scanning nonlinear optical imaging platform for large batch crystal screening. The compatibility of this technique should enable its implementation in various of optical imaging modalities including bright-field, fluorescence, and multiphoton microscopes. As another demonstration of utilizing the multiple foci generated by polarization wavefront shaping, *Chapter 7* proposes a method for multifocus imaging that could potentially be beneficial to some community in the field of multiscale imaging. A mathematical framework to demultiplex the bright field images from three focal planes was built and validated. The illustrated approach could potentially be applied in more complex imaging modalities such as two photon excited fluorescence and second harmonic generation microscopy.

1.5 References

1. Hopkins, H. H.; Barham, P. M., The Influence of the Condenser on Microscopic Resolution. *Proceedings of the Physical Society. Section B* **1950**, *63* (10), 737-744.
2. Zernike, F., Phase contrast, a new method for the microscopic observation of transparent objects part II. *Physica* **1942**, *9* (10), 974-986.
3. Zernike, F., How I discovered phase contrast. *Science* **1955**, *121* (3141), 345-349.
4. Georges, N., Interferential polarizing device for study of phase objects. Google Patents: 1960.
5. Lichtman, J. W.; Conchello, J.-A., Fluorescence microscopy. *Nature Methods* **2005**, *2* (12), 910-919.

6. Mann, M.; Højrup, P.; Roepstorff, P., Use of mass spectrometric molecular weight information to identify proteins in sequence databases. *Biological Mass Spectrometry* **1993**, 22 (6), 338-345.
7. Aebersold, R.; Mann, M., Mass spectrometry-based proteomics. *Nature* **2003**, 422 (6928), 198-207.
8. Creek, D. J.; Jankevics, A.; Burgess, K. E. V.; Breitling, R.; Barrett, M. P., IDEOM: an Excel interface for analysis of LC-MS-based metabolomics data. *Bioinformatics* **2012**, 28 (7), 1048-1049.
9. Davy, A. M.; Kildegaard, H. F.; Andersen, M. R., Cell Factory Engineering. *Cell Systems* **2017**, 4 (3), 262-275.
10. Tsien, R. Y., THE GREEN FLUORESCENT PROTEIN. *Annual Review of Biochemistry* **1998**, 67 (1), 509-544.
11. Cormack, B. P.; Valdivia, R. H.; Falkow, S., FACS-optimized mutants of the green fluorescent protein (GFP). *Gene* **1996**, 173 (1), 33-38.
12. Heim, R.; Prasher, D. C.; Tsien, R. Y., Wavelength mutations and posttranslational autoxidation of green fluorescent protein. *Proceedings of the National Academy of Sciences* **1994**, 91 (26), 12501-12504.
13. Hell, S. W.; Wichmann, J., Breaking the diffraction resolution limit by stimulated emission: stimulated-emission-depletion fluorescence microscopy. *Optics Letters* **1994**, 19 (11), 780-782.
14. Hein, B.; Willig, K. I.; Hell, S. W., Stimulated emission depletion (STED) nanoscopy of a fluorescent protein-labeled organelle inside a living cell. *Proceedings of the National Academy of Sciences* **2008**, 105 (38), 14271-14276.
15. Rittweger, E.; Han, K. Y.; Irvine, S. E.; Eggeling, C.; Hell, S. W., STED microscopy reveals crystal colour centres with nanometric resolution. *Nature Photonics* **2009**, 3 (3), 144-147.
16. Hell, S. W.; Kroug, M., Ground-state-depletion fluorescence microscopy: A concept for breaking the diffraction resolution limit. *Applied Physics B* **1995**, 60 (5), 495-497.
17. Fölling, J.; Bossi, M.; Bock, H.; Medda, R.; Wurm, C. A.; Hein, B.; Jakobs, S.; Eggeling, C.; Hell, S. W., Fluorescence nanoscopy by ground-state depletion and single-molecule return. *Nature Methods* **2008**, 5 (11), 943-945.
18. Rust, M. J.; Bates, M.; Zhuang, X., Sub-diffraction-limit imaging by stochastic optical reconstruction microscopy (STORM). *Nature Methods* **2006**, 3 (10), 793-796.
19. Betzig, E.; Patterson, G. H.; Sougrat, R.; Lindwasser, O. W.; Olenych, S.; Bonifacino, J. S.; Davidson, M. W.; Lippincott-Schwartz, J.; Hess, H. F., Imaging Intracellular Fluorescent Proteins at Nanometer Resolution. *Science* **2006**, 313 (5793), 1642-1645.

20. Zhu, M.-Q.; Zhang, G.-F.; Li, C.; Aldred, M. P.; Chang, E.; Drezek, R. A.; Li, A. D. Q., Reversible Two-Photon Photoswitching and Two-Photon Imaging of Immunofunctionalized Nanoparticles Targeted to Cancer Cells. *Journal of the American Chemical Society* **2011**, *133* (2), 365-372.
21. Frost, N. A.; Shroff, H.; Kong, H.; Betzig, E.; Blanpied, T. A., Single-Molecule Discrimination of Discrete Perisynaptic and Distributed Sites of Actin Filament Assembly within Dendritic Spines. *Neuron* **2010**, *67* (1), 86-99.
22. Wang, W.; Li, G.-W.; Chen, C.; Xie, X. S.; Zhuang, X., Chromosome Organization by a Nucleoid-Associated Protein in Live Bacteria. *Science* **2011**, *333* (6048), 1445-1449.
23. Cheng, J.-X.; Xie, X. S., Vibrational spectroscopic imaging of living systems: An emerging platform for biology and medicine. *Science* **2015**, *350* (6264), aaa8870.
24. Ando, J.; Palonpon, A. F.; Sodeoka, M.; Fujita, K., High-speed Raman imaging of cellular processes. *Current Opinion in Chemical Biology* **2016**, *33*, 16-24.
25. Zumbusch, A.; Holtom, G. R.; Xie, X. S., Three-Dimensional Vibrational Imaging by Coherent Anti-Stokes Raman Scattering. *Physical Review Letters* **1999**, *82* (20), 4142-4145.
26. Saar, B. G.; Freudiger, C. W.; Reichman, J.; Stanley, C. M.; Holtom, G. R.; Xie, X. S., Video-Rate Molecular Imaging in Vivo with Stimulated Raman Scattering. *Science* **2010**, *330* (6009), 1368-1370.
27. Yue, S.; Li, J.; Lee, S.-Y.; Lee, Hyeon J.; Shao, T.; Song, B.; Cheng, L.; Masterson, Timothy A.; Liu, X.; Ratliff, Timothy L.; Cheng, J.-X., Cholesteryl Ester Accumulation Induced by PTEN Loss and PI3K/AKT Activation Underlies Human Prostate Cancer Aggressiveness. *Cell Metabolism* **2014**, *19* (3), 393-406.
28. Zhang, D.; Li, C.; Zhang, C.; Slipchenko, M. N.; Eakins, G.; Cheng, J.-X., Depth-resolved mid-infrared photothermal imaging of living cells and organisms with submicrometer spatial resolution. *Science advances* **2016**, *2* (9), e1600521.
29. Ring, E. F. J., The discovery of infrared radiation in 1800. *The Imaging Science Journal* **2000**, *48* (1), 1-8.
30. Coblentz, W. W., *Investigations of Infra-red Spectra...: pt. I. Infra-red absorption spectra. pt. II. Infra-red emission spectra.* Carnegie institution of Washington: 1908; Vol. 35.
31. Griffiths, P. R., Fourier transform infrared spectrometry. *Science* **1983**, *222* (4621), 297-302.
32. Lewis, E. N.; Treado, P. J.; Reeder, R. C.; Story, G. M.; Dowrey, A. E.; Marcott, C.; Levin, I. W., Fourier transform spectroscopic imaging using an infrared focal-plane array detector. *Analytical chemistry* **1995**, *67* (19), 3377-3381.

33. Baker, M. J.; Trevisan, J.; Bassan, P.; Bhargava, R.; Butler, H. J.; Dorling, K. M.; Fielden, P. R.; Fogarty, S. W.; Fullwood, N. J.; Heys, K. A., Using Fourier transform IR spectroscopy to analyze biological materials. *Nature protocols* **2014**, *9* (8), 1771.
34. Tiwari, S.; Reddy, V. B.; Bhargava, R.; Raman, J., Computational Chemical Imaging for Cardiovascular Pathology: Chemical Microscopic Imaging Accurately Determines Cardiac Transplant Rejection. *PLOS ONE* **2015**, *10* (5), e0125183.
35. Bhargava, R.; Fernandez, D. C.; Hewitt, S. M.; Levin, I. W., High throughput assessment of cells and tissues: Bayesian classification of spectral metrics from infrared vibrational spectroscopic imaging data. *Biochimica et Biophysica Acta (BBA) - Biomembranes* **2006**, *1758* (7), 830-845.
36. Towrie, M.; Grills, D. C.; Dyer, J.; Weinstein, J. A.; Matousek, P.; Barton, R.; Bailey, P. D.; Subramaniam, N.; Kwok, W. M.; Ma, C.; Phillips, D.; Parker, A. W.; George, M. W., Development of a Broadband Picosecond Infrared Spectrometer and its Incorporation into an Existing Ultrafast Time-Resolved Resonance Raman, UV/Visible, and Fluorescence Spectroscopic Apparatus. *Applied Spectroscopy* **2003**, *57* (4), 367-380.
37. Yang, Q.; Liu, L.; Sun, J., Optimized phase pupil masks for extended depth of field. *Optics Communications* **2007**, *272* (1), 56-66.
38. Nixon, M.; Katz, O.; Small, E.; Bromberg, Y.; Friesem, A. A.; Silberberg, Y.; Davidson, N., Real-time wavefront shaping through scattering media by all-optical feedback. *Nature Photonics* **2013**, *7* (11), 919-924.

CHAPTER 2. DEPTH-RESOLVED MID-INFRARED PHOTOTHERMAL IMAGING OF LIVING CELLS AND ORGANISMS WITH SUBMICROMETER SPATIAL RESOLUTION

A version of this chapter has been published by *Science Advances*. Adapted with permission from Zhang, D., Li, C., Zhang, C., Slipchenko, M. N., Eakins, G., & Cheng, J. X. (2016). Depth-resolved mid-infrared photothermal imaging of living cells and organisms with submicrometer spatial resolution. *Science advances*, 2(9), e1600521. Copyright 2016 American Association for the Advancement of Science.

Label-free chemical imaging of complex samples in biological and materials sciences has been sought for years. Although mid-infrared spectromicroscopy has made numerous progresses towards in vivo or in situ imaging, the technique is still restricted to the applications in dehydrated tissues due to the broad water band across the infrared region. In addition, direct infrared transmittance measurement results in the lack of depth resolution making it impossible to perform multidimensional imaging. Last but not the least, the spatial resolution of conventional mid-infrared imaging is poor due to the long wavelength. Herein, we report an approach that overcomes the abovementioned limitations by probing the photothermal effect induced by infrared absorption using a visible laser. The present mid-infrared photothermal (MIP) microscopy achieved 10 μM detection limit and submicron lateral resolution, enabling sensitive three-dimensional label-free chemical imaging. Visualization of lipids, proteins, and drug molecules inside single cells and living microorganisms were demonstrated.

2.1 Introduction

Infrared (IR) spectromicroscopy has enabled discoveries in various fields including materials science, oncology, histology, etc.¹⁻⁴ Ever since the early 20th century when the first IR spectrum database was established by W. W. Coblentz,⁵ IR spectroscopy has come a long way to achieve diffraction limited chemical imaging with the development Fourier transform infrared (FTIR) spectrometer,⁶⁻⁷ IR sensitive focal plane array detectors,⁸ and better IR sources such as quantum cascade laser (QCL)⁹⁻¹⁰ and synchrotron radiation.¹¹⁻¹² Among all the advances, QCL enables rapid wavelength scanning with sub-wavenumber spectral resolution across a broad bandwidth, which significantly increases the imaging speed without sacrificing the underlying

chemical information.¹⁰ However, several fundamental limitations have hindered IR spectromicroscopy from further applications in *in vivo* imaging of complex biological systems. First, the spatial resolution of conventional IR imaging has not exceeded several micrometers due to the long excitation wavelength. Second, the broad bandwidth of IR sources results in wavelength dependence in spatial resolution. Third, light scattering fluctuations induced by sample heterogeneity as well as broad IR bandwidth have been found to bring inevitable baseline artifacts.¹³ Furthermore, the direct measurement of IR transmittance does not provide depth-resolution. Last but not the least, the strong water absorption across the IR region prohibited the technique being used for the analysis of biological functions of molecules in living organisms.

These limitations were overcome by introducing the mid-IR photothermal (MIP) microscopy, in which IR absorption at the focus is probed with a visible light. In particular, the absorbed IR photons excite vibrational resonances of chemical bonds resulting in a local temperature jump that alters the refractive index, which affects the divergency of the probe beam. As a consequence, an intensity fluctuation of the probe beam can be sensitively detected through a dark-field geometry. Since our MIP scheme utilizes a single wavelength visible laser as the probe beam, it gets rid of the wavelength dependent artifacts and spatial resolution. The spatial resolution of the microscopy is only determined by the diffraction limit of the visible probe beam, which is ~10-fold improvement compared to that of the mid-IR excitation beam. In addition, the pump-probe mechanism of the MIP approach enables optical sectioning for three-dimensional (3D) imaging, which is not available by conventional IR imaging that measures the linear-absorption. Since the attenuation depth in water for both the mid-IR and visible beams are over 100 μm , it is feasible to apply MIP microscopy in *in vitro* and *in vivo* imaging in cell culture medium. Last, owing to the small temperature dependence of the refractive index¹⁴ and relatively large heat capacity, water generates low MIP signal which improves the signal-to-background ratio for the study of living cells and small organisms in aqueous medium.

The report of photothermal experiment dates back to the 1960s, in which Gordon *et al.* discovered the long transients of refractive index gradient when a liquid cell filled with various chemicals were illuminated by a He-Ne laser.¹⁵⁻¹⁶ The photothermal contrast was then demonstrated using both electronic and plasmonic absorption of visible photons to reveal subcellular structures.¹⁷ The detection limit of the photothermal approach has also improved to single nanoparticle¹⁸ and single molecule¹⁹ level. More recently, with the deployment of a QCL as

the excitation laser, Furstenberg *et al.*²⁰ demonstrated chemical imaging of microscale crystals and polymer coating on microdevices. Mërtiri²¹⁻²² and colleagues further performed selective imaging of proteins (Amide I band) in a dehydrated tissue slice by probing the mid-IR absorption with a near-IR fiber laser. Later, Li *et al.* presented photothermal imaging of polystyrene microspheres (~1.1 μm diameter) and studied the impact of heat capacity of surrounding mediums to the photothermal signal intensity by conducting the counterpropagation apparatus.²³ In the meantime, there have been some reports on improving the signal-to-noise ratio (SNR) of the MIP spectra including investigating the nonlinear photothermal process²⁴ and utilizing asymptotic analysis of the probe power.²⁵ In our work, although based on the same contrast mechanism and pump-probe scheme, we have pushed the performance of the MIP microscope to a historical high that enables *in vivo* bond-selective imaging with submicrometer resolution. In the following sections, we report, to our knowledge, the first demonstration of photothermal imaging of intracellular molecules and *Caenorhabditis elegans* (*C. elegans*) with 0.6 μm spatial resolution and microsecond pixel dwell time based on IR absorption.

2.2 Methods

2.2.1 Origin of the MIP contrast

In our MIP microscope, the thermal effect is generated from the linear absorption of the mid-IR photons that are resonant with the vibrational frequencies of endogenous chemical bonds in the sample. Meanwhile, the heat dissipation to the surrounding medium counter reacts with the heating process at the focal spot which suppresses the refractive index gradient. Therefore, several physical property of the molecules and mediums contribute to the refractive index gradient $\frac{\partial n}{\partial T}$, including the absorption cross section σ , number density of molecules N , heat capacity of the sample C_p , heat conductivity of the medium κ , and the power of the IR beam at the sample P_{IR} . The photothermal signal is typically measured as the fluctuations in the intensity of detected probe beam $\frac{\Delta P_{pr}}{P_{pr}}$, which can be derived as²⁶:

$$\frac{\Delta P_{pr}}{P_{pr}} \propto \frac{\sigma N}{\kappa C_p} \cdot \frac{\partial n}{\partial T} P_{IR} \quad (1)$$

If the power of the probe beam is fixed, the MIP signal can also be written as the modulation of the probe beam:

$$\Delta P_{pr} \propto \frac{\sigma N}{\kappa C_p} \cdot \frac{\partial n}{\partial T} \cdot P_{pr} \cdot P_{IR} \quad (2)$$

Eq. 2 indicated that the MIP signal is proportional to three independent variables: the number density of molecules, the power of probe beam and pump beam. For a determined system, in which the power of each laser beam is known, the MIP microscope is capable to measure the concentration of a certain molecule quantitatively. It is noteworthy that the relatively large heat capacity of water [4.18 J/g · K, compared to that of protein (2.04 J/g · K) or lipid (2.02 J/g · K) at 303 K²⁷] results in minimal nonresonant water background in MIP imaging, enabling decent signal-to-background in aqueous mediums.

2.2.2 Strategies to improve the SNR

Despite the small absorption cross section of mid-IR compared to that of visible photons, three strategies were used in the present work to improve the SNR of the MIP microscope. First, the microscope was built in a dark-field geometry to reduce the background level and maximize the intensity fluctuation of the detected probe beam as shown in Figure 2-1 A and B. Second, we modulated the mid-IR pump beam and deployed phase-sensitive synchronized detection using a lock-in amplifier to filter out-of-phase noises. Third, a high-Q factor resonant amplifier (Figure 2-1 C) was designed and fabricated to selectively amplifies the modulated probe intensity fluctuation at the QCL repetition rate while suppressing electronical noises with different frequencies. The resonant amplifier was based on a previous work in our group demonstrating a narrow-band amplifier at the frequency of a few megahertz for stimulated Raman scattering imaging.²⁸ In order to determine the resonant frequency of the circuit for optimized MIP microscope, we first measured the frequency dependence of the laser noise and MIP signal level. As shown in Figure 2-1 E, the SNR increases as the modulation frequency decreases. However, lower frequency results in longer data acquisition time. We chose a modulation frequency of 100 kHz as a trade-off between SNR and imaging speed. The manufactured resonant circuit has a central frequency at 102.5 kHz and a bandwidth of 1.44 kHz, leaving the Q factor as 71.2 with tunable gain ranging from 10 to 1000 (Figure 2-1 D). The abovementioned strategies collectively ensured high-performance MIP microscopy.

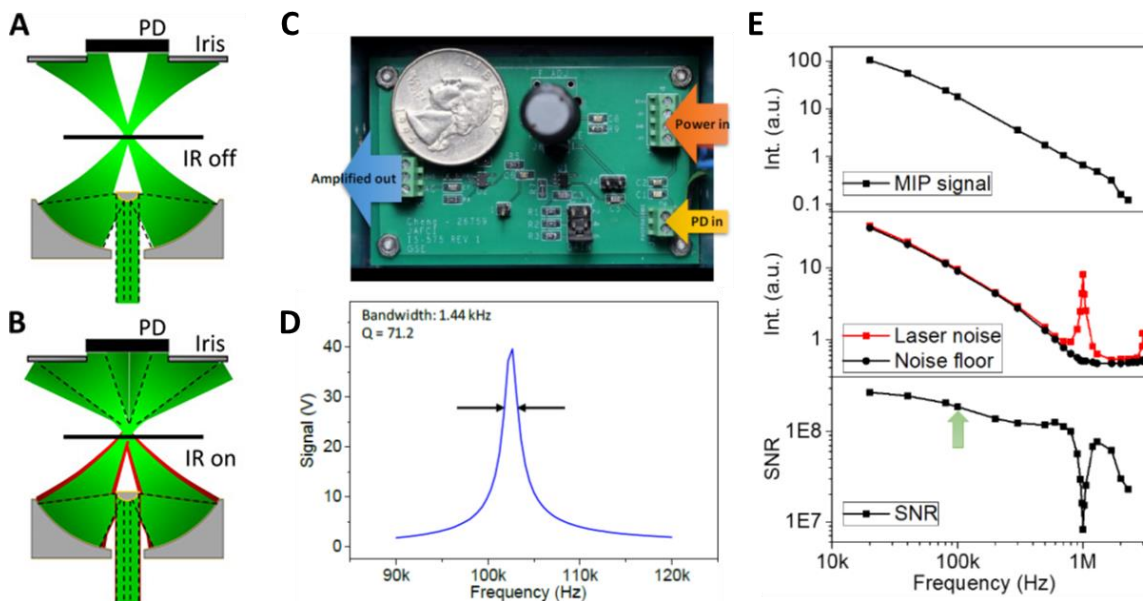


Figure 2-1 Strategies for improved SNR of MIP microscopy. (A) Probe beam propagation through the sample via a dark-field objective (not to scale; condenser was omitted for simplicity). PD, photodiode; IR, infrared. (B) The probe beam propagation is perturbed by the addition of an infrared pump beam due to infrared absorption and the development of a thermal lens. (C) Photograph of the resonant amplifier used for MIP imaging. Coin is placed for reference. (D) Frequency response of the tunable resonant amplifier. The -3 dB bandwidth indicated by the arrows is measured to be 1.44 kHz. The calculated Q-factor is 71.2. (E) Frequency dependence of MIP signal, laser noise, and signal-noise-ratio. Arrow indicates the frequency chosen to fabricate the resonant amplifier.

2.2.3 Schematic of the MIP microscope

The schematic of the MIP microscope is shown in Figure 2-2. The mid-IR pump laser is a QCL operating at 102.5 kHz repetition rate with an average power of 2 mW delivered to the sample plane (Block Engineering, LaserTune LT2000). The QCL output ranges from 1345 cm^{-1} to 1905 cm^{-1} with 0.2 cm^{-1} spectral resolution. A pair of off-axis parabolic mirrors were used to expand the mid-IR beam to match the back aperture of the objective lens to maximize the numerical aperture (NA). The visible probe laser is a continuous-wave diode laser with an output wavelength at 785 nm (Thorlabs, LD785-SE400). After beam expansion, the mid-IR and visible beams were combined at a silicon-based dichroic mirror (Edmund Optics, #68654) and sent to an inverted microscope (Olympus, IX71). A small portion of the QCL power was reflected by the dichroic mirror to a mercury-cadmium-telluride detector (Vigo Inc., PVM-10.6) to monitor the wavelength-dependent mid-IR laser power in real time, which serves as the reference for IR spectra

normalization in quantitative analysis. A Cassegrain objective lens with gold coating (52 \times , NA 0.65, Edmund Optics #66589) was used to focus both the IR and visible at the sample plane without chromatic aberration. The samples were placed on a sample scanning stage (Mad City Labs, Nano-Bio 2200) with a maximum scanning speed of 200 ms per pixel. The probe beam was collected through a condenser lens (NA 0.55) with tunable aperture and directed to a silicon-based photodiode (Hamamatsu, S3994-01), whose signal was selectively amplified by the resonant amplifier. The pre-amplified photothermal signal was then sent to a digitized lock-in amplifier (Zurich Instruments, HF2LI) for phase-sensitive detection of the MIP signal. The inset of Figure 2-2 shows the electronic communications for synchronized measurement.

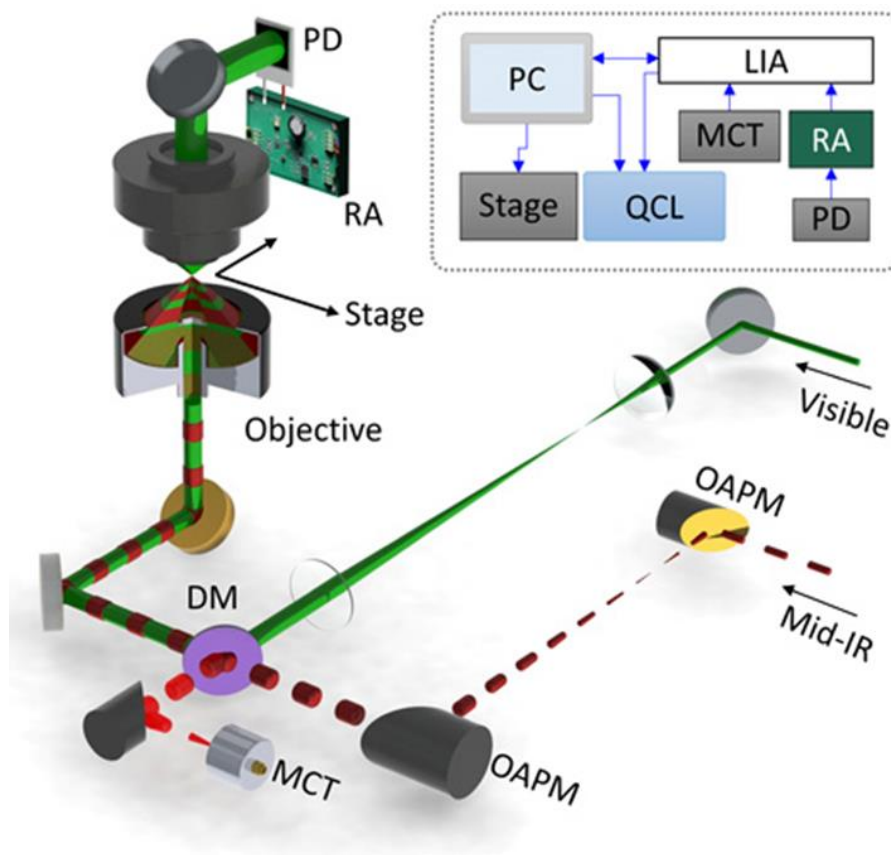


Figure 2-2 Schematic of the MIP microscope. A pulsed mid-infrared pump beam is provided by a QCL, and a continuous probe beam is provided by a visible laser, both of which are collinearly combined by a silicon dichroic mirror (DM) and sent into a reflective objective. The residual reflection of the infrared beam from the dichroic mirror is measured by a mercury cadmium telluride (MCT) detector. The probe beam is collected by a condenser with a variable iris and sent to a silicon PD connected to a resonant amplifier (RA). Inset: The photothermal signal is selectively amplified by the RA and detected by a lock-in amplifier (LIA). A computer is used for control and data acquisition. OAPM, off-axis parabolic mirror.

2.2.4 Materials and sample preparation

All samples were sandwiched between calcium fluoride (CaF₂) windows (ø12 mm, Eksma Optics, 530-6121) to ensure the transmittance of mid-IR photons. For spectral fidelity experiments, a polystyrene IR standard film (International Crystal Laboratories, 0009-8181) and a bottle of olive oil were used to compare the spectra acquired on both the MIP microscope and an attenuated total reflection FTIR (ATR-FTIR) spectrometer (Thermo Nicolet).

For the limit-of-detection (LoD) evaluation, we designed a flow cell which consists of two borosilicate capillary tubes sandwiched by two pieces of the CaF₂ windows. The boundary was confined by #1 cover classes stitched by silicone encapsulant (Dow SYLGARD 182). The flow cell was mounted on the sample stage to investigate the LoD of the MIP microscope. We used a syringe to inject γ -valerolactone (Sigma-Aldrich, W310301-1KG-K) at carbon disulfide (CS₂) solution with a flow rate at 1 mL/min. The concentration of γ -valerolactone was calculated based on the volume of solvent and analyte used for sample preparation. The MIP signal intensities for each measurement were calculated using the integrated area of the 1775 cm⁻¹ peak after baseline (solvent spectrum) subtraction.

To determine the spatial resolution of the MIP microscope, 500 nm PMMA microspheres (Phosphorex, #MMA500) were dispersed in deionized water and spread on the surface of CaF₂ window for MIP imaging. The concentration of the PMMA suspension was controlled at ~0.1% wt/wt to obtain isolated microspheres. To measure as many data points as possible, the step size was set at 10 nm and the pixel dwell time was 50 ms.

Live cell imaging on the microscope were performed with two types of cell lines, PC-3 and MIA PaCa-2 respectively. All cells used in the present work were cultured on our home-built petri dishes modified with CaF₂-bottom. The PC-3 cells were cultured for 1 day before MIP imaging. The MIA PaCa-2 cells were cultured in normal medium for the first 12 hours before adding the inhibitor for monoacylglycerol lipase, JZL-184, and maintain the concentration as 20 μ M for another 12 hours. All cell culture dishes were rinsed with phosphate buffered saline for three times prior to MIP imaging. To achieve higher SNR, the saline can be replaced by 0.9% NaCl/D₂O solution. In practical experiments, the pixel dwell time was set as 1 ms for PC-3 and 500 μ s for MIA PaCa-2 cells.

Wildtype *C. elegans* was cultured in liquid medium until mature. For MIP imaging, live *C. elegans* was treated with 200 mM sodium azide solution for anesthesia. Then the worms were

transferred to the CaF₂-bottom petri dishes and sandwiched between the #0 cover glass and CaF₂ window. To maintain the worms alive, phosphate buffered saline was added in the dish during the whole experiment. The pixel dwell time was set as 500 μ s to achieve a relatively higher imaging speed.

2.2.5 Image analysis

We utilized ImageJ (National Institute of Health) to analyze all MIP images. For the spatial resolution analysis, both the horizontal and vertical line profiles of MIP signal intensities were plotted at the center of the PMMA microsphere. The intensity profiles were fitted to a Gaussian function in OriginLab to determine the full-width at half-maximum (FWHM) of the microsphere, which was considered as the spatial resolution of the system. The 3D reconstruction of the PC-3 cells was generated by importing the z stack to the 3D viewer plugin in ImageJ.

For the multivariate analysis of multispectral MIP imaging of MIA PaCa-2 cells, the x-y- λ stack was saved as raw data and analyzed in MATLAB (MathWorks Inc.) using the multivariate curve resolution-alternating least squares (MCR-ALS) toolbox. The output of the MCR-ALS analysis were the concentration map and the spectrum of each component exhibited in two matrices. The concentration matrix was refolded as a stack of images while the spectral matrix was plotted at corresponding frequencies.

The chemical imaging of *C. elegans* consisted of 18 individual images with 200 \times 200 pixels. We used the Mosaic plugin in ImageJ to stitch elemental images together. To improve the visual clarity, random noise, which has the same mean and standard deviation as that of the background of the elemental images, was added to the blank area in the stitched image.

2.3 Results

2.3.1 Spectral fidelity and LoD of the MIP spectromicroscopy

The spectral fidelity of the MIP spectromicroscopy was assessed by comparing the MIP spectral profiles to that of the reference spectra acquired using an ATR-FTIR spectrometer. As illustrated in Figure 2-3 (A-C), all raw MIP spectra were normalized by the laser power of the QCL at each wavenumber across the spectral window. To achieve optimal SNR, purging dry N₂ prior to the measurement suppresses the ambient water absorption significantly (Figure 2-3D). The

MIP and FTIR spectra of polystyrene and olive oil were shown head-to-head in red and black lines in Figure 2-3 E. The MIP spectra of both samples exhibit good consistency with that acquired with conventional FTIR.

To know the LoD of our MIP approach, we measure the strong carbonyl band (C=O, peak appears at 1775 cm^{-1}) vibration of γ -valerolactone/ CS_2 solution. The analyte was prepared by serial dilution ranging from $10\text{ }\mu\text{M}$ to 100 mM . As the calibration curve shown in Figure 2-3 F, the LoD of our MIP approach for carbonyl band was $10\text{ }\mu\text{M}$ with $\sim 2\text{ mW}$ mid-IR power and $\sim 10\text{ mW}$ probe power delivered to the sample. Note such LoD is out of the reach of the complementary vibrational spectroscopy technique, Raman scattering. To the best of our knowledge, the detection limit of stimulated Raman scattering was no less than $200\text{ }\mu\text{M}$ with a laser power of 120 mW for the pump and 130 mW for the Stokes beam.²⁹ By comparison, the MIP approach is roughly 10^5 times more sensitive than techniques based on Raman scattering.

2.3.2 Characterization of the spatial resolution of the MIP microscope

The spatial resolution of the MIP microscope was evaluated by extracting the point spread function from single color MIP imaging of a PMMA microsphere ($\phi\ 500\text{ nm}$) at 1730 cm^{-1} as shown in Figure 2-4. The measured FWHM along horizontal and vertical directions were $0.63\text{ }\mu\text{m}$ and $0.61\text{ }\mu\text{m}$ respectively. It is noteworthy that the excitation 1730 cm^{-1} mid-IR beam has a diffraction limit of $5.5\text{ }\mu\text{m}$ through the same Cassegrain objective (NA 0.65) lens, which is the best spatial resolution that can be achieved with a conventional far-field mid-IR microscope. Such a result indicated a 9-fold improvement in spatial resolution enabled by the MIP approach, which

will provide the opportunity for chemical imaging of nanoscale materials and subcellular structures with vibrational spectroscopy.

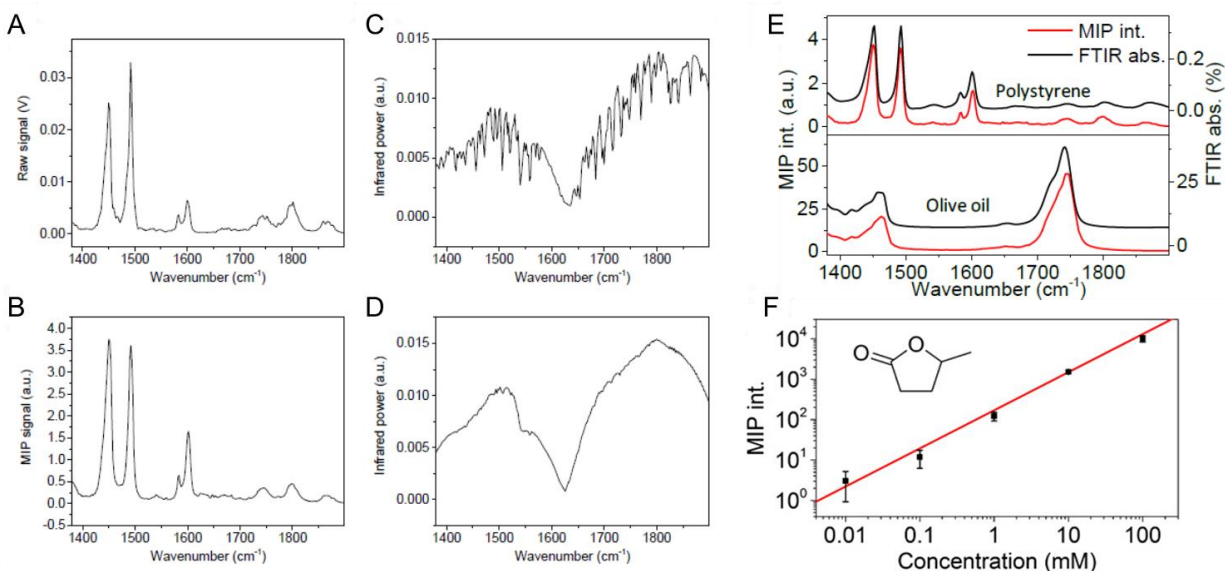


Figure 2-3 (A) Raw MIP spectrum of polystyrene film. (B) Infrared power across the spectral window, recorded by the MCT detector. Negative spikes in the curve are due to water vapor absorption. (C) MIP spectrum after power normalization. The power drop at around 1629 cm^{-1} are due to the gap between two laser tuners. (D) Infrared power profile when the system is being purged by dry nitrogen. This step can eliminate the errors caused by the water vapor absorption. (E) Spectral fidelity. Comparison of MIP spectral profiles (red) and FTIR spectra (black) of polystyrene film (top) and olive oil (bottom). The FTIR spectra were acquired by an attenuated total reflection FTIR spectrometer. The spectra are offset for clarity. The MIP signal was normalized by the QCL power measured simultaneously via the same lock-in amplifier. Note that the unit for FTIR spectra is percent absorption, rather than the conventional absorbance, so that it is proportional to the infrared energy absorbed by the sample. int., intensity; abs., absorption; a.u., arbitrary units. (F) Sensitivity. MIP signal of γ -valerolactone in carbon disulfide at various concentrations. Inset shows the molecular structure. The limit of detection is found to be 10 μM when the SD is equal to the solution-solvent difference. The time constant of the lock-in amplifier was set to 50 ms, and the spectral scanning speed was set to 50 ms.

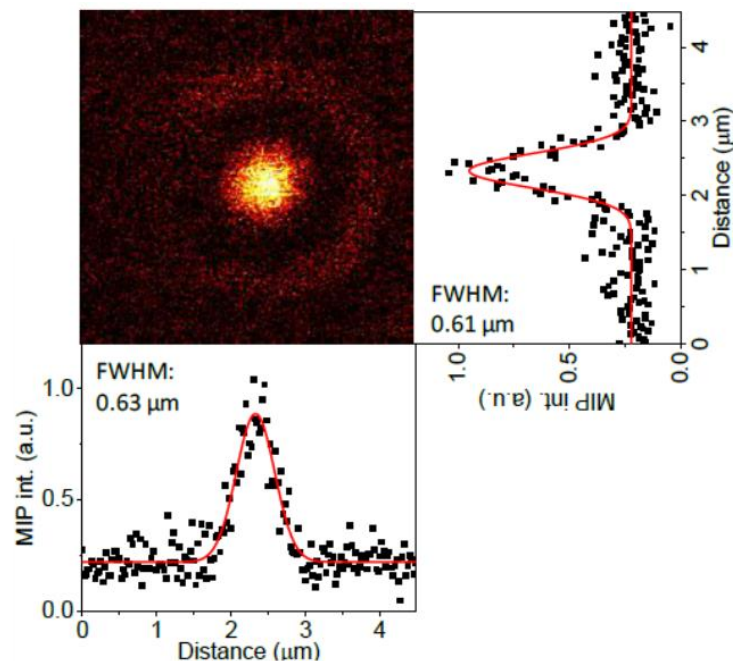


Figure 2-4 Spatial resolution. MIP imaging of a 500-nm PMMA bead. The horizontal and vertical intensity profiles are plotted at the bottom and on the right side of the image. The measured FWHM is 0.63 and 0.61 μm , respectively. Pixel dwell time, 5 ms.

2.3.3 Multiscale MIP imaging of lipids in live cells

Based on the characterization of the MIP microscope, we further demonstrated label-free chemical imaging of endogenous intracellular molecules in live PC-3 cells. Since intensified lipogenesis has been reported as one of the biomarkers for aggressive prostate cancer,³⁰ we performed 3D MIP imaging of lipid droplets to evaluate the lipid storage in PC-3 cells. The optical sections from three selected focal planes are shown in Figure 2-5(A-C). We also measured the line profile of a single lipid droplet showing a FWHM of 0.83 μm (Figure 2-5D), which was consistent with the hypothesis that the MIP microscope could remain submicrometer resolving power in live cell imaging. The 3D reconstruction of the investigated PC-3 cell was produced from a z-scanning stack with the excitation wavelength fixed at 1750 cm^{-1} (Figure 2-5E), showing spatial distribution of individual lipid droplets. In addition, we showed that no MIP contrast was observed when the QCL was tuned off the resonant frequency (1850 cm^{-1}) of endogenous chemical bonds in cells (Figure 2-5F). This is by far the first report of 3D chemical imaging of living cells via mid-IR spectroscopy contrast mechanism.

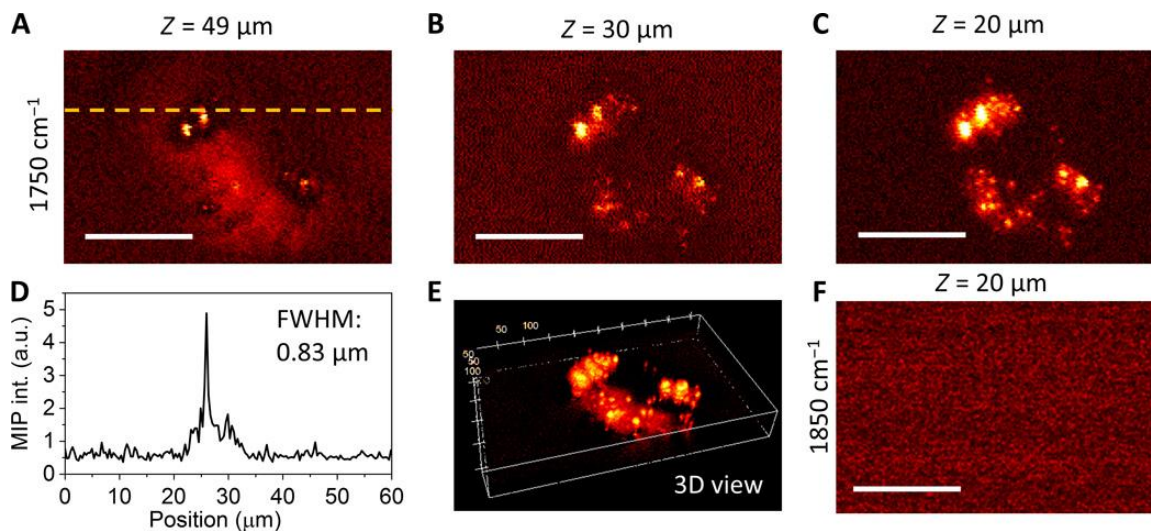


Figure 2-5 3D MIP imaging of lipids in live cells. (A to C) Depth-resolved MIP imaging of PC-3 cells at the 1750 cm^{-1} C=O band at different Z positions. (D) The line profile indicated in (A), showing an FWHM of $0.83\text{ }\mu\text{m}$ of a small lipid droplet. (E) The reconstructed 3D view of the same cell, showing individual lipid droplets over the cell body. (F) Off-resonance image at 1850 cm^{-1} , showing no contrast. Pixel dwell time, 1 ms. Scale bars, $20\text{ }\mu\text{m}$.

2.3.4 Multispectral MIP imaging of intracellular molecules

We also demonstrated multispectral MIP imaging of living cells to visualize the drug molecules and lipids by taking advantage of the rapid spectral tuning capability of the QCL. The drug being studied was a monoacylglycerol lipase inhibitor JZL184, which was found to be capable to suppress the migration of cancer cells in previous reports.³¹ However, the intracellular uptake, transportation, and metabolism was not investigated. The infrared spectrum of JZL184 indicates three characteristic peaks at 1420 , 1480 , and 1720 cm^{-1} (Figure 2-6A, top curve). The MIA PaCa-2 cells were treated with JZL184 for 12 hours and maintained in D_2O saline solution prior to MIP imaging. A total of 9 MIP images were acquired at the following wavenumbers: 1380 , 1400 , 1480 , 1700 , 1720 , 1724 , 1750 , 1800 , and 1850 cm^{-1} . We implemented the MCR-ALS algorithm to perform quantitative analysis and retrieve the spectral profiles and the concentration map of both JZL184 and the lipids (Figure 2-6B, C). The retrieved spectral points from MCR analysis showed excellent agreement with the corresponding FTIR spectra (Figure 2-6A). As expected, the JZL184 concentration map were distinctively different from that of the lipid droplets. The drug molecules were concentrated at the nucleoplasm since its intracellular receptor, monoacylglycerol lipases locate mainly in the cell nucleus. On the contrary, the lipid droplets are

mostly distributed in the cytoplasm to assist cell metabolism. The visualization of JZL184 in MIA PaCa-2 cells provides spatial-temporal information of the drug-cell interactions, enabling more insights into the understanding of anti-cancer drugs based on lipogenesis pathway block.

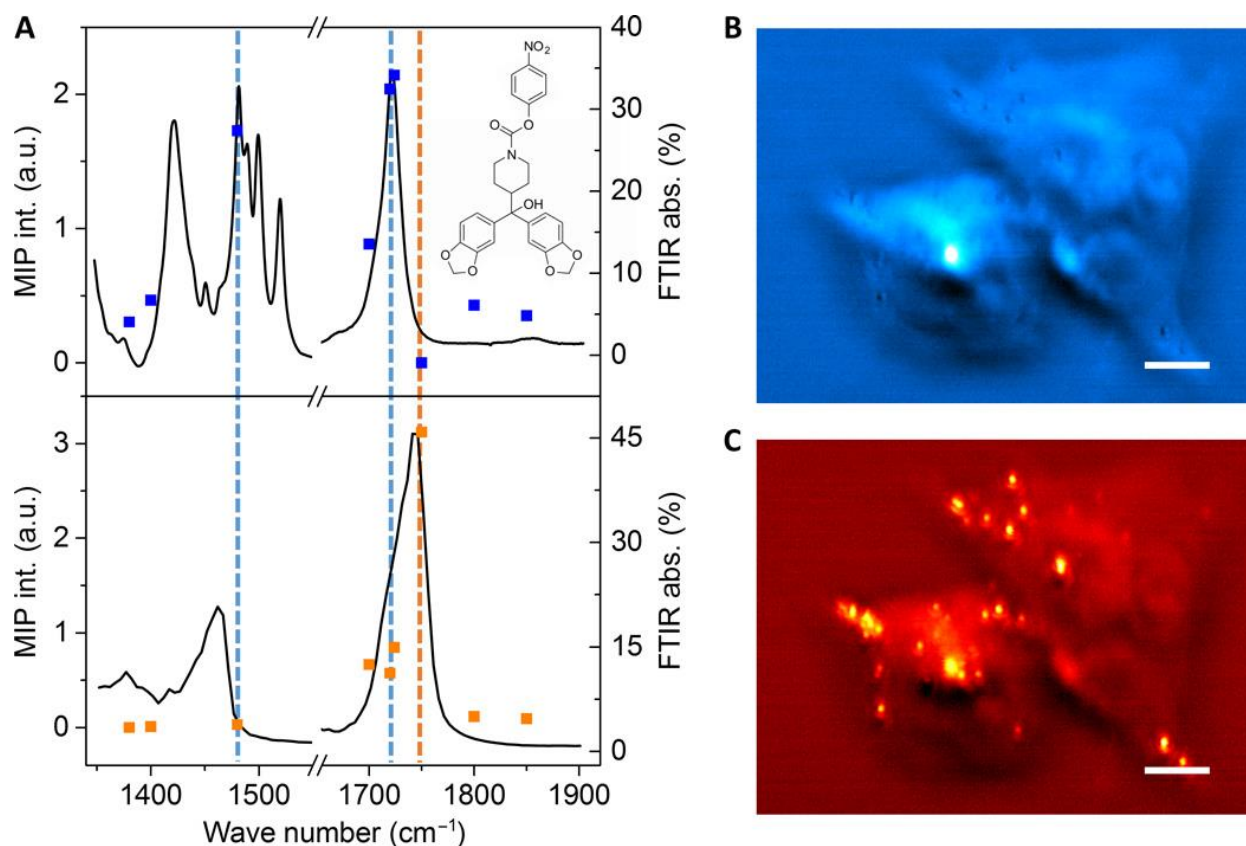


Figure 2-6 (A). IR spectra of JZ-184 (top) and lipid content (bottom). A stack of MIP images acquired at 9 different frequencies were analyzed with MCR-ALS to generate the intracellular distribution of the drug molecule (B) and lipid droplets (C).

2.3.5 *In vivo* MIP imaging of living *C. elegans*

As the last demonstration, we explored the potential of the MIP microscope in *in vivo* chemical imaging of microorganism (Figure 2-7). The lipid contents were imaged with the excitation wavelength at 1750 cm^{-1} (Figure 2-7A) corresponding to the carbonyl band, whereas the proteins were mapped using the 1645 cm^{-1} (Figure 2-7B) amide I band. We also collected the single point MIP spectra at 3 marked locations in the map. Point 1 represented lipid droplet and the spectrum showed a strong peak at 1750 cm^{-1} (Figure 2-7C). Although the profiles of IR spectra of protein and water are alike in the amide I region, significant intensity difference was observed

in the MIP spectra at 1650 cm^{-1} (Figure 2-7E, F). We further investigated the imaging depth of the MIP microscope in *C. elegans* to be $80\text{ }\mu\text{m}$ by performing depth-resolved MIP imaging. All these results proved the capability of MIP microscopy for *in vivo* mid-IR imaging of small organisms collectively.

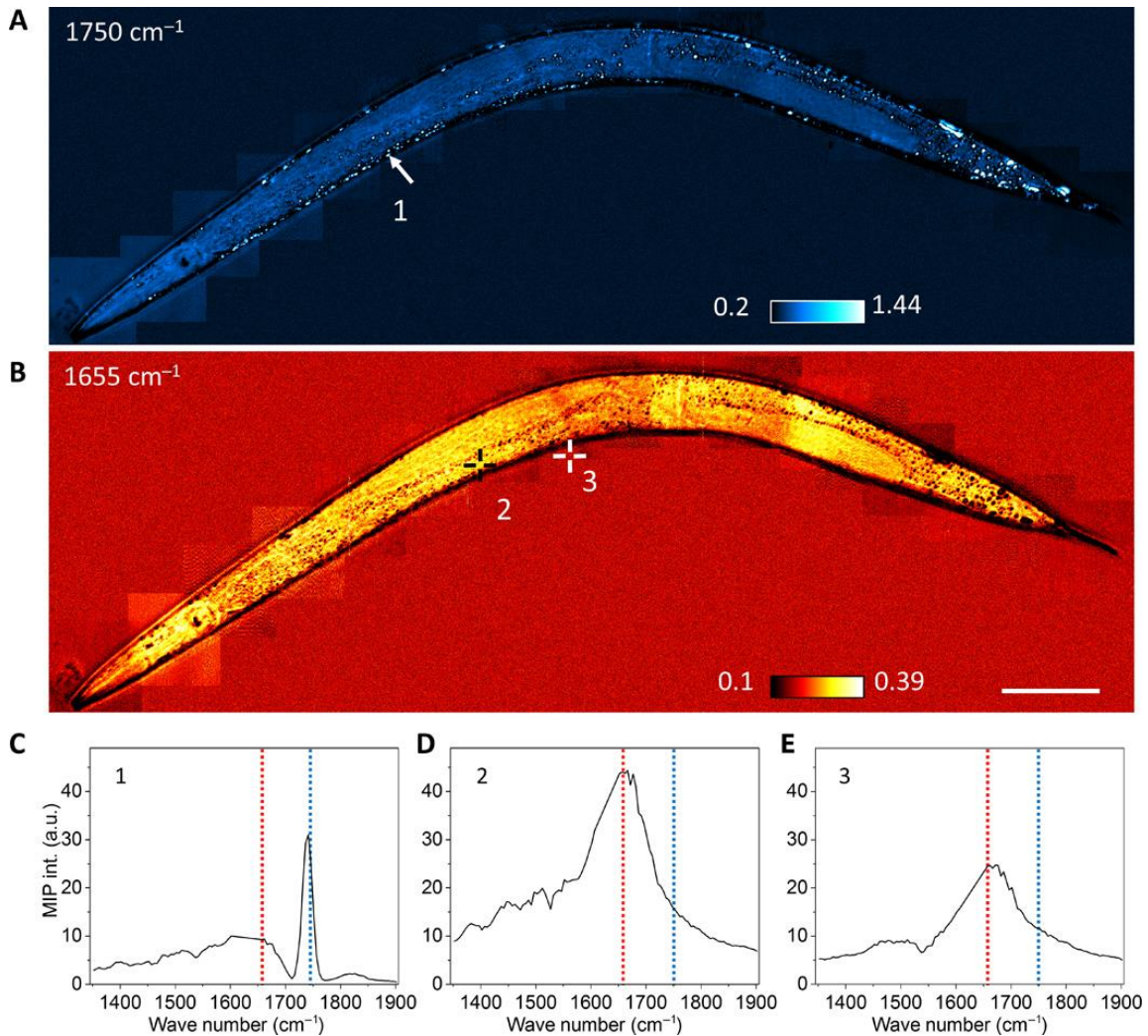


Figure 2-7 In vivo MIP imaging of lipid and protein in *C. elegans*. (A) MIP imaging of the worm body at the 1750-cm^{-1} lipid C=O band. 1, Lipid droplet. (B) MIP imaging of the same area at the 1655-cm^{-1} protein amide I band. 2, Worm body; 3, medium. (C to E) Pinpoint spectra of locations 1, 2, and 3, as indicated in (A) and (B). Blue and red lines indicate the wavelengths used in (A) and (B), respectively. Pixel dwell time, $500\text{ }\mu\text{s}$. Scale bar, $200\text{ }\mu\text{m}$.

2.4 Discussion

Vibrational spectromicroscopy has become an emerging field in the branch of biomedical imaging since it utilizes the endogenous vibrational fingerprint as the signal and preserves the biofunctions of intracellular molecules.³² In this chapter, a novel mid-IR spectroscopic imaging system based on photothermal contrast was demonstrated. The micromolar LoD, submicrometer spatial resolution, as well as depth resolving power, collectively enabled label-free imaging of endogenous biomolecules and drug molecules in living cells and microorganism. With the development of advanced mid-IR laser sources, the MIP approach is capable to cover a broader spectral window to utilize the established mid-IR spectrum database in the past century. The abovementioned advantages promise numerous applications in both fundamental sciences and industrial productions including research fields of biological, pharmaceutical, and materials.

Identifying the experimental factors that could affect the spatial resolution of the system has been an eternal topic in the field of optical microscopy, including photothermal imaging. One of the well-studied factors is the density of hot spots in the focal volume, since the thermal dissipation accounts for most resolution degradation in photothermal measurements. Baffou *et al.* have reported a model by investigating patterned metallic nanostructures with designed intervals.³³⁻³⁴ In their experiments, both the pump and the probe beams were visible lasers which have similar focal volumes, whereas the photothermal lensing effect was mainly induced by the medium that was heated by the dissipated thermal flux from the focus. By defining a dimensionless parameter $\xi = p^2/(PR)$ describing the situation where N particles with an average diameter of R and distance of p were distributed in the range of P , the model predicted that the thermal gradients generated from adjacent heat spots start to overlap and result in worse spatial resolution when $\xi \ll 1$. In the case of our MIP microscope, the model lacks universality due to the fact that the mid-IR pump beam focal spot is about 10 times the size of the visible probe beam spot. In our case, water is the dominating medium in the samples studied by MIP microscope while its weak photothermal contribution minimizes the interference signal generated from environment and the adjacent heat spots. Thus, the spatial resolution of the MIP microscope is hardly affected by the same effects. Experimental evidence has been found in Figure 2-5 and Figure 2-7 where the lipid droplets in the field of views were well resolved with the ξ value of both 0.81 and 2.16.

It is worthwhile to discuss the potential strategies to further improve the imaging speed and LoD of our MIP approach. First, the imaging speed of the current scheme is limited by both the

scanning speed of the sample stage and the SNR. The sample stage has a minimum pixel dwell time of 200 μ s which is far from enough for video rate imaging. We expect a significant speed boost with the implementation of beam scanning apparatus. In addition, wide-field MIP imaging has been demonstrated by Bai *et al.* when this chapter is written.³⁵ To enhance the SNR of the current system, the most intuitive approach is to increase the laser power delivered to the sample plane since the pump and probe power in our MIP microscope was only \sim 2 mW and \sim 10 mW respectively. With new laser sources providing much higher power and broader spectral window, the MIP microscopy can be deployed to study much more biological processes in cells. Such work is described in Chapter 4.

2.5 References

1. Prati, S.; Joseph, E.; Sciutto, G.; Mazzeo, R., New advances in the application of FTIR microscopy and spectroscopy for the characterization of artistic materials. *Accounts of chemical research* **2010**, *43* (6), 792-801.
2. Bhargava, R., Infrared spectroscopic imaging: the next generation. *Applied spectroscopy* **2012**, *66* (10), 1091-1120.
3. Bellisola, G.; Sorio, C., Infrared spectroscopy and microscopy in cancer research and diagnosis. *American journal of cancer research* **2012**, *2* (1), 1.
4. Baker, M. J.; Trevisan, J.; Bassan, P.; Bhargava, R.; Butler, H. J.; Dorling, K. M.; Fielden, P. R.; Fogarty, S. W.; Fullwood, N. J.; Heys, K. A., Using Fourier transform IR spectroscopy to analyze biological materials. *Nature protocols* **2014**, *9* (8), 1771.
5. Coblenz, W. W., *Investigations of Infra-red Spectra...: pt. I. Infra-red absorption spectra. pt. II. Infra-red emission spectra.* Carnegie institution of Washington: 1908; Vol. 35.
6. Griffiths, P. R., Fourier transform infrared spectrometry. *Science* **1983**, *222* (4621), 297-302.
7. Dluhy, R. A.; Mendelsohn, R., Emerging techniques in biophysical FT-IR. *Analytical chemistry* **1988**, *60* (4), 269A-278A.
8. Lewis, E. N.; Treado, P. J.; Reeder, R. C.; Story, G. M.; Dowrey, A. E.; Marcott, C.; Levin, I. W., Fourier transform spectroscopic imaging using an infrared focal-plane array detector. *Analytical chemistry* **1995**, *67* (19), 3377-3381.
9. Faist, J.; Capasso, F.; Sivco, D. L.; Sirtori, C.; Hutchinson, A. L.; Cho, A. Y., Quantum cascade laser. *Science* **1994**, *264* (5158), 553-556.

10. Kole, M. R.; Reddy, R. K.; Schulmerich, M. V.; Gelber, M. K.; Bhargava, R., Discrete frequency infrared microspectroscopy and imaging with a tunable quantum cascade laser. *Analytical chemistry* **2012**, *84* (23), 10366-10372.
11. Dumas, P.; Miller, L., The use of synchrotron infrared microspectroscopy in biological and biomedical investigations. *Vibrational spectroscopy* **2003**, *32* (1), 3-21.
12. Nasse, M. J.; Walsh, M. J.; Mattson, E. C.; Reininger, R.; Kajdacsy-Balla, A.; Macias, V.; Bhargava, R.; Hirschmugl, C. J., High-resolution Fourier-transform infrared chemical imaging with multiple synchrotron beams. *Nature methods* **2011**, *8* (5), 413-416.
13. Chalmers, J.; Griffiths, P., *Handbook of Vibrational Spectroscopy*, 5 volumes set. Wiley: 2002.
14. Schiebener, P.; Straub, J.; Levelt Sengers, J.; Gallagher, J., Refractive index of water and steam as function of wavelength, temperature and density. *Journal of physical and chemical reference data* **1990**, *19* (3), 677-717.
15. Gordon, J.; Leite, R.; Moore, R. S.; Porto, S.; Whinnery, J., Long-transient effects in lasers with inserted liquid samples. *Journal of Applied Physics* **1965**, *36* (1), 3-8.
16. Long, M.; Swofford, R. L.; Albrecht, A., Thermal lens technique: a new method of absorption spectroscopy. *Science* **1976**, *191* (4223), 183-185.
17. Lasne, D.; Blab, G. A.; De Giorgi, F.; Ichas, F.; Lounis, B.; Cognet, L., Label-free optical imaging of mitochondria in live cells. *Optics express* **2007**, *15* (21), 14184-14193.
18. Boyer, D.; Tamarat, P.; Maali, A.; Lounis, B.; Orrit, M., Photothermal imaging of nanometer-sized metal particles among scatterers. *Science* **2002**, *297* (5584), 1160-1163.
19. Gaiduk, A.; Yorulmaz, M.; Ruijgrok, P.; Orrit, M., Room-temperature detection of a single molecule's absorption by photothermal contrast. *Science* **2010**, *330* (6002), 353-356.
20. Furstenberg, R.; Kendziora, C. A.; Papantonakis, M. R.; Nguyen, V.; McGill, R. In *Chemical imaging using infrared photothermal microspectroscopy*, Next-Generation Spectroscopic Technologies V, International Society for Optics and Photonics: 2012; p 837411.
21. Mertiri, A.; Totachawattana, A.; Liu, H.; Hong, M. K.; Gardner, T.; Sander, M. Y.; Erramilli, S. In *Label free mid-IR photothermal imaging of bird brain with quantum cascade laser*, 2014 Conference on Lasers and Electro-Optics (CLEO)-Laser Science to Photonic Applications, IEEE: 2014; pp 1-2.
22. Sander, M. Y. In *Mid-infrared photothermal imaging*, Laser Science, Optical Society of America: 2015; p LM11. 2.
23. Li, Z.; Kuno, M.; Hartland, G. In *Super-resolution imaging with mid-IR photothermal microscopy on the single particle level*, Physical Chemistry of Interfaces and Nanomaterials XIV, International Society for Optics and Photonics: 2015; p 954912.

24. Mertiri, A.; Altug, H.; Hong, M. K.; Mehta, P.; Mertz, J.; Ziegler, L. D.; Erramilli, S., Nonlinear midinfrared photothermal spectroscopy using Zharov splitting and quantum cascade lasers. *ACS photonics* **2014**, *1* (8), 696-702.
25. Totachawattana, A.; Liu, H.; Mertiri, A.; Hong, M. K.; Erramilli, S.; Sander, M. Y., Vibrational mid-infrared photothermal spectroscopy using a fiber laser probe: asymptotic limit in signal-to-baseline contrast. *Optics letters* **2016**, *41* (1), 179-182.
26. Meyers, R. A., Encyclopedia of Analytical Chemistry: Applications, Theory and Instrumentation, Supplementary Volumes S1-S3.
27. Zhu, X. Prediction of specific heat capacity of food lipids and foods. The Ohio State University, 2015.
28. Slipchenko, M. N.; Oglesbee, R. A.; Zhang, D.; Wu, W.; Cheng, J. X., Heterodyne detected nonlinear optical imaging in a lock-in free manner. *Journal of biophotonics* **2012**, *5* (10), 801-807.
29. Wei, L.; Hu, F.; Shen, Y.; Chen, Z.; Yu, Y.; Lin, C.-C.; Wang, M. C.; Min, W., Live-cell imaging of alkyne-tagged small biomolecules by stimulated Raman scattering. *Nature methods* **2014**, *11* (4), 410.
30. Menendez, J. A.; Lupu, R., Fatty acid synthase and the lipogenic phenotype in cancer pathogenesis. *Nature Reviews Cancer* **2007**, *7* (10), 763-777.
31. Long, J. Z.; Li, W.; Booker, L.; Burston, J. J.; Kinsey, S. G.; Schlosburg, J. E.; Pavón, F. J.; Serrano, A. M.; Selley, D. E.; Parsons, L. H., Selective blockade of 2-arachidonoylglycerol hydrolysis produces cannabinoid behavioral effects. *Nature chemical biology* **2009**, *5* (1), 37.
32. Cheng, J.-X.; Xie, X. S., Vibrational spectroscopic imaging of living systems: An emerging platform for biology and medicine. *Science* **2015**, *350* (6264), aaa8870.
33. Baffou, G.; Berto, P.; Bermúdez Ureña, E.; Quidant, R.; Monneret, S.; Polleux, J.; Rigneault, H., Photoinduced heating of nanoparticle arrays. *Acs Nano* **2013**, *7* (8), 6478-6488.
34. Berto, P.; Mohamed, M. S.; Rigneault, H.; Baffou, G., Time-harmonic optical heating of plasmonic nanoparticles. *Physical Review B* **2014**, *90* (3), 035439.
35. Bai, Y.; Zhang, D.; Lan, L.; Huang, Y.; Maize, K.; Shakouri, A.; Cheng, J.-X., Ultrafast chemical imaging by widefield photothermal sensing of infrared absorption. *Science advances* **2019**, *5* (7), eaav7127.

CHAPTER 3. MID-INFRARED PHOTOTHERMAL IMAGING OF ACTIVE PHARMACEUTICAL INGREDIENTS AT SUBMICROMETER SPATIAL RESOLUTION

A version of this chapter has been published by *Analytical Chemistry*. Reprint with permission from Li, C., Zhang, D., Slipchenko, M. N., & Cheng, J. X. (2017). Mid-infrared photothermal imaging of active pharmaceutical ingredients at submicrometer spatial resolution. *Analytical chemistry*, 89(9), 4863-4867. Copyright 2017 American Chemical Society.

Chemical imaging with sufficient spatial resolution to resolve microparticles in tablets is essential to ensure high quality and efficacy in controlled release. The existing modalities fall short in either time consuming, poor spatial resolution, or low chemical specificity. Here, we demonstrate an epi-detected mid-infrared photothermal (epi-MIP) microscope at a spatial resolution of 0.65 μm . Providing identical spectral profiles as conventional infrared spectroscopy, our epi-MIP microscope enabled mapping of both active pharmaceutical ingredients and excipients of a drug tablet.

3.1 Introduction

Pharmaceutical tablets, as one of the most consumed oral solid dosage forms across the world,¹ are composed of active pharmaceutical ingredients (API) that have biological activities and excipients that are inert but assure the pharmacological performance of API. The potency of medicine mainly depends on the formulation, particle size, and content uniformity. So far, it is still hard to control these properties at a low dosage of contents.² The bioactivity of API could be altered by inhomogeneous distribution or deformation of pharmaceutical particles, not to mention drug counterfeiting, which may be deleterious to patients. To produce high-quality medicines, it is essential to monitor and visualize the API and excipients in tablets in the quality control process. Specifically, as controlled release becoming an emerging trend in pharmacy, the size of API and excipients particulates are being made from the order of 100 μm down to submicrometer and nanometer scale, making the current bulk imaging methods unable to cope with the new trend in the production line.^{3,4} As an example, high resolution chemical mapping of amlodipine besylate tablets from different vendors⁵ revealed heterogeneity differences in submicrometer scale between Pfizer and Ethex tables (Note the Ethex tablets was later recalled by FDA due to quality issues).

Therefore, an increasing demand for high resolution imaging methods with chemical selectivity has arisen.

Various non-optical imaging methods have been developed to address the above-mentioned challenge. Time-of-flight secondary ion mass spectrometry imaging ionizes and analyzes molecules over a spot of $\sim 1 \mu\text{m}$, which has excellent chemical specificity and limit of detection.⁶ X-ray powder diffraction analysis^{7,8} and X-ray microtomography⁹ provides crystalline properties and element mapping, with a limit of detection sensitivity at the level of typically 1%. Nuclear magnetic resonance imaging is a noninvasive method elucidating the structure of molecules,¹⁰ with a long analysis time (order of 10 minutes). Terahertz imaging measures the thickness of tablet coating with a penetration depth of 0.45 mm but low spatial resolution 0.15 mm.¹¹ These imaging approaches were not adopted by industry due to low throughput.

Alternatively, optical imaging has the potential to provide high speed, sub-micrometer resolution, and chemical specificity. Toth et al. combined second order nonlinear optical imaging and two-photon fluorescence to deliver fluorescent API imaging in powdered blends with common excipients.¹² Besides, vibrational spectroscopy based imaging, which probes the intrinsic molecular vibration, provides rich chemical information and are widely used in industry. Commonly used vibrational imaging modalities are based on Raman scattering, near-infrared (NIR), or mid-infrared (MIR) spectroscopy.¹³ NIR and Raman imaging have been applied to analyses of pharmaceutical formulations and/or counterfeit owing to advantages such as little/no sample preparation, chemical selectivity, and nondestructive measurement.¹⁴⁻¹⁹ However, the spectral bands used in NIR spectroscopy, mostly overtone absorption, are broad, weak, and usually severely overlapped, resulting in low chemical specificity.²⁰ Spontaneous Raman scattering has relatively high chemical specificity but is a feeble effect (Raman cross section on the order of $10\text{-}30 \text{ cm}^2/\text{sr}$), thus requires long integration time ($>30 \text{ h}$ per 500×500 hyperspectral image).²¹ Although recent progress of epi-detected coherent Raman scattering microscopy has demonstrated fast imaging of tablet sections and dissolution of drug molecules,^{5,22,23} the cost and complexity, along with small Raman cross section, limited further adoption of the technique. In contrast, MIR imaging appreciates 100 million times larger absorption cross section (typ. $10\text{-}22 \text{ cm}^2/\text{sr}$), and has shown applications in pharmaceuticals, including API mapping and counterfeit tablet investigation.^{24,25} Yet, the relatively poor spatial resolution and low reflectance of MIR light prohibited its wide use for pharmaceuticals.

In this paper, we report a compact mid-infrared photothermal microscope for imaging tablets at sub-micron spatial resolution. Photothermal microscopy, first reported in the early 1980s,²⁶ detects the photothermal lensing effect induced by the absorption of pump beam at focus using another probe beam. Modalities based on electronic or plasmonic absorption have been demonstrated for single nanoparticle and single molecule imaging.²⁷⁻²⁸ The deployment of a MIR beam as pump and a visible or NIR beam as probe was realized lately. Furstenberg et al.²⁹ demonstrated a back-detected photothermal microscope pumped by a mid-infrared quantum cascade laser (QCL). To further improve the spatial resolution, Li et al.³⁰ adopted a counter-propagation modality and applied a high NA objective for the visible probe beam. As a result, they obtained photothermal images of 1.1 μm polystyrene beads in three different solvents. With an increased signal to baseline ratio, Mërtiri et al.³¹ performed photothermal imaging of dried tissue slices. Nevertheless, the spatial resolution and sensitivity were not sufficient for detection of sub-micrometer features within a cell.

We recently demonstrated a forward-detected mid-infrared photothermal (MIP) microscope with 0.6 μm spatial resolution and 10 μM sensitivity, which allowed MIR imaging of living cells and organisms.³² Our MIP microscope exploits a resonant amplifier that selectively probes the photothermal signal at the repetition rate of the pulsed IR laser. We showed that the MIP signal is linearly proportional to the number density of molecules and the power of each beam, which makes MIP a quantitative approach.³² Herein, we demonstrate sub-micrometer imaging of API and excipients microparticles in tablets by an epi-detected MIP microscope.

3.2 Methods

3.2.1 Components of the epi-detected MIP microscope

A pulsed quantum cascade laser (Block Engineering, LaserTune LT2000) operated at 100 kHz repetition rate and ~ 2 mW average power provided the tunable (ranges from 1345 to 1905 cm^{-1}) mid-infrared (MIR) pump beam. Meanwhile, a continuous-wave 785 nm laser (Thorlabs, LD-785-SE-400) was used as the probe beam. Both beams were combined at a long pass dichroic mirror (Edmund Optics, #68654) and, then, sent to an inverted microscope (Olympus, IX-71) installed with a gold-coated reflective objective lens (52 \times ; NA, 0.65; Edmund Optics, #66589). All samples were placed on a piezo scanning stage (Mad City Labs, Nano-Bio 2200) with a

maximum scanning speed of 200 μs / pixel. The residue of MIR beam generated at the dichroic mirror was guided to a room temperature mercury cadmium telluride (MCT) infrared detector (Vigo Inc., PVM-10.6) to monitor the infrared power. To detect the backward propagated MIP signal, a polarizing beam splitter (Thorlabs, PBS122) was placed in the path of probe beam to transmit the linearly polarized light and reflect the polarization scrambled epi-MIP signal to the detector. When the sample is reflective, such as samples on a reflective mirror, a quarter-wave plate (Thorlabs, WPQ05M-780) is needed to induce a 90° polarization change to the backward signal to be coupled out. The detector was a silicon photodiode (Hamamatsu S3994-1). The photocurrent produced by the detector was amplified by a laboratory-built resonant circuit (resonant frequency at 103.8 kHz, gain 100) and then sent to a lock-in amplifier (Zurich Instruments, HF2LI) for phase-sensitive detection. The power spectrum of MIR beam was acquired by MCT via another lock-in amplifier input channel. It was used to normalize the epi-MIP signal to obtain the absorption spectrum of samples.

3.2.2 Fourier-transform infrared spectra measurement

To validate the spectral fidelity of the epi-detected MIP microscope, FTIR spectra of chemicals were acquired using conventional IR spectrometer as well. Samples were measured on an attenuated total reflection (ATR) FTIR spectrometer (Thermo Nicolet Nexus) with diamond as the internal reflection element. The spectra were acquired after the internal baseline correction with a blank sample. The spectra were recorded using the built-in software interface.

3.2.3 Samples

The polystyrene film was a standard FT-IR test film (International Crystal Laboratories, 0009-8181). The Tylenol tablet was Tylenol Extra Strength, 500 mg of acetaminophen each (~83 wt%/wt). The pure chemicals including acetaminophen (analytical standard), corn starch (analytical standard), polyvinylpyrrolidone (analytical standard), and sodium starch glycolate (type A, pharmaceutical grade) were all purchased from Sigma-Aldrich.

3.3 Results and discussion

3.3.1 Schematic of the microscope

Figure 3.1 shows the schematic of our epi-MIP setup (details in the Experimental Section). Being different from the setup in ref. 32, we placed a polarizing beam splitter to the probe beam path to transmit the linearly polarized probe beam to the sample and reflect the backward propagated signal to the photodiode. To acquire an epi-MIP image, a sample was raster scanned on a piezoelectric scanning stage and the epi-MIP signal was recorded as a function of sample position. A computer was used to synchronize QCL tuning, stage scanning, and data acquisition.

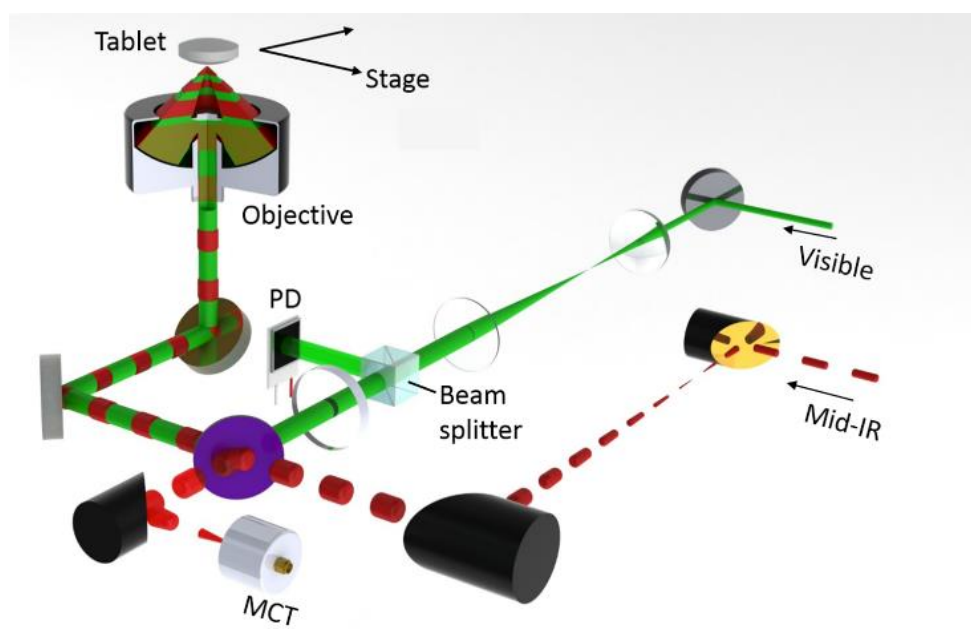


Figure 3-1 Schematic of the epi-MIP microscope. A pulsed QCL source provides the MIR beam and a continuous wave visible laser is used as the probe beam. Both beams are combined collinearly by a silicon dichroic mirror, and then sent into a reflective objective. The residue of MIR is monitored by a mercury cadmium telluride (MCT) detector. The backward propagated probe beam is reflected by a beam splitter and sent to a silicon photodiode (PD).

3.3.2 Characterization

We first explored the spectral fidelity of epi-MIP signals by comparing the epi-MIP spectrum of a 60 μm polystyrene film to that from an attenuated total reflection (ATR) FTIR spectrometer (Figure 3.2A). The epi-MIP spectrum showed good agreement with the FTIR spectrum, notably for the phenyl ring semicircle stretching modes at 1450 and 1490 cm^{-1} . The

1450 cm^{-1} peak is also contributed by the backbone CH_2 scissors deformation. Note the ATR-FT-IR spectra require ATR correction to avoid the distortion of band shapes and relative peak intensities induced by the ATR process. In contrast to ATR-FTIR, the epi-MIP spectra do not need such baseline correction, which simplifies data processing and reduces calibration errors.

We then examined the spatial resolution of our epi-MIP microscope by measuring the sharp edge response of a 1951 USAF test target. A thin film ($<5 \mu\text{m}$, determined by Newton ring method) of olive oil was sandwiched by a CaF_2 plate and the resolution target. The MIP signal from the oil film, carried by the probe light, was reflected by the coating of the target, immediately at the oil film, into the detector, which mimics the condition with real samples. Even though the infrared light heated up a large area, only the small area of the probe light focus generated MIP signal. Note the chrome coating did not generate MIP signal.

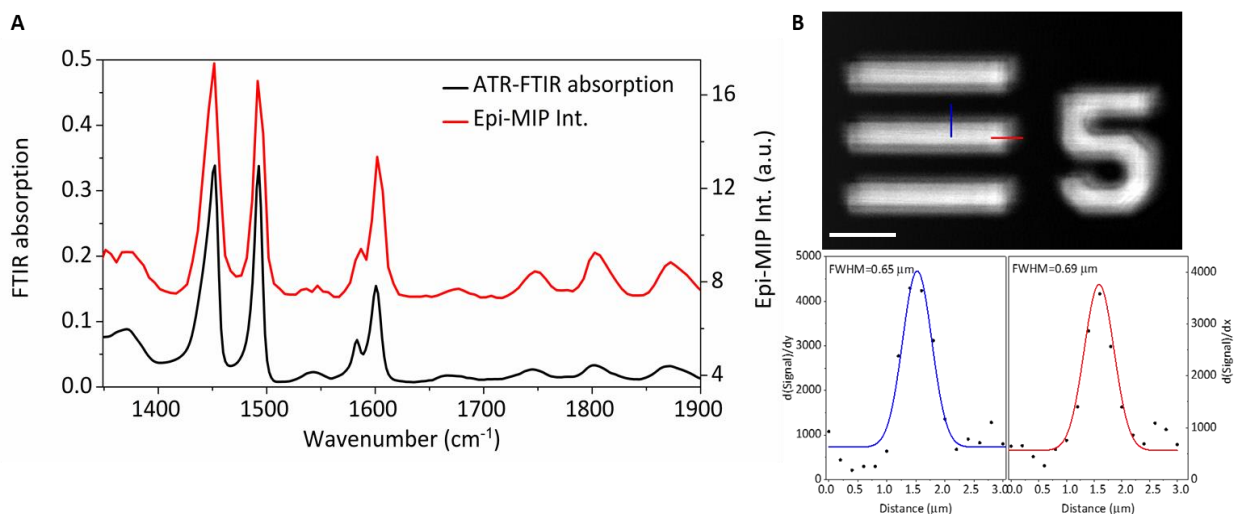


Figure 3-2 Characterization of the epi-MIP microscope. (A). Comparison of epi-MIP spectral profiles (red) and FT-IR spectra (black) of polystyrene film. The spectra were offset for visual clarity. (B) Epi-MIP image of the element 5 of group 5 on a positive 1951 USAF test target. The 1st order derivative of the profiles of the horizontal (red) and vertical (blue) lines are plotted at the bottom. The measured FWHM is 0.69 and 0.65 μm , respectively. Pixel dwell time: 1 ms. Scale bar: 20 μm .

The result is shown in Figure 3.2B. We took the first derivative of the marked line profiles in the MIP image and fitted the derivative data points with a Gaussian function. It is noteworthy that the diffraction limit of 1742 cm^{-1} MIR beam is 5.5 μm focused by our 0.65 NA objective. However, our measured full width at half-maximum (FWHM) was 0.69 μm horizontally and 0.65

μm vertically. By comparison, even installed with a high NA (~ 2) germanium ATR-objective, the ATR-FT-IR microscope can hardly resolve features smaller than $4\ \mu\text{m}$ in tablet sections.³³ The 6-fold improvement of spatial resolution enabled us to acquire MIR spectra of a single pharmaceutical microparticle.

3.3.3 Tablet imaging

After the above characterizations, we deployed the epi-MIP microscope to identify and visualize the API and excipients in real tablets. As one of the most consumed pain relief in the US, the Tylenol tablet was used as a test bed. The API is acetaminophen, whose MIR spectrum has characteristic peaks at $1500\ \text{cm}^{-1}$ (phenyl ring semicircle stretching modes) and $1666\ \text{cm}^{-1}$ (amide I). Besides, three of the most abundant excipients include corn starch, polyvinylpyrrolidone (PVP), and sodium starch glycolate (SSG). As shown in Figure 3.3, the molecular structures indicate that these three excipients show characteristic peaks at C–H bending mode (corn starch), amide I band (PVP), and carboxylic acid C=O stretching mode (SSG), respectively. On the basis of the knowledge above, we can identify and differentiate those substances referring to the epi-MIP signal at different excitation wavelengths within our QCL tunable range.

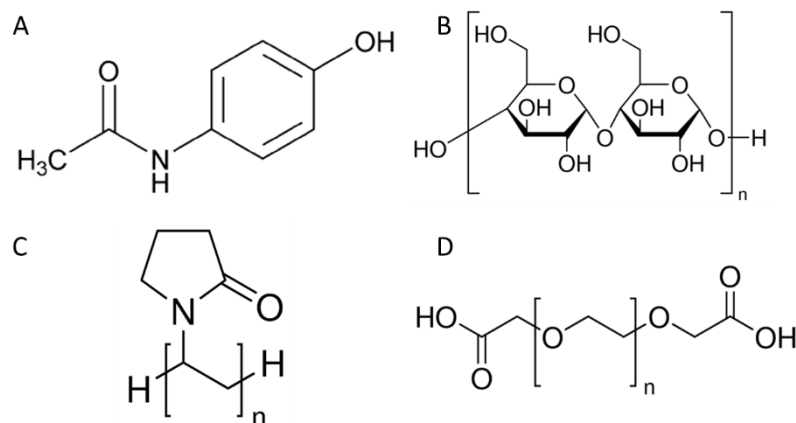


Figure 3-3 The structures of selected molecules in Tylenol. (A): acetaminophen, (B): starch (corn), (C): PVP and (D): starch glycolate (the acid form of sodium starch glycolate).

We first performed single color epi-MIP imaging of the Tylenol tablet at 1502 cm^{-1} to visualize the API distribution. The tablet was sectioned at the center and mounted on scanning stage for imaging without other preparation. Figure 3.4A shows that particles containing API (bright spots) were uniformly distributed in the $190 \times 190\ \mu\text{m}^2$ region with some large clusters. In general, the API particles should be closely surrounded by excipients particles, which means the dark regions on our API map should be excipients dominant. To prove this hypothesis, we obtained pinpoint epi-MIP spectra at three different positions as shown in Figure 3.4B. Points 1 and 2, whose pinpoint spectra indicate that API is the dominant molecule, were selected from the bright regions in Figure 3.4A. By comparison, point 3, which is the dark point on the API map, shows a distinct pinpoint spectrum from the other points, indicating that starch, PVP, and SSG are more abundant than the API. To confirm the species assigned from pinpoint spectra, we collected ATR-FTIR spectra of the API and excipients for comparison as shown in Figure 3.4C. The characteristic peaks we employed for chemical identification were all in good agreement with the ATR-FTIR spectra.

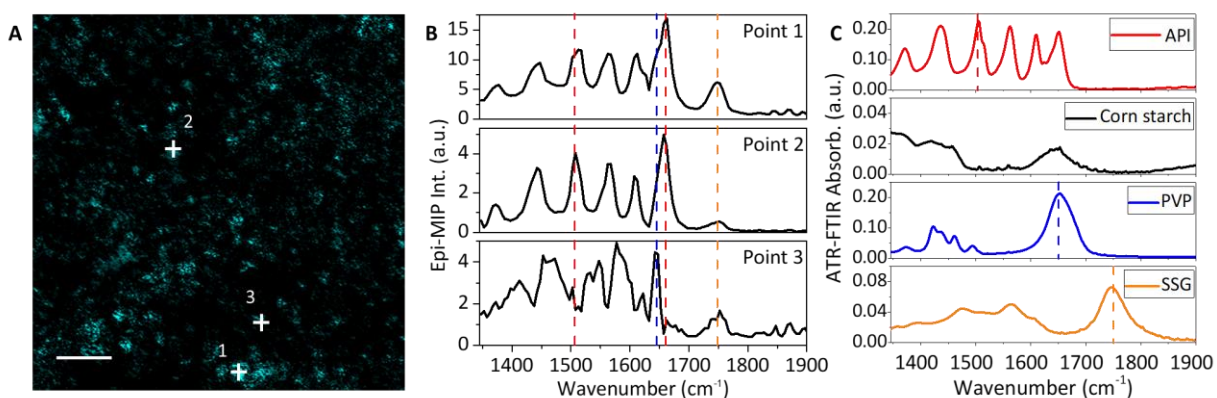


Figure 3-4 Identification of different species in Tylenol tablet. (A) Epi-MIP imaging of tablet obtained at 1502 cm^{-1} API benzene band. (B) Pinpoint spectra of locations 1, 2 and 3, as indicated in A. Red, blue and orange lines indicate 3 different substances' characteristic absorbance bands respectively. (C) ATR-FTIR spectra of pure chemicals we assigned in Tylenol® tablet. Pixel dwell time: $500\ \mu\text{s}$. Scale bar: $50\ \mu\text{m}$.

We further explored the capability of our epi-MIP microscope in integrated mapping of API and excipients (Figure 3.5). We tuned the MIR excitation wavenumbers to 1413 , 1502 , 1656 , and 1750 cm^{-1} which correlate to the absorption bands of corn starch, API, PVP, and SSG, respectively (Figure 3.5A–D). Each substance showed a unique spatial distribution and dosage in the region

we observed. By merging images A–D, we obtained the overlaid image as Figure 3.5E exhibiting the relative distributions of the four substances in Tylenol tablet. Most of the bright spots contained more than one molecule, which implies that API and excipients were fully mixed before the tablet compression process.

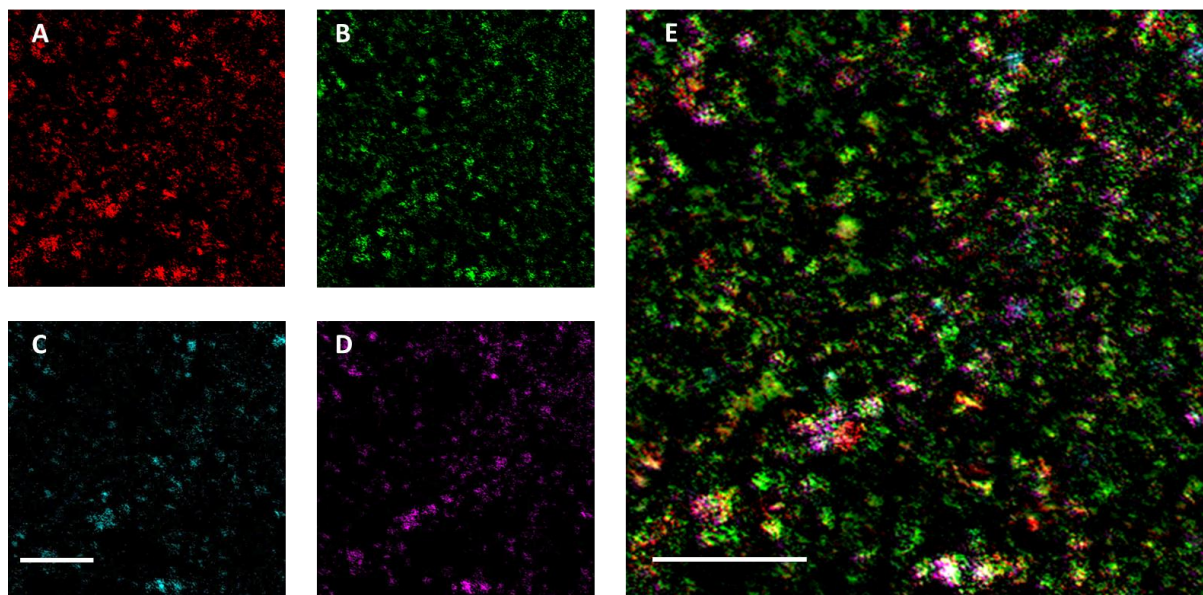


Figure 3-5 Epi-MIP images of API and excipients in a Tylenol tablet. (A-D) Epi-MIP image obtained at 1413 cm^{-1} , 1502 cm^{-1} , 1656 cm^{-1} and 1750 cm^{-1} which correlates to corn starch, acetaminophen (API), PVP and sodium starch glycolate respectively. (E) Overlaid image of A-D showing the distribution of API (green), corn starch (red), PVP (cyan) and SSG (magenta). Images were acquired by a raster scan. Pixel dwell time: 1 ms. Scale bars are $50\text{ }\mu\text{m}$.

Note the dark area in the merged chemical map. This seemingly erroneous image was a result of out-of-focus particles generating a lower MIP intensity, due to the surface roughness of the tablet section. As an example, we tested epi-MIP imaging of the tablet at varying depth (Figure 3.6). The features and signal intensity varied dramatically as the focus changed by $20\text{ }\mu\text{m}$. Furthermore, by applying Isodata threshold (an unsupervised thresholding method) to four different API maps, the average captured area in the binary map was calculated to be 82.6%, which was consistent with the listed weight percentage of acetaminophen, 83.3%.

The results above collectively demonstrate the potential of the epi-MIP microscope as a new chemical imaging modality for pharmaceutical tablet manufacturing. The epi-MIP spectra are identical to the conventional FTIR spectra, which simplifies the postprocessing of data and allows users to take advantage of the wealth of FTIR spectra database collected in the past century. With the excellent chemical selectivity, quantitative measurement capability, simple sample preparation requirement, and the relatively low cost, our epi-MIP microscope could not only be useful for manufacturing quality control but also enable the detection of high-quality counterfeit tablets.

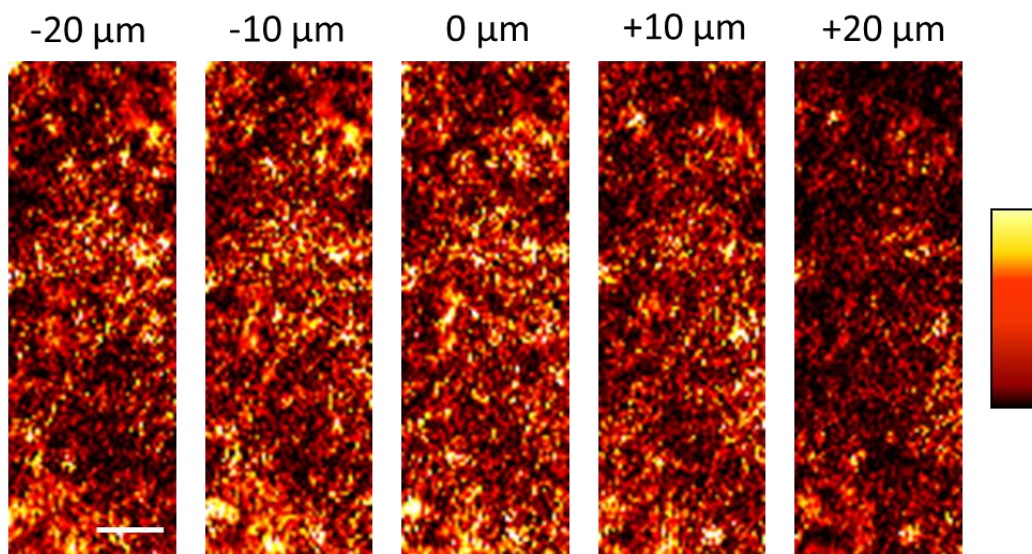


Figure 3-6 Epi-MIP imaging of acetaminophen at 5 different depth covering a 40 μm range from the surface. The intensity of 5 images are uniform. MIR excitation wavenumber: 1502 cm^{-1} . Pixel dwell time: 500 μs . Scale bar: 20 μm .

In our current setup, the QCL has a tunable range of 1345–1900 cm^{-1} , which covers many important MIR absorption bands, and has successfully differentiated the API molecule and three other excipients in Tylenol tablet sections by their characteristic peaks. Nevertheless, there are several other listed excipients that we could not map because their characteristic MIR peaks exceed our tunable range. We can readily expand the spectral range with the deployment of different pump sources to further exploit the abundant infrared libraries developed by previous researchers. In addition, advanced multivariate methods, such as multivariate curve resolution,³⁴ can further endow the epi-MIP microscope with a robust analytical ability in more complex sample analysis. It is worth mentioning that the power of both the pump and probe beams in our epi-MIP

microscope were low due to the limitations of laser sources, ~2 mW for the pump beam and ~10 mW for the probe beam at the sample. With the recently available high power MIR laser, the epi-MIP microscope will achieve higher sensitivity and imaging speed. Moreover, the spatial resolution of the epi-MIP microscope will be improved by using a probe laser wavelength that is shorter than the current 785 nm.

3.4 Conclusion

In summary, we developed a submicrometer-resolution, epi-detected MIP microscope and applied the setup to API visualization in drug tablets. As compared to the previous MIR microscopes, our epi-MIP microscope offered 5-fold better spatial resolution. Since we have demonstrated the application of MIP microscopy in imaging drug accumulation in living cells,³² it is feasible to perform the dissolution test and controlled release experiments of tablets on the forward detected MIP modality. As the current trend in pharmaceuticals is the combination of multiple techniques to provide integrated understanding, our MIP platform, with both forward and epi-detected modalities, could potentially provide comprehensive information on the factors correlating to drug efficacy and boost the future research in pharmaceutical sciences.

3.5 References

1. Ansel, H. C., Introduction to pharmaceutical dosage forms. **1969**.
2. Augsburger, L. L.; Hoag, S. W., *Pharmaceutical dosage forms-tablets*. CRC press: 2016.
3. Wong, D., Oral solid composition. Google Patents: 2012.
4. Salata, O. V., Applications of nanoparticles in biology and medicine. *Journal of Nanobiotechnology* **2004**, 2 (1), 3.
5. Slipchenko, M. N.; Chen, H.; Ely, D. R.; Jung, Y.; Carvajal, M. T.; Cheng, J.-X., Vibrational imaging of tablets by epi-detected stimulated Raman scattering microscopy. *Analyst* **2010**, 135 (10), 2613-2619.
6. Belu, A. M.; Davies, M. C.; Newton, J. M.; Patel, N., TOF-SIMS characterization and imaging of controlled-release drug delivery systems. *Analytical chemistry* **2000**, 72 (22), 5625-5638.

7. Bates, S.; Zografi, G.; Engers, D.; Morris, K.; Crowley, K.; Newman, A., Analysis of amorphous and nanocrystalline solids from their X-ray diffraction patterns. *Pharmaceutical research* **2006**, *23* (10), 2333-2349.
8. Nunes, C.; Mahendrasingam, A.; Suryanarayanan, R., Quantification of crystallinity in substantially amorphous materials by synchrotron X-ray powder diffractometry. *Pharmaceutical research* **2005**, *22* (11), 1942-1953.
9. Hancock, B. C.; Mullarney, M. P., X-ray microtomography of solid dosage forms. *Pharm Technol* **2005**, *29* (44), 92-100.
10. Djemai, A.; Sinka, I., NMR imaging of density distributions in tablets. *International journal of pharmaceutics* **2006**, *319* (1-2), 55-62.
11. Fitzgerald, A. J.; Cole, B. E.; Taday, P. F., Nondestructive analysis of tablet coating thicknesses using terahertz pulsed imaging. *Journal of pharmaceutical sciences* **2005**, *94* (1), 177-183.
12. Toth, S.; Madden, J.; Taylor, L.; Marsac, P.; Simpson, G., Selective imaging of active pharmaceutical ingredients in powdered blends with common excipients utilizing two-photon excited ultraviolet-fluorescence and ultraviolet-second order nonlinear optical imaging of chiral crystals. *Analytical chemistry* **2012**, *84* (14), 5869-5875.
13. Gendrin, C.; Roggo, Y.; Collet, C., Pharmaceutical applications of vibrational chemical imaging and chemometrics: a review. *Journal of pharmaceutical and biomedical analysis* **2008**, *48* (3), 533-553.
14. Cruz, J.; Bautista, M.; Amigo, J. M.; Blanco, M., Nir-chemical imaging study of acetylsalicylic acid in commercial tablets. *Talanta* **2009**, *80* (2), 473-478.
15. Amigo, J. M.; Ravn, C., Direct quantification and distribution assessment of major and minor components in pharmaceutical tablets by NIR-chemical imaging. *European Journal of Pharmaceutical Sciences* **2009**, *37* (2), 76-82.
16. Šašić, S., Raman mapping of low-content API pharmaceutical formulations. I. Mapping of alprazolam in alprazolam/xanax tablets. *Pharmaceutical research* **2007**, *24* (1), 58-65.
17. de Veij, M.; Deneckere, A.; Vandenabeele, P.; de Kaste, D.; Moens, L., Detection of counterfeit Viagra® with Raman spectroscopy. *Journal of pharmaceutical and biomedical analysis* **2008**, *46* (2), 303-309.
18. Rodionova, O. Y.; Houmøller, L. P.; Pomerantsev, A. L.; Geladi, P.; Burger, J.; Dorofeyev, V. L.; Arzamastsev, A. P., NIR spectrometry for counterfeit drug detection: a feasibility study. *Analytica Chimica Acta* **2005**, *549* (1-2), 151-158.
19. Rodionova, O. Y.; Pomerantsev, A., NIR-based approach to counterfeit-drug detection. *TrAC Trends in Analytical Chemistry* **2010**, *29* (8), 795-803.

20. Andersson, M.; Josefson, M.; Langkilde, F.; Wahlund, K.-G., Monitoring of a film coating process for tablets using near infrared reflectance spectrometry. *Journal of pharmaceutical and biomedical analysis* **1999**, *20* (1-2), 27-37.
21. Gordon, K. C.; McGoverin, C. M., Raman mapping of pharmaceuticals. *International journal of pharmaceutics* **2011**, *417* (1-2), 151-162.
22. Windbergs, M.; Jurna, M.; Offerhaus, H. L.; Herek, J. L.; Kleinebudde, P.; Strachan, C. J., Chemical imaging of oral solid dosage forms and changes upon dissolution using coherent anti-Stokes Raman scattering microscopy. *Analytical chemistry* **2009**, *81* (6), 2085-2091.
23. Kang, E.; Wang, H.; Kwon, I. K.; Robinson, J.; Park, K.; Cheng, J.-X., In situ visualization of paclitaxel distribution and release by coherent anti-Stokes Raman scattering microscopy. *Analytical chemistry* **2006**, *78* (23), 8036-8043.
24. Wray, P. S.; Clarke, G. S.; Kazarian, S. G., Dissolution of tablet-in-tablet formulations studied with ATR-FTIR spectroscopic imaging. *European Journal of Pharmaceutical Sciences* **2013**, *48* (4-5), 748-757.
25. Ricci, C.; Eliasson, C.; Macleod, N. A.; Newton, P. N.; Matousek, P.; Kazarian, S. G., Characterization of genuine and fake artesunate anti-malarial tablets using Fourier transform infrared imaging and spatially offset Raman spectroscopy through blister packs. *Analytical and bioanalytical chemistry* **2007**, *389* (5), 1525.
26. Fournier, D.; Lepoutre, F.; Boccara, A., Tomographic approach for photothermal imaging using the mirage effect. *Le Journal de Physique Colloques* **1983**, *44* (C6), C6-479-C6-482.
27. Boyer, D.; Tamarat, P.; Maali, A.; Lounis, B.; Orrit, M., Photothermal imaging of nanometer-sized metal particles among scatterers. *Science* **2002**, *297* (5584), 1160-1163.
28. Gaiduk, A.; Yorulmaz, M.; Ruijgrok, P.; Orrit, M., Room-temperature detection of a single molecule's absorption by photothermal contrast. *Science* **2010**, *330* (6002), 353-356.
29. Furstenberg, R.; Kendziora, C. A.; Papantonakis, M. R.; Nguyen, V.; McGill, R. In *Chemical imaging using infrared photothermal microspectroscopy*, Next-Generation Spectroscopic Technologies V, International Society for Optics and Photonics: 2012; p 837411.
30. Li, Z.; Kuno, M.; Hartland, G. In *Super-resolution imaging with mid-IR photothermal microscopy on the single particle level*, Physical Chemistry of Interfaces and Nanomaterials XIV, International Society for Optics and Photonics: 2015; p 954912.
31. Märtiri, A.; Totachawattana, A.; Liu, H.; Hong, M. K.; Gardner, T.; Sander, M. Y.; Erramilli, S. In *Label free mid-IR photothermal imaging of bird brain with quantum cascade laser*, 2014 Conference on Lasers and Electro-Optics (CLEO)-Laser Science to Photonic Applications, IEEE: 2014; pp 1-2.

32. Zhang, D.; Li, C.; Zhang, C.; Slipchenko, M. N.; Eakins, G.; Cheng, J.-X., Depth-resolved mid-infrared photothermal imaging of living cells and organisms with submicrometer spatial resolution. *Science advances* **2016**, *2* (9), e1600521.
33. Chan, K. A.; Hammond, S. V.; Kazarian, S. G., Applications of attenuated total reflection infrared spectroscopic imaging to pharmaceutical formulations. *Analytical chemistry* **2003**, *75* (9), 2140-2146.
34. Felten, J.; Hall, H.; Jaumot, J.; Tauler, R.; De Juan, A.; Gorzsás, A., Vibrational spectroscopic image analysis of biological material using multivariate curve resolution–alternating least squares (MCR-ALS). *Nature Protocols* **2015**, *10* (2), 217.

CHAPTER 4. MID-INFRARED PHOTOTHERMAL IMAGING OF NEWLY SYNTHESIZED LIPIDS IN CELLS BY FEMTOSECOND LASER

A version of this chapter has been published by *Journal of Physical Chemistry B*. Reprint with permission from Bai, Y., Zhang, D., Li, C., Liu, C., & Cheng, J. X. (2017). Bond-selective imaging of cells by mid-infrared photothermal microscopy in high wavenumber region. *The Journal of Physical Chemistry B*, 121(44), 10249-10255. Copyright 2017 American Chemical Society.

Using a visible beam to probe the thermal effect induced by infrared absorption, mid-infrared photothermal (MIP) microscopy allows bond-selective chemical imaging at submicron spatial resolution. Current MIP microscopes cannot reach the high wavenumber region due to the limited tunability of the existing quantum cascade laser source. We extend the spectral range of MIP microscopy by difference frequency generation (DFG) from two chirped femtosecond pulses. Flexible wavelength tuning in both C–D and C–H regions was achieved with mid-infrared power up to 22.1 mW and spectral width of 29.3 cm^{-1} . Distribution of fatty acid in live human lung cancer cells was revealed by MIP imaging of the C–D bond at 2192 cm^{-1} .

4.1 Introduction

Chemical imaging with high spatial resolution and spectroscopic information opens a new window in understanding molecular behavior in a complex system, such as a live cell. Among the various modalities, vibrational spectroscopic imaging based on infrared (IR) absorption offers a way for mapping specific chemical bonds. Different molecular environments differ in spectral peaks and intensities, and through analyzing the IR spectra, these changes can be extracted to provide chemical and structural information. Combined with wide-field illumination and focal plane array, IR spectrometers can provide spatially resolved images where each pixel in the image presents an IR spectrum.¹⁻³ Using quantum cascade lasers (QCL),⁴⁻⁶ wavelengths can be selected to perform non-interferometry discrete IR imaging. However, the direct IR imaging techniques suffer from poor spatial resolution due to long excitation wavelength, preventing them from resolving subcellular structures. To overcome the barrier, indirect measurements were developed, such as atomic force microscopy infrared spectroscopy (AFM-IR) that combines the chemical selectivity offered by IR absorption and high resolution of AFM.⁷⁻⁸

Photothermal spectroscopic imaging is another way to improve spatial resolution and has shown notable sensitivity in characterizing down to single molecules based on electronic absorption in the visible region.⁹⁻¹⁰ For vibrational absorption in the mid-IR region, the implementation involves a modulated/pulsed mid-IR laser as the pump with a continuous visible or near-IR laser as the probe. When the mid-IR beam is absorbed in certain vibrational frequency, thermal effect leads to a local temperature change and then a change of refractive index. By measuring the corresponding change in probe beam intensity, a photothermal imaging contrast is created. Furstenberg and colleagues demonstrated IR pump and visible probe photothermal imaging by scanning the edge of a calibration slide and estimated the spatial resolution to be ~ 2 μm .¹¹ Erramilli and colleagues demonstrated photothermal spectroscopy between 1860 and 1980 cm^{-1} of a liquid crystal in different phases.¹² Sander and co-workers imaged bird brain tissue slices and characterized cancerous and healthy mouse brain tissue using the photothermal contrast for amide I band.¹³⁻¹⁴ Zhang et al. improved the spatial resolution to 0.61 μm and demonstrated imaging of live cells and *Caenorhabditis elegans* in transmission mode.¹⁵ Li et al. illustrated the mapping of pharmaceutical ingredients in the fingerprint region with an epi-detected configuration.¹⁶ Using mid-IR optical parametric oscillator (OPO) output as the pump source, Hartland and colleagues demonstrated photothermal imaging of single *E. coli* by combining a reflective objective focusing the IR beam and a regular high numerical aperture (NA) objective focusing the visible probe beam in a counter-propagation scheme.¹⁷

Thus, far, no literature has illustrated mid-infrared photothermal (MIP) imaging of live cells at the high wavenumber region. One technical barrier is the limited spectral coverage of mid-IR laser sources. Though customized QCLs can cover the C–D region around 2100 cm^{-1} ,¹⁸⁻²⁰ the C–H region have mainly been achieved in laboratories for requirements on special design of materials.²¹⁻²³ In addition, the limited tunability of individual QCL chip requires multiple units to cover the meaningful high wavenumber region, which increases the complexity of the product. Another way to generate mid-IR radiation is through frequency down-conversion from near-IR beams, among which the OPO and difference frequency generation (DFG) are most widely applied. Tunable mid-IR frequency combs based on OPO have been utilized in the spectroscopy applications,²⁴⁻²⁵ yet it requires resonant cavity design to lock the synchronous pump laser, drastically decreasing the stability and performance of such lasers. On the other hand, DFG utilizes single-path scheme and the output idler wavelength is determined by the input wavelengths, which

simplifies the setup design and improves the wavelength stability. DFG from well-developed mode-locked Ti:sapphire lasers has been typically used to achieve stable wavelength tuning in terms of IR generation.²⁶⁻²⁷

In this work, we reported a DFG based mid-IR source and its use for photothermal imaging with submicron spatial resolution at high wavenumber region. To maximum the DFG output, we conducted theoretical calculations with different focusing parameters. Our experimental results showed a linear relationship between DFG idler powers with the input pump powers. We took the advantage of the spectral focusing scheme and decreased the spectral width by 5.5 times to 29.3 cm^{-1} . The calibration of motorized stage positions with corresponding central wavenumbers was performed. In addition, the spectrum of deuterated glycerol acquired from Fourier-transform infrared (FTIR) and DFG-pumped MIP were compared in order to demonstrate the spectral fidelity. Furthermore, we employed deuterated fatty acid to confirm the correlation of our cell imaging results with the established metabolic pathways.

4.2 Theoretical calculation

The DFG process involves three interactive waves: two fundamental laser beams are focused into a nonlinear frequency conversion crystal to generate a third radiation with the frequency equal to the energy difference of fundamental beams. The efficiency of this process depends on the nonlinear frequency conversion crystal and can be optimized by carefully designing the beam coupling and focusing conditions. We used magnesium oxide doped periodically poled lithium niobite (MgO:PPLN) as the frequency conversion crystal based on the following considerations. (1) The quasi-phase matching (QPM) merit of the crystal requires the sign of nonlinear coefficient χ_2 periodically changed. As a result, constructively interference enables continuously buildup of the generated light.²⁸ (2) The effective nonlinear coefficient is large with typically value of 14.9 pm/V .²⁹ Since the phase-matching condition is satisfied by QPM, the largest component ($d_{33}= 25 \text{ pm/V}$) in the 2D matrix of the second-order susceptibility tensor can be used. (3) Lithium niobate is widely transparent from 0.34 to 5 μm ³⁰ compared AgGaS₂ (AGS) with the transparent window in 0.5–1.3 μm .³¹ (4) Doping MgO could improve the photorefractive damage threshold.³⁰ In addition, crystal length is selected to be 5 mm in order to minimize group velocity mismatch for femtosecond laser pulses.²⁰

We then performed a theoretical calculation of DFG output power as a function of input powers, crystal-related parameters, and focusing conditions. For Gaussian beams, under no absorption and phase-matching condition, the power of generated DFG is given by³²:

$$P_i = P_p P_s \frac{32\pi^2 d_{eff}^2 L}{\varepsilon_0 c n_i \lambda_i^2 (n_s \lambda_p + n_p \lambda_s)} h(\xi, L) \quad (1)$$

where P_i represents the generated mid-IR ‘‘idler’’ beam, and P_p and P_s are the powers of pump (higher frequency) and signal (lower frequency) of fundamental wave. d_{eff} and L represent the effective nonlinear coefficient and crystal length. λ is the wavelength and n is the refractive index of crystal calculated by the Sellmeier equation with the parameters given by the manufacturer. $h(\xi, L)$ is the focusing function:

$$h(\xi, L) = Re\left(\frac{1}{4\xi} \times \int_{-\xi}^{\xi} d\tau \int_{-\xi}^{\xi} d\tau' \frac{1}{1+\tau\tau' - i\frac{1+u^2}{1-u^2}(\tau-\tau')}\right) \quad (2)$$

fwhere $\xi = \frac{L}{b}$, $\mu = \frac{n_s \lambda_p}{n_p \lambda_s}$, and b is the confocal parameter defined by beam waist ω : $b = \frac{1}{2}(k_p \omega_p^2 + k_s \omega_s^2)$. For $\lambda_p = 830$ nm, $\lambda_s = 1080$ nm, $L = 5$ mm and phase-matching temperature 185 °C, a numerical calculation results of $h(\xi)$ is shown in Figure 4-1. The maximum value of $h_{max} = 0.282$ is achieved at $\xi = 1.3$ which corresponds to optimal focusing condition with a focal length of 133 mm. We have calculated the $h(\xi)$ for 4 frequently used achromatic lenses, and the results were: $h(f_{150mm}) = 0.279$, $h(f_{100mm}) = 0.269$, $h(f_{75mm}) = 0.234$, $h(f_{60mm}) = 0.197$. With a negligible difference between $h(f_{150mm})$ and $h(f_{133mm})$, we utilized an achromatic lens with the focal length of 150 mm to focus two beams.

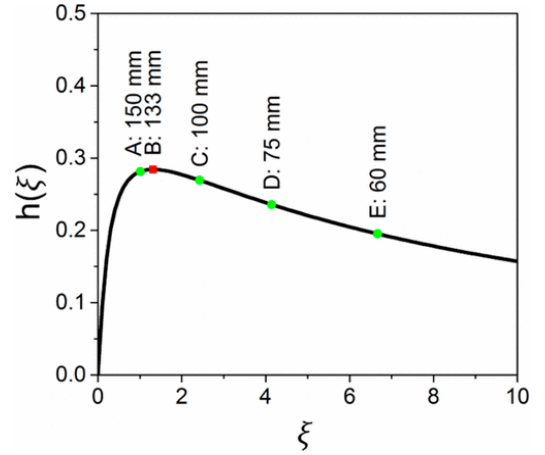


Figure 4-1 Focusing function $h(\xi)$ versus ξ calculated for $\lambda_p = 830$ nm, $\lambda_s = 1080$ nm, and crystal length of 5 mm. The typical values of 5 lenses with different focal length were labeled in the curve.

To gain the spectral resolution of the generated mid-IR beam, we used spectral focusing in which high refractive index glass rods are used to chirp the femtosecond pulses. Although the achievements of narrowband DFG pulses were demonstrated by grating or prism pairs,³³⁻³⁴ the implementation of pulse chirping by inserting highly dispersive materials in the beam path reduces

the requirements on adjusting the delicate dispersion optics.³⁵ Spectral focusing schemes have been extensively utilized for hyperspectral coherent anti-Stokes Raman scattering and SRS imaging.³⁶⁻³⁷ Here, we show the first demonstration of spectral focusing DFG for mid-infrared photothermal imaging purposes. Traditionally, DFG with narrow line width fundamental pulses achieves tunability by tuning one laser while the other remains fixed.³⁸ After pulses are chirped, the overlapping of two pulses leads to reduced frequency bandwidth, and hence the spectral resolution of the generated mid-IR beam is improved. In the spectral focused DFG setup, varying the time delay will change the frequency overlapping of two fundamental pulses, thus the central wavelength of the generated beam will also be changed.

4.3 Methods

4.3.1 DFG Implementation

To generate the high wavenumber radiation for the MIP pump source, we utilized the DFG process by coupling a DFG crystal (MDFG2 – 5, Coersion) to a femtosecond laser system (Chameleon Vision, Coherent) and achieved flexible spectral tunability (Figure 4-2). The crystal is 5 mm long and has 9 adjacent poling periods in the range of 20.9 to 23.3 μm . We used two spatially and spectrally overlapped femtosecond near-IR beams, with one beam modulated by an acousto-optic modulator (AOM, 15180–1.06-LTD-GAP, Gooch & Housego) at the frequency around 100 kHz.¹⁵ A motorized stage was used as a delay line to adjust the temporal overlap of the two pulses. The oven holding the nonlinear crystal was mounted on a 2D translation stage enabling both the precise adjustment of focusing position and the switching between poling channels. A germanium window (WG91050- C9, Thorlabs) was used to remove beams with wavelength below 2 μm .

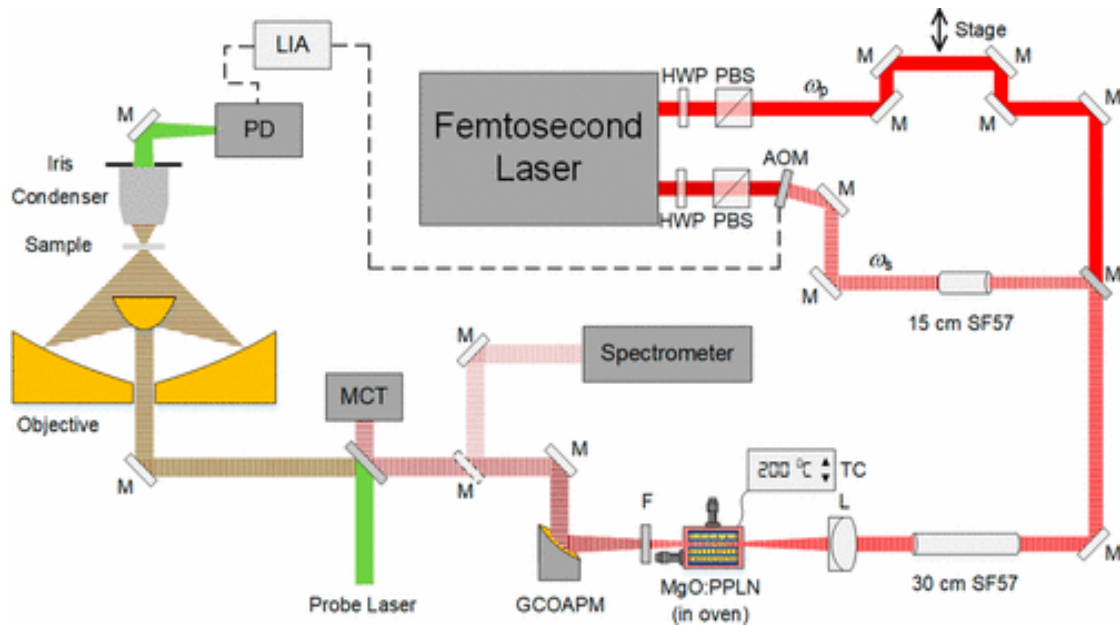


Figure 4-2 Schematic of a DFG-pumped MIP microscope. The mid-IR source was generated by two spatially and spectrally overlapped femtosecond beams and a MgO:PPLN crystal. The thermal lensing effect was probed by a continuous 785 nm laser diode. HWP: half-wave plate. PBS: polarizing beam splitter. ω_p : pump beam. ω_s : signal beam. M: mirror. Dashed M: flip mirror. AOM: acousto-optic modulator. SF57: SF57 glass rod. L: lens. TC: temperature control. F: filter. GCOAPM: gold coated off-axis parabolic mirror. MCT: mercury cadmium telluride. PD: photodiode. LIA: lock-in amplifier.

4.3.2 MIP microscope

The generated mid-IR beam was collimated using a gold-coated off-axis parabolic mirror to avoid aberration and then coupled into the existing MIP microscope, serving as the pump beam for vibrational excitation of the sample (Figure 4-2). A flip mirror was inserted after beam collimation, guiding the mid-IR beam into a spectrometer (FTIR Rocket, Arcoptix) and central wavelengths as well as spectral widths can be measured. A laser diode with central wavelength at 785 nm served as probe laser (LD-785-SE-400, Thorlabs). The pump and probe beams were collinearly combined with a platinum coated dichroic mirror (BSP-PD-25-2, ISP Optics) and then focused by a gold coated reflective objective with NA of 0.65 (#66589, Edmund Optics). The back-reflected mid-IR beam was recorded by a mercury cadmium telluride detector (PVM-10.6, Vigo System) for the purpose of spectrum normalization. The MIP signal was collected by a microscope condenser with a variable iris (NA = 0.55), and then detected by a photodiode (S3994-1, Hamamatsu). The modulation frequency of the pump beam in DFG processes was

controlled by the lock-in amplifier (HF2LI, Zurich Instruments) by sending out triggers to the AOM, thus the generated mid-IR beam shared the same modulation frequency and the MIP signal was synchronously detected.

4.3.3 Spectral focusing

We used one SF57 glass rod with a length of 15 cm in the signal (ω_s) beam and two SF57 glass rods after the dichroic mirror that combined the pump (ω_p) and signal beams. The chirped pulse duration was measured to be about 1.48 ps using an autocorrelator. The delay between two beams was controlled by a motorized stage (T-LS, Zaber Technologies).

4.3.4 A549 cell imaging

D₃₁-palmitic acid powder (Cambridge Isotope Laboratories, Inc.) was dissolved in dimethyl sulfoxide at the final concentration of 50 mM and A549 human lung cancer cells were treated for 10 h after the cells were attached to the custom-built calcium fluoride bottom Petri dish. In the control group, the cell culture medium was supplemented with 50 mM regular palmitic acid and the cells were cultured for 10 h before MIP imaging. During the cell imaging processes, phosphate-buffered saline was supplemented every 15 min to prevent cells from drying.

4.4 Results

4.4.1 DFG output

With the configuration described in methods and by adjusting the angle of the half-wave plate to control powers, we measured DFG idler average powers as a function of pump powers with the signal power fixed at 280 mW. The fitting of data points showed a linear relationship and we got the maximum idler power of 30.2 mW with the pump power of 360 mW (Figure 4-3). The power density at the crystal was 2.69 GW/cm², which was below the estimated damage threshold of 4 GW/cm². The quantum efficiency is defined as pump photons divided by idler photons, which gave 28%, and the result was comparable with the values in the literature.³⁹ Theoretically, DFG tunable range is from 2050 to 5300 cm⁻¹ with various fundamental wavelength, temperature, and poling period combinations.

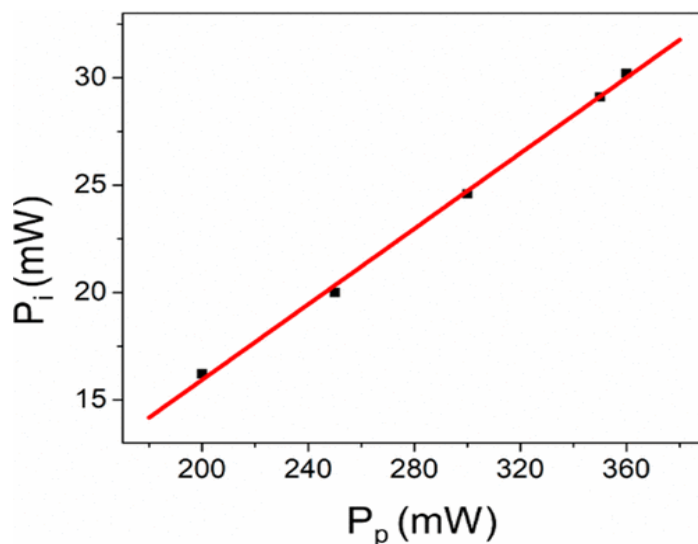


Figure 4-3 DFG average output idler powers versus input pump powers with the signal power fixed at 280 mW. Maximum of 30.2 mW was achieved with the pump power of 360 mW.

4.4.2 Improved spectral resolution based on spectral focusing

To characterize our DFG output, we centered the IR beam at the C–D vibration of 2092 cm^{-1} and demonstrated the spectral resolution and tuning capability of the spectral focusing system. The full width at half-maximum (FWHM) of the spectrum centered at 2092 cm^{-1} was 29.3 cm^{-1} (Figure 4-4a) measured with the IR spectrometer and the maximum output power was 22.1 mW. In comparison, the FWHM of output DFG for unchirped pulses was 162 cm^{-1} . As a result, the spectral width decreased by 5.5 times with our spectral focusing setup. Furthermore, we measured the output spectra when tuning the delay between two fundamental pulses (Figure 4-4a). The measured FWHM for each delay remained mostly the same. The motorized stage step position, as well as corresponding spectra, were simultaneously recorded for calibration (Figure 4-4b), in which the linear fitting showed a $R^2 = 0.99$.

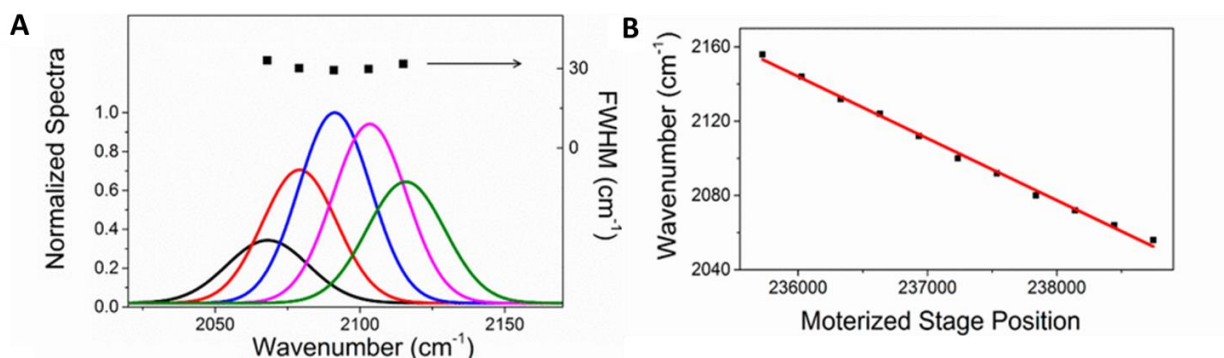


Figure 4-4 Performance and calibration of spectral focusing. (A) A series of DFG output spectra were recorded by changing the delay between two input pulses. (B) The calibration of generated mid-IR central wavenumber with motorized stage positions. The red line is the linear fitting result.

4.4.3 Spectral fidelity of DFG-pumped MIP microscope

To test the spectral fidelity as well as the enhanced spectral resolution, we centered at the C–D vibrational bond and used deuterated glycerol as the sample. The FTIR spectra showed 2 peaks in the C–D region (Figure 4-5). For the 2092 cm⁻¹ peak, two fundamental beams at 830 and 1005 nm were focusing at 22.4 μm poling channel with the crystal temperature at 200 °C; while for 2209 cm⁻¹ peak, 830 and 1015 nm beams were focused at 21.8 μm poling period with the crystal temperature at 198 °C. Since the spectra on the tuning edge within single poling channel were distorted, corresponding data points were abandoned, which causes the discontinuousness in the final spectrum. Overall consistency was observed between the FTIR and MIP spectra, which confirmed the spectral fidelity of DFG pumped MIP microscope.

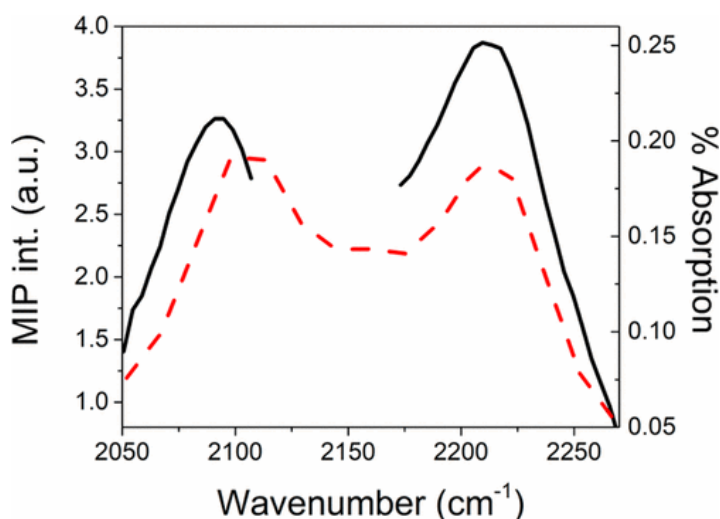


Figure 4-5 Spectral fidelity of the DFG-pumped MIP microscope. FTIR (dashed) and MIP spectrum (solid) showed overall consistency. Raw MIP spectra were normalized by the mid-IR intensities recorded by the MCT detector.

4.4.4 High-wavenumber MIP imaging of live A549 cells

The performance of the DFG-pumped MIP system was evaluated by imaging the uptake of deuterium-labeled fatty acid in A549 human lung cancer cells. Inside cells, fatty acid can be converted to lipid droplets that are closely related to energy generation, membrane formation, and intracellular protein metabolism.⁴⁰⁻⁴¹ Isotope labels enable tracking of the dynamic process of small molecules in live cells and organelles due to their small size and nontoxic merit. The deuterium isotope label has been used to investigate protein synthesis and degradation,⁴² track lipogenesis from glucose in cancer cells,⁴³ probe intracellular cholesterol storage. Here, we demonstrate the visualization of fatty acid uptake in a single cell using the MIP imaging method. We used d_{31} -palmitic acid as a testing bed. The measured FTIR spectrum of the d_{31} -palmitic acid powder showed 2092 and 2190 cm^{-1} peaks in the C–D region. The MIP image at 2940 cm^{-1} showed a combined concentration map of lipid and protein (Figure 6A). When tuned to 2092 cm^{-1} , the C–D on MIP image depicted the distribution of the d_{31} -palmitic acid metabolites (Figure 4-6B). When tuning away from the high wavenumber region to 1850 cm^{-1} , no MIP contrast was observed (Figure 6-6C), verifying the background free capability of MIP microscopy. In the control group, no MIP contrast was revealed in either the C–D on channel or the off-resonance channel (Figure 6-6D–F), confirming the contrast in Figure 6-6B was indeed from the isotope molecule. Single lipid droplets were resolved in both C–D and C–H MIP images with submicron spatial resolution (Figure 6-6G–I). The probe power measured at the sample was 8.86 mW and the pump powers at the sample were 0.99 mW, 2.86 mW, and 4.7 mW for 1850 cm^{-1} , 2092 cm^{-1} , and 2940 cm^{-1} , respectively. The C–D signal appearing in the lipid droplets colocalized with the intracellular droplets, as well as in the cytoplasm, indicating of the conversion of d_{31} -palmitic acid into triglycerides and membrane components. These observation were consistent with the established metabolic pathways of fatty acid uptake.⁴⁴ We note that similar work revealing the influence of saturated and unsaturated fatty acid on cell lipotoxicity using an SRS microscope has been demonstrated.⁴⁵ Due to the different physical mechanism of absorption and scattering processes, IR and Raman techniques can provide complementary information. However, lower power at sample is expected for IR methods because of the larger cross section (2.86 mW and 8.86 mW for pump and probe in MIP microscope; 10 mW and 40 mW for pump and Stokes in SRS microscope). The spatial resolution is another critical factor to resolve subcellular structures. Compared with the 0.42 μm lateral FWHM resolution of the SRS microscope, our MIP microscope

achieved the submicron resolution of $0.61\ \mu\text{m}$ (Figure 6-6G–I) and further improvement is possible by using shorter wavelength for the probe beam.

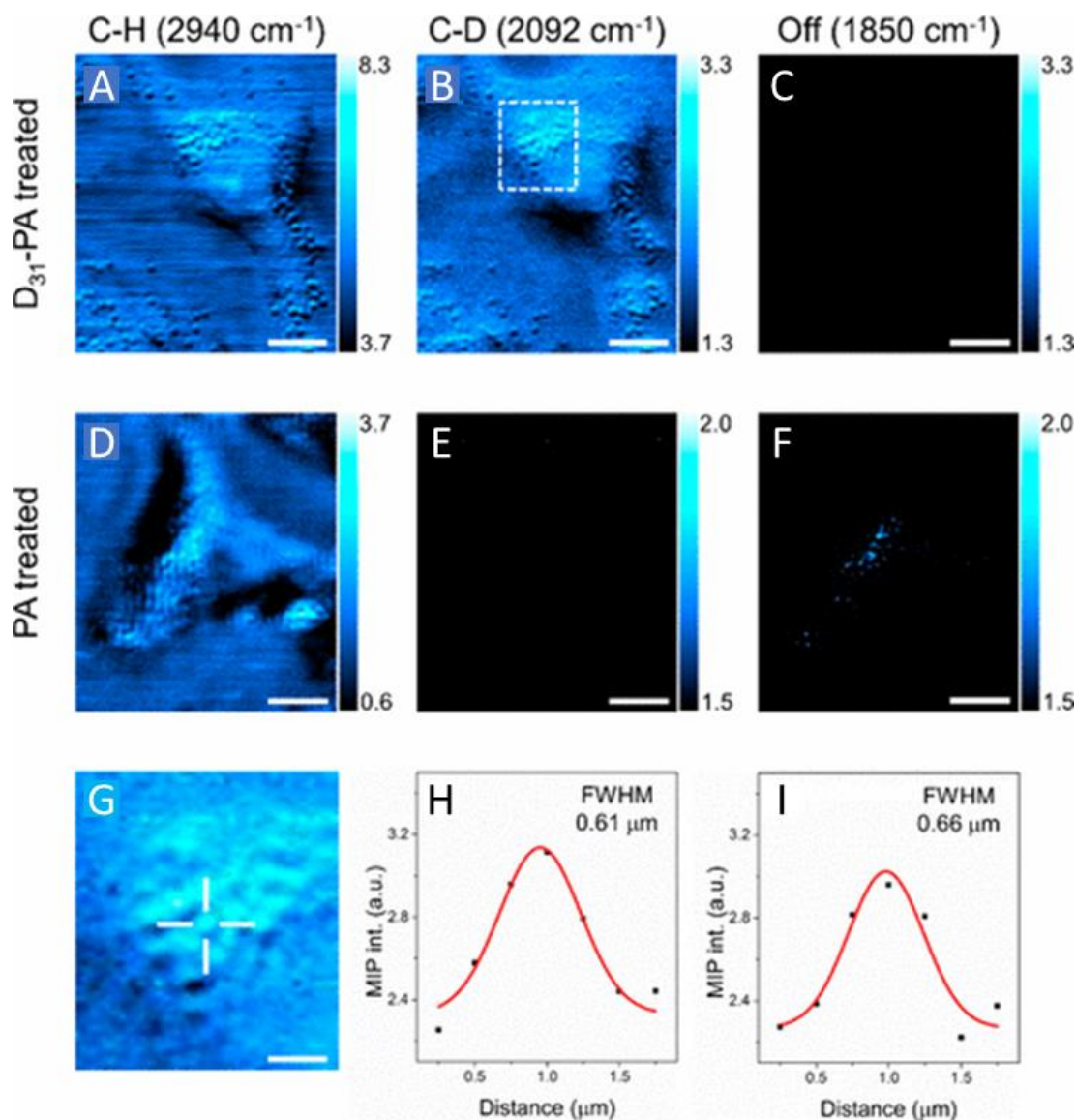


Figure 4-6 High-wavenumber MIP image of A549 lung cancer cells. (A) MIP image at $2940\ \text{cm}^{-1}$ reveals C–H rich lipid and protein contents in d_{31} -palmitic acid treated A549 cells. (B) C–D image showing the distribution of fatty acid metabolites. (C) Off-resonance image showing no MIP contrast. (D–F) Corresponding MIP images for control group treated with regular palmitic acid. (G) Expanded view of the dashed square in (B). (H–I) The intensity profiles of selected droplet indicated in (G) along the horizontal and vertical direction, respectively. Gaussian fits and FWHM were shown. Image acquisition speed: 5 ms per pixel; Scale bars: $10\ \mu\text{m}$ in (A–F), and $3\ \mu\text{m}$ in (G).

4.5 Conclusions

We reported a mid-IR source by utilizing a femtosecond Ti:sapphire laser and a nonlinear crystal through the DFG process. Compared to QCLs which have limited tunability on a single chip, a key advantage of the DFG-based mid-IR source is its possibility to cover a broad spectral region. Spectral focusing narrowed the spectral width from 162 to 29.3 cm^{-1} . Using the DFG output as the pump source for the MIP microscope, we demonstrated the capability to map C–H and C–D bonds in live cells. With extended spectral window, MIP microscopy can be used to resolve more subcellular structures. Furthermore, by employing deuterium labels to small molecules, visualization of metabolic activities, such as de novo lipogenesis and protein synthesis via IR based approach is expected.

4.6 References

1. Lasch, P.; Boese, M.; Pacifico, A.; Diem, M., FT-IR spectroscopic investigations of single cells on the subcellular level. *Vibrational spectroscopy* **2002**, *28* (1), 147-157.
2. Chan, K. A.; Kazarian, S. G., Detection of trace materials with Fourier transform infrared spectroscopy using a multi-channel detector. *Analyst* **2006**, *131* (1), 126-131.
3. Kazarian, S. G.; Chan, K. A., ATR-FTIR spectroscopic imaging: recent advances and applications to biological systems. *Analyst* **2013**, *138* (7), 1940-1951.
4. Kole, M. R.; Reddy, R. K.; Schulmerich, M. V.; Gelber, M. K.; Bhargava, R., Discrete frequency infrared microspectroscopy and imaging with a tunable quantum cascade laser. *Analytical chemistry* **2012**, *84* (23), 10366-10372.
5. Bassan, P.; Weida, M. J.; Rowlette, J.; Gardner, P., Large scale infrared imaging of tissue micro arrays (TMAs) using a tunable Quantum Cascade Laser (QCL) based microscope. *Analyst* **2014**, *139* (16), 3856-3859.
6. Kröger, N.; Egl, A.; Engel, M.; Gretz, N.; Haase, K.; Herpich, I.; Kränzlin, B.; Neudecker, S.; Pucci, A.; Schönhals, A., Quantum cascade laser-based hyperspectral imaging of biological tissue. *Journal of biomedical optics* **2014**, *19* (11), 111607.
7. Huth, F.; Schnell, M.; Wittborn, J.; Ocelic, N.; Hillenbrand, R., Infrared-spectroscopic nanoimaging with a thermal source. *Nature materials* **2011**, *10* (5), 352-356.
8. Huth, F.; Govyadinov, A.; Amarie, S.; Nuansing, W.; Keilmann, F.; Hillenbrand, R., Nano-FTIR absorption spectroscopy of molecular fingerprints at 20 nm spatial resolution. *Nano letters* **2012**, *12* (8), 3973-3978.

9. Gaiduk, A.; Yorulmaz, M.; Ruijgrok, P.; Orrit, M., Room-temperature detection of a single molecule's absorption by photothermal contrast. *Science* **2010**, *330* (6002), 353-356.
10. Ding, T. X.; Hou, L.; Meer, H. v. d.; Alivisatos, A. P.; Orrit, M., Hundreds-fold sensitivity enhancement of photothermal microscopy in near-critical Xenon. *The journal of physical chemistry letters* **2016**, *7* (13), 2524-2529.
11. Furstenberg, R.; Kendziora, C. A.; Papantonakis, M. R.; Nguyen, V.; McGill, R. In *Chemical imaging using infrared photothermal microspectroscopy*, Next-Generation Spectroscopic Technologies V, International Society for Optics and Photonics: 2012; p 837411.
12. Märtiri, A.; Jeys, T.; Liberman, V.; Hong, M.; Mertz, J.; Altug, H.; Erramilli, S., Mid-infrared photothermal heterodyne spectroscopy in a liquid crystal using a quantum cascade laser. *Applied physics letters* **2012**, *101* (4), 044101.
13. Märtiri, A.; Totachawattana, A.; Liu, H.; Hong, M. K.; Gardner, T.; Sander, M. Y.; Erramilli, S. In *Label free mid-IR photothermal imaging of bird brain with quantum cascade laser*, 2014 Conference on Lasers and Electro-Optics (CLEO)-Laser Science to Photonic Applications, IEEE: 2014; pp 1-2.
14. Totachawattana, A.; Liu, H.; Mertiri, A.; Hong, M. K.; Erramilli, S.; Sander, M. Y., Vibrational mid-infrared photothermal spectroscopy using a fiber laser probe: asymptotic limit in signal-to-baseline contrast. *Optics letters* **2016**, *41* (1), 179-182.
15. Zhang, D.; Li, C.; Zhang, C.; Slipchenko, M. N.; Eakins, G.; Cheng, J.-X., Depth-resolved mid-infrared photothermal imaging of living cells and organisms with submicrometer spatial resolution. *Science advances* **2016**, *2* (9), e1600521.
16. Li, C.; Zhang, D.; Slipchenko, M. N.; Cheng, J.-X., Mid-infrared photothermal imaging of active pharmaceutical ingredients at submicrometer spatial resolution. *Analytical chemistry* **2017**, *89* (9), 4863-4867.
17. Li, Z.; Aleshire, K.; Kuno, M.; Hartland, G. V., Super-resolution far-field infrared imaging by photothermal heterodyne imaging. *The Journal of Physical Chemistry B* **2017**, *121* (37), 8838-8846.
18. Grills, D. C.; Cook, A. R.; Fujita, E.; George, M. W.; Preses, J. M.; Wishart, J. F., Application of external-cavity quantum cascade infrared lasers to nanosecond time-resolved infrared spectroscopy of condensed-phase samples following pulse radiolysis. *Applied spectroscopy* **2010**, *64* (6), 563-570.
19. Lopatik, D.; Lang, N.; Macherius, U.; Zimmermann, H.; Röpcke, J., On the application of cw external cavity quantum cascade infrared lasers for plasma diagnostics. *Measurement Science and Technology* **2012**, *23* (11), 115501.
20. Wörle, K.; Seichter, F.; Wilk, A.; Armacost, C.; Day, T.; Godejohann, M.; Wachter, U.; Vogt, J.; Radermacher, P.; Mizaikoff, B., Breath analysis with broadly tunable quantum cascade lasers. *Analytical chemistry* **2013**, *85* (5), 2697-2702.

21. Faist, J.; Capasso, F.; Sivco, D. L.; Hutchinson, A. L.; Chu, S.-N. G.; Cho, A. Y., Short wavelength ($\lambda \sim 3.4 \mu\text{m}$) quantum cascade laser based on strained compensated InGaAs/AlInAs. *Applied Physics Letters* **1998**, *72* (6), 680-682.
22. Commin, J.; Revin, D.; Zhang, S.; Krysa, A.; Kennedy, K.; Cockburn, J., High peak power $\lambda \sim 3.3$ and $3.5 \mu\text{m}$ InGaAs/AlAs (Sb) quantum cascade lasers operating up to 400 K. *Applied Physics Letters* **2010**, *97* (3), 031108.
23. Revin, D. G.; Commin, J. P.; Zhang, S. Y.; Krysa, A. B.; Kennedy, K.; Cockburn, J. W., InP-based midinfrared quantum cascade lasers for wavelengths below $4 \mu\text{m}$. *IEEE Journal of Selected Topics in Quantum Electronics* **2011**, *17* (5), 1417-1425.
24. Adler, F.; Masłowski, P.; Foltynowicz, A.; Cossel, K. C.; Briles, T. C.; Hartl, I.; Ye, J., Mid-infrared Fourier transform spectroscopy with a broadband frequency comb. *Optics express* **2010**, *18* (21), 21861-21872.
25. Foltynowicz, A.; Masłowski, P.; Fleisher, A. J.; Bjork, B. J.; Ye, J., Cavity-enhanced optical frequency comb spectroscopy in the mid-infrared application to trace detection of hydrogen peroxide. *Applied Physics B* **2013**, *110* (2), 163-175.
26. Chen, W.; Mouret, G.; Boucher, D.; Tittel, F., Mid-infrared trace gas detection using continuous-wave difference frequency generation in periodically poled RbTiOAsO₄. *Applied Physics B* **2001**, *72* (7), 873-876.
27. Xuan, H.; Zou, Y.; Wang, S.; Han, H.; Wang, Z.; Wei, Z., Generation of ultrafast mid-infrared laser by DFG between two actively synchronized picosecond lasers in a MgO: PPLN crystal. *Applied Physics B* **2012**, *108* (3), 571-575.
28. Boyd, R. W., *Nonlinear optics*. Elsevier: 2003.
29. Cruz, F. C.; Maser, D. L.; Johnson, T.; Ycas, G.; Klose, A.; Giorgetta, F. R.; Coddington, I.; Diddams, S. A., Mid-infrared optical frequency combs based on difference frequency generation for molecular spectroscopy. *Optics express* **2015**, *23* (20), 26814-26824.
30. Ishizuki, H.; Taira, T., High-energy quasi-phase-matched optical parametric oscillation in a periodically poled MgO: LiNbO₃ device with a $5 \text{ mm} \times 5 \text{ mm}$ aperture. *Optics letters* **2005**, *30* (21), 2918-2920.
31. Pires, H.; Baudisch, M.; Sanchez, D.; Hemmer, M.; Biegert, J., Ultrashort pulse generation in the mid-IR. *Progress in Quantum Electronics* **2015**, *43*, 1-30.
32. Borri, S.; Cancio, P.; De Natale, P.; Giusfredi, G.; Mazzotti, D.; Tamassia, F., Power-boosted difference-frequency source for high-resolution infrared spectroscopy. *Applied Physics B* **2003**, *76* (4), 473-477.

33. Danielson, J.; Jameson, A.; Tomaino, J.; Hui, H.; Wetzel, J.; Lee, Y.-S.; Vodopyanov, K., Intense narrow band terahertz generation via type-II difference-frequency generation in ZnTe using chirped optical pulses. *Journal of Applied Physics* **2008**, *104* (3), 033111.
34. Jin, L.; Yamanaka, M.; Sonnenschein, V.; Tomita, H.; Iguchi, T.; Sato, A.; Oh-hara, T.; Nishizawa, N., Highly coherent tunable mid-infrared frequency comb pumped by supercontinuum at 1 μm . *Applied Physics Express* **2016**, *10* (1), 012503.
35. Cartella, A.; Nova, T. F.; Oriana, A.; Cerullo, G.; Först, M.; Manzoni, C.; Cavalleri, A., Narrowband carrier-envelope phase stable mid-infrared pulses at wavelengths beyond 10 μm by chirped-pulse difference frequency generation. *Optics letters* **2017**, *42* (4), 663-666.
36. Rocha-Mendoza, I.; Langbein, W.; Borri, P., Coherent anti-Stokes Raman microspectroscopy using spectral focusing with glass dispersion. *Applied Physics Letters* **2008**, *93* (20), 201103.
37. Fu, D.; Holtom, G.; Freudiger, C.; Zhang, X.; Xie, X. S., Hyperspectral imaging with stimulated Raman scattering by chirped femtosecond lasers. *The Journal of Physical Chemistry B* **2013**, *117* (16), 4634-4640.
38. Théberge, F.; Châteauneuf, M.; Dubois, J.; Villeneuve, A.; Salhany, J.; Burgoyne, B. In *Tunable mid-infrared generation using a synchronized programmable fiber lasers*, 2011 IEEE Photonics Society Summer Topical Meeting Series, IEEE: 2011; pp 71-72.
39. Erny, C.; Moutzouris, K.; Biegert, J.; Kühlke, D.; Adler, F.; Leitenstorfer, A.; Keller, U., Mid-infrared difference-frequency generation of ultrashort pulses tunable between 3.2 and 4.8 μm from a compact fiber source. *Optics letters* **2007**, *32* (9), 1138-1140.
40. Farese Jr, R. V.; Walther, T. C., Lipid droplets finally get a little RESPECT. *Cell* **2009**, *139* (5), 855-860.
41. Welte, Michael A., Expanding Roles for Lipid Droplets. *Current Biology* **2015**, *25* (11), R470-R481.
42. Wei, L.; Yu, Y.; Shen, Y.; Wang, M. C.; Min, W., Vibrational imaging of newly synthesized proteins in live cells by stimulated Raman scattering microscopy. *Proceedings of the National Academy of Sciences* **2013**, *110* (28), 11226-11231.
43. Li, J.; Cheng, J.-X., Direct Visualization of De novo Lipogenesis in Single Living Cells. *Scientific Reports* **2014**, *4* (1), 6807.
44. Kuhajda, F. P., Fatty Acid Synthase and Cancer: New Application of an Old Pathway. *Cancer Research* **2006**, *66* (12), 5977-5980.
45. Zhang, D.; Slipchenko, M. N.; Cheng, J.-X., Highly Sensitive Vibrational Imaging by Femtosecond Pulse Stimulated Raman Loss. *The Journal of Physical Chemistry Letters* **2011**, *2* (11), 1248-1253.

CHAPTER 5. POLARIZATION WAVEFRONT SHAPING FOR QUANTITATIVE PHASE CONTRAST IMAGING BY AXIALLY-OFFSET DIFFERENTIAL INTERFERENCE CONTRAST (ADIC)

A version of this chapter has been published by *Proceedings of SPIE*. Reprint with permission from Ding, C., Li, C., Deng, F., & Simpson, G. J. (2019, March). Polarization wavefront shaping for quantitative phase contrast imaging by axially-offset differential interference contrast (ADIC) microscopy. In *Quantitative Phase Imaging V* (Vol. 10887, p. 1088728). International Society for Optics and Photonics. Copyright 2019 Society of Photo-Optical Instrumentation Engineers (SPIE).

Axially-offset differential interference contrast (ADIC) microscopy was developed for quantitative phase contrast imaging (QPI) by using polarization wavefront shaping approach with a matched pair of micro-retarder arrays. In ADIC microscopy, wavefront shaping with a micro-retarder array (μ RA) produces a pattern of half-wave retardance varying spatially in the azimuthal orientation of the fast-axis. For a linearly polarized input beam, the polarization pattern induced from the linearly polarized plane wave through the μ RA is identical to the interference between a slightly diverging right circularly polarized (RCP) and a slightly converging left circularly polarized (LCP) plane wave. Using a $10\times$ objective, two axially offset foci separated by $70\ \mu\text{m}$ are consequently generated from the patterned wavefront with orthogonal polarization states, serving as the sample and reference focal planes respectively for QPI. A paired μ RA in transmission coherently recombines the two orthogonal components to recover the incident polarization state in the absence of sample. The large spatial offset (roughly $1/10$ of the field of view) between the two foci provides a stable and uniform reference. Quantitative phase contrast images are directly recovered from sample-scan measurements with a single-channel detector and lock-in amplification with fast polarization modulation. This method has been successfully used for bio-sample imaging, nanoparticle detection and refractive index calculation of silica microbeads.

5.1 Introduction

Phase-sensitive microscopy allows visualization of weakly scattered sample with low contrast in conventional bright field microscopy¹. It has been widely used in biological research for neurons behavior², kinesin-driven movement³, microtubule-related motility visualization⁴, etc. Zernike phase contrast microscopy and Nomarski differential interference contrast (DIC)

microscopy are two of the most common phase contrast imaging methods. In Zernike phase contrast microscopy, phase contrast is produced by intensity differences dependent on spatial interference between patterned light from an annular ring. Nomarski DIC microscopy generates phase-related intensity contrast from interference between laterally offset locations within the field of view using a matched set of Nomarski prisms. Two orthogonally polarized components with a small angle offset are generated when linearly polarized incident light passes through a Nomarski prism. Recombining the two components using a matched Nomarski prism, the resulting interference provides image contrast scaling with the phase difference between the two spatially offset positions in the field of view corresponding to the two orthogonal polarization components. In both Zernike and Nomarski phase contrast imaging, artifacts complicate the image interpretation since the interferences are generated between locations within the same sample plane, such as ‘halo’ effects for Zernike microscopy and ‘side lighting’ artifacts in Nomarski microscopy. Furthermore, these two methods typically lack the capability for quantitatively absolute phase retrieval without careful calibration⁵.

For artifact-free quantitative phase imaging (QPI), most current QPI approaches measure the interference patterns arising from recombination of split beams followed by image analysis, including asymmetric illumination-based differential phase contrast microscopy⁶⁻⁸, digital holography microscopy⁹, and spatial light interference microscopy¹⁰. However, these approaches suffer from subtle mechanical vibrations along the two separate beam paths and the indirect recovery of phase information from image analysis. In addition, the requirement for long coherence-length reference beam makes the current dual-beam QPI methods incompatible with straight forward retrofitting into existing microscope systems using LEDs and/or white light sources. Therefore, the requirement for instrument compatible with existing microscopes should have the potential to greatly expand the application of the artifact-free QPI approach with the capability of independently recovering absolute phase at every pixel for complex objects with low spatial correlation.

In this work, wavefront shaping was used to generate two axis-offset focal planes along z-direction with orthogonal polarization states. Compared with the contrast generated from Normarski phase contrast microscopy, the detected phase contrast was generated between two z positions in the sample, getting rid of the side light effects. A custom set of microretarder arrays was designed with retardance patterning of fast axis orientation of a liquid crystal on a per-pixel

basis. ADIC microscopy for quantitative phase contrast imaging was developed based on the polarization wavefront shaping using a matched pair of μ RAs. Polarization wavefront shaping using one μ RA produced a polarization-dependent pattern identical with the combination of orthogonally polarized diverging and converging beams. With a linearly polarized incident plane wave, the polarization wavefront after one μ RA is identical with the expectation from the interference between a slightly diverging right circular polarized (RCP) plane wave and a slightly converging left circularly polarized (LCP) plane wave. The two orthogonal polarization components were focused into two focal planes separated by 70 μ m with a 10 \times objective. With a fast polarization modulation of the incident light, a lock-in amplifier (LIA) was used in ADIC microscopy for simultaneous retrieval of transmittance and quantitative phase images. The quantitative phase for each pixel is recovered in a range of $[-\pi, \pi]$ and a detection limit of 0.033 radians. This strategy has been used for quantitative phase contrast imaging for tissue section sample. ADIC microscopy has also been used for refractive index investigation of silica microbeads with an agreement between the measurement and the refractive index of amorphous bulk silica.

5.2 Methods

5.2.1 Polarization wavefront shaping of μ RA

While most optics are designed to affect the polarization state of the entire beam identically, waveplate arrays allow the tailoring of the polarization state of light on a per pixel basis¹¹. Orientation modulation of liquid crystal polymers on a thin substrate can achieve geometrical phase modulation with one thin film optic. Based on different geometric design, waveplate arrays have been designed for adaptable lenses¹²⁻¹³, grating prisms¹⁴⁻¹⁵, spiral phase retarders¹⁶⁻¹⁸, etc.

In the present work, a retardance pattern of concentric rings with a quadratic spacing was designed to produce an orthogonally polarized pair of converging and diverging beams. In order to design the pattern necessary to produce the beam pair, the anticipated polarization-dependent pattern produced by the interference of orthogonally polarized converging and diverging plane waves is first considered. In general cases, the polarization state of light at any position on the Poincaré sphere can also be defined by a coherent combination of two orthogonally polarized components, such as RCP and LCP light, or horizontally polarized light and vertically polarized

light. A Nomarski prism can split linearly polarized incident light into two components which are horizontally polarized and vertically polarized, respectively. Wavefront shaping from the designed waveplate array has been used to split the beam into beamlets of orthogonally polarized light focused or defocused depending on the handedness of polarization of the beam¹¹. The overlay of converging RCP and diverging LCP beams produces linearly polarized light with the axis of polarization rotated in a radial pattern as shown in Figure 5-1A. As the reverse process, a converging RCP and diverging LCP beams are generated co-axially with a pure linear polarized incident beam into a designed μ RA with such a pattern. When focusing on the same objective lens, two axially-offset foci will be generated with orthogonally polarized states as shown in Figure 5-1B. Axially offsetting of the two focal planes allows the use of a homogeneous medium (e.g, glass, solvent, or air) as a reference. In absence of a sample, the diverging and converging components can be coherently recombined using a paired μ RA in transmission to recover the beam with the same polarization state as the incidence beam. Modulating the polarization states of the incident light allows quantitative phase change recovery and signal to noise enhancement through LIA detection.

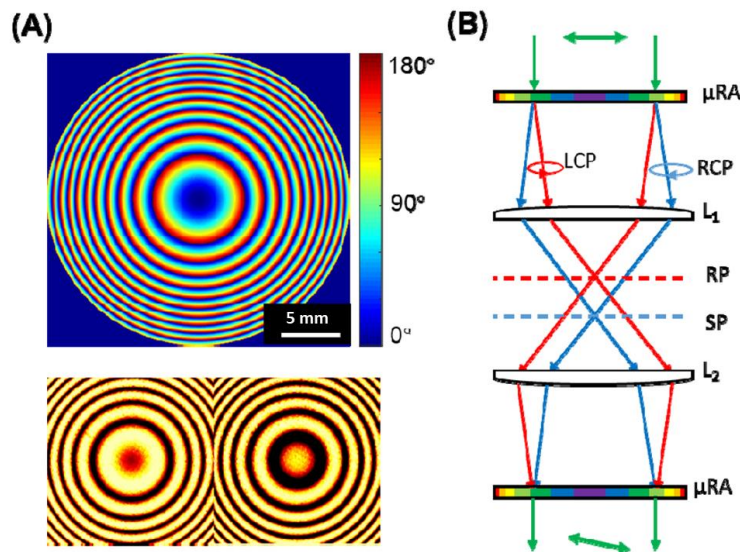


Figure 5-1 (A) The design of μ RA as half-wave retardance with the spatially varied azimuthal orientation of the fast-axis targeted for 532 nm light. Scale bar: 500 μ m. Bottom: part of the measured different intensity distribution with horizontal (H) and vertical (V) polarization detection when horizontally polarized light passing through the μ RA. (B) The working principle of ADIC microscope. L1 and L2: lens; RP: reference plane; SP: sample plane.

For linearly polarized incident light with the plane of polarization given by the angle γ , decomposition into the RCP and LCP contributions yields the expression shown in Eq. (1).

$$\begin{pmatrix} \cos \gamma \\ \sin \gamma \end{pmatrix} = \frac{1}{2} \cdot e^{-i\gamma} \cdot \begin{pmatrix} 1 \\ i \end{pmatrix} + \frac{1}{2} \cdot e^{i\gamma} \cdot \begin{pmatrix} 1 \\ -i \end{pmatrix} \quad (1)$$

To design such a μ RA with the proper pattern as shown in Figure 1(A), the wave plate retardance should have a similar radial modulation pattern as a Fresnel lens. In this work, μ RAs were designed with the pattern of half-wave retardance of 532 nm light varying spatially in the azimuthal orientation of the fast-axis. The azimuthal orientation γ was designed as a function of x , y position: $\gamma(x, y) = 2\pi[(x - r)^2 + (y - r)^2]/4f\lambda$, in which r is the active radius as 12 mm, f is focal length designed as 6.28 m and λ is the targeting wavelength as 532 nm. The azimuthal orientation angle was then wrapped into the range of $[0, \pi]$. Following passage through an objective lens, the separation distance between the two foci depends on the designed periods of the centric polarization rotation pattern of μ RAs. Larger separation is expected with smaller periods of the centric modulation. With a much smaller separation distance, the setup qualitatively converges to Zernike phase contrast, in which the reference plane is so close to the sample plane that the contrast is simply a halo. The upper limit for separating distance is ultimately dictated by the manufacturing precision of the μ RAs. Manufacture with the maximum stated manufacturing resolution of 30 μ m corresponds to a maximum fringe period of 60 μ m (with Nyquist sampling), producing a theoretical separation distance of up to 360 μ m when using a 10 \times objective. In this work, a 60 μ m \times 60 μ m pixel size per entry was used to reduce the potential for artifacts from the discretization effects at the extrema, giving a separation distance around 70 μ m as shown in Section 5.3.1.

5.2.2 Instrumentation

The quantitative phase contrast images were recovered from an ADIC microscope depicted in Figure. 5-2. In brief, a 532 nm continuous laser (Millenia Vs J) was used for illumination with horizontally polarized incident light, followed with a half wave plate (HWP) inserted in a rotation stage. A photoelastic modulator (PEM, Hinds instrument PEM-90M) and a quarter waveplate (QWP) were used after the HWP before the first μ RA. The PEM was made of isotropic optical materials and introduced retardance to the incident light as a function of time when driven at a standing acoustic wave resonance. It has two electrical outputs with one as the acoustic modulation frequency ($1f$) and the other as the doubled frequency ($2f$) of the sinusoidal driven electric field.

The fast axes of the HWP, PEM, and QWP were rotated to 22.5° , 0° , and 45° , respectively so that a modulated linearly polarized light was generated before entering the μ RA. The beam was expanded to 15 mm in diameter to fill approximately half the area of the μ RA. The light was then focused onto the sample with an average laser power around 5 mW with a $10\times$ objective (0.3 NA, Nikon). An identical $10\times$ 0.3 NA objective was used as a condenser in transmittance. In the absence of a sample, the transmittance passing through a paired μ RA in proper orientation recovered the same linearly polarized plane wave as the incidence. A sample scanning stage (Mad city labs Nano-Bio300) was used for image acquisition with a frame rate of 20 s and a $250\ \mu\text{m} \times 250\ \mu\text{m}$ field of view (FoV). Horizontally polarized transmittance was detected by passing the beam through a polarizer and a photodiode (DET-10A, Thorlabs). For the fast demodulation detection, the PEM was operating at its resonance frequency of 50 kHz, with both $1f$ (50 kHz) and $2f$ (100 kHz) outputs delivered as the reference signals to a lock-in amplifier (LIA, Stanford Research Systems SR810). Both the quadrature (Y) and in-phase (X) components of the LIA output were acquired simultaneously. The per-pixel integration time of the LIA was $30\ \mu\text{s}$. Signals were digitized at 20 kHz using a PCI-E digitizer oscilloscope cards (AlazarTech ATS-9462) and remapped into 200×200 images via custom software (MATLAB), giving a pixel size of $1.25\ \mu\text{m}/\text{pixel}$.

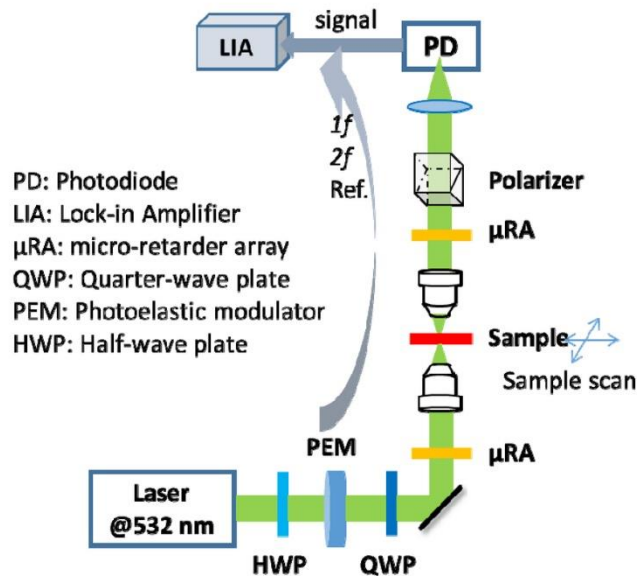


Figure 5-2 Instrumentation set-up for ADIC with a $10\times$ objective to recover both bright field images and quantitative phase contrast images. Orientations of the fast axis: HWP at 22.5° , PEM at 0° , and QWP at 45° . Incident light before the HWP was horizontally polarized with polarizer before the photodiode passing horizontally polarized light.

5.2.3 Sample preparation

Mouse tail sections and silica microbeads were used for quantitative phase analysis by ADIC. Mouse tail sections were provided by Prof. Philip Low (Purdue University, West Lafayette, IN). After decalcified in the solution of 23% formic acid, 4% formalin, and 1% methanol for 2 hours, the mouse tail was sectioned longitudinally to ensure that sections were retrieved from the central region of the tail. The mouse tail section was then fixed in 10% formalin and cryosectioning into 4 μm thick slices. After sectioning, the mouse tail was stained by hematoxylin and eosin. Silica microbeads sized were donated by Prof. Marry Wirth (Purdue University, West Lafayette, IN) with a diameter of 8 μm . For quantitative phase imaging and reflective index calculation, the silica microbeads were dispersed by ultrasonication in a commercially available nitrocellulose matrix with a high vapor pressure solvent plasticizer (Sally Hanson nail polish, Hardener) before sealing between a coverslip and a glass slide. After solvent evaporation, the silica microbeads disperse slides were directly used for ADIC imaging.

5.2.4 Quantitative phase recovery

In the absence of a sample, the Jones vector describing the detecting light (\vec{e}_{tot}) is identical to the incident light, which can be treated as a production of an identity matrix and the Jones vector of the incidence. The identity matrix can be decomposed as a linear combination of two Hermitian Pauli matrices as shown in Eq. (2). The decomposed matrices describe the Jones matrices corresponding to the two foci with orthogonally polarized components.

$$\vec{e}_{tot} = \begin{pmatrix} 1 & 0 \\ 0 & 1 \end{pmatrix} \cdot \vec{e}_o = \frac{1}{2} \left\{ \left[\begin{pmatrix} 1 & 0 \\ 0 & 1 \end{pmatrix} + \begin{pmatrix} 0 & i \\ -i & 0 \end{pmatrix} \right] + \begin{pmatrix} 1 & 0 \\ 0 & 1 \end{pmatrix} + \begin{pmatrix} 0 & -i \\ i & 0 \end{pmatrix} \right\} \cdot \vec{e}_o \quad (2)$$

When sample-induced phase shift and transmittance difference are introduced in either focal plane, Eq. (2) changes to form as Eq. (3). The complex-valued amplitude transmittances t^+ and t^- describe the field detected the following interaction in the two foci separately. The phase shift δ between the two orthogonally polarized focal planes (sample and reference planes) is described as the phase change induced by the sample at a given location. In the absence of a sample, $t^+ = t^- = 1$ and $\delta = 0$, so that the detecting signals are identical to the incident light.

$$\vec{e}_{tot} = \frac{1}{2} \left(|t^+| \cdot \begin{bmatrix} 1 & i \\ -i & 1 \end{bmatrix} \cdot e^{i\frac{\delta}{2}} + |t^-| \cdot \begin{bmatrix} 1 & -i \\ i & 1 \end{bmatrix} \cdot e^{-i\frac{\delta}{2}} \right) \cdot \vec{e}_o \quad (3)$$

It should be noticed that the (+) and (-) focal planes produced by the μ RA are orthogonally polarized relative to each other and 90 degrees phase-shifted relative to the incident polarization state. For linearly polarized incident light, the polarization states of the (+) and (-) focal planes are RCP and LCP, respectively, as mentioned in Section 5.2.1. When the incident light is RCP polarized, the (+) and (-) focal planes are horizontally and vertically polarized light. When the fast axes of the HWP, PEM, and QWP were rotated to 22.5° , 0° , and 45° with a horizontally polarized fundamental light, a linearly polarized light was generated after HWP, PEM, and QWP to pass through the μ RA. The retardance modulation frequency for the PEM was $f = 50$ kHz. As detailed in the previous report¹⁹, only odd harmonics of the Taylor series of the detecting signal have non-zero quadrature components (sine, Y) while the only even harmonics have non-zero in-phase components (cosine, X) terms. In this work, the proportionality evaluated at seventh order was used with negligible errors for the half amplitude of PEM modulation as $A = 0.3\pi$. The quadrature components (sine, Y) of the first harmonic ($1f$) and the in-phase components (cosine, X) of the second harmonic ($2f$) were expressed as Eqs. (4) and (5), respectively.

$$1f_Y \approx 2|t^+||t^-| \cdot \left(2A - A^3 + \frac{A^5}{6} - \frac{A^7}{72}\right) \cdot \cos \delta \quad (4)$$

$$2f_X \approx -2|t^+||t^-| \cdot \left(A^2 - \frac{A^4}{3} + \frac{A^6}{24}\right) \cdot \sin \delta \quad (5)$$

Once values of $\cos(\delta)$ and $\sin(\delta)$ are recovered regarding $1f_Y$, $2f_X$, and PEM modulation amplitude A , the absolute value of δ can be achieved through Eq. (6) in a range of $[-\pi, \pi]$. The relative transmittance image recovered from the LIA detection is then defined as $|t^+||t^-|$.

$$\delta = \text{Im}[\log(\cos \delta + i \sin \delta)] \quad (6)$$

5.3 Results and discussion

5.3.1 Axially-offset dual-foci produced by μ RA

The 3D point spread functions of the microscope with and without μ RA were measured with a 1951 USAF resolution test chart and shown in Figure 5-3. Edge analysis was used to evaluate the radial extent of the point spread function, in which the derivatives of the intensity profile were fit to Gaussian function to recover the root mean square beam width. Plots of the recovered Gaussian beam cross-section were achieved with multiple z-position of the test grid in order to map the beam profile in three dimensions assuming cylindrical symmetry. It can be seen that the

addition of μ RA resulted blurring for an object initially in the focal plane of the microscope. When axially translation of the objective either $\pm 35\mu\text{m}$, sharp images were recovered, indicating that μ RA produced two focus planes separated by $70\ \mu\text{m}$ symmetrically distributed about the original focal plane. The cross-sections of the axially offset foci were statistically indistinguishable with the original focus, with the spatial resolution unchanged ($\sim 2\ \mu\text{m}$) upon addition of the μ RA. The spatial offset between the two foci was roughly 1/4 of the $250\ \mu\text{m} \times 250\ \mu\text{m}$ FoV, making it possible to create a stable and uniform reference plane within a homogeneous medium immediately adjacent to the sample plane.

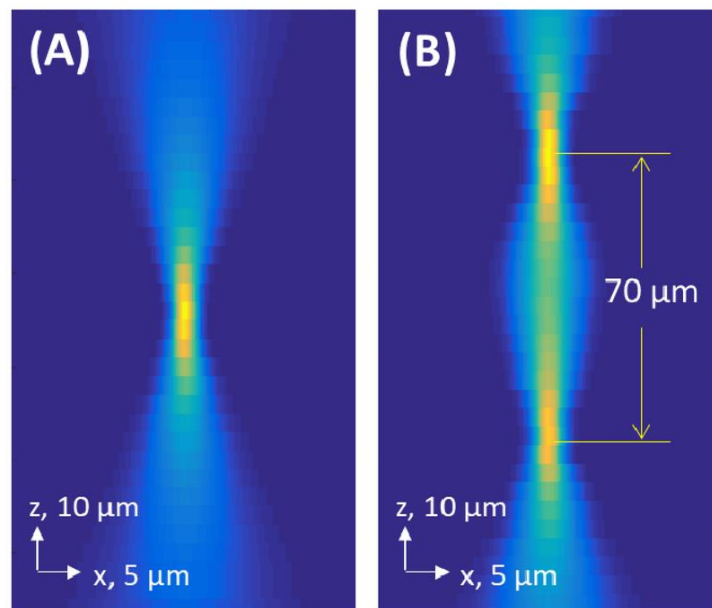


Figure 5-3 Measured point spread functions in the x-z plane without (A) and with (B) the μ RA placed in the beam path.

Due to the large axial offset between the two focal planes, the reference beam was significantly defocused in the sample plane to a spot size of $\sim 44\ \mu\text{m}$ in diameter with a 10×0.3 NA objective. The phase shift induced between a given $\sim 3\ \mu\text{m}^2$ area of the sample beam interfered with an average phase within a $\sim 1500\ \mu\text{m}^2$ area comprising the cross-sectional area of the reference beam within the sample plane. The reference effectively spanned the optical phase averaged over an area in the field of view ~ 500 -fold larger than the focal volume using common-path optics, leading to the ability of quantitative absolute phase recovery of the sample. With the well-separated objects, the phase-bias in the reference path induced by the sample was negligible. The large

separation distance between the two focal planes can remove imaging artifacts arising from the sample and reference locations cohabitating in the focal plane as in Nomarski and Zernike phase contrast microscopy.

5.3.2 Quantitative phase contrast imaging using ADIC

As detailed in Section 5.2.4, both the pure-tone $1f$ (50 kHz) and $2f$ (100 kHz) signals generated by the PEM with a modulation frequency of 50 kHz was used as the reference for the quantitative phase recover of sample imaging. A mouse tail section was used for the quantitative phase image recovery. Figure 5-4(A-D) shows both cosine (X) components and sine (Y) components collected from LIA detector with both $1f$ and $2f$ signals as the reference. Figure 5-4(A-B) shares the same contrast setting, so as Figure 5-4(C-D). As predicted, only Y components of $1f$ and X components of $2f$ show nonzero signals. The relatively transmittance bright field image (Figure 5-4E) and quantitative phase images (Figure 5-4F) were calculated based on Eqs. (4)-(6). As predicted from Eqs. (4) and (5), with a relatively small phase and shifts and high transmittance, similarities should be observed between the transmittance bright field image and the Y components of $1f$ detection, as well as between the quantitative phase image and the X components of $2f$ detection. It is also noticed that higher contrast has been seen for the detailed structures with higher transmittance as shown in Figure 5-4F.

5.3.3 Limit of detection (LoD) of quantitative phase recovery

Phase contrast images produced by ADIC are free of halo and side-lighting artifacts existed in Zernike and Nomarski phase contrast. The LoD of the phase shift calculation from ADIC was investigated. Quantitative phase recovery images were required in the absence of samples. The measured standard deviation (σ) of the images was 0.011 rad, resulting in a LoD (3σ) as 0.033 rad. For analysis of the thickness of thin lipid film ($n = 1.50$)²⁰⁻²² in an aqueous environment ($n = 1.33$). The smallest optical path length that ADIC can determine is as short as 16.4 nm. The LoD of ADIC is limited by the capability of the LIA used in our experiments that ADIC raw images demodulated from $1f$ and $2f$ signals have to be acquired separately. In addition, a smaller LoD is expected with a longer LIA integration time relative to the $30\mu\text{s}$ (3 modulation periods) in this experiment.

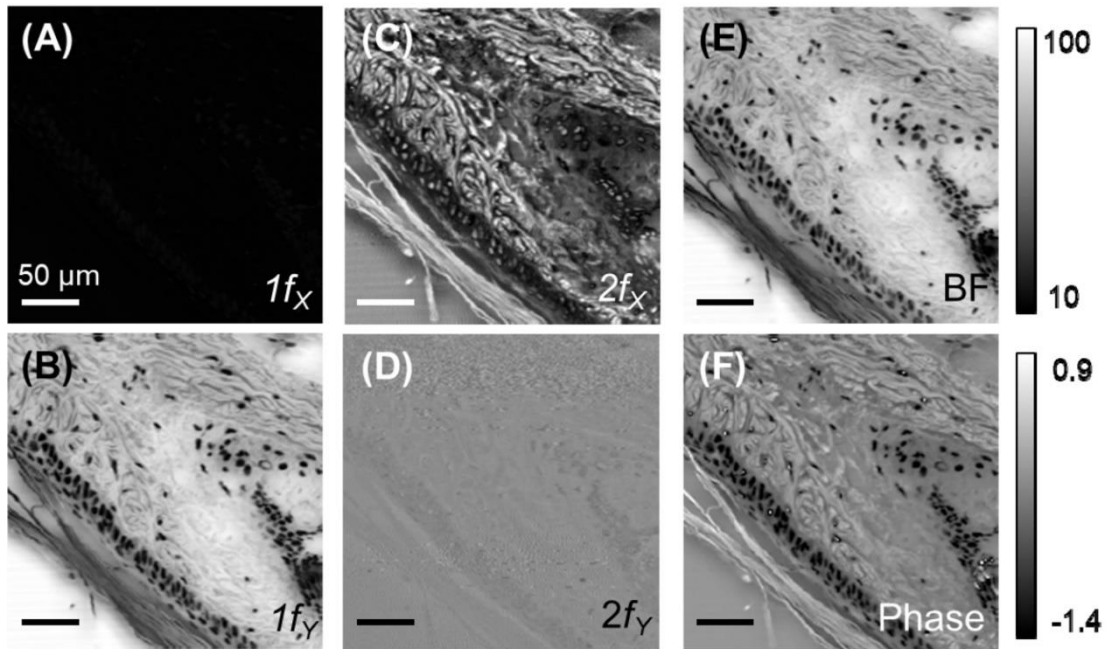


Figure 5-4 Images measured from LIA detection with $1f$ (A, B) and $2f$ (C, D) as the reference, and the recovered transmittance bright field image (E) and quantitative phase contrast image (F) of a single FoV of mouse tail section. Color bar unit: (E) transmittance percentage, (F) phase shift in radian. Scale bar: $50\ \mu\text{m}$.

5.3.4 Refractive index calculation of microspheres

The refractive index of silica beads $8\ \mu\text{m}$ in diameter was calculated using ADIC. Figure 5-5 shows the relative transmittance and quantitative phase recovery images for the same FoV of $8\ \mu\text{m}$ silica microbeads. The refractive index of silica microbeads was calculated based on the measurement phase shift and bead size. As an example, one line profile of the phase shift from a single bead (inset) is plotted in Figure 5-5C. The highest phase shift at the center of the single silica microbead was measured as 2.53 radian, with a measured bead size as $7.3\ \mu\text{m}$. Statistical analysis of the silica microbeads in several fields of view allowed the calculation between the refractive index induced between the silica microbead and nitrocellulose matrix: $\Delta n = \delta\lambda/2\pi D = 0.0293 \pm 0.0007$, in which D was the measurement bead diameter. Using the refractive index of nitrocellulose of 1.505 at $543.5\ \text{nm}$ wavelength²³, the refractive index of silica microbeads was determined as 1.4757 ± 0.0007 at $523\ \text{nm}$ wavelength. This result was in good agreement with the refractive index of amorphous bulk silica as 1.461 ²⁴.

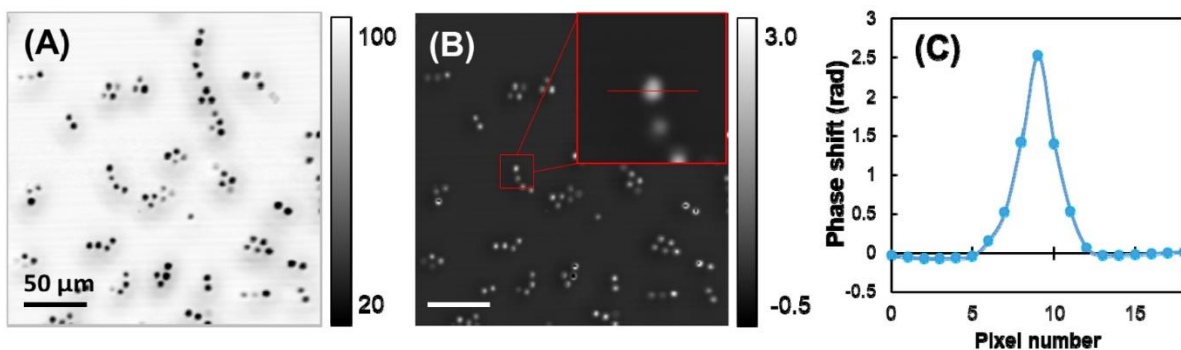


Figure 5-5 Recovered transmittance (A) and quantitative phase contrast images (B) of the same FoV of 8 μm silica microbeads. Color bar unit: (A) transmittance percentage; (B) phase shift in radian. Scale bar: 50 μm . Inserts: zoom-in for one single bead. (C) Phase shift line profiles of the cross line in the insert.

5.4 Conclusion

ADIC microscopy was developed for quantitative phase contrast imaging via polarization wavefront shaping with a pair of custom designed μRAs . Using a $10\times$ objective, two focal planes generated from the inserting μRA were separated by 70 μm with orthogonal polarization state. A lock-in amplifier was used to simultaneously recover both transmittance and quantitative phase contrast images. The LoD of this strategy was 0.033 radians with 30 μs integration time for each pixel. Tissue samples and silica beads were used for the proof of concept of the quantitative phase contrast imaging. The μRAs can be customized for other application-specific imaging targeting particular wavelengths and axial offsets. In an ongoing work, the ADIC will be extended into an autocorrelation method for quantitative phase information and particle size distribution retrieval for calculation of the absolute refractive index of freely diffusing nanoparticles; as well as a wide field quantitative phase contrast imaging using an LED illumination source.

5.5 References

1. Zernike, F., Phase contrast, a new method for the microscopic observation of transparent objects part II. *Physica* **1942**, 9 (10), 974-986.
2. Dodt, H.-U.; Zieglgänsberger, W., Visualizing unstained neurons in living brain slices by infrared DIC-videomicroscopy. *Brain research* **1990**, 537 (1-2), 333-336.
3. Gelles, J.; Schnapp, B. J.; Sheetz, M. P., Tracking kinesin-driven movements with nanometre-scale precision. *Nature* **1988**, 331 (6155), 450-453.

4. Allen, R. D.; Allen, N. S.; Travis, J. L., Video-enhanced contrast, differential interference contrast (AVEC-DIC) microscopy: A new method capable of analyzing microtubule-related motility in the reticulopodial network of *Allogromia laticollaris*. *Cell motility* **1981**, *1* (3), 291-302.
5. Ikeda, T.; Popescu, G.; Dasari, R. R.; Feld, M. S., Hilbert phase microscopy for investigating fast dynamics in transparent systems. *Optics letters* **2005**, *30* (10), 1165-1167.
6. Mehta, S. B.; Sheppard, C. J. R., Quantitative phase-gradient imaging at high resolution with asymmetric illumination-based differential phase contrast. *Optics Letters* **2009**, *34* (13), 1924-1926.
7. Vellekoop, I. M., Feedback-based wavefront shaping. *Optics Express* **2015**, *23* (9), 12189-12206.
8. Lin, Y.-Z.; Huang, K.-Y.; Luo, Y., Quantitative differential phase contrast imaging at high resolution with radially asymmetric illumination. *Optics Letters* **2018**, *43* (12), 2973-2976.
9. Shaked, N. T., Quantitative phase microscopy of biological samples using a portable interferometer. *Optics Letters* **2012**, *37* (11), 2016-2018.
10. Wang, Z.; Millet, L.; Mir, M.; Ding, H.; Unarunotai, S.; Rogers, J.; Gillette, M. U.; Popescu, G., Spatial light interference microscopy (SLIM). *Optics express* **2011**, *19* (2), 1016-1026.
11. Serak, S. V.; Roberts, D. E.; Hwang, J.-Y.; Nersisyan, S. R.; Tabiryan, N. V.; Bunning, T. J.; Steeves, D. M.; Kimball, B. R., Diffractive waveplate arrays [Invited]. *J. Opt. Soc. Am. B* **2017**, *34* (5), B56-B63.
12. Sato, S., Liquid-crystal lens-cells with variable focal length. *Japanese Journal of Applied Physics* **1979**, *18* (9), 1679.
13. Ren, H.; Fox, D. W.; Wu, B.; Wu, S.-T., Liquid crystal lens with large focal length tunability and low operating voltage. *Optics express* **2007**, *15* (18), 11328-11335.
14. Ren, H.; Fan, Y.-H.; Wu, S.-T., Prism grating using polymer stabilized nematic liquid crystal. *Applied physics letters* **2003**, *82* (19), 3168-3170.
15. Sun, J.; Xu, S.; Ren, H.; Wu, S.-T., Reconfigurable fabrication of scattering-free polymer network liquid crystal prism/grating/lens. *Applied Physics Letters* **2013**, *102* (16), 161106.
16. Yamaguchi, R.; Nose, T.; Sato, S., Liquid crystal polarizers with axially symmetrical properties. *Japanese journal of applied physics* **1989**, *28* (9R), 1730.
17. Morita, Y.; Stockley, J. E.; Johnson, K. M.; Hanelt, E.; Sandmeyer, F., Active liquid crystal devices incorporating liquid crystal polymer thin film waveplates. *Japanese journal of applied physics* **1999**, *38* (1R), 95.

18. Woltman, S. J.; Jay, G. D.; Crawford, G. P., Liquid-crystal materials find a new order in biomedical applications. *Nature materials* **2007**, *6* (12), 929-938.
19. Ding, C.; Li, C.; Deng, F.; Simpson, G. J., Axially-offset differential interference contrast microscopy via polarization wavefront shaping. *Optics Express* **2019**, *27* (4), 3837-3850.
20. Ohki, S., Dielectric constant and refractive index of lipid bilayers. *Journal of theoretical biology* **1968**, *19* (1), 97-115.
21. Huang, W.-T.; Levitt, D. G., Theoretical calculation of the dielectric constant of a bilayer membrane. *Biophysical journal* **1977**, *17* (2), 111-128.
22. Tiffany, J. M., Refractive index of meibomian and other lipids. *Current eye research* **1986**, *5* (11), 887-889.
23. Cui, Y.; Azzam, R., Determination of the refractive index and thickness of transparent pellicles by use of the polarization-independent absentee-layer condition. *Applied optics* **1996**, *35* (25), 5040-5043.
24. Malitson, I. H., Interspecimen comparison of the refractive index of fused silica. *Josa* **1965**, *55* (10), 1205-1209.

CHAPTER 6. DEPTH-OF-FIELD EXTENSION IN OPTICAL IMAGING FOR RAPID CRYSTAL SCREENING

The depth-of-field (DoF) of optical imaging systems was extended to three times to achieve rapid crystal screening by retrofitting a custom-designed micro-retarder array (μ RA) in the existing optical beam path. Second harmonic generation images of a variety of crystals acquired via the extended DoF approach were compared with the results obtained from conventional method to assess the improvement of performance and throughput of the present method. It was found that DoF extension enables more crystals to be detected owing to the polarization wavefront shaping via the μ RA. In addition, wavelength dependence of the extended DoF was investigated through experiments in comparison with theoretical predictions. These results provide a simple approach to increase the throughput of existing optical imaging based crystal screening processes.

6.1 Introduction

Elucidation of macromolecular structures is an essential step in understanding biological functions of proteins. Facilitated by the development of synchrotron sources, conventional x-ray crystallography has contributed to ~89% of protein structures recorded in the Protein Bank Database. Recent advances have seen ever-higher throughput assays using ever-smaller volume of solutions with the emerging techniques such as serial femtosecond crystallography using x-ray free-electron laser radiation,¹ which has enabled near-atomic resolution of protein structures with microcrystals to nanocrystals². However, the time-consuming data analysis process and limited public resource demand high quality crystals in every trial. Therefore, high-throughput crystal screening techniques to support the above-mentioned analyses are poised to enable further advances. A variety of fluorescence imaging techniques with submicrometer resolution and chemical specificities have been exploited to score protein crystals during the crystallization condition screening process, such as UV fluorescence,³ intrinsic two-photon excited UV fluorescence (TPE-UVF),⁴ and externally trace-labeled fluorescence.⁵ Although widely applicable, all the above-mentioned techniques are still limited in crystalline selectivity and sensitivity due to the non-zero background contributed from the non-crystallized aggregates or free fluorophores, which could generate false positives during crystal scoring.

Second harmonic generation (SHG) is a second order nonlinear optical process that is highly selective to noncentrosymmetric crystalline with negligible contribution from disordered molecules. By utilizing a femtosecond laser and beam-scanning apparatus, SHG microscope has been developed as an ultrasensitive approach for optical screening of microcrystals at video rate.⁶ Automated multimodal optical imaging platform integrated with SHG and TPE-UVF has been developed for macromolecule crystal screening to take advantages of both techniques.⁷ Polarization analysis has enabled extra assessment of crystal quality.^{6, 8} However, the nonlinear optical phenomena usually require a tightly focused excitation beam with relatively narrow depth-of-field (DoF) limiting further reduction of the overall measurement time.

Extending the DoF of an imaging system has been extensively investigated to increase the throughput of optical microscopic approaches. The simplest way of DoF extension is to decrease the tightness of the focal spot by lowering the numerical aperture (NA) of excitation by using a narrow beam (relative to the back aperture of the objective). However, NA reduction also increases the diameter of the point-spread-function, which sacrifices resolution. More significantly, increasing the beam waist in the focal plane reduces the efficiency of both SHG and TPE-UVF, which scale quadratically with the incident intensity and approximately quadratically with the NA. Other efforts are mostly based on wavefront shaping approaches to elongate the axial point-spread-function (PSF) of beams. Phase masks designed as an optical power apodizer have been reported to extend the DoF with the cost of ~50% of power loss at the sample plane.⁹ Axicons have been deployed in a variety of nonlinear optical microscopes including two-photon fluorescence microscopy¹⁰ and stimulated Raman scattering microscopy¹¹ to achieve improved DoF by converting Gaussian beam to Bessel beam. Although such methods maximized the photon efficiency, retrofitting into high-speed beam-scanning microscope configurations is prohibited due to the technical challenges of aligning the axicon pair into existing optical beam path.

The present study reports an approach to extend the DoF of various optical imaging systems to ~3-fold with the addition of a single 1-inch optic to an existing optical microscope. By installing a lab-designed micro-retarder array (μ RA) in the beam path, SHG images of a variety of crystalline samples were acquired in comparison with the z-scanning images measured without the μ RA. The extended DoF of an optical imaging system was both theoretically predicted and characterized via experimental measurements. Furthermore, the capability of polarization modulation and analysis endowed by the μ RA was observed in SHG images and discussed for potential applications.

6.2 Experimental Methods

BaTiO₃ nanocrystals (Sigma-Aldrich, 300 nm diameters) were immobilized in poly(ethylene glycol) (PEG, Sigma-Aldrich) with ~1 mm thickness. BaTiO₃ nanocrystals were first suspended in deionized water (~ 1% wt/wt) with 30 minutes sonication prior to use. PEG was mixed with 1 mL water (50% wt/wt) in glass container and heated to melting (~75 °C) via a hot plate. After combining 100 µL with the BaTiO₃ suspension, the BaTiO₃-PEG mixture was sonicated for 1 min before sprayed on a glass slide and cooled in room temperature until PEG film was solidified.

Ritonavir crystals were grown from seeded microcrystals sandwiched between ritonavir-copovidone amorphous solid dispersion (ASD) thin films prepared by a hydraulic press (Atlas Manual Hydraulic Press 15). To prepare the ASD films, 50-60 mg of ASD powder was spread between two discs of aluminium foil placed in the film making accessory with 100 µm spacer. The chamber was heated to 115 °C for 5 minutes and compressed with a pressure of 4 tons for 10 min. Then the temperature was set to 65 °C while keeping the pressure at 4 tons until the chamber was cooled to the setting point. The ritonavir-copovidone ASD films were removed from the press and cooled to room temperature. After ritonavir microcrystals were placed in between two ASD films, a similar process was performed with a 250 µm spacer to make a crystal seeded ritonavir-copovidone sandwich. The prepared sandwich was kept in room temperature with controlled humidity for 48 hrs allowing ritonavir crystals to grow in all directions.

Tetragonal lysozyme crystals were prepared using a protocol adapted from Yaoi, M. et al¹² and previously detailed in Newman, J.A. et al¹³. In brief, chicken egg-white lysozyme was used to prepare a 12.5 mg·ml⁻¹ solution in nanopure water. Crystallization was achieved in 96-well plates by combining 1 µL of protein solution with 1 µL of NaCl-acetate buffer solution and keeping the wells sealed with tape overnight. Malachite green oxalate salt (Sigma-Aldrich) was dissolved in ethyl ethanoate (Sigma-Aldrich) to prepare 500 µM solution prior to use. Malachite green was introduced by adding 1 µL of the dye solution into the 2 µL crystal mother liquor. The well was kept open for 10 minutes to allow the dye molecules to intercalate in protein crystals and evaporate the ethyl ethanoate prior to SHG imaging.

Detailed design of the µRA was described in our recent research article¹⁴. In brief, the µRA was designed with concentric patterns to induce half-wave retardance at every position varying spatially in the azimuthal orientation of the fast axis. The patterns are distributed quadratically on the 1-inch optic, generating 22 concentric rings in total. The custom µRA was manufactured by

Thorlabs, Inc. by growing polymer liquid crystal pixels on a BK-7 glass substrate covered with anti-reflection coating targeting at near-infrared wavelength. Characterizations of the μ RA and the extension ratio of the DoF were performed on a lab-built beam-scanning SHG microscope. Beam scanning was performed with a resonant vibrating mirror (~ 8 kHz, EOPC) along the fast-axis scan and a galvanometer (Cambridge) for slow-axis scanning. The incident beam was provided by an 80 MHz Ti:Sapphire pulsed laser (Spectra-Physics Mai Tai) of 100 fs pulse. The beam was focused on the sample with both a 10 \times objective with a working distance of 16 mm (Nikon, NA = 0.30) and a 20 \times objective with a working distance of 6 mm (Nikon, NA = 0.45). The incident wavelength was tunable within the range of 750 ~ 1000 nm with an average power of 50 mW at the sample plane. Each SHG image is obtained by signal averaging 4 sequential raw images with a total acquisition time of 250 ms. SHG signal was collected with a KG-3 heat absorbing glass and a short pass filter (cut-off wavelength at 600 nm) placed before the photomultiplier tube detector (PMT) to remove the fundamental light. MATLAB code was written in-house to control the scanning mirrors and communication with the data acquisition electronics.

To evaluate applications in automated crystal screening, SHG images of BaTiO₃ nanocrystals, ritonavir crystals, and lysozyme crystals intercalated with the SHG-contrast agent malachite green were acquired on a commercialized second harmonic generation microscope capable of supporting high-throughput chiral crystal screening (SONICC, Formulatrix). ImageJ was used to analyse and produce all SHG images.

6.3 Results and Discussion

A simulated pattern of the μ RA and schematic of DoF extension in imaging systems are shown in Figure 6-1. The μ RA used in this work was designed with a liquid crystal film producing half-wave retardance of 1064 nm light at every pixel with the fast-axis angle rotated radially, which has qualitative similarities with a Fresnel zone plate (FZP) as shown in Figure 6.1(A). The coherent combination of right and left circularly polarised beams of equal amplitude produces linearly polarised light, the axis of polarization of which is dictated by the phase shift between the two circular polarisations. As such, the particular pattern of linearly polarised light programmed to be produced by the μ RA is identical to that expected from the interference between a pair of slightly converging and slightly diverging circularly polarised beams of orthogonal polarisation. Once this pattern for the spatially varying polarisation is produced by the μ RA, the wavefront will simply

propagate as if produced by the coherent combination of the two orthogonally polarized beamlets. The azimuthal angle (θ) as a function of position coordinates (x, y) on the μ RA on a per-pixel basis is described as $\theta(x, y) = 2\pi[(x - R)^2 + (y - R)^2]/4\lambda f$, where R is the active radius of the μ RA, λ is the design wavelength (in this case 1064 nm), and f is the focal length designed to be 6.28 m with 1064 nm incident beam. As the schematic shown in Figure 6.1(B), an objective lens focuses all beamlets at different focal planes, resulting in an extended DoF compared to that of a conventional imaging system.

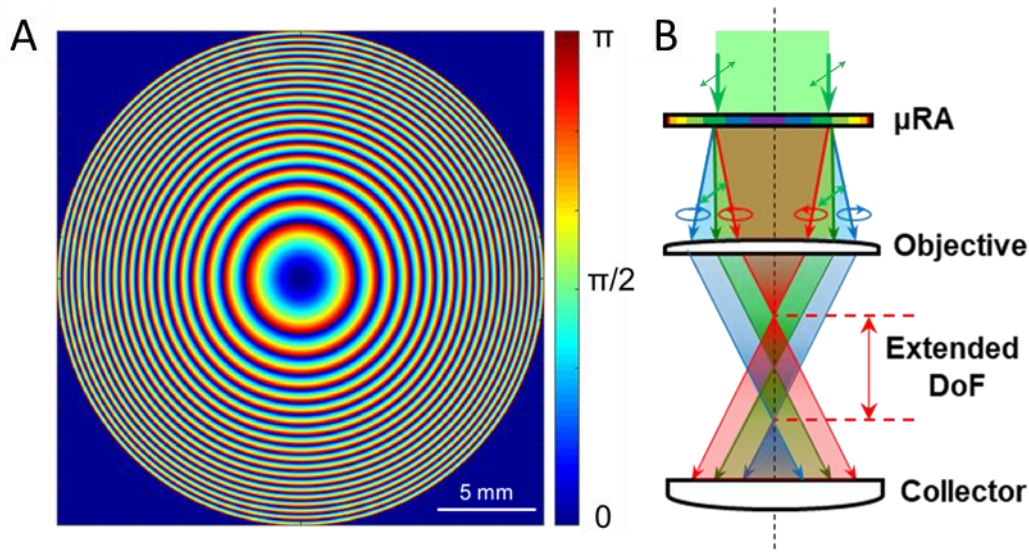


Figure 6-1 Schematic of the μ RA and the extension of the DoF. (A) The designed pattern of the μ RA as half-wave retardance with varied azimuthal orientation of the fast-axis targeted for 1064 nm light. Scale bar: 5 mm. (B) Working principle of the μ RA to generate the extended DoF via polarization wavefront shaping. The arrows indicate polarization states of the incident light and decomposed beamlets. Note different colours for the beamlets are used for better visualization of the divergency not for varied wavelengths.

To assess the practical performance of the extended DoF for crystal screening with improved throughput, SHG images of BaTiO_3 nanoparticles were collected as the proof-of-concept using an SHG microscope with and without the μ RA installed. As shown in Figure 6.2(A-D), a series of SHG images acquired at 4 different z-axis positions represent a typical crystal screening process, registering BaTiO_3 crystals located in multiple focal planes. Figure 6.2(E) is the z-projection of Figure 6.2(A-D) and exhibits the intact information of all crystals distributed within the 160 μm z-scanning range. Figure 6.2(F) is the single SHG image of the same field-of-view obtained with

the μ RA in the system. A side-by-side comparison between Figure 6.2(E) and Figure 6.2(F) shows that all crystals appeared in the z-projection of four SHG images were registered in the snapshot with the μ RA indicating the data acquisition time could be reduced by a factor of four in a practical crystal screening process.

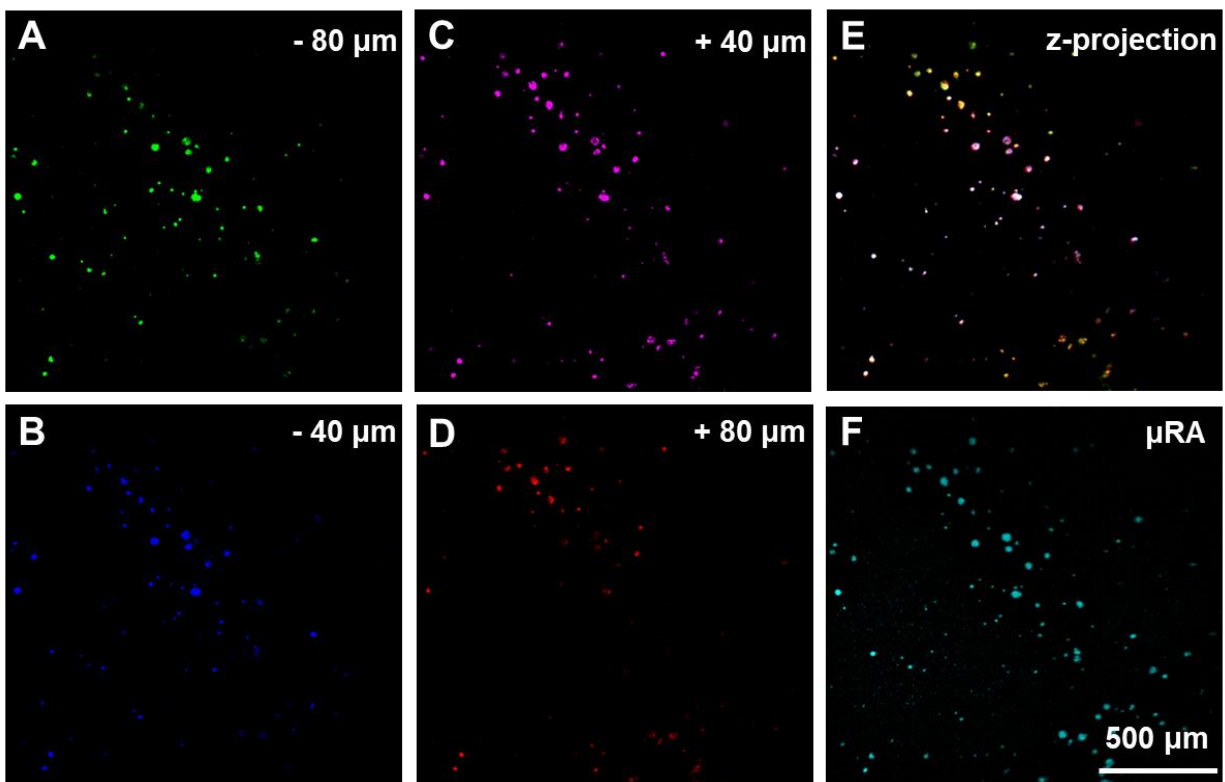


Figure 6-2 SHG images of BaTiO₃ nanoparticles immobilized in PEG. (A-D) SHG images measured at different z-axis positions. (E) Z-projection of (A-D). (F) Single SHG image of the same field-of-view with the μ RA. Scale bar: 500 μ m.

The presented approach was also investigated with ritonavir crystals grown in copovidone matrix in comparison with z-scanning SHG imaging. The z-projection of multiple SHG images collected at different x-axis positions and the single SHG image of the same field-of-view with extended DoF are shown in Figure 6.3(A) and (B) respectively. To better compare the detected crystals in both methods, an overlay of the two images was generated as Figure 6.3(C), in which most pixels are yellow representing crystals detected both in Figure 6.3(A) and (B). Note there exist some pure green pixels in Figure 6.3(C) that were those ritonavir crystals detected only in the image measured with the μ RA installed in the microscope (Figure 6.3(B)). Such observation

could be explained as a result of the azimuthal dependence of the SHG signal intensity¹⁵. Since linearly polarised excitation light was used in the measurement of Figure 3a, those rod-like ritonavir crystals stretching perpendicular to the polarization orientation became invisible due to the negligible contribution to the detected SHG signal. However, the majority of the excitation light was circularly polarised with the deployment of the μ RA in the measurement of Figure 3b, which exhibited more uniformly SHG intensity for randomly oriented ritonavir crystals compared to Figure 6.3(A).

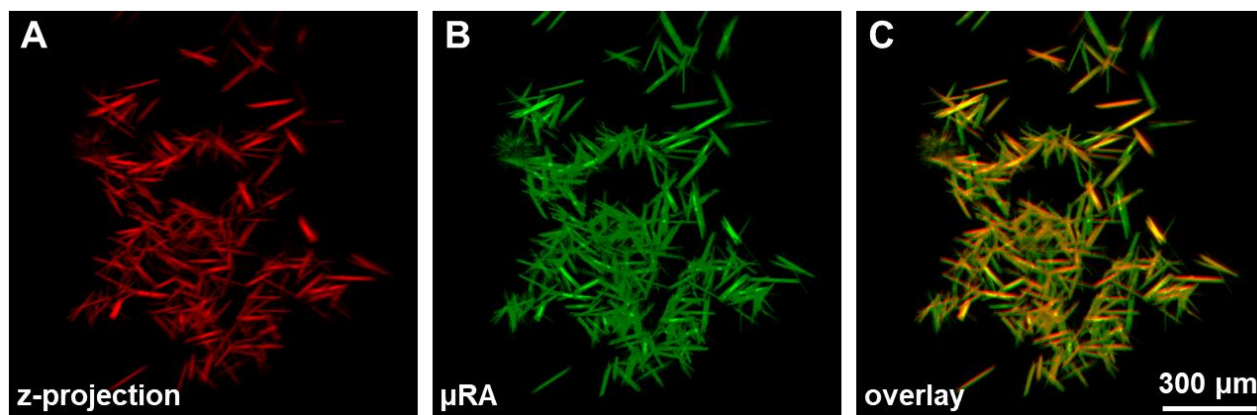


Figure 6-3 (A) Z-projection of a series of SHG images of ritonavir crystals measured with conventional method. (B) Single SHG image of the same field-of-view with the μ RA. (C) An overlay of (A) and (B). Scale bar: 300 μ m.

To further demonstrate the universality of the presented approach in macromolecule crystal screening, SHG images of tetragonal lysozyme crystals intercalated with malachite green molecules were acquired and summarized in Figure 6.4. Figure 6.4 (A-C) show three SHG images obtained at different z-axis positions covering 300 μ m via the conventional approach. The z-projection of all three images shown in Figure 4d registered all lysozyme crystals detected in the whole z-scanning process. In comparison, SHG image of the same field-of-view collected with the extended DoF was shown in Figure 6.4(E). It can be seen that all crystals detected in Figure 6.4(D) were observed in Figure 6.4(E). Figure 6.4(F) shows the SHG image acquired with the extended DoF and doubled exposure time for improved SNR to visualize crystals with weaker SHG signal. In addition, the yellow and red circles selected several crystals that are dim in conventional SHG image but bright in the extended DoF measurements due to the azimuthal dependence of SHG signals discussed in the preceding section.

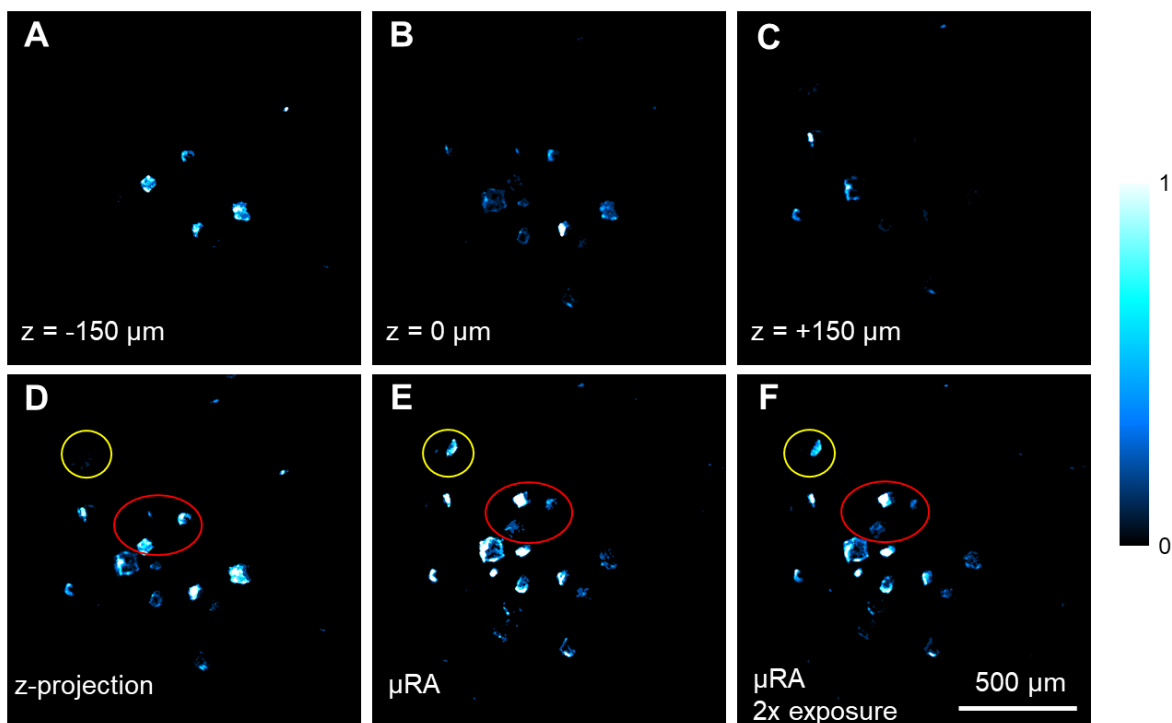


Figure 6-4 (A-C) SHG images of intercalated lysozyme crystals at various z-axis positions. (D) Z-projection of (A-C). SHG image of the same field-of-view with the μ RA using (E) the same exposure time and (F) doubled exposure time. Scale bar: 500 μ m.

Unlike laboratory-scale frame-by-frame imaging, the throughput of an autonomous detection system is determined by both the data acquisition time and dead time. To better assess the improvement of the practical throughput and performance, large-batch crystal screening experiments with the extended DoF were performed on automated SHG microscope to compare with the conventional screening process. Both trials of experiments were set to measure the z-scanning SHG images in square field-of-views covering an area of 20.25 mm² and z-axis depth of 4 mm in 7 different wells. It cost 96 minutes to complete data acquisition for the conventional crystal screening process using SHG microscopy, while the extended DoF reduced the measurement time to 34 minutes. The number of crystals counted by particle analysis algorithm in both trials were summarized in Table 6.1, indicating an average of 4.64% more crystals detected by deploying the extended DoF in the crystal screening process. Such difference can be attributed to either higher z-axis coverage or the circularly polarised light excitation provided by the extended DoF approach enabling detection of more crystals comparing with the conventional SHG microscopy method.

Table 6-1 Comparison of crystal counts in 9 different wells with the extended DoF approach and conventional SHG microscopy.

	Extended DoF	Conventional	Relative Difference
Well 1	1463	1352	8.21%
Well 2	1281	1226	4.49%
Well 3	1265	1195	5.86%
Well 4	1343	1372	-2.11%
Well 5	1359	1160	17.15%
Well 6	926	1013	-8.59
Well 7	819	763	7.34%
Sum	8456	8081	4.64%

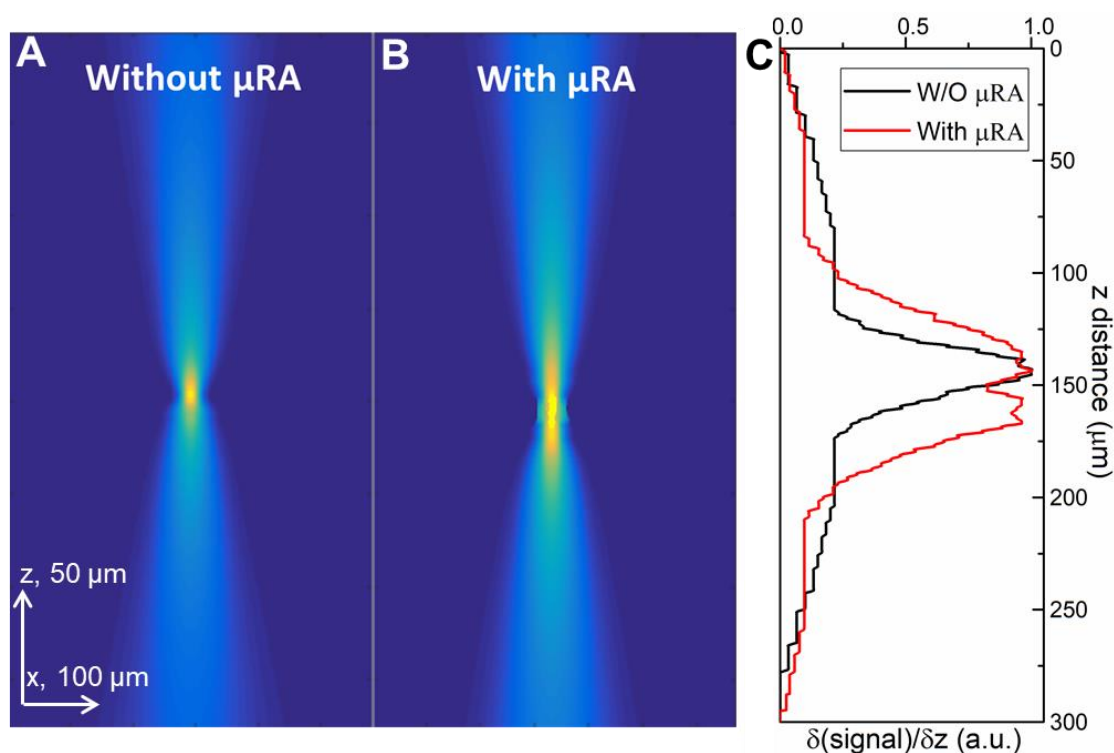


Figure 6-5 Measured point spread functions in the x-z plane before (A) and after (B) the installation of the μ RA in the optical beam path. (C) Point spread functions along z-axis with and without the μ RA provide quantitative analysis of the extension ratio of the DoF as 2.8.

Apart from experimental performances, it is essential to investigate the impact of the μ RA to the wavefront in order to provide feedbacks to the optimization of the μ RA design for future applications. As shown in Figure 6.5, the axial beam profile of an imaging system with a 20X objective lens was measured with and without the μ RA installed in the beam path. To recover the beam profile in the x-z plane (Figure 6.5 A, B), sharp edge analysis was performed on a stack of

z-scanning bright field images of a razor blade placed at the centre of the beam focus, in which the derivative of the intensity profile along an edge was fit to Gaussian function to retrieve the RMS (root mean squared) of beam width. It is noteworthy that the beam width at the focus remained unchanged following installation of the μ RA, consistent with no detectable loss in the spatial resolution of the microscope with this approach. The PSFs of the system measured under both imaging conditions were plotted in Figure 6.5C, indicating an extension ratio of ~ 2.8 by comparing the FWHM (full width at half maximum) of the original DoF (black) with the extended DoF (red).

It is also interesting to reveal the wavelength dependence of the extended DoF considering a broader scope of applications involving various optical microscopy configurations. Knowledge in geometrical optics describing FZP and thin lenses were deployed to predict the extended DoF with the μ RA as a function of incident light wavelength in an imaging system. For instance, the μ RA serves as a positive FZP for the converging LCP component, whose focal length is expressed as:¹⁶

$$f_{\mu RA} = \frac{R_n^2}{n \cdot \lambda} - \frac{n \cdot \lambda}{4} \approx \frac{R_n^2}{n \cdot \lambda} \quad (1)$$

where R_n is the radius of the n^{th} zone of the zone plate. For the μ RA used in this work, $n = 22$ and $R_n = 12.5 \text{ mm}$. On the contrary, the μ RA serves as a negative FZP for the diverging RCP light with a focal length of $-f_{\mu RA}$. Thus, the combination of the μ RA and an objective lens were then considered as either a convex-convex system (the converging LCP component) or a concave-convex (the diverging RCP component) system. Denote the focal length of the objective lens as f_{obj} , the equivalent focal lengths are described by the following equations with the thin-lens assumption respectively.

$$f_{LCP} = \frac{f_{obj} f_{\mu RA}}{f_{\mu RA} + f_{obj}} \quad (2)$$

$$f_{RCP} = \frac{f_{obj} f_{\mu RA}}{f_{\mu RA} - f_{obj}} \quad (3)$$

The distance between the LCP and RCP foci is defined as the extended DoF shown as:

$$DoF_{extended} = f_{RCP} - f_{LCP} = \frac{2f_{obj}^2 f_{\mu RA}}{f_{\mu RA}^2 - f_{obj}^2} \quad (4)$$

Given the fact that $f_{\mu RA} \gg f_{obj}$ in a typical microscope, Eq. 4 can be rewrite as:

$$DoF_{extended} \cong \frac{2f_{obj}^2}{f_{\mu RA}} \quad (5)$$

After plugging Eq. 1 into Eq. 5, the relationship between the extended DoF and the incident beam wavelength is expressed as:

$$DoF_{extended} = \frac{2f_{obj}^2 \cdot n}{R_n^2} \cdot \lambda \quad (6)$$

In brief, the wavelength dependence of the extended DoF is determined mainly by the focal length of the objective lens for a determined μ RA.

To assess the validity of the theoretical prediction in Eq. 6, z-scanning SHG images of z-cut quartz with different excitation wavelengths were acquired using a 10X objective ($f_{obj} = 19.5 \text{ mm}$). The integrated SHG intensity at each z-axis position with varying excitation wavelength was summarized in Figure 6.6(A). Each peak in the SHG intensity trace indicates that one surface of the z-cut quartz was placed at one of the axially offset foci. As it was mentioned in previous section, laser power distributed to the middle focus decreases as the incident wavelength approaches 1064 nm. Therefore, 6 peaks were observed in traces with shorter excitation wavelengths while only 4 peaks were seen when it was tuned to above 850 nm. The separation distances at various excitation wavelengths between the side peaks (top LCP plane and bottom RCP plane) were plotted in comparison with the predicted extended DoF (red line) as shown in Figure 6.6(B). The predicted line has a slope of 107.08 while linear fitting of the measured plots results in a slope of 108.55, indicating an excellent agreement between the experimental results and the predicted values based on Eq. 6.

6.4 Conclusion

The use of a lab-designed μ RA to extend the DoF of optical microscopy has been demonstrated for rapid crystal screening. With the addition of the μ RA in an existing imaging system, the DoF has been shown to increase to ~3-fold. Experimental measurements of the wavelength dependence of the extended DoF were consistent with theoretical predictions with a determined imaging system. SHG images of BaTiO₃ nanoparticles, ritonavir crystals, and malachite green intercalated protein crystals were acquired to validate the universality of the presented approach in the detection of salts, small molecules, and macromolecules. Furthermore, polarization wavefront shaping of the excitation light performed by the μ RA might be advantageous in certain circumstances when linearly polarised excitation light meets problems. Last but not the least, the presented approach for DoF extension is readily applicable to many other

optical imaging techniques including bright field imaging, UV fluorescence, TPE-UVF, etc., leading to broad interests and applications of this work.

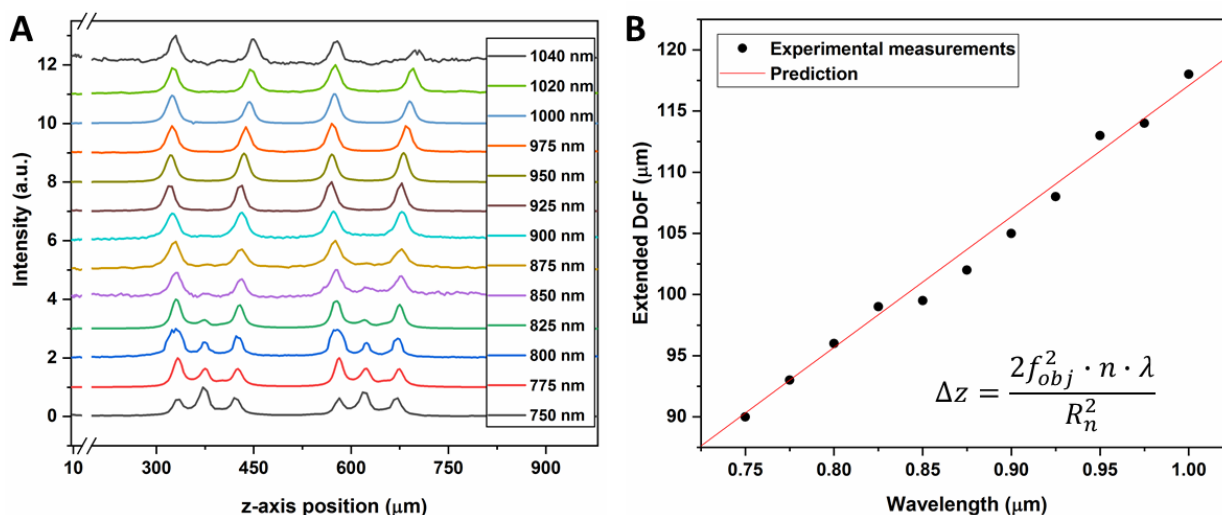


Figure 6-6 (A) Depth-resolved SHG intensity of z-cut quartz measured with extended DoF and varied excitation wavelength. (B) Comparison of theoretical prediction (red line) and measurements (plots) of the extended DoF as a function of excitation wavelength.

6.5 References

1. Neutze, R.; Wouts, R.; van der Spoel, D.; Weckert, E.; Hajdu, J., Potential for biomolecular imaging with femtosecond X-ray pulses. *Nature* **2000**, *406* (6797), 752-757.
2. Boutet, S.; Lomb, L.; Williams, G. J.; Barends, T. R. M.; Aquila, A.; Doak, R. B.; Weierstall, U.; DePonte, D. P.; Steinbrener, J.; Shoeman, R. L.; Messerschmidt, M.; Barty, A.; White, T. A.; Kassemeyer, S.; Kirian, R. A.; Seibert, M. M.; Montanez, P. A.; Kenney, C.; Herbst, R.; Hart, P.; Pines, J.; Haller, G.; Gruner, S. M.; Philipp, H. T.; Tate, M. W.; Hromalik, M.; Koerner, L. J.; van Bakel, N.; Morse, J.; Ghonsalves, W.; Arnlund, D.; Bogan, M. J.; Caleman, C.; Fromme, R.; Hampton, C. Y.; Hunter, M. S.; Johansson, L. C.; Katona, G.; Kupitz, C.; Liang, M.; Martin, A. V.; Nass, K.; Redecke, L.; Stellato, F.; Timneanu, N.; Wang, D.; Zatsepin, N. A.; Schafer, D.; Defever, J.; Neutze, R.; Fromme, P.; Spence, J. C. H.; Chapman, H. N.; Schlichting, I., High-Resolution Protein Structure Determination by Serial Femtosecond Crystallography. *Science* **2012**, *337* (6092), 362.
3. Vernede, X.; Lavault, B.; Ohana, J.; Nurizzo, D.; Joly, J.; Jacquamet, L.; Felisaz, F.; Cipriani, F.; Bourgeois, D., UV laser-excited fluorescence as a tool for the visualization of protein crystals mounted in loops. *Acta Crystallographica Section D* **2006**, *62* (3), 253-261.
4. Madden, J. T.; DeWalt, E. L.; Simpson, G. J., Two-photon excited UV fluorescence for protein crystal detection. *Acta Crystallographica Section D* **2011**, *67* (10), 839-846.

5. Groves, M. R.; Muller, I. B.; Kreplin, X.; Muller-Dieckmann, J., A method for the general identification of protein crystals in crystallization experiments using a noncovalent fluorescent dye. *Acta Crystallographica Section D* **2007**, *63* (4), 526-535.
6. DeWalt, E. L.; Sullivan, S. Z.; Schmitt, P. D.; Muir, R. D.; Simpson, G. J., Polarization-Modulated Second Harmonic Generation Ellipsometric Microscopy at Video Rate. *Analytical Chemistry* **2014**, *86* (16), 8448-8456.
7. Hauptert, L. M.; Simpson, G. J., Screening of protein crystallization trials by second order nonlinear optical imaging of chiral crystals (SONICC). *Methods* **2011**, *55* (4), 379-386.
8. Begue, N. J.; Simpson, G. J., Chemically Selective Analysis of Molecular Monolayers by Nonlinear Optical Stokes Ellipsometry. *Analytical Chemistry* **2010**, *82* (2), 559-566.
9. Welford, W. T., Use of Annular Apertures to Increase Focal Depth. *J. Opt. Soc. Am.* **1960**, *50* (8), 749-753.
10. Dufour, P.; Piché, M.; De Koninck, Y.; McCarthy, N., Two-photon excitation fluorescence microscopy with a high depth of field using an axicon. *Appl. Opt.* **2006**, *45* (36), 9246-9252.
11. Chen, X.; Zhang, C.; Lin, P.; Huang, K.-C.; Liang, J.; Tian, J.; Cheng, J.-X., Volumetric chemical imaging by stimulated Raman projection microscopy and tomography. *Nature Communications* **2017**, *8*, 15117.
12. Yaoi, M.; Adachi, H.; Takano, K.; Matsumura, H.; Inoue, T.; Mori, Y.; Sasaki, T., Effect of Stirring Method on Protein Crystallization. *Japanese Journal of Applied Physics* **2004**, *43* (No. 10A), L1318-L1319.
13. Newman, J. A.; Scarborough, N. M.; Pogranichniy, N. R.; Shrestha, R. K.; Closser, R. G.; Das, C.; Simpson, G. J., Intercalating dyes for enhanced contrast in second-harmonic generation imaging of protein crystals. *Acta Crystallographica Section D* **2015**, *71* (7), 1471-1477.
14. Ding, C.; Li, C.; Deng, F.; Simpson, G. J., Axially-offset differential interference contrast microscopy via polarization wavefront shaping. *Opt. Express* **2019**, *27* (4), 3837-3850.
15. Takebayashi, M.; Mizutani, G.; Ushioda, S., Azimuthal angle dependence of optical second harmonic intensity from a vicinal GaAs(001) wafer. *Optics Communications* **1997**, *133* (1), 116-122.
16. Cao, Q.; Jahns, J., Comprehensive focusing analysis of various Fresnel zone plates. *J. Opt. Soc. Am. A* **2004**, *21* (4), 561-571.

CHAPTER 7. MULTIFOCUS IMAGING VIA POLARIZATION WAVEFRONT SHAPING

A version of this chapter has been published by *Proceedings of SPIE*. Reprint with permission from Chen Li, Changqin Ding, Minghe Li, Jiayue Rong, James Ulcickas, Garth J. Simpson, "Multifocus imaging via polarization wavefront shaping," Proc. SPIE 11245, Three-Dimensional and Multidimensional Microscopy: Image Acquisition and Processing XXVII, 112450T. Copyright 2020 Society of Photo-Optical Instrumentation Engineers (SPIE).

Conventional three-dimensional (3D) images of biological samples are typically assembled from a stack of two-dimensional images acquired sequentially at different focal planes. This time-consuming manner hinders the application of 3D imaging techniques to the investigation of fast biochemical dynamics and light-sensitive biological events. The concept of multifocus imaging, which enables simultaneous acquisition of images from multiple focal planes, was introduced to achieve rapid 3D imaging. In the present study, we achieved multifocus imaging through polarization wavefront shaping via a micro-retarder array which splits the incident linearly polarized light into three beamlets that are focused to three axially-offset focal planes with ~ 100 μm separation. Append to an existing beam-scanning microscope, this multifocus system enables rapid 3D imaging compatible with a variety of optical microscopic approaches including laser transmittance, two-photon excited fluorescence, and second harmonic generation microscopy.

7.1 Introduction

The development of optical microscopy based volumetric imaging techniques has enabled numerous breakthrough discoveries in the field of life science and medical sciences by the visualization of microstructures of tissues and cells in a non-destructive manner.¹⁻² However, conventional volumetric imaging techniques mostly rely on reconstruction of three-dimensional (3D) information through a stack of raster scanned two-dimensional images, which is time consuming and vulnerable to photo damage to the samples.³ To address such problem, rapid 3D imaging approaches were developed recently to achieve dynamic tracking of the metabolism of organelles, visualization of neuronal activities, and etc.³⁻⁶ One of the emerging approach is to use adaptive optics to perform dynamic correction to the optical beam paths in real-time and acquire images from different focal planes sequentially. Electrically-controllable liquid-crystal varifocal

lens and acoustically driven optofluidic lens have been used for volume imaging.⁷⁻⁸ These techniques have achieved the imaging depth of several micrometers in samples along the axial direction. Another popular approach is multifocus imaging which usually utilizes the chromatic aberration to generate multiple focal planes that cover a large volume of the sample and record the signals from each depth simultaneously.⁵⁻⁶ The feature of multi-channel acquisition enables even higher throughput.

Although precedent microscopic approaches have all enabled rapid volumetric imaging with extreme resolution (<100 nm) and sensitivity, there remains a technical gap in the range of 50~100 μm corresponding to the size of large cells, microorganisms, and thick tissue slices. In our recent work demonstrating the axially-offset differential interference contrast phase imaging approach, polarization wavefront shaping (PWS) via a lab designed micro-retarder array (μRA) was studied systematically.⁹⁻¹⁰ By deploying the 1-inch μRA in a conventional optical microscope and tuning off the targeting wavelength, three axially-offset foci are generated enabling multifocus illumination. With the ability to retrofit in a beam-scanning microscope, the present approach has the potential to enable video rate 3D imaging.¹¹ Polarization analysis of the entangled signals from multiple focal planes will therefore yield demultiplexed multifocal images. In the present work, the theoretical framework for polarization demultiplexing of bright field imaging will be constructed and validated with preliminary experimental results. The analytical solution to the multifocus two-photon excited fluorescence (TPEF) imaging will also be discussed in specific cases, in which symmetry reduction will be applied to simplify the derived equation.

7.2 Theory

7.2.1 Multifocus generation via polarization wavefront shaping

The generation of two axially offset foci based on PWS was first demonstrated in our previous work. As a follow-up investigation, it was found that when the incident beam is tuned off from the designed working wavelength of the μRA , another focus arises in the middle of the two axially offset foci which enables multifocus imaging using all three foci. The key optic enabling axially offset foci generation is a polymer liquid crystal based micro-retarder array (μRA). As depicted in Figure 7-1A, the μRA was designed with concentric patterns to induce half-wave retardance at every position varying spatially in the azimuthal orientation of the fast axis. The

patterns are distributed quadratically on the 1-inch optic, generating 22 concentric rings that arrange alike a Fresnel zone plate (FZP). Figure 7-1B shows the patterns observed through a polarizer at two orthogonal orientations. The working principle of multifocus imaging based on PWS via the μ RA is shown in Figure 7-1C. In brief, the incident linearly polarised light is decomposed to three beamlets with different divergency and polarization states including left circular polarization (LCP), right circular polarization (RCP), and unchanged linear polarization, producing three axially offset focal planes. Photons from all three focal planes are collected simultaneously through the collector enabling rapid multifocus imaging.

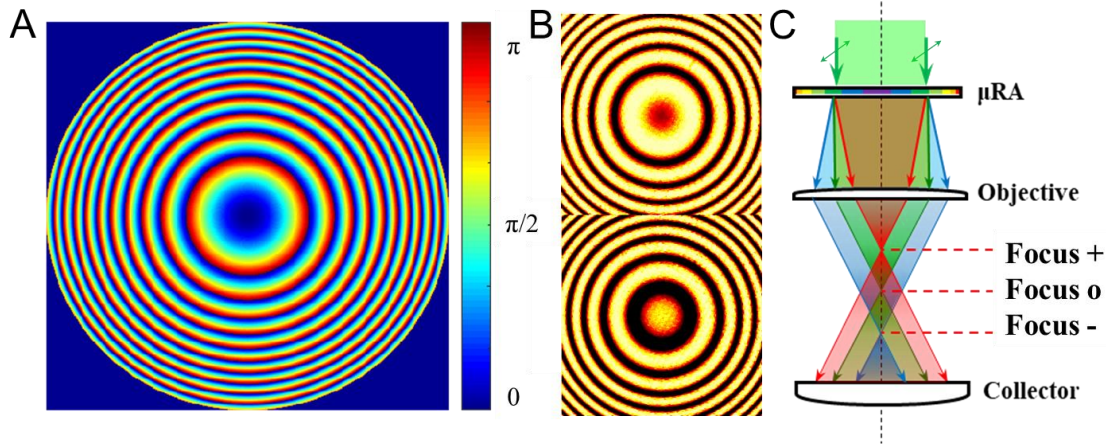


Figure 7-1 Instrument schematic of the custom-built beam-scanning microscope for method validation. The μ RA is installed right before the objective lens. The system was operated in one channel mode (photodiode only) for bright-field imaging.

It is convenient to describe the mechanism mathematically with Jones calculus.¹²⁻¹³ Consider the most general case in Figure 7-1C, in which the electric field of the incident linearly polarised light is denoted as $\vec{e}_{in} = [a \ b]^T$ and the only polarization manipulation optic before the objective is the μ RA set at an arbitrary angle γ with effective retardance δ . The light delivered to the objective lens can be written as:

$$\vec{e}_{obj} = \vec{J}_{\mu RA} \cdot \vec{e}_{in} = \begin{bmatrix} \cos\gamma & -\sin\gamma \\ \sin\gamma & \cos\gamma \end{bmatrix} \begin{bmatrix} e^{-\frac{i\delta}{2}} & 0 \\ 0 & e^{\frac{i\delta}{2}} \end{bmatrix} \begin{bmatrix} \cos\gamma & \sin\gamma \\ -\sin\gamma & \cos\gamma \end{bmatrix} \vec{e}_{in} \quad (1)$$

Plug \vec{e}_{in} into Eq. 1, the electric field of the light at the sample plane is expressed as:

$$\begin{aligned}
\vec{e}_{obj} = & -i \cdot \sin(\delta/2) \cdot (a + bi) \cdot \frac{e^{i \cdot 2\gamma}}{2} \begin{bmatrix} 1 \\ i \end{bmatrix} \\
& + \cos(\delta/2) \begin{bmatrix} a \\ b \end{bmatrix} \\
& -i \cdot \sin(\delta/2) \cdot (a - bi) \cdot \frac{e^{-i \cdot 2\gamma}}{2} \begin{bmatrix} 1 \\ -i \end{bmatrix}
\end{aligned} \tag{2}$$

Eq. 2 indicates that the incident light is decomposed to LCP, RCP, and residue linear polarization as expected. Considering that the μ RA works as either a positive or negative FZP based on the polarization state of the beamlet, the LCP and the RCP components are focused at the top (Focus +) and bottom (Focus -) focal planes with identical axial distance from the central focal plane (Focus o) formed by the linearly polarised residue. Therefore, the electric fields describing each of the three focal planes can be written as:

$$\begin{aligned}
\vec{e}_+ = & -i \cdot \sin(\delta/2) \cdot (a + bi) \cdot \frac{e^{i \cdot 2\gamma}}{2} \begin{bmatrix} 1 \\ i \end{bmatrix} \\
\vec{e}_o = & \cos(\delta/2) \begin{bmatrix} a \\ b \end{bmatrix} \\
\vec{e}_- = & -i \cdot \sin(\delta/2) \cdot (a + bi) \cdot \frac{e^{i \cdot 2\gamma}}{2} \begin{bmatrix} 1 \\ i \end{bmatrix}
\end{aligned} \tag{3}$$

With the mathematical expression shown in Eq. 3, it is feasible to disentangle images from multiple focal planes when the number of experimental observables is larger than the number of foci. To achieve analytical demultiplexing using experimental readouts, it is necessary to introduce an approach to rapidly alter the polarization states of the incident light. In the present work, electro-optic modulator (EOM) was deployed to achieve phase modulation within microsecond time scale. The Jones matrix of a phase only EOM setting at angle φ can be expressed as:

$$\vec{J}_{EOM} = \begin{bmatrix} \cos \varphi & -\sin \varphi \\ \sin \varphi & \cos \varphi \end{bmatrix} \begin{bmatrix} e^{-i \frac{\Delta(\tau)}{2}} & 0 \\ 0 & e^{i \frac{\Delta(\tau)}{2}} \end{bmatrix} \begin{bmatrix} \cos \varphi & \sin \varphi \\ -\sin \varphi & \cos \varphi \end{bmatrix} \tag{4}$$

Thus, the electric field of the light entering the μ RA can be derived from:

$$\vec{e}_{\mu RA} = \vec{J}_{EOM} \cdot \begin{bmatrix} a \\ b \end{bmatrix} \tag{5}$$

In practice, the polarization state of the incident light is rotated to horizontal direction and EOM is usually set at 45° to induce a time dependent retardance $\Delta(\tau)$. Combining Eq. 1, 4 and 5 yields the expression of the electric fields at each focal plane in the phase modulation case as:

$$\begin{aligned}
\vec{e}_+ &= -i \cdot \sin(\delta/2) \cdot \frac{e^{i \cdot 2\gamma}}{2} \cdot \left(\cos \frac{\Delta(\tau)}{2} + \sin \frac{\Delta(\tau)}{2} \right) \cdot \begin{bmatrix} 1 \\ i \end{bmatrix} \\
\vec{e}_o &= \cos(\delta/2) \begin{bmatrix} \cos \frac{\Delta(\tau)}{2} \\ -i \cdot \sin \frac{\Delta(\tau)}{2} \end{bmatrix} \\
\vec{e}_- &= -i \cdot \sin(\delta/2) \cdot \frac{e^{-i \cdot 2\gamma}}{2} \cdot \left(\cos \frac{\Delta(\tau)}{2} - \sin \frac{\Delta(\tau)}{2} \right) \cdot \begin{bmatrix} 1 \\ -i \end{bmatrix}
\end{aligned} \tag{6}$$

7.2.2 Demultiplexing of multifocus images in bright field microscopy

The above mathematical framework can be readily used to demultiplex the measured intensity, which is the squared magnitude of the electric field, of each focal plane in the case of bright field imaging. In the absence of any disturbance induced by sample, the overall detected intensities are described as:

$$\begin{aligned}
I_+ &\propto |\vec{e}_+|^2 = \frac{1}{2} \cdot \sin(\delta/2)^2 \cdot [\sin \Delta(\tau) + 1] \\
I_o &\propto |\vec{e}_o|^2 = \cos(\delta/2)^2 \\
I_- &\propto |\vec{e}_-|^2 = \frac{1}{2} \cdot \sin(\delta/2)^2 \cdot [1 - \sin \Delta(\tau)]
\end{aligned} \tag{7}$$

Eq. 7 indicated that the azimuthal orientation of the μ RA in the beam path does not impact the detected signal intensity. By placing a polarizer before the detector to only measure the horizontally polarised photons, the expression of the detected total signal is derived as a function of time:

$$I_{tot}(\tau) = I_{+H} + I_{oH} + I_{-H} = S_+^{BF} \cdot [\sin \Delta(\tau) + 1] + S_o^{BF} \cdot [\cos \Delta(\tau) + 1] + S_-^{BF} \cdot [1 - \sin \Delta(\tau)] \tag{8}$$

Once the incident light wavelength is determined, the retardance δ induced by the μ RA will be a constant leading to solutions to the bright field signals S_+ , S_o , and S_- . Note the above mathematical framework also applied to single photon fluorescence. The workflow of the demultiplexing and reconstruction process is briefly depicted in Figure 7-2.

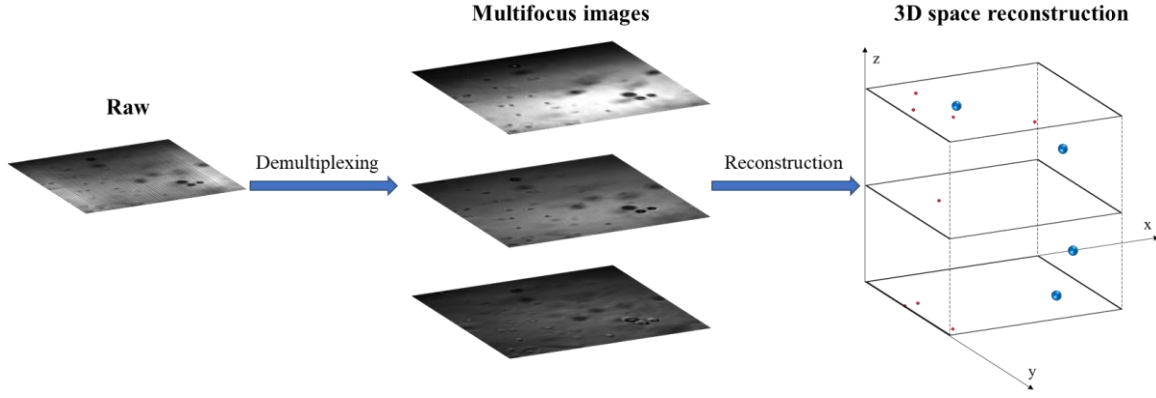


Figure 7-2 Workflow of the demultiplexing and 3D reconstruction process of multifocus imaging via PWS. The blue and red particles represent different species with various special locations.

7.2.3 Demultiplexing of multifocus images in TPEF microscopy

Based on the mathematical expression of the electric fields of the excitation light on each focus, the TPEF signals generated from fluorophores located at the top and bottom focal planes are simply the second-order nonlinear response to LCP or RCP and can be expressed as:

$$\begin{aligned}
 I_{+}^{TPEF}(\tau) &= S_{+}^{TPEF} \cdot |\vec{e}_{+}|^4 = S_{+}^{TPEF} \cdot \frac{\sin^4(\delta/2)}{8} [3 + 4 \cdot \sin \Delta(\tau) - \cos 2\Delta(\tau)] \\
 I_{-}^{TPEF}(\tau) &= S_{-}^{TPEF} \cdot |\vec{e}_{-}|^4 = S_{-}^{TPEF} \cdot \frac{\sin^4(\delta/2)}{8} [3 - 4 \cdot \sin \Delta(\tau) - \cos 2\Delta(\tau)]
 \end{aligned} \tag{9}$$

While for the central focal plane, the analytical description of the TPEF signal intensity is hard to derive from the above mathematical framework due to the complexity of the entangled response to linearly polarised light and circularly polarised light. However, if the TPEF signal with phase modulation is detected without bias of any polarization, the problem could be solved by a separate analysis to relate the measured Fourier coefficient tensor $\vec{a}_n = [a_n \ b_n \ c_n \ d_n \ e_n]^T$ in Eq. 10 to the polynomial coefficient tensor $\vec{A}_n = [A_n \ B_n \ C_n \ D_n \ E_n]^T$ in Eq. 11, which represents the polarization dependence of the local orientation, molecular structure, and molecular orientation distribution relative to the reference frame.

$$I_n(\Delta) = a_n + b_n \cdot \cos 2\Delta + c_n \cdot \cos \Delta + d_n \cdot \sin \Delta + e_n \cdot \sin 2\Delta \tag{10}$$

$$\begin{aligned}
 I_n(\Delta) &= A_n \cos^4(\Delta/2) + B_n \cos^3(\Delta/2) \sin(\Delta/2) + C_n \cos^2(\Delta/2) \sin^2(\Delta/2) + \\
 &D_n \cos(\Delta/2) \sin^3(\Delta/2) + E_n \sin^4(\Delta/2), \text{ where } n = H, V \text{ orientation}
 \end{aligned} \tag{11}$$

To solve for the polynomial coefficients, symmetry reduction can be applied to reduce the number of coefficients prior to fitting. In the most common case of TPEF measurements, where the fluorophores are distributed isotropically in the local frame, only A_n , C_n , and E_n in the polynomial coefficient tensor are non-zero and will contribute to the non-zero parameters a_n , b_n , and d_n in the Fourier coefficient tensor. Such dimension reduction yields the relationship between \vec{a}_n and \vec{A}_n to be:

$$\begin{bmatrix} a \\ b \\ d \end{bmatrix}_n = \frac{1}{8} \begin{bmatrix} 3 & 1 & 3 \\ 1 & -1 & 1 \\ 4 & 0 & -4 \end{bmatrix} \cdot \begin{bmatrix} A \\ C \\ E \end{bmatrix}_n \quad (12)$$

The symmetry also requires that $A_H = E_V$, $A_V = E_H$, and $C_H = C_V$. Therefore, the TPEF signal intensity in the central focal plane can be written in the Fourier expression shown as:

$$I_o^{TPEF}(\tau) = S_o^{TPEF} \cdot \frac{\cos^4(\delta/2)}{8} \{ [6(A_H + E_H) + 2C_H] + [2(A_H + E_H) - 2C_H] \cdot \cos 2\Delta(\tau) \} \quad (13)$$

To simplify the equation, substitute the polynomial parameters as $\rho_L = 6(A_H + E_H) + 2C_H$ and $\rho_C = 2(A_H + E_H) - 2C_H$. Combining Eq. 9 and 13 yields the total detected TPEF signal intensity $I_{tot}^{TPEF}(\tau)$ of an isotropic system shown in Eq. 14, indicating that the detected signal is a linear combination of three EOM phase terms: constant, $\sin \Delta$, and $\cos 2\Delta$.

$$I_{tot}^{TPEF}(\tau) = a_{tot} + b_{tot} \cdot \cos 2\Delta(\tau) + d_{tot} \cdot \sin \Delta(\tau) \quad (14)$$

$$\begin{bmatrix} a_{tot} \\ b_{tot} \\ d_{tot} \end{bmatrix} = \frac{1}{8} \cdot \begin{bmatrix} \rho_L \cos^4(\delta/2) & 3\rho_C \sin^4(\delta/2) & 3\rho_C \sin^4(\delta/2) \\ \rho_C \cos^4(\delta/2) & -\rho_C \sin^4(\delta/2) & -\rho_C \sin^4(\delta/2) \\ 0 & 4\rho_C \sin^4(\delta/2) & -4\rho_C \sin^4(\delta/2) \end{bmatrix} \cdot \begin{bmatrix} S_o^{TPEF} \\ S_+^{TPEF} \\ S_-^{TPEF} \end{bmatrix} \quad (15)$$

Solving for the signal tensor $\vec{S}_{TPEF} = [S_o^{TPEF} \ S_+^{TPEF} \ S_-^{TPEF}]^T$ will result in demultiplexed TPEF images of three different focal planes. Although the value of ρ_L and ρ_C of fluorophores are usually not available in current databases, it is feasible to perform separate TPEF measurements with phase modulation to determine these two parameters of specific fluorophores. In the present work, rhodamine 6G was suspended in 50% ethanol solution to validate the hypothesis that ρ_L and ρ_C are fixed values for a certain fluorophore.

7.3 Methods

7.3.1 Microscopy

To validate the theoretical prediction for the analytical expressions of images from different focal planes, a custom-built microscope was used to acquire experimental data (Figure 7-3). The light source of the microscope is a femtosecond Ti:Sapphire laser (SpectraPhysics) operating at a repetition rate of 80 MHz. In the experiments presented in this work, the wavelength of the output was tuned to 765 nm to achieve uniform power distribution among the three focal planes. Synchronized with the master clock from the laser, the EOM was set at 45° and operating at 8 MHz to perform polarization modulation with a period of ten laser pulses, allowing the construction of ten separate polarization-modulated images acquired simultaneously. A broadband wire grid polarizer (0.2-2 μ m, Thorlabs) was set at cross-polarised orientation to analyze the EOM retardance. The scan head comprises a resonant mirror (EOPC) operating at 8.8 kHz and a galvanometer mirror synchronized with the resonant mirror such that 512 repetitions of the fast axis paths occur for one ramp from the galvo mirror. The beam is expanded to fill the active area of the μ RA and the back aperture of the objective lens (Nikon Fluor 10X, 0.3 NA). Following collection through the condenser lens, a dichroic mirror (Edmund Optics, 550 nm) passes the fundamental light and reflects the TPEF signals to a PMT (Hamamatsu H12310-40). The fundamental is detected on a photodiode (DET10, Thorlabs) after passing through the polarizer placed in precision automated rotation stages (Universal Motion Controller, ESP300).

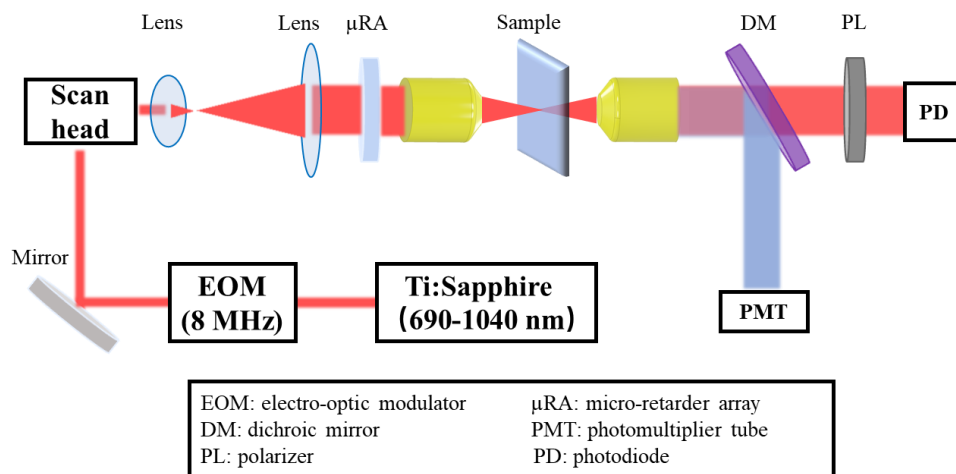


Figure 7-3 Instrument schematic of the custom-built beam-scanning microscope for method validation. The μ RA is installed before the objective lens.

7.3.2 Sample preparation

To demonstrate bright field multifocus imaging, a thick (~ 1 mm) and relatively transparent sample was prepared on glass slides. A mixture of silica microspheres (Spherotech, 6.0-8.0 μm dia.) and polyethylene particles (Cospheric, 10-27 μm dia.) were added in agarose gel suspension (SigmaAldrich, 0.75% wt/wt) and cooled in room temperature to immobilize the gel. To demonstrate the approach in TPEF measurements, Rhodamine 6G dye was selected as the model molecule. The sample was prepared by compressing three 100 μm copovidone films doped with Rhodamine 6G powder in a hydraulic press (Atlas Manual Hydraulic). The actual thickness of the compressed fluorescent sample was about 250 μm .

7.4 Results and discussion

7.4.1 Demonstration of multifocus imaging in bright field microscopy

Multifocus imaging of silica/polyethylene microsphere mixture was demonstrated with laser transmittance images on a bright field microscope. As stated in section 7.3.2, the wavelength of the laser was 765 nm to achieve uniform illumination power. Such incident light wavelength results in a separation distance of ~ 90 μm from the top plane to the bottom plane. As shown in Figure 7-4, images of three focal planes covering roughly 100 μm in the axial direction exhibit variation of signal intensity as well as sharpness for microspheres distributed across the whole 3D space. In a separate comparison (data not included), the spatial information delivered in each of the three focal planes agrees well with that seen in the 2D images acquired with the conventional sectioning manner.

The success of demultiplexing of the measured image stack on bright field microscopy indicates that the mathematical framework derived in Eq. 8 does foresee the experimental results. Note the data analysis and demultiplexing rely heavily on the accuracy of the retrieved EOM retardance from blank areas in the field of view. Thus, this approach might perform better in the imaging of samples with relatively low particle density.

7.4.2 Demonstration of multifocus imaging in TPEF microscopy

On the basis of the bright-field multifocus imaging, the mathematical framework was further deployed to investigate the case of TPEF microscopy. As illustrated in section 7.3.2, the TPEF

measurement was performed using Rhodamine 6G powder dispersed in copovidone films with a thickness of around 250 μm through heat compress. The spacer between each layer of copovidone film was 100 μm to control the distances among Rhodamine 6G aggregates located in different layers were in the range of the axial offsets among different focal planes. To determine the ratio of polarization dependent cross section parameters (ρ_L and ρ_C), TPEF measurement was first performed in phase modulation scheme using the same sample. In postprocessing, the retrieved value ρ_L/ρ_C was used to demultiplex the raw multifocus TPEF images. The demultiplexed TPEF images from the top, middle, and bottom focal planes are shown in Figure 7-5 (A-C), respectively. To compare the differences in spatial information obtained from demultiplexed images, an overlay image (Figure 7-5 D) was produced by projecting all three focal planes in one image, in which the top, middle, and bottom planes are represented in yellow, white, and blue, respectively. The demultiplexing worked for a couple particles locating on the edge of the field-of-view. However, it appears that it did not demultiplex all particles successfully. There are two possible reasons for the failure of the demultiplexing. First, the Rhodamine 6G/copovidone sample may not be an ideal isotropic system to retrieve the correct ρ_L/ρ_C value. Second, the heat compress method cannot guarantee the separation of all particles be exactly the same as the thickness of the spacer. This will result in smaller separations among all Rhodamine 6G in the axial direction.

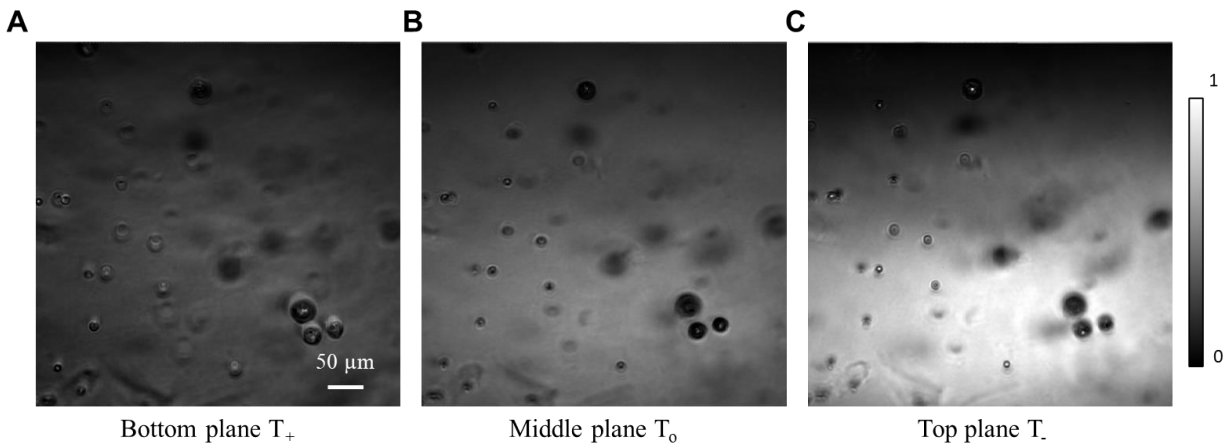


Figure 7-4 Demultiplexed bright field images of microsphere mixture at three focal planes. The raw image stack was acquired within half second. The intensity of each image was normalized to the rescale.in the range of 0-1. The scale bar is 50 μm .

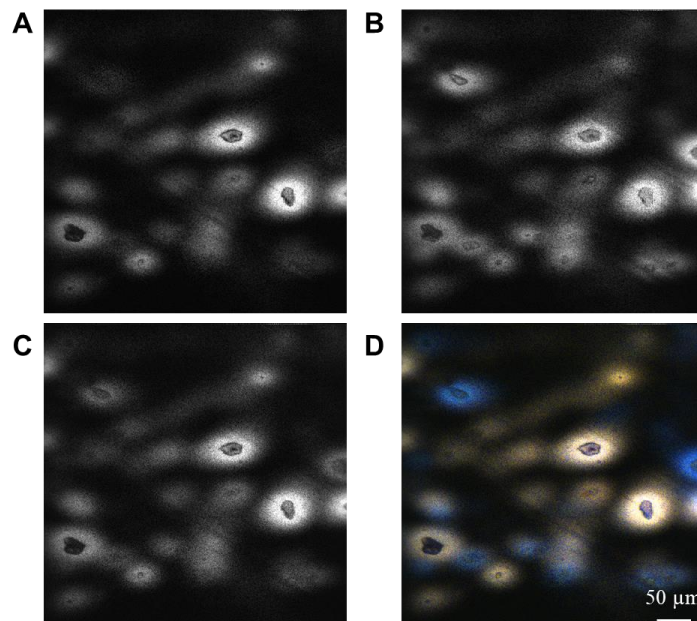


Figure 7-5 Demultiplexed TPEF images of Rhodamine 6G at three focal planes. The raw image stack was acquired within half second. The intensity of each image was normalized to the rescale in the range of 0-1. The scale bar is 50 μm

7.5 References

1. Huang, B.; Wang, W.; Bates, M.; Zhuang, X., Three-Dimensional Super-Resolution Imaging by Stochastic Optical Reconstruction Microscopy. *Science* **2008**, *319* (5864), 810-813.
2. Chen, X.; Zhang, C.; Lin, P.; Huang, K.-C.; Liang, J.; Tian, J.; Cheng, J.-X., Volumetric chemical imaging by stimulated Raman projection microscopy and tomography. *Nature Communications* **2017**, *8* (1), 15117.
3. Bewersdorf, J.; Pick, R.; Hell, S. W., Multifocal multiphoton microscopy. *Optics Letters* **1998**, *23* (9), 655-657.
4. Berkovitch, A.; Belfer, I.; Hassin, Y.; Landa, E.; Klem-Musatov, K.; Hoerber, H.; Pelissier, M.; Moser, T. J., Diffraction imaging by multifocusing. In *Seismic Diffraction*, Society of Exploration Geophysicists: 2016; Vol. 30, p 0.
5. Abrahamsson, S.; Chen, J.; Hajj, B.; Stallinga, S.; Katsov, A. Y.; Wisniewski, J.; Mizuguchi, G.; Soule, P.; Mueller, F.; Darzacq, C. D.; Darzacq, X.; Wu, C.; Bargmann, C. I.; Agard, D. A.; Dahan, M.; Gustafsson, M. G. L., Fast multicolor 3D imaging using aberration-corrected multifocus microscopy. *Nature Methods* **2013**, *10* (1), 60-63.
6. Prevedel, R.; Yoon, Y.-G.; Hoffmann, M.; Pak, N.; Wetzstein, G.; Kato, S.; Schrödel, T.; Raskar, R.; Zimmer, M.; Boyden, E. S.; Vaziri, A., Simultaneous whole-animal 3D imaging of neuronal activity using light-field microscopy. *Nature Methods* **2014**, *11* (7), 727-730.

7. Lin, Y.-H.; Wang, Y.-J.; Reshetnyak, V., Liquid crystal lenses with tunable focal length. *Liquid Crystals Reviews* **2017**, 5 (2), 111-143.
8. Suyama, S.; Date, M.; Takada, H., Three-Dimensional Display System with Dual-Frequency Liquid-Crystal Varifocal Lens. *Japanese Journal of Applied Physics* **2000**, 39 (Part 1, No. 2A), 480-484.
9. Ding, C.; Li, C.; Deng, F.; Simpson, G., *Polarization wavefront shaping for quantitative phase contrast imaging by axially-offset differential interference contrast (ADIC) microscopy*. SPIE: 2019; Vol. 10887.
10. Ding, C.; Li, C.; Deng, F.; Simpson, G. J., Axially-offset differential interference contrast microscopy via polarization wavefront shaping. *Optics Express* **2019**, 27 (4), 3837-3850.
11. DeWalt, E. L.; Sullivan, S. Z.; Schmitt, P. D.; Muir, R. D.; Simpson, G. J., Polarization-Modulated Second Harmonic Generation Ellipsometric Microscopy at Video Rate. *Analytical Chemistry* **2014**, 86 (16), 8448-8456.
12. Simpson, G. J., Connection of Jones and Mueller Tensors in Second Harmonic Generation and Multi-Photon Fluorescence Measurements. *The Journal of Physical Chemistry B* **2016**, 120 (13), 3281-3302.
13. Simpson, G. J., *Nonlinear Optical Polarization Analysis in Chemistry and Biology*. Cambridge University Press: Cambridge, 2017.

VITA

Chen Li attended University of Science and Technology of China (USTC) from 2011 to 2015 to obtain his bachelor's degree in chemistry. He then moved to Purdue University in 2015 to start his Ph.D. study. During 2015-2017, he worked in Dr. Ji-Xin Cheng's group focusing on the development of MIP microscopy which enables unprecedented *in vivo* chemical imaging of biological systems via the contrast of IR-absorption. After the Cheng group moved to Boston University, he joined Dr. Garth J. Simpson's group to continue pursuing his doctoral degree. His recent research interest is to exploit polarization wavefront shaping to develop new phase contrast mechanism, improve throughput and other performances of optical microscopes.

Mid-Infrared Photothermal Imaging of Active Pharmaceutical Ingredients at Submicrometer Spatial Resolution

Chen Li,^{†,||} Delong Zhang,^{‡,||} Mikhail N. Slipchenko,[§] and Ji-Xin Cheng^{*,†,‡}

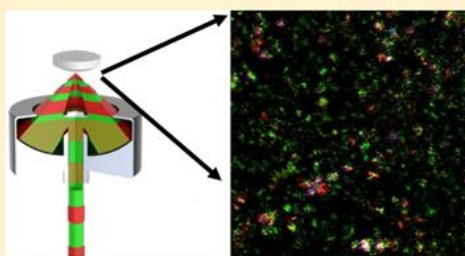
[†]Department of Chemistry, Purdue University, West Lafayette, Indiana 47907, United States

[‡]Weldon School of Biomedical Engineering, Purdue University, West Lafayette, Indiana 47907, United States

[§]Department of Mechanical Engineering, Purdue University, West Lafayette, Indiana 47907, United States

Supporting Information

ABSTRACT: Chemical imaging with sufficient spatial resolution to resolve microparticles in tablets is essential to ensure high quality and efficacy in controlled release. The existing modalities have the following disadvantages: they are time-consuming or have poor spatial resolution or low chemical specificity. Here, we demonstrate an epi-detected mid-infrared photothermal (epi-MIP) microscope at a spatial resolution of 0.65 μm . Providing identical spectral profiles as conventional infrared spectroscopy, our epi-MIP microscope enabled mapping of both active pharmaceutical ingredients and excipients of a drug tablet.



Pharmaceutical tablets, as one of the most consumed oral solid dosage forms across the world,¹ are composed of active pharmaceutical ingredients (API) that have biological activities and excipients that are inert but ensure the pharmacological performance of the API. The potency of medicine mainly depends on the formulation, particle size, and content uniformity. So far, it is still hard to control these properties at a low dosage of contents.² The bioactivity of API could be altered by inhomogeneous distribution or deformation of pharmaceutical particles, not to mention drug counterfeiting, which may be deleterious to patients. To produce high-quality medicines, it is essential to monitor and visualize the API and excipients in tablets in the quality control process. Specifically, as controlled release becomes an emerging trend in pharmaceuticals, the size of API and excipients particulates are being made from the order of 100 μm down to submicrometer and nanometer scale, making the current bulk imaging methods unable to cope with the new trend in the production line.^{3,4} As an example, high resolution chemical mapping of amlodipine besylate tablets from different vendors⁵ revealed heterogeneity differences in submicrometer scale between Pfizer and Ethex tables. (Note the Ethex tablets were later recalled by FDA due to quality issues.) Therefore, an increasing demand for high resolution imaging methods with chemical selectivity has arisen.

Various nonoptical imaging methods have been developed to address the above-mentioned challenge. Time-of-flight secondary ion mass spectrometry imaging ionizes and analyzes molecules over a spot of $\sim 1 \mu\text{m}$, which has excellent chemical specificity and limit of detection.⁶ X-ray powder diffraction analysis^{7,8} and X-ray microtomography⁹ provides crystalline

properties and element mapping, with a limit of detection sensitivity at the level of typically 1%. Nuclear magnetic resonance imaging is a noninvasive method elucidating the structure of molecules,¹⁰ with a long analysis time (order of 10 min). Terahertz imaging measures the thickness of tablet coating with a penetration depth of 0.45 mm but low spatial resolution of 0.15 mm.¹¹ These imaging approaches were not adopted by the industry due to low throughput.

Alternatively, optical imaging has the potential to provide high speed, submicrometer resolution, and chemical specificity. Toth et al. combined second order nonlinear optical imaging and two-photon fluorescence to deliver fluorescent API imaging in powdered blends with common excipients.¹² Besides, vibrational spectroscopy based imaging, which probes the intrinsic molecular vibration, provides rich chemical information and is widely used in industry. Commonly used vibrational imaging modalities are based on Raman scattering, near-infrared (NIR), or mid-infrared (MIR) spectroscopy.¹³ NIR and Raman imaging have been applied to analyze pharmaceutical formulations and/or counterfeits owing to advantages such as little/no sample preparation, chemical selectivity, and nondestructive measurement.^{14–19} However, the spectral bands used in NIR spectroscopy, mostly overtone absorption, are broad, weak, and usually severely overlapped, resulting in low chemical specificity.²⁰ Spontaneous Raman scattering has relatively high chemical specificity but is a feeble effect (Raman cross section on the order of $10^{-30} \text{ cm}^2/\text{sr}$) and thus requires a

Received: November 23, 2016

Accepted: April 11, 2017

Published: April 11, 2017

long integration time (>30 h per 500×500 hyperspectral image).²¹ Although recent progress of epi-detected coherent Raman scattering microscopy has demonstrated fast imaging of tablet sections and dissolution of drug molecules,^{5,22,23} the cost and complexity, along with small Raman cross section, limited further adoption of the technique. In contrast, MIR imaging appreciates a 100 million times larger absorption cross section (typ. 10^{-22} cm²/sr) and has shown applications in pharmaceuticals, including API mapping and counterfeit tablet investigation.^{24,25} However, the relatively poor spatial resolution and low reflectance of MIR light prohibited its wide use for pharmaceuticals.

In this paper, we report a compact mid-infrared photothermal microscope for imaging tablets at submicrometer spatial resolution. Photothermal microscopy, first reported in the early 1980s,²⁶ detects the photothermal lensing effect induced by the absorption of pump beam at focus using another probe beam. Modalities based on electronic or plasmonic absorption have been demonstrated for single nanoparticle and single molecule imaging.^{27,28} The deployment of a MIR beam as pump and a visible or NIR beam as probe was realized lately. Furstenberg and co-workers²⁹ demonstrated a back-detected photothermal microscope pumped by a mid-infrared quantum cascade laser (QCL). To further improve the spatial resolution, Li et al.³⁰ adopted a counter-propagation modality and applied a high NA objective for the visible probe beam. As a result, they obtained photothermal images of $1.1 \mu\text{m}$ polystyrene beads in three different solvents. With an increased signal to baseline ratio, Mèrtiri et al.³¹ performed photothermal imaging of dried tissue slices. Nevertheless, the spatial resolution and sensitivity were not sufficient for detection of submicrometer features within a cell.

We recently demonstrated a forward-detected mid-infrared photothermal (MIP) microscope with $0.6 \mu\text{m}$ spatial resolution and $10 \mu\text{M}$ sensitivity, which allowed MIR imaging of living cells and organisms.³² Our MIP microscope exploits a resonant amplifier that selectively probes the photothermal signal at the repetition rate of the pulsed IR laser. We showed that the MIP signal is linearly proportional to the number density of molecules and the power of each beam, which makes MIP a quantitative approach.³² Herein, we demonstrate submicrometer imaging of API and excipients microparticles in tablets by an epi-detected MIP microscope.

EXPERIMENTAL SECTION

epi-detected Mid-Infrared Photothermal (epi-MIP) Microscope. A pulsed quantum cascade laser (Block Engineering, LaserTune LT2000) operated at 100 kHz repetition rate and ~ 2 mW average power provided the tunable (ranges from 1345 to 1905 cm^{-1}) mid-infrared (MIR) pump beam. Meanwhile, a continuous-wave 785 nm laser (Thorlabs, LD-785-SE-400) was used as the probe beam. Both beams were combined at a long pass dichroic mirror (Edmund Optics, #68654) and, then, sent to an inverted microscope (Olympus, IX-71) installed with a gold-coated reflective objective lens (52 \times ; NA, 0.65; Edmund Optics, #66589). All samples were placed on a piezo scanning stage (Mad City Labs, Nano-Bio 2200) with a maximum scanning speed of $200 \mu\text{s}/\text{pixel}$. The residue of MIR beam generated at the dichroic mirror was guided to a room temperature mercury cadmium telluride (MCT) infrared detector (Vigo Inc., PVM-10.6) to monitor the infrared power. To detect the backward propagated MIP signal, a polarizing beam splitter (Thorlabs,

PBS122) was placed in the path of probe beam to transmit the linearly polarized light and reflect the polarization scrambled epi-MIP signal to the detector. When the sample is reflective, such as samples on a reflective mirror, a quarter-wave plate (Thorlabs, WPQ05M-780) is needed to induce a 90° polarization change to the backward signal to be coupled out. The detector was a silicon photodiode (Hamamatsu S3994-1). The photocurrent produced by the detector was amplified by a laboratory-built resonant circuit (resonant frequency at 103.8 kHz, gain 100) and then sent to a lock-in amplifier (Zurich Instruments, HF2LI) for phase-sensitive detection. The power spectrum of MIR beam was acquired by MCT via another lock-in input channel. It was used to normalize the epi-MIP signal to obtain the absorption spectrum of samples.

Infrared Spectra Measurements. Samples were measured on an ATR-FT-IR spectrometer (Thermo Nicolet Nexus) with diamond as the internal reflection element. The spectra were acquired after the internal baseline correction with a blank sample. The spectra were recorded using the built-in software interface.

Chemicals. The polystyrene film was a standard FT-IR test film (International Crystal Laboratories, 0009-8181). The Tylenol tablet was Tylenol Extra Strength, 500 mg of acetaminophen each (~ 83 wt %/wt). The pure chemicals including acetaminophen (analytical standard), corn starch (analytical standard), polyvinylpyrrolidone (analytical standard), and sodium starch glycolate (type A, pharmaceutical grade) were all purchased from Sigma-Aldrich.

RESULTS AND DISCUSSION

Figure 1 shows the schematic of our epi-MIP setup (details in the Experimental Section). Being different from the setup in ref

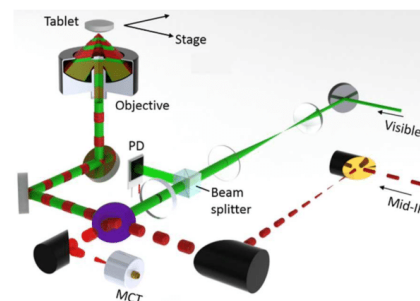


Figure 1. Schematic of the epi-MIP microscope. A pulsed QCL source provides the MIR beam, and a continuous wave visible laser is used as the probe beam. Both beams are combined collinearly by a silicon dichroic mirror and then sent into a reflective objective. The residue of MIR is monitored by a mercury cadmium telluride (MCT) detector. The backward propagated probe beam is reflected by a beam splitter and sent to a silicon photodiode (PD).

³², we placed a polarizing beam splitter to the probe beam path to transmit the linearly polarized probe beam to the sample and reflect the backward propagated signal to the photodiode. To acquire an epi-MIP image, a sample was raster scanned on a piezoelectric scanning stage and the epi-MIP signal was recorded as a function of sample position. A computer was

used to synchronize QCL tuning, stage scanning, and data acquisition.

Characterization. We first explored the spectral fidelity of epi-MIP signals by comparing the epi-MIP spectrum of a 60 μm polystyrene film to that from an attenuated total reflection (ATR) FT-IR spectrometer (Figure 2A). The epi-MIP

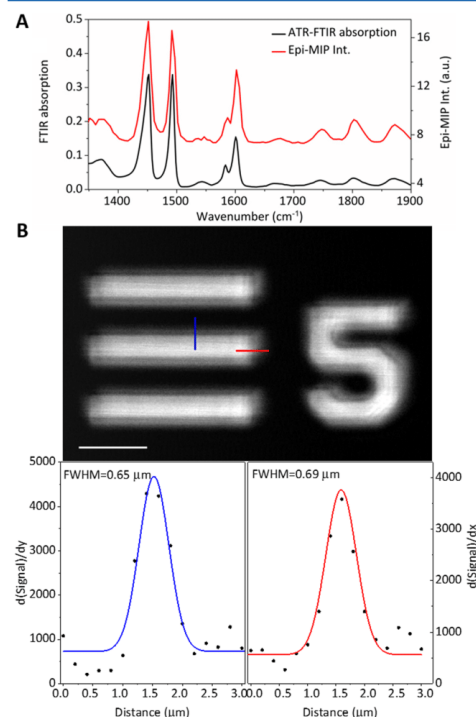


Figure 2. Characterization of the epi-MIP microscope. (A) Comparison of epi-MIP spectral profiles (red) and FT-IR spectra (black) of polystyrene film. The spectra were offset for visual clarity. (B) Epi-MIP image of the element 5 of group 5 on a positive 1951 USAF test target. The 1st order derivative of the profiles of the horizontal (red) and vertical (blue) lines are plotted at the bottom. The measured FWHM is 0.69 and 0.65 μm , respectively. Pixel dwell time: 1 ms. Scale bar: 20 μm .

spectrum showed good agreement with the FT-IR spectrum, notably for the phenyl ring semicircle stretching modes at 1450 and 1490 cm^{-1} . The 1450 cm^{-1} peak is also contributed by the backbone CH_2 scissors deformation. Note the ATR-FT-IR spectra require ATR correction to avoid the distortion of band shapes and relative peak intensities induced by the ATR process. In contrast to ATR-FT-IR, the epi-MIP spectra do not need such baseline correction, which simplifies data processing and reduces calibration errors.

We then examined the spatial resolution of our epi-MIP microscope by measuring the sharp edge response of a 1951 USAF test target. A thin film ($<5 \mu\text{m}$, determined by Newton ring method) of olive oil was sandwiched by a CaF_2 plate and the resolution target. The MIP signal from the oil film, carried

by the probe light, was reflected by the coating of the target, immediately at the oil film, into the detector, which mimics the condition with real samples. Even though the infrared light heated up a large area, only the small area of the probe light focus generated MIP signal. Note the chrome coating did not generate MIP signal.

The result is shown in Figure 2B. We took the first derivative of the marked line profiles in the MIP image and fitted the derivative data points with a Gaussian function. It is noteworthy that the diffraction limit of 1742 cm^{-1} MIR beam is 5.5 μm focused by our 0.65 NA objective. However, our measured full width at half-maximum (FWHM) was 0.69 μm horizontally and 0.65 μm vertically. By comparison, even installed with a high NA (~ 2) germanium ATR-objective, the ATR-FT-IR microscope can hardly resolve features smaller than 4 μm in tablet sections.³³ The 6-fold improvement of spatial resolution enabled us to acquire MIR spectra of a single pharmaceutical microparticle.

Tablet Imaging. After the above characterizations, we deployed the epi-MIP microscope to identify and visualize the API and excipients in real tablets. As one of the most consumed pain relief in the US, the Tylenol tablet was used as a test bed. The API is acetaminophen, whose MIR spectrum has characteristic peaks at 1500 cm^{-1} (phenyl ring semicircle stretching modes) and 1666 cm^{-1} (amide I). Besides, three of the most abundant excipients include corn starch, polyvinylpyrrolidone (PVP), and sodium starch glycolate (SSG). As shown in Figure S1, the molecular structures indicate that these three excipients show characteristic peaks at C–H bending mode (corn starch), amide I band (PVP), and carboxylic acid C=O stretching mode (SSG), respectively. On the basis of the knowledge above, we can identify and differentiate those substances referring to the epi-MIP signal at different excitation wavelengths within our QCL tunable range.

We first performed single color epi-MIP imaging of the Tylenol tablet at 1502 cm^{-1} to visualize the API distribution. The tablet was sectioned at the center and mounted on scanning stage for imaging without other preparation. Figure 3A shows that particles containing API (bright spots) were uniformly distributed in the 190 \times 190 μm^2 region with some large clusters. In general, the API particles should be closely surrounded by excipients particles, which means the dark regions on our API map should be excipients dominant. To prove this hypothesis, we obtained pinpoint epi-MIP spectra at three different positions as shown in Figure 3B. Points 1 and 2, whose pinpoint spectra indicate that API is the dominant molecule, were selected from the bright regions in Figure 3A. By comparison, point 3, which is the dark point on the API map, shows a distinct pinpoint spectrum from the other points, indicating that starch, PVP, and SSG are more abundant than the API. To confirm the species assigned from pinpoint spectra, we collected ATR-FT-IR spectra of the API and excipients for comparison as shown in Figure 3C. The characteristic peaks we employed for chemical identification were all in good agreement with the ATR-FT-IR spectra.

We further explored the capability of our epi-MIP microscope in integrated mapping of API and excipients (Figure 4). We tuned the MIR excitation wavenumbers to 1413, 1502, 1656, and 1750 cm^{-1} which correlate to the absorption bands of corn starch, API, PVP, and SSG, respectively (Figure 4A–D). Each substance showed a unique spatial distribution and dosage in the region we observed. By merging images A–D, we obtained the overlaid image as Figure 4E exhibiting the relative

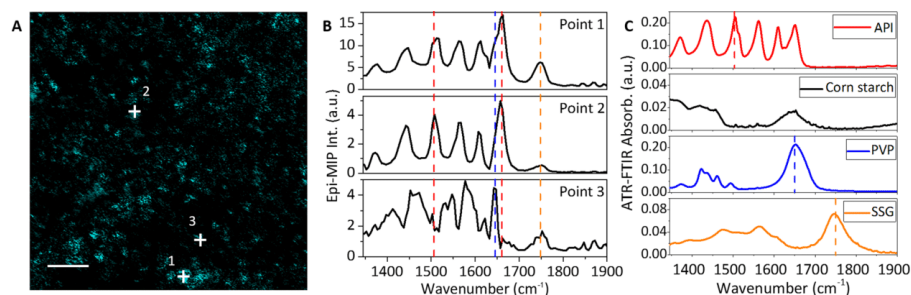


Figure 3. Identification of different species in a Tylenol tablet. (A) The epi-MIP image of tablet obtained at 1502 cm^{-1} API benzene band. (B) Pinpoint spectra of locations 1, 2, and 3, as indicated in (A). Dashed lines (red, blue, and orange) indicate the characteristic absorbance peaks of the three substances. (C) FT-IR spectra of the pure chemicals assigned. API denotes acetaminophen. Pixel dwell time: $500\ \mu\text{s}$. Scale bar: $50\ \mu\text{m}$.

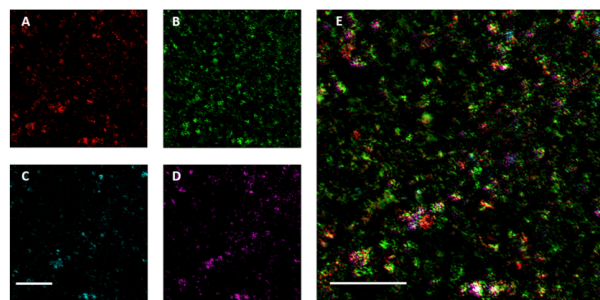


Figure 4. Epi-MIP image of API and excipients in a Tylenol tablet. (A–D) Epi-MIP images obtained at 1413 , 1502 , 1656 , and 1750 cm^{-1} which correlate to corn starch, acetaminophen (API), PVP, and SSG, respectively. (E) Overlaid image of A–D showing the distribution of API (green), corn starch (red), PVP (cyan), and SSG (magenta). Pixel dwell time: 1 ms . Scale bars: $50\ \mu\text{m}$.

distributions of the four substances in Tylenol tablet. Most of the bright spots contained more than one molecule, which implies that API and excipients were fully mixed before the tablet compression process. Note the dark area in the merged chemical map. This seemingly erroneous image was a result of out-of-focus particles generating a lower MIP intensity, due to the surface roughness of the tablet section. As an example, we tested epi-MIP imaging of the tablet at varying depth (Figure S2). The features and signal intensity varied dramatically as the focus changed by $20\ \mu\text{m}$. Furthermore, by applying Isodata threshold (an unsupervised thresholding method) to four different API maps, the average captured area in the binary map was calculated to be 82.6% , which was consistent with the listed weight percentage of acetaminophen, 83.3% .

The results above collectively demonstrate the potential of the epi-MIP microscope as a new chemical imaging modality for pharmaceutical tablet manufacturing. The epi-MIP spectra are identical to the conventional FT-IR spectra, which simplifies the postprocessing of data and allows users to take advantage of the wealth of FT-IR spectra database collected in the past century. With the excellent chemical selectivity, quantitative measurement capability, simple sample preparation requirement, and the relatively low cost, our epi-MIP microscope could not only be useful for manufacturing quality control but also enable the detection of high-quality counterfeit tablets.

In our current setup, the QCL has a tunable range of 1345 – 1900 cm^{-1} , which covers many important MIR absorption

bands, and has successfully differentiated the API molecule and three other excipients in Tylenol tablet sections by their characteristic peaks. Nevertheless, there are several other listed excipients that we could not map because their characteristic MIR peaks exceed our tunable range. We can readily expand the spectral range with the deployment of different pump sources to further exploit the abundant infrared libraries developed by previous researchers. In addition, advanced multivariate methods, such as multivariate curve resolution,³⁴ can further endow the epi-MIP microscope with a robust analytical ability in more complex sample analysis. It is worth mentioning that the power of both the pump and probe beams in our epi-MIP microscope were low due to the limitations of laser sources, $\sim 2\text{ mW}$ for the pump beam and $\sim 10\text{ mW}$ for the probe beam at the sample. With the recently available high power MIR laser, the epi-MIP microscope will achieve higher sensitivity and imaging speed. Moreover, the spatial resolution of the epi-MIP microscope will be improved by using a probe laser wavelength that is shorter than the current 785 nm .

CONCLUSION

In summary, we developed a submicrometer-resolution, epi-detected MIP microscope and applied the setup to API visualization in drug tablets. As compared to the previous MIR microscopes, our epi-MIP microscope offered 5-fold better spatial resolution. Since we have demonstrated the application of MIP microscopy in imaging drug accumulation in living

cells,³² it is feasible to perform the dissolution test and controlled release experiments of tablets on the forward detected MIP modality. As the current trend in pharmaceuticals is the combination of multiple techniques to provide integrated understanding, our MIP platform, with both forward and epide- tected modalities, could potentially provide comprehensive information on the factors correlating to drug efficacy and boost the future research in pharmaceutical sciences.

■ ASSOCIATED CONTENT

● Supporting Information

The Supporting Information is available free of charge on the ACS Publications website at DOI: 10.1021/acs.analchem.6b04638.

Materials and methods, molecular structures, and epi- MIP images versus focus positions (PDF)

■ AUTHOR INFORMATION

Corresponding Author

*E-mail: jcheng@purdue.edu.

ORCID

Chen Li: 0000-0002-4391-6196

Delong Zhang: 0000-0002-9734-3573

Author Contributions

^{||}C.L. and D.Z. contributed equally. J.-X.C. and D.Z. conceived the idea. C.L. and D.Z. designed the experiment. C.L. and D.Z. conducted the experiment. C.L., D.Z., and M.N.S. analyzed the data. C.L., D.Z. and J.-X.C. cowrote the manuscript. All authors have given approval to the final version of the manuscript.

Notes

The authors declare no competing financial interest.

■ ACKNOWLEDGMENTS

The authors thank Dr. Chi Zhang from the same group for constructive discussions. This research was supported by a Keck Foundation Science & Engineering Grant to J.-X.C.

■ REFERENCES

- (1) Ansel, H. C. *Introduction to Pharmaceutical Dosage Forms*; Lea & Febiger: Philadelphia, 1985.
- (2) Augsburger, L. L.; Hoag, S. W. *Pharmaceutical Dosage Forms-Tablets*, 3rd ed.; CRC Press: Boca Raton, FL, 2008.
- (3) Wong, D. Oral solid composition. U.S. Patent 8,313,774 B1, Nov. 20, 2012.
- (4) Salata, O. V. *J. Nanobiotechnol.* **2004**, *2*, 3.
- (5) Slipchenko, M. N.; Chen, H.; Ely, D. R.; Jung, Y.; Carvajal, M. T.; Cheng, J. X. *Analyst* **2010**, *135*, 2613–2619.
- (6) Belu, A. M.; Davies, M. C.; Newton, J. M.; Patel, N. *Anal. Chem.* **2000**, *72*, 5625–5638.
- (7) Bates, S.; Zografi, G.; Engers, D.; Morris, K.; Crowley, K.; Newman, A. *Pharm. Res.* **2006**, *23*, 2333–2349.
- (8) Nunes, C.; Mahendrasingam, A.; Suryanarayanan, R. *Pharm. Res.* **2005**, *22*, 1942–1953.
- (9) Hancock, B. C.; Mullarney, M. P. *Pharm. Technol.* **2005**, *29*, 92–100.
- (10) Djemai, A.; Sinka, I. *Int. J. Pharm.* **2006**, *319*, 55–62.
- (11) Fitzgerald, A. J.; Cole, B. E.; Taday, P. F. *J. Pharm. Sci.* **2005**, *94*, 177–183.
- (12) Toth, S. J.; Madden, J. T.; Taylor, L. S.; Marsac, P.; Simpson, G. *J. Anal. Chem.* **2012**, *84*, 5869–5875.
- (13) Gendrin, C.; Roggo, Y.; Collet, C. *J. Pharm. Biomed. Anal.* **2008**, *48*, 533–553.

- (14) Cruz, J.; Bautista, M.; Amigo, J. M.; Blanco, M. *Talanta* **2009**, *80*, 473–478.
- (15) Amigo, J. M.; Ravn, C. *Eur. J. Pharm. Sci.* **2009**, *37* (2), 76–82.
- (16) Sasic, S. *Pharm. Res.* **2007**, *24*, 58–65.
- (17) de Veij, M.; Deneckere, A.; Vandenberghe, P.; de Kaste, D.; Moens, L. *J. Pharm. Biomed. Anal.* **2008**, *46*, 303–309.
- (18) Rodionova, O. Y.; Houmoller, L. P.; Pomerantsev, A. L.; Geladi, P.; Burger, J.; Dorofeyev, V. L.; Arzamastsev, A. P. *Anal. Chim. Acta* **2005**, *549*, 151–158.
- (19) Rodionova, O. Y.; Pomerantsev, A. L. *TrAC, Trends Anal. Chem.* **2010**, *29*, 795–803.
- (20) Andersson, M.; Josefson, M.; Langkilde, F.; Wahlund, K.-G. *J. Pharm. Biomed. Anal.* **1999**, *20*, 27–37.
- (21) Gordon, K. C.; McGovern, C. M. *Int. J. Pharm.* **2011**, *417*, 151–162.
- (22) Windbergs, M.; Jurna, M.; Offerhaus, H. L.; Herek, J. L.; Kleinebudde, P.; Strachan, C. J. *Anal. Chem.* **2009**, *81*, 2085–2091.
- (23) Kang, E.; Wang, H.; Kwon, I. K.; Robinson, J.; Park, K.; Cheng, J.-X. *Anal. Chem.* **2006**, *78*, 8036–8043.
- (24) Wray, P. S.; Clarke, G. S.; Kazarian, S. G. *Eur. J. Pharm. Sci.* **2013**, *48*, 748–757.
- (25) Ricci, C.; Eliasson, C.; Macleod, N. A.; Newton, P. N.; Matousek, P.; Kazarian, S. G. *Anal. Bioanal. Chem.* **2007**, *389*, 1525–1532.
- (26) Fournier, D.; Lepoutre, F.; Boccard, A. C. *J. Phys. Colloq.* **1983**, *44*, C6-479–C6-482.
- (27) Boyer, D.; Tamarat, P.; Maali, A.; Lounis, B.; Orrit, M. *Science* **2002**, *297*, 1160–1163.
- (28) Gaiduk, A.; Yorulmaz, M.; Ruijgrok, P.; Orrit, M. *Science* **2010**, *330*, 353–356.
- (29) Druy, M. A.; Furstenberg, R.; Crocombe, R. A.; Kendziora, C. A.; Papantonakis, M. R.; Nguyen, V.; McGill, R. A. Chemical imaging using infrared photothermal microspectroscopy. In *Proceedings of SPIE Defense, Security, and Sensing Conference*, Baltimore, MA, Apr 23–29, 2012; Druy, M., Crocombe, R., Eds.; SPIE: Bellingham, WA, 2012; 837411.
- (30) Li, Z.; Kuno, M.; Hartland, G. Super-resolution Mid-infrared Imaging using Photothermal Microscopy. In *Proceedings of Conference on Lasers and Electro-Optics*, San Jose, CA, Jun. 5–10, 2016; Optical Society of America: Washington, DC, 2016; p ATu3J.7.
- (31) Mértiri, A.; Totachawattana, A.; Liu, H.; Hong, M. K.; Gardner, T.; Sander, M. Y.; Erramilli, S. Label free mid-IR photothermal imaging of bird brain with quantum cascade laser. In *Proceedings of Conference on Lasers and Electro-Optics*, San Jose, CA, Jun. 8–13, 2014; Optical Society of America: Washington, DC, 2014; p AF1B.4.
- (32) Zhang, D.; Li, C.; Zhang, C.; Slipchenko, M. N.; Eakins, G.; Cheng, J.-X. *Sci. Adv.* **2016**, *2*, e1600521.
- (33) Chan, K. A.; Hammond, S. V.; Kazarian, S. G. *Anal. Chem.* **2003**, *75*, 2140–2146.
- (34) Felten, J.; Hall, H.; Jaumot, J.; Tauler, R.; De Juan, A.; Gorzús, A. *Nat. Protoc.* **2015**, *10*, 217–240.

Chapter 6

Absorption-Based Far-Field Label-Free Super-Resolution Microscopy



Chen Li and Ji-Xin Cheng

Abstract Materials absorption, which happens in all light–matter interactions, has been studied systematically and inspires various chemical-specific measurement methods for extensive non-fluorescent species. In this chapter, we review recent achievements of far-field label-free super-resolution microscopy (LFSRM) that deploys materials absorption to provide the contrast. In the linear absorption modalities, samples convert photon energy to heat efficiently, which turns the photothermal detection with single-molecule sensitivity into possible. The photothermal microscope breaks the diffraction limit of the excitation beam by probing the localized thermal lens effect using a shorter-wavelength beam. In the nonlinear absorption modalities, one pump beam profile could be engineered to doughnut shape and reduce the size of the nonlinear region, which helps achieve sub-diffraction resolution. Both mechanisms use the intrinsic vibrational or electronic absorption of molecules, through which different species are readily discriminated. Owing to the chemical specificity and high sensitivity, this label-free LFSRM provides unique advantages in various materials and in biomedical applications, including nanomaterial inspection and in vivo imaging of living cells and organisms.

6.1 Introduction to Absorption-Based Far-Field Label-Free Super-Resolution Microscopy

The development of biological and biomedical sciences in the twentieth century has expedited the growth of far-field microscopy, which enabled numerous intracellular studies with minimal invasion [1]. However, traditional far-field microscopy cannot focus light onto a spot that is smaller than the diffraction limit [2]. As a consequence,

C. Li
Department of Chemistry, Purdue University, West Lafayette, IN 47906, USA

J.-X. Cheng (✉)
Boston University Photonics Center, Boston, MA 02215, USA
e-mail: jxcheng@bu.edu
URL: <http://sites.bu.edu/cheng-group/>

© Springer Nature Switzerland AG 2019
V. Astratov (ed.), *Label-Free Super-Resolution Microscopy*,
Biological and Medical Physics, Biomedical Engineering,
https://doi.org/10.1007/978-3-030-21722-8_6

137

objects that are closer or smaller than about half the wavelength cannot be discerned and those sub-cellular structures such as organelles can only be visualized down to this scale [3]. To break the diffraction limit, the last two decades have seen an emerging interest of developing fluorescence-based far-field super-resolution microscopy, or the so-called “far-field fluorescence nanoscopy”. Among them, photoactivated localization microscopy and stochastic optical reconstruction microscopy use the on/off blinking and switching behavior of fluorescent proteins to partially excite and localize the fluorophores with ~ 10 nm precision [4–7]. Stimulated emission depletion microscopy [8–10], along with ground-state depletion (GSD) microscopy [11] and saturated structured illumination microscopy [12, 13] are based on nonlinear optical effects that reduce the point spread function (PSF) of the focused light by controlling the excitation beam geometry.

Although the power of far-field fluorescence nanoscopy approaches enabled many breakthrough and discoveries in cell biology and biomedical sciences, due to the necessity of employing fluorescent labeling, many important intracellular processes that could be perturbed by the fluorophores remain unexplored [14–18]. In addition, many intrinsic biomolecules and nanomaterials, such as hemes, nanotubes, and graphene, have strong absorption yet low quantum efficiency [19–21], which makes it hard to visualize these species using far-field fluorescence nanoscopy. Label-free super-resolution microscopy (LFSRM), which uses other inherent chemical or physical properties from the samples to provide the contrast, thus shows advantages over fluorescence-based approaches for *in vivo* imaging of cells and organisms and draws increasing interests in the recent years.

One way to provide contrast mechanism in the label-free imaging manner is to use the intrinsic molecular absorption that is prevalent from inorganic materials to biomolecules. Linear absorption has been well studied since the early twentieth century and inspired various widely used measurement methods, including infrared (IR) spectroscopy (vibrational state absorption) [22] and UV–Vis spectroscopy (electronic state absorption) [23]. On comparing with scattering or multiphoton processes, we found that the large cross-section of linear absorption allows researchers to push the sensitivity of absorption spectroscopy to single-molecule detection [24, 25]. The application of Fourier transform in the interferometric spectroscopy enables the extraction of absorption spectra with high spectral resolution from the measured interferogram [26–29]. The development of bright coherent sources, like synchrotron radiation or quantum cascade lasers [30, 31], along with the deployment of fast electronics or sensitive detectors [27, 32] has improved not only the signal-to-noise ratio to an extreme but also the spectral resolution and has reduced the data acquisition time. These advancements in linear absorption spectroscopy have all facilitated the deployment of spectroscopic imaging in chemistry, materials science, pharmaceuticals, and polymer sciences [33–36]. Meanwhile, the advancements in nonlinear optics have also seen the growth of nonlinear absorption-based spectroscopy, such as transient absorption spectroscopy and stimulated Raman scattering spectroscopy [15, 19, 37–41]. Transient absorption microscopy, being able to provide the time-resolved spectroscopic imaging of various ultra-fast processes, is deployed in the field of nanomaterials, semiconductors, catalysts, and so on [42–46]. Stimulated Raman scattering

microscopy, on the other hand, is rising as a popular tool in biology, biomedicine, and so on [47–49].

Although absorption-based spectroscopic imaging techniques have come a long way to pursue fast and sensitive measurement, the limited spatial resolution remains to be a problem for further applications that require sub-micron or nanoscale resolution. In particular, the most popular absorption-based spectroscopic imaging techniques, such as mid-IR microscopy, near-IR microscopy, and transient-absorption microscopy, all use long wavelength light source (0.8–10 μm) whose spatial resolution stay in the micrometer scale. To achieve higher resolution, many methods have been reported during the recent years. One way of improving the image resolution is to deconvolve the captured image with the PSF of the system through image processing [50, 51]. Albeit widely applied and ready to use, deconvolution method could not really break the diffraction limit in far-field imaging systems. Thus, other methods using near-field configuration to achieve absorption-based super-resolution imaging were proposed. In 2000s, scanning near-field microscopy was combined with IR spectroscopy to achieve 20 nm resolution [52]. Later, atomic force microscope tips were used to probe the thermal expansion of objects induced by the absorption of IR, which obtained IR absorption spectroscopy from samples smaller than 10 nm [53–56]. However, the low throughput and sample-probe contact of these near-field methods limited their applications in biomedical sciences.

To address this problem, ideas of absorption-based far-field LFSRM were proposed in recent years. The first category is featured as photothermal (PT) microscopy, which uses a probe beam to detect the subtle PT lens effect induced by the linear absorption of the excitation (pump) beam. The PT lens measurement was first conducted in 1965 in a single-beam apparatus which uses the same beam for both pump and detection [57]. The dual-beam apparatus was then exploited to further take advantage of the sensitivity of PT detection [58]. It was not until the twenty-first century when PT detection was realized to be an approach to break the diffraction limit of the pump beam. As an example, various mid-infrared PT microscopes achieve sub-micron IR spectroscopic imaging by confocally exciting the objects with a mid-IR beam and probing with another tightly focused visible or near-IR beam [59]. The improved spatial resolution (~ 700 nm) allows those methods to obtain the IR spectra from the sub-cellular structures of living organisms or tissue slices for the first time. Besides, recent attempts which deploy counter-propagation measures have pushed the resolution up to 300 nm to obtain the IR spectrum of single *Escherichia coli* and local cation heterogeneities in mixed cation perovskite [60]. The idea of detecting the nonlinear PT terms to further increase the spatial resolution has also been demonstrated [61].

The second category of absorption-based far-field LFSRM, instead of probing the linear absorption, uses an apparatus that is inspired by super-resolution GSD microscopy and measures the nonlinear absorption of incident beams [62]. In the saturated transient absorption, a doughnut-shaped saturation pump beam was applied to confine the transient absorption signal within the very center of the focal spot to achieve super-resolution pump-probe imaging. The same apparatus can be used in other nonlinear optical processes to detect the materials absorption with sub-

diffraction resolution. In one example, a doughnut-shaped decoherence beam was combined with the confocal pump and probe beams to confine the stimulated Raman gain within the center of the beams, which enables sub-diffraction Raman imaging [63].

In this review, we review the history and fundamental principles of both linear and nonlinear absorption-based LFSRM techniques, scrutinize the pros and cons of different modalities, and present the latest applications and possible future directions of the field.

6.2 Breaking the Diffraction Limit in IR Microscopy Through Photothermal Detection

6.2.1 Laser-Induced Photothermal Lens Effect: The Origin of the Photothermal Contrast

The PT lens effect was first reported and discussed by Gordon et al., whose analysis built the basis of later works in this field [57]. In that experiment, a liquid sample cell filled with various pure samples was placed in the beam path and heated by the absorption of the laser power to produce a thermal gradient in the vicinity of the incident beam, which resulted in long transients of intensity profiles of the transmitted beam. It is believed that such observations were induced by the lens effect arising from the refractive index change near the beam as a result of the thermal gradient. To further explain it, Gordon et al. built a model to quantitatively depict the refractive index gradient produced by the PT process as a function of the temperature coefficient of the refractive index ($\partial n/\partial T$), through which the detected beam intensity profile could be used to retrieve the unknown quantities related to the sample, such as concentration and thermal constants. Since most liquids have a negative value of $\partial n/\partial T$, the thermal lens effect is usually divergent [58]. That very first experiment achieved measurement of absorptivity as low as 10^{-4} cm^{-1} , indicating a promising approach to probe weak absorptions indirectly with high sensitivity.

6.2.2 Improvement of Detection Sensitivity of Photothermal Spectroscopy

Soon after Gordon's experiment, many other works were reported to improve the physical model of the PT lens effect [64–68]. On the other hand, more efforts were dedicated to the enhancement of detection sensitivities of the PT measurements [69–71]. Stone designed an interferometry to better resolve the phase shift induced by the PT lens effect and achieved $\sim 10^{-5} \text{ cm}^{-1}$ sensitivity [72]. Boccara et al. exploited an accurate position sensor and applied fast modulation to the pump beam to measure

the periodic distortion induced by the PT process and deduced the sample absorptivity with high sensitivity [73]. It is also suggested that heat dissipation from the hot spot, located at the center of the beam, to the surrounding medium will affect the detected PT lens profile. Therefore, liquids with lower heat conductivity tend to produce larger thermal gradient in smaller space, which leads to higher detection sensitivity [74]. Note that all those attempts deployed the single-beam apparatus in which only one laser was used to both excite and probe the PT lens effect. And the best sensitivity for absorptivity measurements reported was limited to $\sim 10^{-6} \text{ cm}^{-1}$ [75].

The breakthrough was not realized until the deployment of the dual-beam apparatus along with the synchronous detection which achieved an ultimate sensitivity of less than 10^{-11} cm^{-1} for absorptivity determination [58]. Unlike its single-beam counterpart, the dual-beam setup uses a second laser to probe the PT lens effect induced by the sample absorption of the pump beam, as illustrated in Fig. 6.1. The probe beam can be either collinear [58] or perpendicular [76, 77] to the pump beam, resulting in similar performances.

Despite the addition of slight complexity of beam path alignment, the dual-beam apparatus has a major advantage over the single-beam apparatus on the improvement of sensitivity because it enables the use of a probe beam that has different wavelengths and beam path from those of the pump beam. First, the probe beam reacts only with the refractive index gradient produced by the PT lens effect, and the wavelength of probe beam can be chosen from low-absorption regions to maintain high probe power at the detector and hence achieves the ultimate signal-to-noise ratio (SNR) [74]. In addition, the pump beam wavelength is usually selected from spectral regions that are strongly absorbed by samples of interest to maximize the PT lens effect at

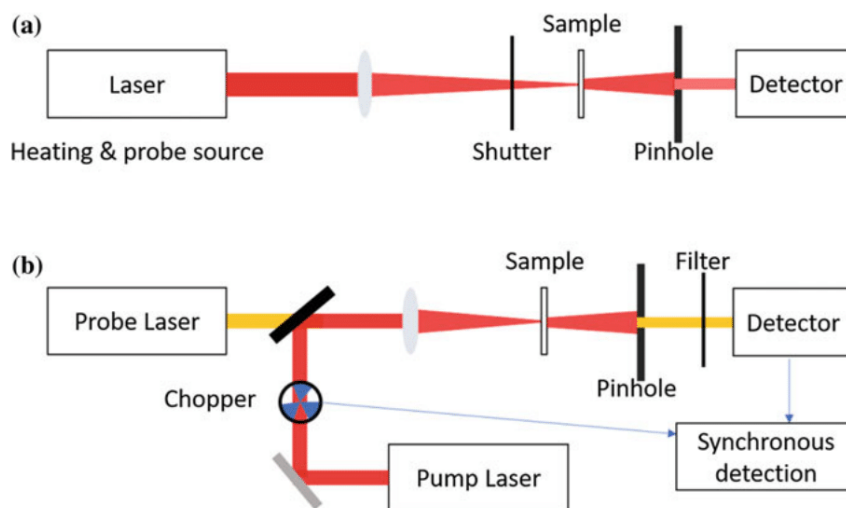


Fig. 6.1 Comparison of two different experimental setups: **a** single-beam apparatus and **b** dual-beam apparatus with pump beam modulation and synchronous detection

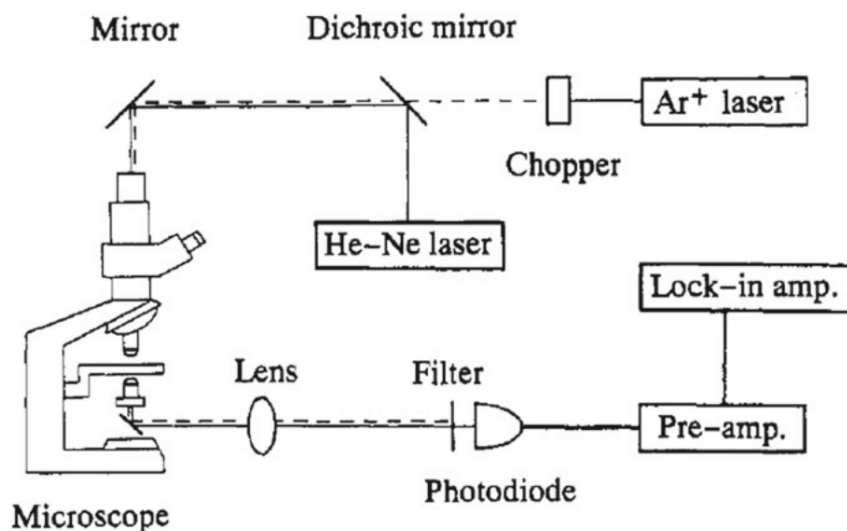


Fig. 6.2 Schematic of the first PT microscopy setup. Reprinted from [83] with permission. Copyright 1993 American Chemistry Society

extremely low concentrations ($<10^{-12}$ mol/L). Last but not the least, the dual-beam apparatus allows separate modulation of both the pump and probe beams, enabling lock-in detections which maximizes the SNR of a periodic process [78]. Single nanocluster and nanoparticle (1.4 nm diameter) imaging [79–81] as well as single-molecule detection [82] via PT imaging have all been reported in recent years. With such extraordinary improvement of sensitivity, the PT spectroscopy is applied in numerous studies in non-fluorescent analytes [80, 81] and further developed as one of the most used absorption-based label-free microscopy by Harada et al. in the early 1990s [83]. As shown in Fig. 6.2, the pump and probe beams are collinearly combined by a dichroic mirror and then sent to the sample through the same objective. Such coaxial configuration is adopted by most of the latest PT microscopes due to the ease of alignment. Details of super-resolution PT microscopy (PTM) techniques will be discussed next.

6.2.3 Beat the Diffraction Limit of the Pump Beam

Consider the Abbe diffraction limit calculated as $d = \lambda/2NA$ of the smallest object that can be resolved by a diffraction-limited optical microscope. Either shorter wavelength (λ) or larger numerical aperture (NA) will result in the improvement of the spatial resolution of microscopes. Since the spatial resolution of PTM is only determined by the probe beam instead of the pump beam, the dual-beam apparatus brings

in possibilities of beating the diffraction limit of the pump beam by manipulating the probe beam. Based on the preceding argument, super-resolution PTM imagings have been achieved mainly in three different ways.

The first method is to choose shorter wavelength laser source as the probe beam. This approach is the simplest way to realize sub-diffraction imaging and most used in vibrational spectromicroscopy such as the detection of mid-IR absorptions. The wavelength of mid-IR pump beam usually falls in the range of 2.5–10 μm and most IR objectives have relatively small NA values (≤ 0.8) given the fact that IR source cannot be used in water or immersion oil. Thus, the best spatial resolution of conventional absorption-based IR microscopes is still limited to $\sim 3 \mu\text{m}$ even with the synchrotron-based diffraction-limited system [31]. Besides, since the IR region covers such a broad spectral window, the chromatic aberration will significantly degrade the image quality. However, with the deployment of a visible probe beam (785 nm), Zhang and colleagues achieved sub-micrometer ($\sim 0.6 \mu\text{m}$) chemical imaging of living cells or microorganisms via confocal mid-IR PTM with a Cassegrain objective (0.65 NA) [59]. As the schematic shows in Fig. 6.3a, b, the probe focus is $\sim 1/10$ of the size of the pump mid-IR beam such that objects outside the probe beam focus are not detected, resulting in the ninefold improvement of the spatial resolution shown in Fig. 6.3c. Since the mid-IR pump beam can fully exploit the rich chemical information encoded in intrinsic chemical bond vibrations, mid-IR PTM emerges as a promising LFSRM approach for biomedical and pharmaceutical applications [59, 84]. We will discuss the recent advances and applications of mid-IR PTM in the following sections.

The second approach is to separate the beam paths and deploy a high NA objective for the counter-propagating probe beam. As shown in Fig. 6.4, Li et al. reached an ultimate resolution of 300 nm using a 532 nm probe beam and a 0.9 NA objective in their counter-propagating mid-IR PT microscope [60]. The main advantage of this approach is that the visible probe beam can go through a refractive objective instead of low NA reflective objectives that are typically used for IR source. Since there are numerous high NA refractive objectives available for visible probe beams, this approach could potentially reach the spatial resolution on the scale of 100 nm. In addition, this approach is often combined with the first approach, which results in higher resolution than those coaxial PT microscopes. However, the counter-propagating configuration does increase the complexity for system alignment in order to overlay the pump and probe beams in the sample plane and maximize the PT signal. Another drawback is that this approach requires the epi-detection design in which the probe photon collection efficiency is lower than that of the transmission mode, resulting in slower data acquisition. Thus, there is a trade-off between spatial resolution and imaging frame rate in this approach.

Last but not the least, super-resolution PTM can be achieved by probing the nonlinear PT lens effect whose signal profile is much narrower than the linear PT signal [61, 85–90]. Zharov first demonstrated the nonlinear dependence of PT signal to the pump beam intensity when the laser energy reaches certain thresholds using nanoparticles, through which the detected nonlinear PT signal arises only from the nonlinear center of the samples [61].

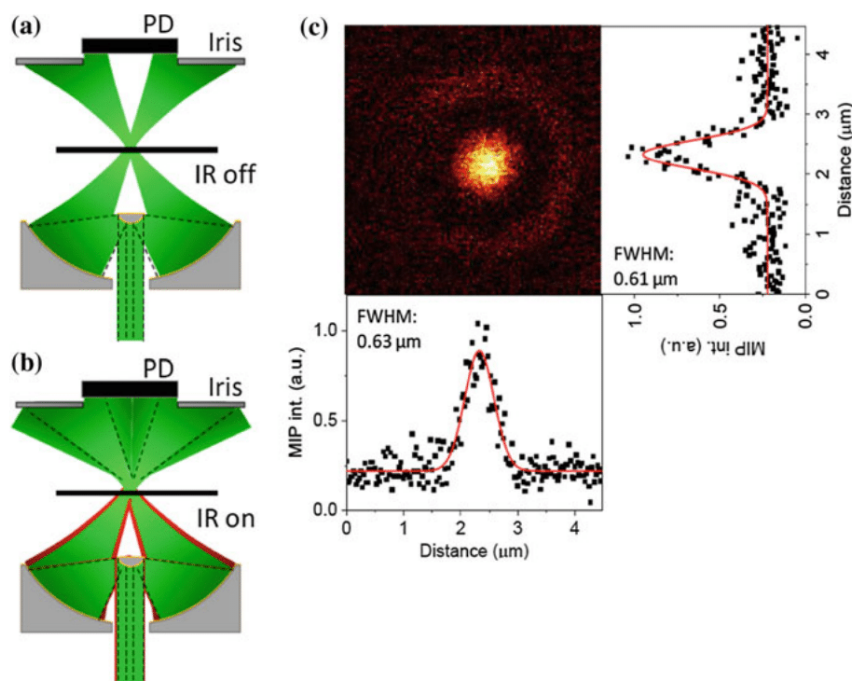


Fig. 6.3 **a** Probe beam propagation through the sample via a dark-field objective without an infrared beam (not to scale, condenser omitted for simplicity). **b** The probe beam propagation is perturbed by the addition of the infrared pump beam due to infrared absorption and development of a thermal lens. **c** Mid-IR PT imaging of a 500 nm PMMA bead. The vertical and horizontal intensity profiles indicate the spatial resolution is $\sim 0.6 \mu\text{m}$. Adapted from [59] with permission. Copyright 2016 American Association for the Advancement of Science

As depicted in Fig. 6.5a, the nonlinear PT resonance intensity profile is much narrower ($\sim 1/2$) than that of either the linear PT signal or the laser beams. Therefore, two adjacent nanoparticles whose distance is smaller than the diffraction limit of both the probe and pump beams are readily resolved by detecting the nonlinear PT signals, as shown in Fig. 6.5b. Experimental results also verified the anticipated improvement of the spatial resolution in nonlinear PTM, as shown in Fig. 6.5c, d. Based on the experimental results, the nonlinear PTM improved the lateral resolution from $(260 \pm 20 \text{ nm})$ to $(90 \pm 20 \text{ nm})$ with laser fluence level just above the threshold (0.7 J/cm^2 in this case). Since the nonlinear configuration requires the use of a stronger beam intensity compared to linear PTM, the concern of laser-induced photodamage was inevitably raised. Nedosekin et al. estimated that the minimum laser fluence needed to achieve spatially selective signal amplification is 10–30% higher than the nonlinear threshold, while the photodamage typically occurs when the laser fluence is at 3–5 times higher than the nonlinear threshold [61]. The early nonlinear PT studies were mainly conducted using plasmonic nanoparticles since the enhancement of

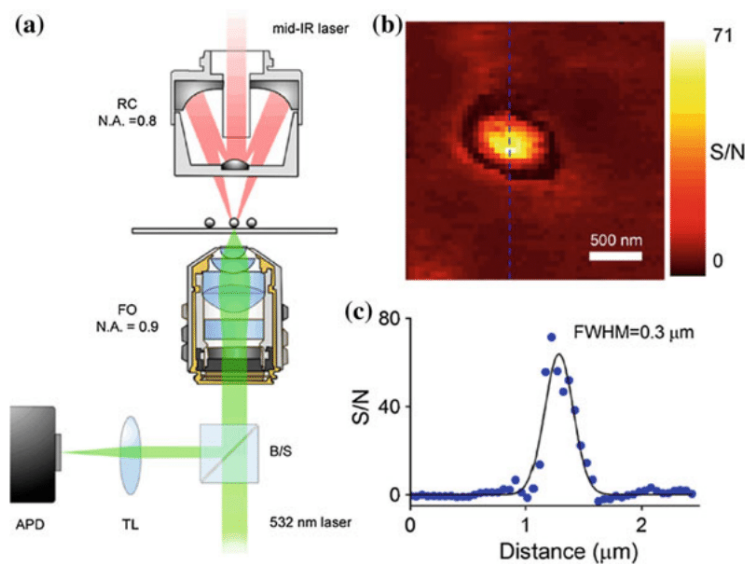


Fig. 6.4 **a** Schematic diagram of the counter-propagating mid-IR PT microscopy. The mid-IR pump and visible probe beams are focused on the sample with separate objectives. APD: avalanche photodiode, RC = reflective Cassegrain, FO = focusing objective, B/S = beam splitter, and TL = tube lens. **b** Mid-IR PT imaging of a 0.1 μm diameter polystyrene bead recorded with a step size of 0.05 μm . **c** Line profile extracted from the image in panel (b) showing a full-width at half-maximum (FWHM) of 0.3 μm . Adapted from [60] with permission. Copyright 2017 American Chemical Society

local electromagnetic field results in stronger nonlinear PT signal. Thanks to the recent development of high power laser sources with broader spectral coverage; this approach has also been demonstrated in liquid crystal [89], cells [91], and tissues [92].

It is noteworthy to mention that another approach uses time-resolved PT response to discriminate adjacent objects within the probe beam and diffraction limit was also realized [85, 91]. The principle behind such approach is that sub-diffraction objects exhibit different photo-induced thermal field dissipation rate. Therefore, by actively tuning the delay between pump and probe beams, time-resolved PT signal can be exploited to retrieve the actual shapes of different hot spots before the thermal fields expands to surroundings and prevent nano-objects from being resolved, as shown in Fig. 6.6a, b. This approach was demonstrated in nanoscale liposome imaging (Fig. 6.6c). Albeit sub-diffraction resolution is achieved, this method requires prior knowledge of physical or chemical parameters of samples to be studied in practical operations to optimize the time delays set between pump and probe beams. In addition, the sub-diffraction images require at least two independent measurements to compose, which prohibits high-speed PT imaging of nano-objects. Consequently, this approach is not widely used in this field.

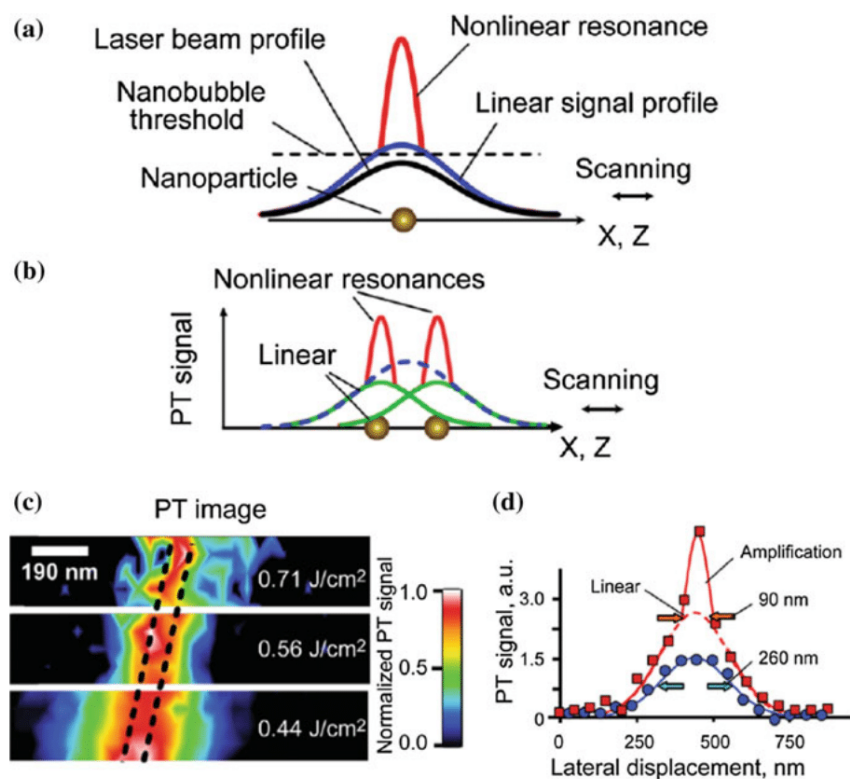


Fig. 6.5 **a** Nonlinear PT amplification for a nano-object in the center of the laser beam. **b** Nonlinear sequential PT spatial resonances during laser scanning from two nano-objects separated by a distance smaller than the size of the diffraction-limited beam spot. The dashed line represents a sum of two linear (green solid lines) PT signals. **c** Super-resolution nonlinear PT imaging of a 75-nm single gold nanowire at different laser fluences. **d** Lateral resolution in linear and nonlinear modes of PT microscopy. Adapted from [61] with permission from Wiley-VCH Verlag GmbH & Co

6.2.4 Visible Beam Excited Photothermal Microscopy

We will discuss more technical details of PTM techniques using visible pump beams. Visible excited PTM was first demonstrated by Harada et al. in 1993 as an extremely sensitive method for non-fluorescent microscale particle analysis [83]. As illustrated in Fig. 6.7, a typical visible excited PT microscope setup consists of a modulated pump beam and a continuous wave or modulated probe beam which are combined at a dichroic mirror and sent to the objective collinearly. Both laser scan and sample scan configurations have been demonstrated [93, 94]. The probe beam is further modulated by the periodic PT effect and detected by either forward or backward mode. With the deployment of a lock-in amplifier, the PT signal modulated at high frequencies (typically 100 kHz–1 MHz) is demodulated with high SNR which enables superb

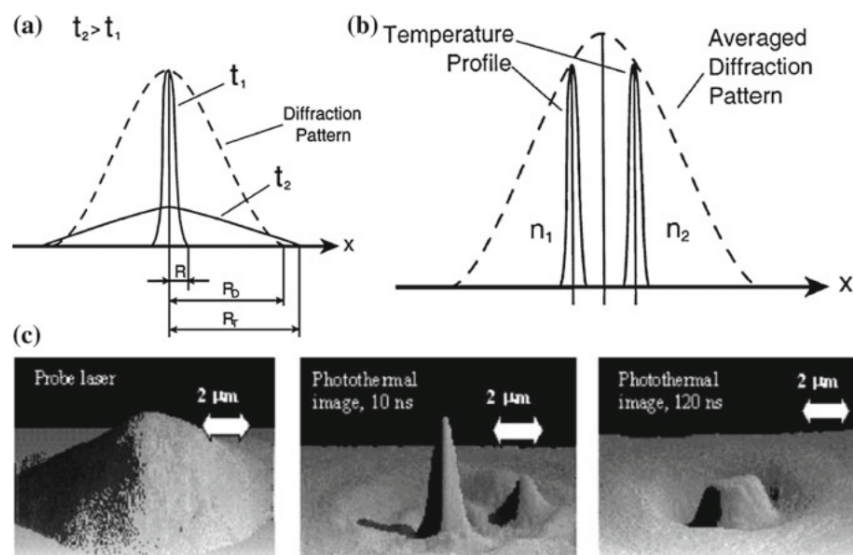


Fig. 6.6 Thermal fields (solid curves) and diffraction pattern (dashed curves) around **a** a single nano-object, and **b** two adjacent nano-objects within the diffraction pattern. Adapted from [85], Copyright 2003 Optical Society of America. **c** Left: Probe laser diffraction pattern. Middle: Super-resolution PT imaging of two 90-nm liposomes with 10 ns time delay. Right: Hardly resolved PT imaging of the same liposomes with 120 ns delay time. Adapted from [91], Copyright 2002 Wiley-Liss, Inc.

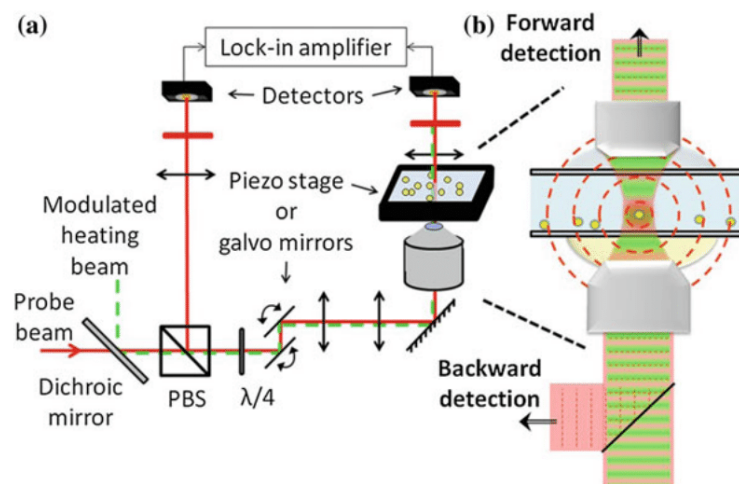


Fig. 6.7 **a** Setup of a typical visible excited PTM with lock-in amplified detection (PBS: polarizing beam splitter; $\lambda/4$: quarter wave plate). **b** Detailed depiction of probe beam propagation in both forward and backward detection. Reprinted from [94] with permission. Copyright 2014 Royal Microscopical Society

sensitivity. The limit of detection of visible excited PTM was first determined to be at femtogram level [95]. This limit was soon pushed to single nanoparticle detection [81], statistically sub-molecule detection [96], and single-molecule imaging [82]. Note that the impact of solvents in sample cells on SNR has already been noticed and investigated. Since the PT signal is proportional to the refractive change rate as a function of the change in temperature ($\partial n/\partial T$), this value determines the signal level and SNR when other parameters are the same. It was demonstrated experimentally that performing PT detections in glycerol results in five times improvement of the SNR than in water [74]. Furthermore, recent experiments indicated that critical Xeon medium will enhance the SNR by over 100 times compared to glycerol [97].

Visible excited PTM endows several advantages over other label-free microscopy techniques. First, for many molecules, electronic state absorption cross-sections are much larger ($>10^9$ times) than vibrational state absorption or Raman scattering processes, resulting in extremely sensitive detection of various species [98]. For instance, heme proteins are known to have extremely fast internal conversion rate and short excited state lifetime (<50 fs) of Soret band such that almost all absorbed photon energy is converted to heat [99, 100]. Therefore, PT effect provides ideal contrast for the detection of these molecules at fairly low concentrations (100 μM hemoglobin solution) [98]. Besides, gold nanoparticles and nanorods are a group of nano-objects that often being studied using visible excited PTM since the plasmonic resonances at 550–800 nm increases local electromagnetic fields and enhances the PT signals allowing nanoparticles as small as 1.4 nm to be detected [80].

Another advantage is that optics are well-designed and readily operated for visible beams compared to mid-IR sources that require special materials for coatings and substrates. There are no specific sample preparation requirements for visible excited PTM compared to fluorescence microscopy or IR microscopy. Liquid sample cells or sandwiched glass slides are usually used for transparent samples at forward detection mode. Although some experiments were conducted in glycerol or other organic solvents in order to enhance the SNR, the practical steps are nothing more complicated than preparing samples suspended in water. For opaque samples, backward detection mode allows visible excited PT imaging of only the surface of the samples due to dramatic power attenuation as both pump and probe beams propagate deep into the samples. But the operation is relatively easy in this case. Such advantage significantly simplifies the customized development, broader applications, and routine maintenance of the PT microscopes.

Third, laser engineering has come a long way in developing visible laser sources with higher power, lower noise, and broader tunable range, which all benefits the overall performances of PTM with visible pump beams. At first, the pump and probe beams power in samples are limited to 2 and 0.1 mW, respectively [96]. The application of high-power lasers increases the power dissipated to samples to 10 times for each beam, which leads to 100 times PT signal and 10 times SNR, given the quadratic relation of laser power and signal level in PT process [74]. Before tunable lasers were implemented, PTM is excited by monochromatic visible pump beams including He–Ne laser, Ar–ion laser, and 532 nm diode laser, through which only one type of molecules can be determined at a time. Then, dual pump beams appa-

ratus was exploited to perform simultaneous multiwavelength PT imaging, enabling the detection of two different species in one measurement [101]. The deployment of diode laser pumped optical parametric oscillator finally enables full coverage of the visible to NIR spectral region in PTM, which significantly enhances the ability to differentiate complex samples using PT spectromicroscopy technique [102].

The concern of laser-induced photodamage, especially thermal damage, also exists in visible beam excited PTM. Unlike fluorescence-based techniques that are vulnerable to photobleaching, the photodamage in visible beam excited PTM mainly comes from local thermal damage. The pump lasers used in PTM are usually nanosecond lasers, while the heat dissipation rate in condensed matters falls in tens of nanoseconds to microsecond scale [103]. Therefore, potential damage from local heat accumulation must be considered when determining the appropriate sampling rate for PT experiments. Some hypothetical and experimental works investigating the damage threshold of various biological samples have been reported [61, 104]. However, the experimental results of cell damage thresholds show dramatic variations among different cell lines and pump beam wavelengths [105]. Thus, more systematic studies on the photodamage in visible excited PTM are in need to facilitate spreading.

6.2.5 Mid-IR Excited Photothermal Microscopy

Ever since the publication of Coblenz's high-quality IR spectral database in 1905 [106], advances in IR spectroscopy and spectromicroscopy including Fourier transform IR (FTIR) spectroscopy [26], FTIR imaging [27] attenuated total reflectance IR imaging [107], and focal plane arrays IR imaging [108] have all improved the measurement of IR absorption from the aspects of higher sensitivity and spatial resolution. However, the fundamental limit of IR diffraction ($\sim 5 \mu\text{m}$) was not defeated by preceding approaches. Besides, the broad spectral window (typically 2–10 μm) invokes the problem of measurement accuracy since the wavelength-dependent light scattering could produce dramatic fluctuations in the IR signal intensity, which leads to huge baseline artifacts [109]. Furthermore, water shows strong absorption in the entire mid-IR region, which hinders the application of IR spectroscopic imaging to investigate biomolecules in living cells or organisms in aqueous environment. These problems were addressed collectively by the invention of mid-IR excited PTM. We will focus on the hardware and practical operation aspects of this technique in detail in this section.

Mid-IR excited PTM was demonstrated by Furstenberg et al. in 2012 [110], about 20 years later than the first demonstration of visible excited PTM. The pivotal difficulties of developing mid-IR based PTM are: (1) the lack of high-quality mid-IR laser sources; and (2) complications to integrate mid-IR pump beam with visible probe beam in the same optical system without introducing severe chromatic aberrations and mid-IR power losses.

The first problem was addressed by recent advances in mid-IR laser sources in the last two decades. In particular, modern quantum cascade laser (QCL) offers the ability to perform broadband wavelength scan with ultra-high spectral resolution ($\sim 0.1 \text{ cm}^{-1}$) discretely [111–113], in which specific vibrational bands of interests are pinpointed at high speed while providing enough chemical information to determine the composition of samples through spectra analysis [30]. Therefore, the majority of mid-IR PT microscopes use QCL as IR pump beam [59, 84, 110]. Besides QCL, difference frequency generation (DFG) is another effective approach to produce tunable mid-IR sources as the pump beam of PT microscope [114–116]. The fundamental beams usually consist of a tunable beam and a monochromatic beam. Both beams are focused onto nonlinear crystals, such as periodically poled LiNbO₃, to produce tunable nanosecond mid-IR pulses whose average power can reach up to 200 mW with less than 10 cm^{-1} linewidth, which is sufficient to induce strong PT effect in most absorption bands and measure liquid phase IR spectra. Despite the additional complexity of DFG, the produced mid-IR pump beam can be tuned to various wavelengths with better coverage of high wavenumber mid-IR regions, including the “cell silent region”, where most intrinsic biomolecules show no absorption, and deuterated molecules are often used to investigate cell metabolisms [116, 117]. Therefore, QCL and DFG collectively provide more options to the pump beam selection of mid-IR excited PTM and enable more important applications in biological studies.

The second problem found a solution by the deployment of reflective optics, including the Cassegrain objectives and off-axis parabolic mirrors, since these optics are immune to chromatic aberration across the whole spectral window. Like visible excited PTM, a typical mid-IR excited PT microscope deploys coaxial configuration, as illustrated in Fig. 6.8a, where the mid-IR pump beam and visible probe beam are combined at the dichroic mirror and collinearly sent to the Cassegrain objective [59]. To avoid mid-IR beam power losses, the reflective optics are usually coated with gold or silver, and the samples are sandwiched by ultra-broadband IR transparent materials such as CaF₂ or MgF₂. Since the water vapor and some other trace organic vapors in air all absorb mid-IR, the beam path of the mid-IR pump beam is usually designed with minimum distance, to further maintain the pump beam power at the sample. In some cases, to diminish the power loss and push the detection limit, methods used in conventional mid-IR measurements, including purging dry nitrogen into the system to reduce water vapor and CO₂ absorption, are needed [118]. Note that the reflected mid-IR residue (power $< 1 \text{ mW}$) from the dichroic mirror is collected by a mercury–cadmium–telluride (MCT) detector to record the IR power at each wavelength in real time. This power spectrum is used to normalize the PT signal acquired by the photodiode to produce the IR absorption spectra of samples.

There have been several reports aiming to improve the SNR in mid-IR excited PTM through various optimization approaches. For instance, Zhang et al. investigated the frequency dependence of the mid-IR PT signal, laser noise, and the system SNR (Fig. 6.8b) [59]. By considering the trade-off between the SNR and data acquisition speed, the pump beam modulation frequency was set at 100 kHz for optimal performance. As shown in Fig. 6.8c, a high-Q tunable resonant amplifier with a center frequency of 102.5 kHz was installed after the photodiode such that the modulated

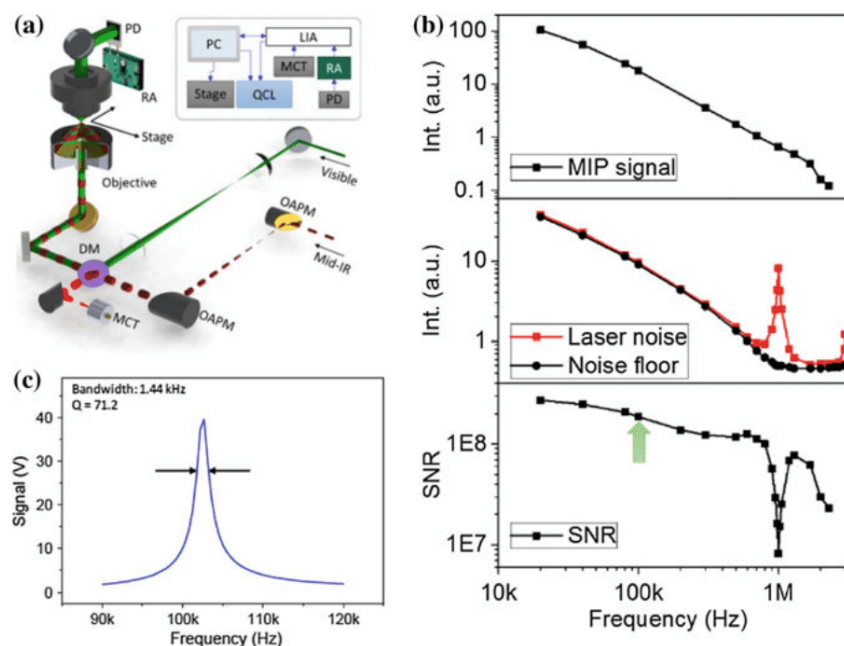


Fig. 6.8 **a** Setup of a typical mid-IR excited PTM using a Cassegrain objective. **b** Comparison of the frequency dependence of the mid-IR photothermal signal, QCL laser noise, and SNR. **c** Frequency response of a high-Q tunable resonant amplifier. Adapted from [59] with permission. Copyright 2016 American Association for the Advancement of Science

PT signal is amplified by 10^3 times while non-resonant noises are suppressed. Apart from the denoise strategies in optimizing the pump beam modulation frequency and detection frequency, Totachawattana et al. proposed a method to reduce background noises and enhance the SNR by introducing high-frequency modulation (1.04 GHz) to the probe beam [118]. On comparing with the results obtained using continuous wave probe beam, they found that the ultra-fast modulation increased the ultimate SNR by nine times. Another strategy was attempted by a couple of reports, in which the excitation wavelength is tuned to a specific “silent spectral region” to minimize the background absorption and maximize the analyte absorption with the prior knowledge of the system to be measured [59, 116].

As discussed in Sect. 6.2.3, the highest spatial resolution that have been achieved in mid-IR PTM is $0.3 \mu\text{m}$ using a highest NA air objective (NA 0.9) among all reported works [60]. In the most recent report on the resolution improvement of mid-IR excited PTM, Huffman et al. claimed that 202 nm resolution was achieved by roughly comparing the images obtained from the PTM and confocal microscope without quantitative evaluations [119]. Although it has been suggested to use water or immersion oil objectives to further increase the NA (to 1.3–1.5) to achieve better spatial resolution, the strong absorption of water and oil in the mid-IR region,

especially in the biologically informative amide I and C=O carboxyl bands [120], limited the broad interests of such strategy in practical applications since the mid-IR pump wavelength has to be tuned off resonance with these bands. The nonlinear PT effect has been observed in spectroscopy studies [89, 121], but super-resolution mid-IR excited PTM has not been enabled via nonlinear PT effects. With this field actively growing, those technical barriers that limit the pursuit of higher resolution will eventually be eliminated.

Similar to the case of visible excited PTM, the pump laser-induced photodamage is also considered in mid-IR excited PTM. Just like what have been discussed in the visible excited PTM in Sect. 6.2.4, the photodamage in mid-IR excited PTM is also induced by the thermal damage instead of direct photon excitation. However, the mid-IR photodamage threshold for most samples is much higher than that in the case of visible excitation since mid-IR photons only induce covalent bond vibrations which are more reversible processes compared to the electronic state excitation induced in visible excited PTM. To avoid accumulated heat causing damage to the sample, it is suggested to control the duty cycle of the mid-IR pump beam according to the heat dissipation rate of the sample and surroundings. Li et al. proposed a model to simulate the PT relaxation time as a function of object size for a series of polystyrene spheres in the air-glass surface [60]. Their results indicated that the accumulated heat will vanish in 10^{-6} s, which is apparently faster than experimental observations in other reports [59, 116]. Therefore, such model needs further amendment to be more accurate in predicting the actual relaxation time in mid-IR excited PT processes. So far, most of the reported mid-IR PTM studies adopted ~ 10 μ s as a single period of PT measurement. Note that some mediums with large heat capacity like water (4.18 J/kg K) will accelerate the heat dissipation, which helps reduce the photodamage from local overheating. Such phenomenon was found in the in vivo mid-IR PT imaging of cells and organisms [59].

6.2.6 Applications of Super-Resolution Photothermal Microscopy

Owing to the superb sensitivity in the detection of non-fluorescent species, both the visible and mid-IR excited super-resolution photothermal microscopies (SR-PTMs) have found numerous applications in the detection of trace analytes in materials science and biomedical studies. As discussed in the preceding sections, compared to mid-IR excitation, visible excited SR-PTM is able to take advantage of plasmonic resonance of metallic analytes to achieve single-molecule detection limit, high spatial resolution (~ 100 nm), and provides electronic absorption information. Therefore, it has been widely applied in the label-free imaging of individual nanoparticles, nanoclusters, and nanocrystals [80, 122]. Note that the size dependence of the PT signal has been well studied, as shown in Fig. 6.9, which enables the discrimination among different-sized particles that are much smaller than the diffraction limits of

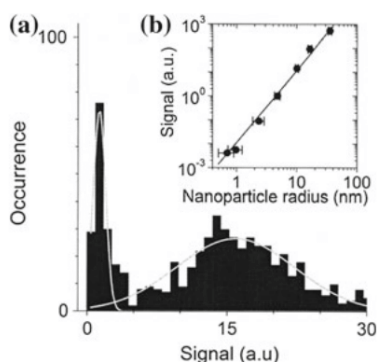


Fig. 6.9 **a** Signal distribution obtained from a sample containing both 2 and 5 nm gold nanoparticles. **b** Size dependence of the signal, that is, absorption cross-section (circles) deduced from a series of histograms as presented in **(a)** and, in comparison to the Mie theory (solid line). Reprinted from [80] with permission. Copyright 2004 The American Physical Society

the PTM. For instance, gold nanoclusters as small as 1.4 nm can be differentiated from 5 nm nanoclusters referring to the differences of their PT signal intensities even though they look alike in the PT images due to the limited spatial resolution [80]. Such observation has been exploited in studying molecular binding dynamics, especially for non-fluorescent molecules, at the single-molecule/single-nanorod level since it allows the researchers to significantly reduce the volume of nanorods to mimic the actual protein receptor sizes and construct better dynamic models (Fig. 6.10) [123]. The size distribution of nanoparticles with varying volumes below the diffraction limit can also be retrieved readily according to the PT signal intensity [74, 79]. Gaiduk et al. further demonstrated single molecule detection at room temperature by fully exploiting the advantage of high sensitivity provided by visible excited SR-PTM [82]. Owing to the label-free nature, Bogart et al. introduced a technique to monitor in vivo cell uptake of dextran-coated iron oxide nanoparticles, which is considered as a useful cell tracker [124]. Kitagawa et al. successfully integrated visible excited PTM with the electrodynamic chromatography, which enables separation and label-free detection of trace amino acids simultaneously [125]. Other reports have demonstrated the application of the visible excited SR-PTM to study the thermal properties of materials such as diamond [126], single-layer thin films [127], nanoscale defects in materials [128], and PT detection sensitivity as a function of temperature increase [129].

Apart from plasmonic nanoparticles, visible excited SR-PTM has found broad applications in label-free imaging of certain intrinsic molecules in biological samples. The greatest challenge of imaging complex biological specimen using visible excited SR-PTM is that the low concentration of most biomolecules requires extremely high sensitivity without surface plasmon. One solution is to select those analytes with relatively large absorption cross-sections such that the PT signal is significantly stronger than background absorptions. For instance, cytochromes as a group of intrinsic intra-

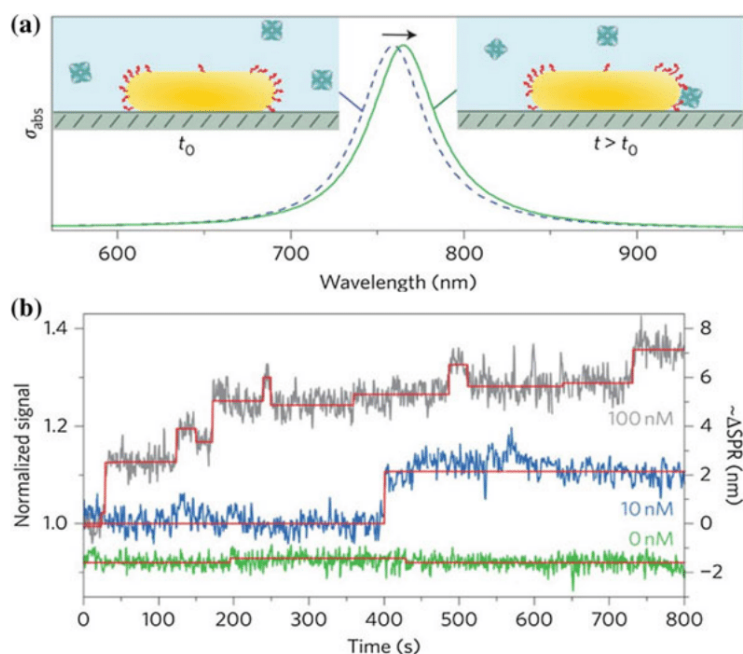


Fig. 6.10 **a** A single gold nanorod functionalized with biotin is introduced into an environment with the protein of interest. Binding of the analyte molecules to the receptors induces a redshift of the longitudinal surface plasmon resonance (exaggerated in the illustration). This shift is monitored at a single frequency using photothermal microscopy. **b** Photothermal time trace showing single-molecule binding events. The normalized photothermal signal as a function of time for biotin-functionalized gold nanorods in the presence of a streptavidin–R-phycoerythrin conjugate. The photothermal signal was recorded on three different nanorods in the presence of different concentrations of the protein. The red lines are fits to the time traces using a step-finding algorithm. Adapted from [123] with permission. Copyright 2012 Macmillan Publishers Limited obtained

cellular proteins that have strong absorption in the visible region are often studied by visible excited SR-PTM [130]. The deployment of tunable pump lasers allows the collection of absorption spectroscopy simultaneously with PT imaging, which enabled identification, quantification, and differentiation of cytochromes *c* in mitochondria, live cells, and solutions [131]. The visible excited SR-PTM has also been demonstrated in tissue histology to image nuclei (hematoxylin), cell bodies (eosin), and melanin with H&E stained skin tissues [132]. However, the number of such intracellular analytes is limited and cannot be applied universally. The other solution is provided by the integration of radially segmented balanced (RSB) detection to the conventional PTM to enhance the modulated PT signal and suppress the noise arising from probe intensity fluctuations as well as electronic cross-talks (Fig. 6.11). As a result, the overall SNR of the SR-PTM with RSB detection is improved by ~ 2.3 times [133, 134]. Such enhancement may not look dramatic but is sufficient to obtain decent label-free images of skin tissues [133], skeletal muscle mitochondria [135],

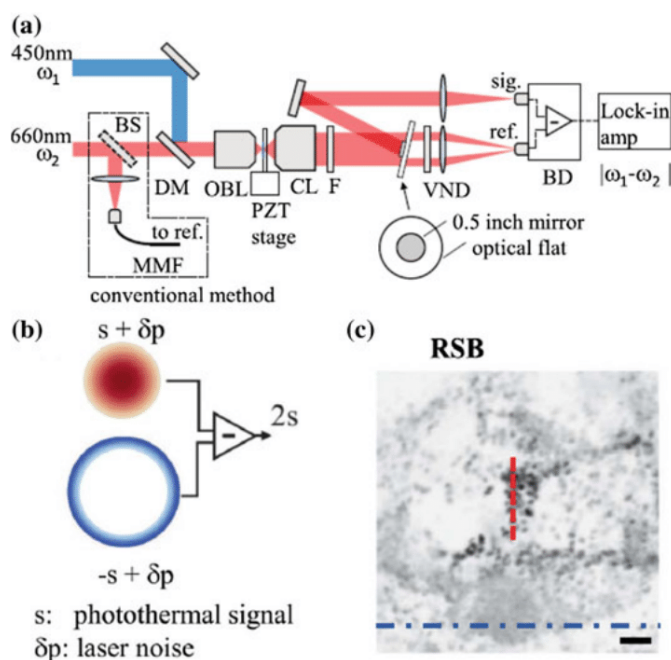


Fig. 6.11 **a** Experimental setup of laser diode-based photothermal microscopy with radially segmented balanced detection. DM: dichroic mirror; BS: beam splitter; OBL: objective lens; CL: condenser lens; F: band pass filter; VND: variable neutral-density filter; BD: balanced photodetector; MMF: multimode fiber. **b** Conceptual scheme of the radially segmented balanced detection for improving signal intensity s and reducing intensity noise of the probe beam δp . **c** PTM image of a slice of mouse melanoma observed by RSB detection. Adapted from [133] with permission. Copyright 2015 Optical Society of America

3-D imaging of non-fluorescent tissues [136], and tumor tissues [137], to provide molecular spectroscopy information to assist disease diagnosis in clinics.

Although mid-IR excited SR-PTM cannot achieve the same spatial resolution as visible excited configurations due to the limitations of optics, the informative IR spectrum strengthens the chemical selectivity for organic molecules in particular, and the detection sensitivity could achieve micromolar in solutions. Compared to visible absorption spectroscopy, mid-IR spectroscopy endows narrower characteristic peaks which is of value in molecule differentiations, and broader spectral coverage that allows detection of all kinds of covalent bond vibrations. Thus, mid-IR excited SR-PTM has been actively used in label-free imaging of complex systems such as live cells [59, 116], microorganisms [60], tissue slices [118, 138], polymer composites [110, 139], pharmaceutical formulations [84], mixed cation perovskites [140], graphene oxide detection [141], trace gas detection [142], and so on. One of the most important applications is the demonstration of label-free multicolor imaging of intracellular distribution of lipid droplets and drug molecules through mid-IR

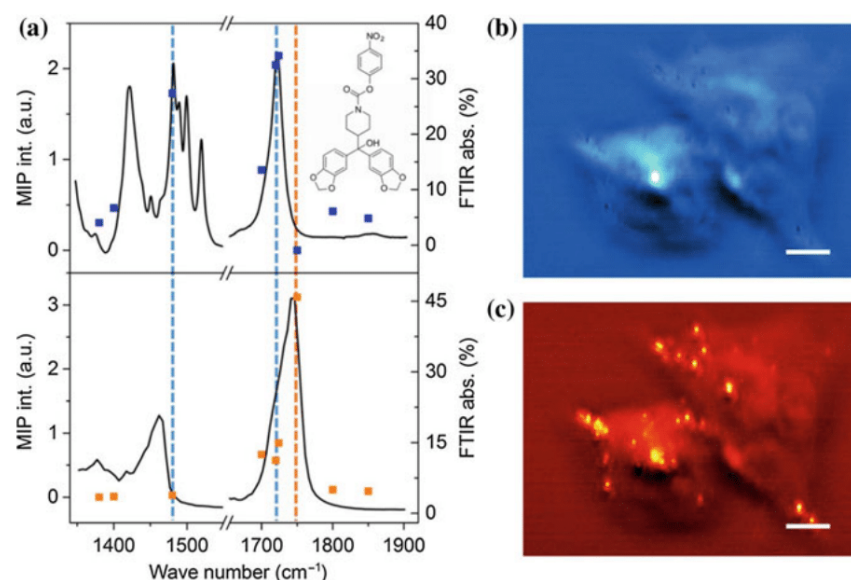


Fig. 6.12 Multispectral mid-IR PT imaging of cellular drug uptake. **a** Infrared spectra of the lipid inhibitor JZL184 (top, line) and olive oil (bottom, line). Squares indicate the multivariate curve resolution results for drug and lipid content. Dashed lines indicate the characteristic peaks for drug (blue) and lipid (orange) content. Inset shows the molecular structure of the drug. **b** and **c** Multivariate curve resolution output of multispectral mid-IR PT imaging of JZL184-treated MIA PaCa-2 cells for drug (**b**) and lipid (**c**) content. Scale bars, 20 μm. Reprinted from [59] with permission. Copyright 2016 American Association for the Advancement of Science

excited SR-PTM since it proves such technique to be a promising imaging platform in the field of cell biology and biomedical studies (Fig. 6.12) [59]. By combining the advantages of conventional IR hyperspectral imaging and submicrometer spatial resolution of confocal optical microscopy, the mid-IR excited SR-PTM for sure will become a powerful analytical approach in scientific researches. Furthermore, the demonstration of fiber-based [143] mid-IR excited PTM increases the portability of the system. Also, the backward detection apparatus (Fig. 6.13) will simplify the sample preparation process and appeal to users from the industry specifically [84]. In short, this field is actively growing since the first report about mid-IR excited SR-PTM in 2012. There will be more technical breakthroughs in the near future.

6.3 Super-Resolution Transient Absorption Microscopy

Owing to the advancement of laser techniques and fast electronics since the 1980s, the field of nonlinear optical microscopy has come a long way in developing imaging techniques with higher resolution, lower detection limit, and higher frame rate with

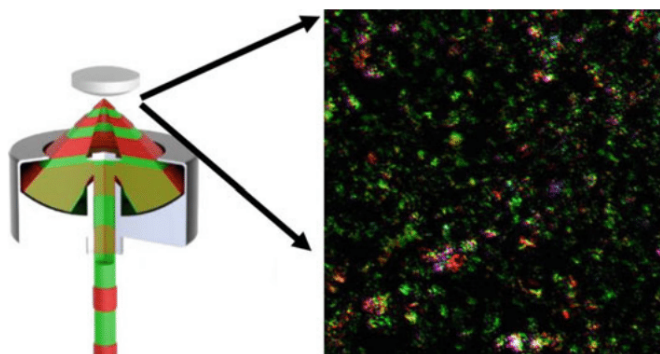


Fig. 6.13 Backward detected mid-IR excited SR-PTM is able to quantify the size distribution and chemical compositions of active pharmaceutical ingredients as well as excipients in pharmaceutical tablets through direct imaging. Reprinted from [84] with permission. Copyright 2017 American Chemical Society

decent chemical selectivity, to attract broader interests in other research areas. Based on the fundamental principles, those nonlinear optical spectromicroscopy approaches can be classified into three main categories, including parametric generation (e.g. second harmonic generation [144], third harmonic generation [145], coherent anti-Stokes Raman scattering [14], etc.), pump-probe (e.g. transient absorption (TA) [46]), and nonlinear dissipation (e.g. two-photon excited fluorescence [146], stimulated Raman scattering (SRS) [15], etc.).

In this section, we focus on the principle and technical details of two novel approaches to perform nonlinear absorption-based LFSRM, saturated TA and SRS microscopy, both of which were realized through nonlinear absorption and implementing the mechanism of reversible saturable optical linear fluorescence transitions (RESOLFT) microscopy in recent years and expected to find interesting applications in biological and materials science.

6.3.1 Transient Absorption Microscopy

TA spectroscopy, also known as pump-probe spectroscopy or time-resolved spectroscopy, has been widely used to elucidate fundamental ultra-fast processes (picoseconds and sub-picoseconds) in chemistry, biology, and condensed matters [19, 46, 147, 148]. In a typical TA experiment, a pump beam is applied to reduce the population of ground states and induce intensity fluctuations of the transmitted probe beam, which is detected as the TA signal. The contrast types that contribute to the TA signals include three main components, including ground-state bleach, stimulated emission, and excited-state absorption (Fig. 6.14) [148]. In ground-state bleach process, an intense pump beam is usually used to deplete molecules in the

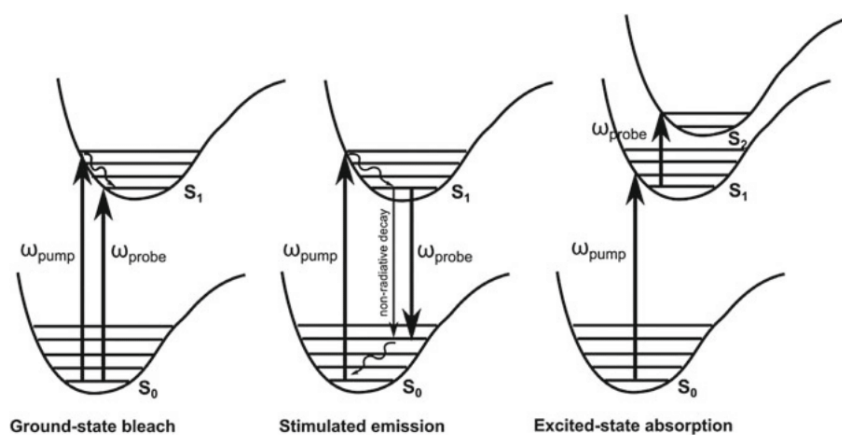


Fig. 6.14 Contributions to TA spectrum: ground-state bleach, stimulated emission, and excited-state absorption. Reprinted from [148] with permission. Copyright 2015 by Wiley-VCH Verlag GmbH & Co. KGaA, Weinheim

ground state such that the absorption of probe beam is suppressed and increases the transmitted probe intensity. While in the case of stimulated emission, the pump beam first excites molecules to excited states and then, the slightly delayed probe beam induces stimulated emission to produce more photons in the probe frequency which increases the probe beam intensity. As for excited-state absorption, the excited molecules keep absorbing probe beam photons and are excited to higher states, which results in the decreased transmitted probe beam intensity. Note that the contributions to TA signals are not limited to the above-mentioned processes, but this review will not include other mechanisms. As a nonlinear optical approach, one advantage of TA microscopy over linear absorption-based microscopy is the removal of off-focal signal. Furthermore, since TA involves nonlinear response from samples, it offers the opportunity to achieve super-resolution by breaking the diffraction limit in conventional confocal microscopy. We will discuss the two recently demonstrated LFSRM approaches in the following sections.

6.3.2 Spatially Controlled Saturated Transient Absorption

The idea of spatially controlled saturated transient absorption (SCSTA) originates from the GSD microscopy first proposed by Hell et al. [149], in which a doughnut-shaped depletion beam and a regularly focused probe beam are overlaid at the sample to reduce the PSF, which represents the smallest spot that can be spatially resolved (Fig. 6.15) [150]. In typical GSD microscopy, fluorophores located at the outer ring will be excited to the T_1 triplet state and have a much longer lifetime ($\sim 10^{-2}$ s level) than normal $S_0 \rightarrow S_1$ relaxation (10^{-9} to 10^{-7} s level). Thus, after the depletion beam

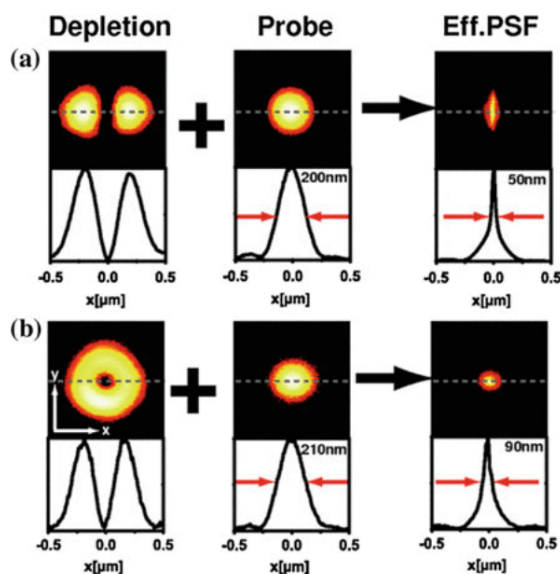


Fig. 6.15 Creating effective PSFs of sub-diffraction extent in a single-point scanning GSD microscope. **a** Squeezing the spot just along the x -axis and **b** along all directions in the focal plane. The depletion spot (Depletion) overlaid with the regularly focused probe spot (Probe) produces the effective PSF (Eff. PSF). The probe spot probes the fluorescence right after the depletion spot has pumped the dye into the triplet state. Focal plane cross-section of the PSF (upper panel) and profiles along the x -axis [dashed line in upper panels] showing FWHM values (lower panels). Wavelengths for depletion and probing: 532 nm; fluorescence wavelength: 560 nm. Reprinted from [150] with permission. Copy right 2007 American Physical Society

bleaches the surrounding fluorophores, the delayed probe beam can only measure the molecular absorption from the very center of the overlaid beams, whose diameter is predicted to be capable of achieving 10–20 nm [149].

Wang et al. introduced such idea to SCSTA experiments by GSD of the electron–charge carrier in graphene-like materials (Fig. 6.16) [62]. The saturable absorption properties of graphene-like structures have been well studied [151–153]. In particular, the charge carrier dynamics in epitaxial graphene has been investigated by TA microscopy [42]. It was observed that the carrier–phonon interactions in graphene-like structures occur in the timescale of 100 fs to a few picoseconds. Therefore, by tuning the temporal delay between pump and probe pulses to sub-picosecond scale, the transient absorption signal is able to be detected. To actively suppress the off-focal signal, an intense doughnut-shaped depletion pulse is temporally inserted between the pump and probe pulses. As a consequence, the transient absorption signal (shown as the probe beam intensity loss) is generated only from the very center of the overlaid beams similar to GSD microscopy. The doughnut-shaped depletion beam is often tailored by spatial light modulator or spatial phase modulator. According to the experimental results shown in Fig. 6.16d–f, the PSF in SCSTA (FWHM

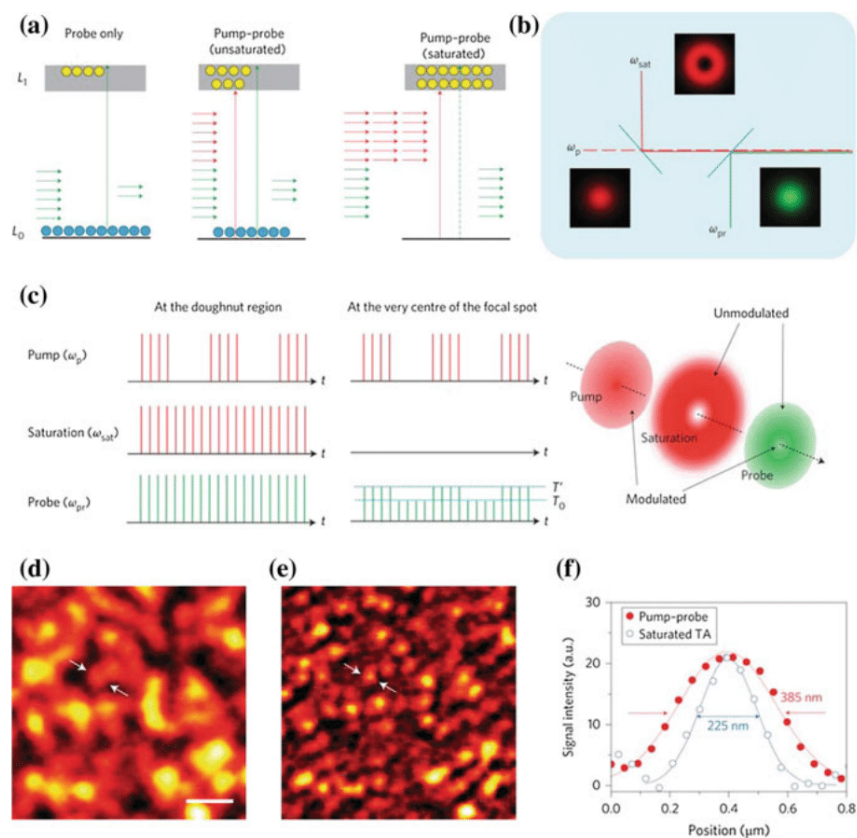


Fig. 6.16 Principle of saturated transient absorption microscopy. **a** Illustration of the saturation effect in a two-level electronic transition. Pump and probe photons are indicated by red and green arrows, respectively. **b** Simple layout of the setup. The dashed line indicates that the pump beam is modulated. **c** The pulse train of pump, saturation, and probe beams at the focused doughnut-shaped region (left panel) and at the very center of the focal spot (middle panel). The modulation transfer from pump to probe only occurs at the center where the saturation field intensity is close to zero (right panel). Sub-diffraction-limited imaging of graphite nanoplates obtained from **d** conventional pump-probe microscopy and **e** SCSTA microscopy. **f** Intensity profiles along the lines indicated by arrows in **(d, e)**. Scale bar: 1 μm . Adapted from [62] with permission. Copyright 2013 Macmillan Publishers Limited

is 225 nm) is 42% of that in the conventional pump-probe microscopy (FWHM is 385 nm).

One of the major concerns of such approach is the issue of photodamage since the molecules are repeatedly excited/depleted by the pump/depletion beam in the raster scanning mode. As Bretschneider et al. discussed in their report on GSD microscopy, care must be taken when determining the pixel dwell time since molecules excited to the triplet state must relax to ground state before beam moves on [150]. In SCSTA experiments, Wang et al. also investigated the photodamage threshold of the intense depletion beam and recovery of TA signals after repeated excitations using graphene nanoplate as a model. The photodamage was observed when power density exceeds $\sim 2.4 \text{ MW cm}^{-2}$, while the TA signal recovery rate could reach 100% below that threshold. This approach can be applied to other materials that have saturable absorption properties, such as single-walled carbon nanotubes [154–156], iron oxides [157], or zinc oxides [158].

6.3.3 Super-Resolution Stimulated Raman Microscopy

Inspired by the success of other super-resolution nonlinear optical microscopy [62, 79], Gong et al. proposed to combine the advantages of stimulated emission depletion (STED) microscopy and SRS microscopy by developing the super-resolution saturated SRS microscopy in a theoretical study [159]. They proposed to split the Stokes beam into two components, one of which is modulated as an intense doughnut-shape by a phase plate and the other one remains a normal Gaussian beam. By recombining the two Stokes components, an effective Stokes beam with narrower PSF is created at the focus. However, according to their simulated results, the power density required for the intense Stokes saturation beam is as high as a few TW cm^{-2} , which is almost impossible to reach in most laboratory conditions.

The super-resolution SRS microscopy was realized in 2015 by Silva et al. using a triple-beam configuration [63]. Instead of splitting the Stokes beam to create a doughnut-shape Stokes, Silva et al. deploy another beam as the decoherence beam whose wavelength is close to that of Stokes beam and destroy the vibrational coherence at the ring of the doughnut-shape. According to some preliminary super-resolution SRS imaging results, the spatial resolution was improved by a factor of ~ 1.7 . As measured in the experiment, the power density of the decoherence beam required to induce the saturation SRS is $\sim 10 \text{ W cm}^{-2}$, which is close to the average power used in previously reported SRS experiments [15, 38, 160]. Note that this approach uses the same idea as STED microscopy. Thus, an ultimate resolution of $\sim 50 \text{ nm}$ is expected as such technique can be actively developed in the future. Along with the ability of SRS microscopy providing the informative vibrational spectroscopy of various biomolecules and inorganic materials, super-resolution SRS microscopy will find broad applications in biological and materials sciences.

6.4 Conclusion and Outlook

The functions of biomolecules, biosystems, and nanomaterials are inextricably linked with the structures and chemical compositions. Absorption-based LFSRM, with superior detection limit and spatial resolution, is growing as a significant tool to enhance the understanding of biology and materials sciences. In this review, we have introduced both linear and nonlinear absorption-based LFSRM techniques that provide excellent sensitivity, fast imaging speed, as well as informative spectroscopic information. We have highlighted how the recent advancements in mid-IR excited PTM have successfully defeated the diffraction limit of mid-IR beam. As a relatively new field, it is to be expected that absorption-based LFSRM approaches will be further improved by ongoing developments in laser engineering, optical and electronic technology.

References

1. J.B. Pawley, in *Handbook of Biological Confocal Microscopy*, ed. by J.B. Pawley (Springer US, Boston, MA, 2006), pp. 20–42
2. E. Abbe, Beiträge zur Theorie des Mikroskops und der mikroskopischen Wahrnehmung. *Archiv für mikroskopische Anatomie* **9**, 413–418 (1873)
3. S.W. Hell, Microscopy and its focal switch. *Nat. Methods* **6**, 24–32 (2009)
4. R.M. Dickson, A.B. Cubitt, R.Y. Tsien, W.J.N. Moerner, On/off blinking and switching behaviour of single molecules of green fluorescent protein. *Nature* **388**, 355–358 (1997)
5. E. Betzig, G.H. Patterson, R. Sougrat, O.W. Lindwasser, S. Olenych, J.S. Bonifacino, M.W. Davidson, J. Lippincott-Schwartz, H.F.J.S. Hess, Imaging intracellular fluorescent proteins at nanometer resolution. *Science* **313**, 1642–1645 (2006)
6. M.J. Rust, M. Bates, X. Zhuang, Sub-diffraction-limit imaging by stochastic optical reconstruction microscopy (STORM). *Nat. Methods* **3**, 793–795 (2006)
7. B. Huang, W. Wang, M. Bates, X.J.S. Zhuang, Three-dimensional super-resolution imaging by stochastic optical reconstruction microscopy. *Science* **319**, 810–813 (2008)
8. S.W. Hell, J.J.O.L. Wichmann, Breaking the diffraction resolution limit by stimulated emission: stimulated-emission-depletion fluorescence microscopy. *Opt. Lett.* **19**, 780–782 (1994)
9. K.I. Willig, B. Harke, R. Medda, S.W. Hell, STED microscopy with continuous wave beams. *Nat. Methods* **4**, 915–918 (2007)
10. K.I. Willig, S.O. Rizzoli, V. Westphal, R. Jahn, S.W. Hell, STED microscopy reveals that synaptotagmin remains clustered after synaptic vesicle exocytosis. *Nature* **440**, 935–939 (2006)
11. S.W. Hell, M.J.A.P.B. Kroug, Ground-state-depletion fluorescence microscopy: a concept for breaking the diffraction resolution limit. *Appl. Phys. B* **60**, 495–497 (1995)
12. M.G. Gustafsson, Surpassing the lateral resolution limit by a factor of two using structured illumination microscopy. *J. Microsc.* **198**, 82–87 (2000)
13. M.G. Gustafsson, Nonlinear structured-illumination microscopy: wide-field fluorescence imaging with theoretically unlimited resolution. *Proc. Natl. Acad. Sci. U.S.A.* **102**, 13081–13086 (2005)
14. J.-X. Cheng, X.S. Xie, Coherent anti-Stokes Raman scattering microscopy: instrumentation, theory, and applications. *J. Phys. Chem. B* **108**, 827–840 (2004)
15. C.W. Freudiger, W. Min, B.G. Saar, S. Lu, G.R. Holtom, C. He, J.C. Tsai, J.X. Kang, X.S.J.S. Xie, Label-free biomedical imaging with high sensitivity by stimulated Raman scattering microscopy. *Science* **322**, 1857–1861 (2008)

16. T.T. Le, I.M. Langohr, M.J. Locker, M. Sturek, J.-X. Cheng, Label-free molecular imaging of atherosclerotic lesions using multimodal nonlinear optical microscopy. *J. Biomed. Opt.* **12**, 054007 (2007)
17. N. Olivier et al., Cell lineage reconstruction of early zebrafish embryos using label-free nonlinear microscopy. *Science* **329**, 967–971 (2010)
18. J.-X. Cheng, X.S. Xie, Vibrational spectroscopic imaging of living systems: an emerging platform for biology and medicine. *Science* **350**, 1054–1063 (2015)
19. A.J. Chen, X. Yuan, J. Li, P. Dong, I. Hamza, J.-X. Cheng, Label-free imaging of heme dynamics in living organisms by transient absorption microscopy. *Anal. Chem.* **90**, 3395–3401 (2018)
20. L. Tong, Y. Liu, B.D. Dolash, Y. Jung, M.N. Slipchenko, D.E. Bergstrom, J.-X. Cheng, Label-free imaging of semiconducting and metallic carbon nanotubes in cells and mice using transient absorption microscopy. *Nat. Nanotechnol.* **7**, 56–61 (2011)
21. K.-C. Huang, J. McCall, P. Wang, C.-S. Liao, G. Eakins, J.-X. Cheng, C. Yang, High-speed spectroscopic transient absorption imaging of defects in graphene. *Nano Lett.* **18**, 1489–1497 (2018)
22. B. Schrader, *Infrared and Raman Spectroscopy: Methods and Applications* (Wiley, Weinheim, 2008)
23. H. Förster, UV/VIS spectroscopy, in *Characterization I*, ed. by H.G. Karge, J. Weitkamp (Springer, Berlin, Heidelberg, 2004), pp. 337–426
24. W.E. Moerner, M.J.S. Orrit, Illuminating single molecules in condensed matter. *Science* **283**, 1670–1676 (1999)
25. M. Celebrano, P. Kukura, A. Renn, V. Sandoghdar, Single-molecule imaging by optical absorption. *Nat. Photonics* **5**, 95–98 (2011)
26. P.R.J.S. Griffiths, Fourier transform infrared spectrometry. *Science* **222**, 297 (1983)
27. E.N. Lewis, P.J. Treado, R.C. Reeder, G.M. Story, A.E. Dowrey, C. Marcott, I.W. Levin, Fourier transform spectroscopic imaging using an infrared focal-plane array detector. *Anal. Chem.* **67**, 3377–3381 (1995)
28. R.A. Dluhy, R. Mendelsohn, Emerging techniques in biophysical FT-IR. *Anal. Chem.* **60**, 269A–278A (1988)
29. A. Thorne, High resolution Fourier transform spectrometry in the visible and ultraviolet regions. *J. Anal. At. Spectrom.* **13**, 407–411 (1998)
30. M.R. Kole, R.K. Reddy, M.V. Schulmerich, M.K. Gelber, R. Bhargava, Discrete frequency infrared microspectroscopy and imaging with a tunable quantum cascade laser. *Anal. Chem.* **84**, 10366–10372 (2012)
31. M.J. Nasse, M.J. Walsh, E.C. Mattson, R. Reininger, A. Kajdacsy-Balla, V. Macias, R. Bhargava, C.J. Hirschmugl, High-resolution Fourier-transform infrared chemical imaging with multiple synchrotron beams. *Nat. Methods* **8**, 413–416 (2011)
32. H. Chih-Cheng, W. Chung-Yu, J. Far-Wen, S. Tai-Ping, Focal-plane-arrays and CMOS readout techniques of infrared imaging systems. *IEEE Trans. Circuits Syst. Video Technol.* **7**, 594–605 (1997)
33. W. Haiss, N.T.K. Thanh, J. Aveyard, D.G. Fernig, Determination of size and concentration of gold nanoparticles from UV-Vis spectra. *Anal. Chem.* **79**, 4215–4221 (2007)
34. S. Wartewig, R.H.H. Neubert, Pharmaceutical applications of mid-IR and Raman spectroscopy. *Adv. Drug Deliv. Rev.* **57**, 1144–1170 (2005)
35. K.A. Bunding Lee, S.C. Johnson, Comparison of mid-IR with NIR in polymer analysis. *Appl. Spectrosc. Rev.* **28**, 231–284 (1993)
36. B. Stuart, *Infrared Spectroscopy* (Kirk-Othmer Encyclopedia of Chemical Technology, 2015)
37. Y. Jung, M.N. Slipchenko, C.H. Liu, A.E. Ribbe, Z. Zhong, C. Yang, J.-X. Cheng, Fast detection of the metallic state of individual single-walled carbon nanotubes using a transient-absorption optical microscope. *Phys. Rev. Lett.* **105**, 217401 (2010)
38. J. Li, W. Zhang, T.-F. Chung, M.N. Slipchenko, Y.P. Chen, J.-X. Cheng, C. Yang, Highly sensitive transient absorption imaging of graphene and graphene oxide in living cells and circulating blood. *Sci. Rep.* **5**, 12394 (2015)

39. C.-S. Liao, M.N. Slipchenko, P. Wang, J. Li, S.-Y. Lee, R.A. Oglesbee, J.-X. Cheng, Microsecond scale vibrational spectroscopic imaging by multiplex stimulated Raman scattering microscopy. *Light Sci. Appl.* **4**, e265 (2015)
40. X. Chen, C. Zhang, P. Lin, K.-C. Huang, J. Liang, J. Tian, J.-X. Cheng, Volumetric chemical imaging by stimulated Raman projection microscopy and tomography. *Nat. Commun.* **8**, 15117 (2017)
41. H. Lin, C.-S. Liao, P. Wang, N. Kong, J.-X. Cheng, Spectroscopic stimulated Raman scattering imaging of highly dynamic specimens through matrix completion. *Light Sci. Appl.* **7**, 17179 (2018)
42. L. Huang, G. V. Hartland, L. Q. Chu, Luxmi, R.M. Feenstra, C. Lian, K. Tahy, H. Xing, *Nano Lett.* **10**, 1308–1313 (2010)
43. Z. Guo, Y. Wan, M. Yang, J. Snaider, K. Zhu, L. Huang, Long-range hot-carrier transport in hybrid perovskites visualized by ultrafast microscopy. *Science* **356**, 59–62 (2017)
44. L. Yuan, T.-F. Chung, A. Kuc, Y. Wan, Y. Xu, Y.P. Chen, T. Heine, L. Huang, Photocarrier generation from interlayer charge-transfer transitions in WS₂-graphene heterostructures. *Sci. Adv.* **4**, e1700324 (2018)
45. T. Yoshihara, R. Katoh, A. Furube, Y. Tamaki, M. Murai, K. Hara, S. Murata, H. Arakawa, M. Tachiya, Identification of reactive species in photoexcited nanocrystalline TiO₂ films by wide-wavelength-range (400–2500 nm) transient absorption spectroscopy. *J. Phys. Chem. B* **108**, 3817–3823 (2004)
46. H. Ohkita et al., Charge carrier formation in polythiophene/fullerene blend films studied by transient absorption spectroscopy. *J. Am. Chem. Soc.* **130**, 3030–3042 (2008)
47. H.J. Lee et al., Assessing cholesterol storage in live cells and *C. elegans* by stimulated Raman scattering imaging of phenyl-diyne cholesterol. *Sci. Rep.* **5**, 7930 (2015)
48. J. Li, S. Condello, J. Thomes-Pepin, X. Ma, Y. Xia, T.D. Hurley, D. Matei, J.-X. Cheng, Lipid desaturation is a metabolic marker and therapeutic target of ovarian cancer stem cells. *Cell Stem Cell* **20**, 303–314.e305 (2017)
49. C. Zhang et al., Stimulated Raman scattering flow cytometry for label-free single-particle analysis. *Optica* **4**, 103–109 (2017)
50. S.W. Hell, Toward fluorescence nanoscopy. *Nat. Biotechnol.* **21**, 1347–1355 (2003)
51. T.A. Klar, S. Jakobs, M. Dyba, A. Egner, S.W. Hell, Fluorescence microscopy with diffraction resolution barrier broken by stimulated emission. *Proc. Natl. Acad. Sci. U.S.A.* **97**, 8206–8210 (2000)
52. B. Knoll, F. Keilmann, Near-field probing of vibrational absorption for chemical microscopy. *Nature* **399**, 134–137 (1999)
53. A. Dazzi, R. Prazeres, F. Glotin, J.M. Ortega, Local infrared microspectroscopy with sub-wavelength spatial resolution with an atomic force microscope tip used as a photothermal sensor. *Opt. Lett.* **30**, 2388–2390 (2005)
54. F. Lu, M. Jin, M.A. Belkin, Tip-enhanced infrared nanospectroscopy via molecular expansion force detection. *Nat. Photonics* **8**, 307–312 (2014)
55. A. Dazzi, C.B. Prater, AFM-IR: technology and applications in nanoscale infrared spectroscopy and chemical imaging. *Chem. Rev.* **117**, 5146–5173 (2017)
56. I. Amenabar, S. Poly, M. Goikoetxea, W. Nuansing, P. Lasch, R. Hillenbrand, Hyperspectral infrared nanoimaging of organic samples based on Fourier transform infrared nanospectroscopy. *Nat. Commun.* **8**, 14402 (2017)
57. J.P. Gordon, R.C.C. Leite, R.S. Moore, S.P.S. Porto, J.R. Whinnery, Long-transient effects in lasers with inserted liquid samples. *J. Appl. Phys.* **36**, 3–8 (1965)
58. M.E. Long, R.L. Swofford, A.C. Albrecht, Thermal lens technique: a new method of absorption spectroscopy. *Science* **191**, 183–185 (1976)
59. D. Zhang, C. Li, C. Zhang, M.N. Slipchenko, G. Eakins, J.-X. Cheng, Depth-resolved mid-infrared photothermal imaging of living cells and organisms with submicrometer spatial resolution. *Sci. Adv.* **2**, e1600521 (2016)
60. Z. Li, K. Aleshire, M. Kuno, G.V. Hartland, Super-resolution far-field infrared imaging by photothermal heterodyne imaging. *J. Phys. Chem. B* **121**, 8838–8846 (2017)

61. D.A. Nedosekin, E.I. Galanzha, E. Dervishi, A.S. Biris, V.P. Zharov, Super-resolution non-linear photothermal microscopy. *Small* **10**, 135–142 (2013)
62. P. Wang, M.N. Slipchenko, J. Mitchell, C. Yang, E.O. Potma, X. Xu, J.X. Cheng, Far-field imaging of non-fluorescent species with sub-diffraction resolution. *Nat. Photonics* **7**, 449–453 (2013)
63. W.R. Silva, C.T. Graefe, R.R. Frontiera, Toward label-free super-resolution microscopy. *ACS Photonics* **3**, 79–86 (2015)
64. R.C.C. Leite, S.P.S. Porto, T.C. Damen, The thermal lens effect as a power-limiting device. *Appl. Phys. Lett.* **10**, 100–101 (1967)
65. R.L. Carman, P.L. Kelley, Time dependence in the thermal blooming of laser beams. *Appl. Phys. Lett.* **12**, 241–243 (1968)
66. F. Dabby, R. Boyko, C. Shank, J. Whinnery, Short time-constant thermal self-defocusing of laser beams. *IEEE J. Quantum Electron.* **5**, 516–520 (1969)
67. J.N. Hayes, Thermal blooming of laser beams in fluids. *Appl. Opt.* **11**, 455–461 (1972)
68. H. Kleiman, R.W. O’Neil, Thermal blooming of pulsed laser radiation. *Appl. Phys. Lett.* **23**, 43–44 (1973)
69. R.C.C. Leite, R.S. Moore, J.R. Whinnery, Low absorption measurements by means of the thermal lens effect using an He-Ne laser. *Appl. Phys. Lett.* **5**, 141–143 (1964)
70. D. Solimini, Loss measurement of organic materials at 6328 Å. *J. Appl. Phys.* **37**, 3314–3315 (1966)
71. D. Solimini, Accuracy and sensitivity of the thermal lens method for measuring absorption. *Appl. Opt.* **5**, 1931–1939 (1966)
72. J. Stone, Measurements of the absorption of light in low-loss liquids. *J. Opt. Soc. Am.* **62**, 327–333 (1972)
73. A.C. Boccara, D. Fournier, J. Badoz, Thermo-optical spectroscopy: detection by the “mirage effect”. *Appl. Phys. Lett.* **36**, 130–132 (1980)
74. A. Gaiduk, P.V. Ruijgrok, M. Yorulmaz, M. Orrit, Detection limits in photothermal microscopy. *Chem. Sci.* **1**, 343–350 (2010)
75. C. Hu, J.R. Whinnery, New thermo-optical measurement method and a comparison with other methods. *Appl. Opt.* **12**, 72–79 (1973)
76. J.C. Murphy, L.C. Aamodt, Photothermal spectroscopy using optical beam probing: mirage effect. *J. Appl. Phys.* **51**, 4580–4588 (1980)
77. L.C. Aamodt, J.C. Murphy, photothermal measurements using a localized excitation source. *J. Appl. Phys.* **52**, 4903–4914 (1981)
78. A.C. Boccara, D. Fournier, W. Jackson, N.M. Amer, Sensitive photothermal deflection technique for measuring absorption in optically thin media. *Opt. Lett.* **5**, 377–379 (1980)
79. D. Boyer, P. Tamarat, A. Maali, B. Lounis, M. Orrit, Photothermal imaging of nanometer-sized metal particles among scatterers. *Science* **297**, 1160–1163 (2002)
80. S. Berciaud, L. Cognet, G.A. Blab, B. Lounis, Photothermal heterodyne imaging of individual nonfluorescent nanoclusters and nanocrystals. *Phys. Rev. Lett.* **93**, 257402 (2004)
81. S. Berciaud, D. Lasne, G.A. Blab, L. Cognet, B. Lounis, Photothermal heterodyne imaging of individual metallic nanoparticles: theory versus experiment. *Phys. Rev. B* **73**, 045424 (2006)
82. A. Gaiduk, M. Yorulmaz, P.V. Ruijgrok, M. Orrit, Room-temperature detection of a single molecule’s absorption by photothermal contrast. *Science* **330**, 353–356 (2010)
83. M. Harada, K. Iwamoto, T. Kitamori, T. Sawada, Photothermal microscopy with excitation and probe beams coaxial under the microscope and its application to microparticle analysis. *Anal. Chem.* **65**, 2938–2940 (1993)
84. C. Li, D. Zhang, M.N. Slipchenko, J.-X. Cheng, Mid-infrared photothermal imaging of active pharmaceutical ingredients at submicrometer spatial resolution. *Anal. Chem.* **89**, 4863–4867 (2017)
85. V.P. Zharov, Far-field photothermal microscopy beyond the diffraction limit. *Opt. Lett.* **28**, 1314–1316 (2003)
86. J. He, J. Miyazaki, N. Wang, H. Tsurui, T. Kobayashi, Biological imaging with nonlinear photothermal microscopy using a compact supercontinuum fiber laser source. *Opt. Express* **23**, 9762–9771 (2015)

87. J. He, J. Miyazaki, N. Wang, H. Tsurui, T. Kobayashi, Label-free imaging of melanoma with nonlinear photothermal microscopy. *Opt. Lett.* **40**, 1141–1144 (2015)
88. K. Nakata, H. Tsurui, T. Kobayashi, Further resolution enhancement of high-sensitivity laser scanning photothermal microscopy applied to mouse endogenous. *J. Appl. Phys.* **120**, 214901 (2016)
89. A. Mertiri, H. Altug, M.K. Hong, P. Mehta, J. Mertz, L.D. Ziegler, S. Erramilli, Nonlinear midinfrared photothermal spectroscopy using Zharov splitting and quantum cascade lasers. *ACS Photonics* **1**, 696–702 (2014)
90. V.P. Zharov, Ultrasharp nonlinear photothermal and photoacoustic resonances and holes beyond the spectral limit. *Nat. Photonics* **5**, 110–116 (2011)
91. D.O. Lapotko, T.Y.R. Romanovskaya, A. Shnip, V.P. Zharov, Photothermal time-resolved imaging of living cells. *Lasers Surg. Med.* **31**, 53–63 (2002)
92. J. Miyazaki, T. Kobayashi, Photothermal microscopy for high sensitivity and high resolution absorption contrast imaging of biological tissues. *Photonics* **4**(2), 32 (2017)
93. S. Arunkarthick, M.M. Bijeesh, G.K. Varier, M. Kowshik, P. Nandakumar, Laser scanning photothermal microscopy: fast detection and imaging of gold nanoparticles. *J. Microsc.* **256**, 111–116 (2014)
94. P. Vermeulen, L. Cognet, B. Lounis, Photothermal microscopy: optical detection of small absorbers in scattering environments. *J. Microsc.* **254**, 115–121 (2014)
95. M. Harada, M. Shibata, T. Kitamori, T. Sawada, Application of coaxial beam photothermal microscopy to the analysis of a single biological cell in water. *Anal. Chim. Acta* **299**, 343–347 (1995)
96. M. Tokeshi, M. Uchida, A. Hibara, T. Sawada, T. Kitamori, Determination of subzeptomole amounts of nonfluorescent molecules using a thermal lens microscope: subsingle-molecule determination. *Anal. Chem.* **73**, 2112–2116 (2001)
97. T.X. Ding, L. Hou, H.V.D. Meer, A.P. Alivisatos, M. Orrit, Hundreds-fold sensitivity enhancement of photothermal microscopy in near-critical Xenon. *J. Phys. Chem. Lett.* **7**, 2524–2529 (2016)
98. S. Lu, W. Min, S. Chong, G.R. Holtom, X.S. Xie, Label-free imaging of heme proteins with two-photon excited photothermal lens microscopy. *Appl. Phys. Lett.* **96**, 113701 (2010)
99. P.M. Champion, G.J. Perreault, Observation and quantitation of light emission from cytochrome c using Soret band laser excitation. *J. Chem. Phys.* **75**, 490–491 (1981)
100. R. Jimenez, F.E. Romesberg, Excited state dynamics and heterogeneity of folded and unfolded states of cytochrome c. *J. Chem. Phys. B* **106**, 9172–9180 (2002)
101. J. Miyazaki, H. Tsurui, K. Kawasumi, T. Kobayashi, Simultaneous dual-wavelength imaging of nonfluorescent tissues with 3D subdiffraction photothermal microscopy. *Opt. Express* **23**, 3647–3656 (2015)
102. V.P. Zharov, D.O. Lapotko, Photothermal imaging of nanoparticles and cells. *IEEE J. Sel. Top. Quantum Electron.* **11**, 733–751 (2005)
103. S.E. Braslavsky, G.E. Heibel, Time-resolved photothermal and photoacoustic methods applied to photoinduced processes in solution. *Chem. Rev.* **92**, 1381–1410 (1992)
104. D.O. Lapotko, V.P. Zharov, Spectral evaluation of laser-induced cell damage with photothermal microscopy. *Lasers Surg. Med.* **36**, 22–30 (2005)
105. D. Lasne, G.A. Blab, S. Berciaud, M. Heine, L. Groc, D. Choquet, L. Cognet, B. Lounis, Single nanoparticle photothermal tracking (SNaPT) of 5-nm gold beads in live cells. *Biophys. J.* **91**, 4598–4604 (2006)
106. W.W. Coblenz, *Investigations of Infra-red Spectra* (Carnegie Institution of Washington, Washington, D.C., 1905), p. 3 v (35, 65, 97)
107. K.L.A. Chan, S.G. Kazarian, A. Mavraki, D.R. Williams, Fourier transform infrared imaging of human hair with a high spatial resolution without the use of a synchrotron. *Appl. Spectrosc.* **59**, 149–155 (2005)
108. P. Heraud, S. Caine, G. Sanson, R. Gleadow, B.R. Wood, D. McNaughton, Focal plane array infrared imaging: a new way to analyse leaf tissue. *New Phytol.* **173**, 216–225 (2006)
109. J. Chalmers, P. Griffiths, *Handbook of Vibrational Spectroscopy, 5 volumes set* (Wiley, 2002)

110. R. Furstenberg, C.A. Kendziora, M.R. Papantonakis, V. Nguyen, R. McGill, Chemical imaging using infrared photothermal microspectroscopy, in *Next-Generation Spectroscopic Technologies V* (International Society for Optics and Photonics, Baltimore, MD, 2012), p. 837411
111. A. Tredicucci, C. Gmachl, F. Capasso, D.L. Sivco, A.L. Hutchinson, A.Y. Cho, A multiwavelength semiconductor laser. *Nature* **396**, 350–353 (1998)
112. C. Gmachl, D.L. Sivco, R. Colombelli, F. Capasso, A.Y. Cho, Ultra-broadband semiconductor laser. *Nature* **415**, 883–887 (2002)
113. Y. Yao, A.J. Hoffman, C.F. Gmachl, Mid-infrared quantum cascade lasers. *Nat. Photonics* **6**, 432–439 (2012)
114. F. Rotermund, V. Petrov, F. Noack, Difference-frequency generation of intense femtosecond pulses in the mid-IR (4–12 μm) using HgGa_2S_4 and AgGaS_2 . *Opt. Commun.* **185**, 177–183 (2000)
115. C. Erny, K. Moutzouris, J. Biegert, D. K hlke, F. Adler, A. Leitenstorfer, U. Keller, Mid-infrared difference-frequency generation of ultrashort pulses tunable between 3.2 and 4.8 μm from a compact fiber source. *Opt. Lett.* **32**, 1138–1140 (2007)
116. Y. Bai, D. Zhang, C. Li, C. Liu, J.-X. Cheng, Bond-selective imaging of cells by mid-infrared photothermal microscopy in high wavenumber region. *J. Phys. Chem. B* **121**, 10249–10255 (2017)
117. L. Wei, Y. Yu, Y. Shen, M.C. Wang, W. Min, Vibrational imaging of newly synthesized proteins in live cells by stimulated Raman scattering microscopy. *Proc. Natl. Acad. Sci. U.S.A.* **110**, 11226 (2013)
118. A. Totachawattana, S. Erramilli, M.Y. Sander, Optimization of mid-IR photothermal imaging for tissue analysis, in *SPIE Optical Engineering + Applications* (SPIE, 2015), p. 7
119. T.J. Huffman, R. Furstenberg, C.A. Kendziora, R.A. McGill, Infrared spectroscopy below the diffraction limit using an optical probe, in *SPIE Commercial + Scientific Sensing and Imaging* (SPIE, 2018), p. 6
120. D. Bashford, M. Karplus, pKa's of ionizable groups in proteins: atomic detail from a continuum electrostatic model. *Biochemistry* **29**, 10219–10225 (1990)
121. A. Totachawattana, M.K. Hong, S. Erramilli, M.Y. Sander, Multiple bifurcations with signal enhancement in nonlinear mid-infrared thermal lens spectroscopy. *Analyst* **142**, 1882–1890 (2017)
122. M. Yorulmaz, S. Nizzero, A. Hoggard, L.-Y. Wang, Y.-Y. Cai, M.-N. Su, W.-S. Chang, S. Link, Single-particle absorption spectroscopy by photothermal contrast. *Nano Lett.* **15**, 3041 (2015)
123. P. Zijlstra, P.M.R. Paulo, M. Orrit, Optical detection of single non-absorbing molecules using the surface plasmon resonance of a gold nanorod. *Nat. Nanotechnol.* **7**, 379–382 (2012)
124. L.K. Bogart, A. Taylor, Y. Cesbron, P. Murray, R. L vy, Photothermal microscopy of the core of dextran-coated iron oxide nanoparticles during cell uptake. *ACS Nano* **6**, 5961–5971 (2012)
125. F. Kitagawa, Y. Akimoto, K. Otsuka, Label-free detection of amino acids using gold nanoparticles in electrokinetic chromatography–thermal lens microscopy. *J. Chromatogr. A* **1216**, 2943–2946 (2009)
126. J. Hartmann, P. Voigt, M. Reichling, Measuring local thermal conductivity in polycrystalline diamond with a high resolution photothermal microscope. *J. Appl. Phys.* **81**, 2966–2972 (1997)
127. M. Reichling, E. Welsch, A. Duparre, E. Matthias, Laterally and depth resolved photothermal absorption measurements on ZrO_2 and MgF_2 single-layer films, in *Optical Systems Design '92* (SPIE, 1993), p. 11
128. A. Doring, M. Commandr , C. Fossati, B. Bertussi, J.-Y. Natoli, J.-L. Rullier, H. Bercegol, P. Bouchut, Integrated photothermal microscope and laser damage test facility for in-situ investigation of nanodefekt induced damage. *Opt. Express* **11**, 2497–2501 (2003)
129. R. Chatterjee, I.M. Pavlovetc, K. Aleshire, M. Kuno, Single semiconductor nanostructure extinction spectroscopy. *J. Phys. Chem. C* **122**, 16443–16463 (2018)

130. V.P. Zharov, E.I. Galanzha, V.V. Tuchin, Photothermal imaging of moving cells in lymph and blood flow in vivo, in *Biomedical Optics 2004* (SPIE, 2004), p. 11
131. A.V. Brusnichkin, D.A. Nedosekin, E.I. Galanzha, Y.A. Vladimirov, E.F. Shevtsova, M.A. Proskurnin, V.P. Zharov, Ultrasensitive label-free photothermal imaging, spectral identification, and quantification of cytochrome c in mitochondria, live cells, and solutions. *J. Biophotonics* **3**, 791–806 (2010)
132. D.A. Nedosekin, E.V. Shashkov, E.I. Galanzha, L. Hennings, V.P. Zharov, Photothermal multispectral image cytometry for quantitative histology of nanoparticles and micrometastasis in intact, stained and selectively burned tissues. *Cytometry Part A* **77A**, 1049–1058 (2010)
133. J. Miyazaki, H. Tsurui, K. Kawasumi, T. Kobayashi, Sensitivity enhancement of photothermal microscopy with radially segmented balanced detection. *Opt. Lett.* **40**, 479–482 (2015)
134. J. Miyazaki, Y. Toumon, Experimental evaluation of temperature increase and associated detection sensitivity in shot noise-limited photothermal microscopy. *Opt. Commun.* **430**, 170–175 (2019)
135. T. Tomimatsu, J. Miyazaki, Y. Kano, T. Kobayashi, Photothermal imaging of skeletal muscle mitochondria. *Biomed. Opt. Express* **8**, 2965–2975 (2017)
136. J. Miyazaki, H. Tsurui, T. Kobayashi, Reduction of distortion in photothermal microscopy and its application to the high-resolution three-dimensional imaging of nonfluorescent tissues. *Biomed. Opt. Express* **6**, 3217–3224 (2015)
137. J. He, N. Wang, H. Tsurui, M. Kato, M. Iida, T. Kobayashi, Noninvasive, label-free, three-dimensional imaging of melanoma with confocal photothermal microscopy: differentiate malignant melanoma from benign tumor tissue. *Sci. Rep.* **6**, 30209 (2016)
138. A. Totachawattana, M.S. Regan, N.Y.R. Agar, S. Erramilli, M.Y. Sander, Label-free mid-Infrared photothermal spectroscopy and imaging of neurological tissue, in *Conference on Lasers and Electro-optics* (Optical Society of America, San Jose, California, 2017), p. ATu4A.3
139. A. Totachawattana, D. Huang, L. Li, K.A. Brown, S. Erramilli, M.Y. Sander, Robust mid-infrared photothermal imaging system for characterization of thin films at high spatial resolution, in *Conference on Lasers and Electro-optics* (Optical Society of America, San Jose, California, 2017), p. JW2A.47
140. R. Chatterjee, I.M. Pavlovetc, K. Aleshire, G.V. Hartland, M. Kuno, Subdiffraction infrared imaging of mixed cation perovskites: probing local cation heterogeneities. *ACS Energy Lett.* **3**, 469–475 (2018)
141. J.J. Bae et al., Sensitive photo-thermal response of graphene oxide for mid-infrared detection. *Nanoscale* **7**, 15695–15700 (2015)
142. J.W. Thomas, A. Polak, G.M. Bonner, S. Enderle, M.H. Dunn, D.J.M. Stothard, Optical parametric oscillator-based trace detection of gases in the mid-infrared region using phase-fluctuation optical heterodyne spectroscopy, in *SPIE Defense + Security* (SPIE, 2018), p. 9
143. Z. Li, Z. Wang, F. Yang, W. Jin, W. Ren, Mid-infrared fiber-optic photothermal interferometry. *Opt. Lett.* **42**, 3718–3721 (2017)
144. R.C. Miller, Optical second harmonic generation in piezoelectric crystals. *Appl. Phys. Lett.* **5**, 17–19 (1964)
145. K. Wang, C. Xu, Tunable high-energy soliton pulse generation from a large-mode-area fiber and its application to third harmonic generation microscopy. *Appl. Phys. Lett.* **99**, 071112 (2011)
146. W. Denk, J.H. Strickler, W.W. Webb, Two-photon laser scanning fluorescence microscopy. *Science* **248**, 73–76 (1990)
147. C.Y. Dong, P.T. So, T. French, E. Gratton, Fluorescence lifetime imaging by asynchronous pump-probe microscopy. *Biophys. J.* **69**, 2234–2242 (1995)
148. D.Y. Davydova, A. Cadena, D. Akimov, B. Dietzek, Transient absorption microscopy: advances in chemical imaging of photoinduced dynamics. *Laser Photonics Rev.* **10**, 62–81 (2015)
149. S.W. Hell, M. Kroug, Ground-state-depletion fluorescence microscopy: a concept for breaking the diffraction resolution limit. *Appl. Phys. B* **60**, 495–497 (1995)

150. S. Bretschneider, C. Eggeling, S.W. Hell, Breaking the diffraction barrier in fluorescence microscopy by optical shelving. *Phys. Rev. Lett.* **98**, 218103 (2007)
151. Q. Bao, H. Zhang, Y. Wang, Z. Ni, Y. Yan, Z.X. Shen, K.P. Loh, D.Y. Tang, Atomic-layer graphene as a saturable absorber for ultrafast pulsed lasers. *Adv. Funct. Mater.* **19**, 3077–3083 (2009)
152. Z. Sun, T. Hasan, F. Torrisi, D. Popa, G. Privitera, F. Wang, F. Bonaccorso, D.M. Basko, A.C. Ferrari, Graphene mode-locked ultrafast laser. *ACS Nano* **4**, 803–810 (2010)
153. F.T. Vasko, Saturation of interband absorption in graphene. *Phys. Rev. B* **82**, 245422 (2010)
154. A.G. Rozhin, Y. Sakakibara, H. Kataura, S. Matsuzaki, K. Ishida, Y. Achiba, M. Tokumoto, Anisotropic saturable absorption of single-wall carbon nanotubes aligned in polyvinyl alcohol. *Chem. Phys. Lett.* **405**, 288–293 (2005)
155. P. Avouris, M. Freitag, V. Perebeinos, Carbon-nanotube photonics and optoelectronics. *Nat. Photonics* **2**, 341–350 (2008)
156. I.H. Baek et al., Single-walled carbon nanotube saturable absorber assisted high-power mode-locking of a Ti:sapphire laser. *Opt. Express* **19**, 7833–7838 (2011)
157. C.P. Singh, K.S. Bindra, G.M. Bhalerao, S.M. Oak, Investigation of optical limiting in iron oxide nanoparticles. *Opt. Express* **16**, 8440–8450 (2008)
158. L. Irimpan, V.P.N. Nampoore, P. Radhakrishnan, Spectral and nonlinear optical characteristics of nanocomposites of ZnO–CdS. *J. Appl. Phys.* **103**, 094914 (2008)
159. L. Gong, H. Wang, Breaking the diffraction limit by saturation in stimulated-Raman-scattering microscopy: a theoretical study. *Phys. Rev. A* **90**, 013818 (2014)
160. B. Liu, H.J. Lee, D. Zhang, C.-S. Liao, N. Ji, Y. Xia, J.-X. Cheng, Label-free spectroscopic detection of membrane potential using stimulated Raman scattering. *Appl. Phys. Lett.* **106** (2015)